

<http://researchcommons.waikato.ac.nz/>

Research Commons at the University of Waikato

Copyright Statement:

The digital copy of this thesis is protected by the Copyright Act 1994 (New Zealand).

The thesis may be consulted by you, provided you comply with the provisions of the Act and the following conditions of use:

- Any use you make of these documents or images must be for research or private study purposes only, and you may not make them available to any other person.
- Authors control the copyright of their thesis. You will recognise the author's right to be identified as the author of the thesis, and due acknowledgement will be made to the author where appropriate.
- You will obtain the author's permission before publishing any material from the thesis.

Nature, Distribution, Origin and Economics of Glaucinite in Carbonate-Phosphate-Glaucinite Surficial Deposits on Central Chatham Rise, Southwest Pacific

A thesis submitted in partial fulfilment
of the requirements for the degree
of

**Master of Science
in Earth and Ocean Sciences**
at

The University of Waikato

by

Anna Shanti Lawless

The University of Waikato
2012



THE UNIVERSITY OF
WAIKATO
Te Whare Wānanga o Waikato

ABSTRACT

Chatham Rise is a broad, elongated submarine platform that extends 1100 km out into the Southwest Pacific off eastern South Island. The surficial sediments on the central portion of the Rise at depths of 200-500 m include significant concentrations of the mineral glauconite (10-80 wt%) associated with skeletal carbonate, fine terrigenous material and locally abundant phosphatic nodules. This is the first study to fully analyse the nature, origin and economic potential of the glauconite component. Sub-bottom 3.5 kHz profiles have established the distribution, geometry and thickness (10-200 cm) of the surficial deposits, which overlie partially indurated Oligocene chalk of probable Whaingaroan age (~34-27 Ma). 137 grab, dredge or piston core samples have been analysed for their texture, mineralogy and geochemistry, which has produced a new surficial sediment map for the central Chatham Rise.

Glauconite most commonly occurs as dark green to black, very fine to fine sand-sized (0.2 mm), polished ovoidal and lobate pellets, and less commonly as infills within foraminiferal tests or as variably replaced rock fragments and phosphatic clasts. Full physical analysis reveals seven morphological types of glauconite including, in order of decreasing abundance, ovoidal, lobate, composite, internal molds, fossil casts, pigmentary, tabular and pellets within rock fragments. Their internal fabrics are dominated by random microcrystalline varieties with some oriented fibroradiating rim and skeletal infill types. Other notable features of some glauconite pellets include their expansion cracks, opaque inclusions and variable degrees of limonitisation. XRF/XRD analyses reveal mainly diagenetically mature varieties having elevated K_2O (7-9 wt%) and Fe_2O_3 (19-23 wt%) values, and a dominant 10\AA glauconitic mica structure involving from 10-20% expandable smectite layers.

K-Ar dates on pellets indicate a Late Miocene age (av. 5.75 Ma). This “old” age, as well as the clear evidence of reworking shown by the dominance of smooth polished ovoidal grains, mean that the central Chatham Rise glauconites are predominantly allogenic (i.e. derived/reworked), and neither strictly authigenic nor *in situ*, despite occurring in “modern” seafloor deposits. The formation of

glaucinite is linked to prominent upwelling within the Subtropical Front (STF) zone over the Rise in the Late Miocene, and the attendant heightened primary productivity, bacterial activity and nutrients associated with widespread biogenic blooms at that time. The source of the smectite required for glauconite formation could have been from the devitrification of volcanic ash from diverse eruptive centres, or through “neof ormation”/authigenic precipitation within pore water solutions of carbonate-rich waters in the Oligocene/Miocene chalk substrate. Glauconite formation largely ceased after the Late Miocene due to an increase in terrigenous input, a reduced smectite source, and a major period of lowered sea level associated with Antarctic ice sheet growth. The “modern” Chatham glauconite pellets were sourced from submarine erosion of the former Late Miocene sediments and have been dispersed by intensified bottom current circulation at times of lowered sea level within the complex STF over Chatham Rise, and possibly ice scouring. Effectively there exists a widespread “Chatham unconformity” (mid-Oligocene to Recent) which cuts out most of the last 30 myr of the sedimentary record on central Chatham Rise, except for the highly condensed surficial deposits whose glauconite grains formed 5-6 Ma, in the Late Miocene. This long-lasting “Chatham unconformity” is a greatly extended version of the well documented Oligocene Marshall Paraconformity.

The thickness of the surficial sediment cover on central Chatham Rise ranges from 0.06-1.35 m. By using a conservative estimate of 0.5 m thick, and the wt% of glauconite within the sediment cover, a resource estimate of the glauconite has been made for various areas. In the most glauconite-rich area (>50 wt% glauconite) in the vicinity of Reserve Bank in 200-300 m water depths, which has an aerial extend of 4,500 km², the glauconite resource amounts to about 2 Bt. The Chatham Rise glauconites have substantial economic potential as a potash fertiliser in support of the strong agricultural-based economy of New Zealand.

Glauconite is widespread in many Late Cretaceous-Cenozoic sedimentary deposits in the New Zealand rock record and the Chatham Rise occurrences provide a useful uniformitarian analogue for at least some of these.

ACKNOWLEDGEMENTS

First and foremost I would like to thank my chief supervisor, Professor Cam Nelson, who is the main person that this thesis could not have been finished without. Cam is especially thanked for the endless time and energy spent editing with the famous “red pen”, as well as his continued encouragement. I also thank my other supervisor Dr Scott Nodder (NIWA, Wellington), for his help in collecting and sorting samples, and for his help during my time spent at NIWA, Wellington and on board the *R.V. Tangaroa*.

Secondly, I must thank all those involved in the technical and analytical support during this study. This includes Associate Professor Roger Briggs, Dr Steve Hood, Renat Radosinsky, Dr Ganqing Xu, Annette Rodgers, Dr Rochelle Hansen, and Chris McKinnon from The University of Waikato, for help with sample preparation and the use of equipment. Ritchie Simms (University of Auckland) kindly provided assistance in using the electron probe micro-analyser, and Kevin Mackay (NIWA, Wellington) produced my GIS base map. Big thanks go to Dr Horst Zwingmann (CSRIO, Perth, Australia) for the absolute dating of samples. And also to my fellow MSc students – Megan, Kirsty, Simon, Josh, Stephanie, Mike, Danielle and Karl – and especially for the distracting conversations and long lunch breaks! Simon and Josh are particularly thanked for their help with GIS.

Thirdly, a big thank you to NIWA for their logistical support during my time spent in Wellington, and during my time spent on board the *R.V. Tangaroa*. A very special thanks to Chris Castle and Dr Robin Falconer of Chatham Rock Phosphate Ltd for their personal support, funding assistance, and encouragement during this project.

The funding support for this study provided by AUSIMM, Brian Perry Charitable Trust, Chatham Rock Phosphate Ltd (i.e. Widespread Energy Ltd), and The University of Waikato is gratefully acknowledged.

Lastly, I would like to thank my family, especially my parents David and Alison Lawless for their love and support. Also to all my friends for their distractions from thesis work, laughter and good times, and in particular my flatmates Tarryn and Rach and of course Toby who at times got the full force of my frustrations brought home from the office!

TABLE OF CONTENTS

	Page
Abstract	iii
Acknowledgements	v
Table of contents	vii
List of figures	xi
List of tables	xvii
Chapter 1 INTRODUCTION	1
1.1 BACKGROUND	1
1.2 STUDY AREA	2
1.3 AIMS OF THIS STUDY	4
1.4 GENERAL PROCEDURES ADOPTED IN THIS STUDY	5
1.5 THESIS CHAPTER FORMAT	7
Chapter 2 GEOLOGICAL AND PHYSICAL SETTING	9
2.1 INTRODUCTION	9
2.2 TOPOGRAPHY AND STRUCTURE	9
2.3 BEDROCK GEOLOGY AND GEOLGICAL HISTORY	17
2.4 CURRENT CIRCULATION PATTERNS AND OCEANIC CLIMATE	23
2.4.1 Current circulation – subtropical front	23
2.4.2 Water movements and speeds	25
2.4.3 Tidal currents	26
2.4.4 Climate	26
2.4.5 General bottom sediment facies	27
Chapter 3 SURFICIAL SEDIMENT FACIES	29
3.1 INTRODUCTION	29
3.2 SURFICIAL SEDIMENTS	29
3.2.1 Munsell colour	31
3.2.2 Texture	33
3.2.3 XRD mineralogy	39
3.2.3A Bulk mineralogy	39
3.2.3B Clay mineralogy	44
3.2.4 Geochemistry	50
3.2.4A XRF elemental composition	50
3.2.4B CaCO ₃ content	56
3.2.5 Petrography	60
3.2.6 SEM	69
3.2.7 Surficial sediment facies map	72
3.3 SHORT CORE STRATIGRAPHY	75
3.4 OLIGOCENE CHALK	77
Chapter 4 ECHO-CHARACTER OF BOTTOM SEDIMENTS	83
4.1 INTRODUCTION	83
4.2 METHODS	83
4.3 CLASSIFICATION TERMINOLOGY	86
4.3.1 Echo-type A	86
4.3.2 Echo-type B	87
4.3.3 Echo-type C	87

4.3.4	Echo-type D	87
4.4	ECHO-CHARACTER MAPS	88
4.4.1	Echo-character	88
4.4.2	Seafloor morphology	90
4.4.3	Sediment thickness	92
Chapter 5	LITERATURE REVIEW OF GLAUCONITE	95
5.1	INTRODUCTION	95
5.2	GLAUCONITE DEFINITION	95
5.3	GENERAL AND PHYSICAL PROPERTIES	96
5.4	EXTERNAL MORPHOLOGY VARIETIES	97
5.5	INTERNAL FABRICS	100
5.6	MINERALOGY AND STRUCTURE	102
5.7	GEOCHEMICAL COMPOSITION	104
5.8	THEORIES OF ORIGIN(S)	107
5.9	SEDIMENTARY CONDITIONS OF FORMATION	109
5.9.1	Water temperature	110
5.9.2	Eh conditions	110
5.9.3	pH conditions	111
5.9.4	Water depth	111
5.9.5	Turbulence	111
5.9.6	Sediment accumulation rate	111
5.9.7	Organic matter	112
5.9.8	Age preferences	112
Chapter 6	PHYSICAL PROPERTIES OF GLAUCONITE	113
6.1	INTRODUCTION	113
6.2	METHODS	114
6.3	DISTRIBUTION	120
6.4	COLOUR	122
6.5	SIZE	125
6.6	MORPHOLOGY	126
6.6.1	Ovoidal	128
6.6.2	Lobate	128
6.6.3	Composite	130
6.6.4	Fossil casts and internal molds	131
6.6.5	Glaucinite pellets within rock fragments	132
6.6.6	Tabular/discoidal and pigmentary	132
6.6.7	Shape	134
6.7	INTERNAL FABRICS	134
6.7.1	Random microcrystalline	136
6.7.2	Oriented fibroradiating rims	136
6.7.3	Skeletal infilled grains	137
Chapter 7	MINERALOGY OF GLAUCONITE	139
7.1	INTRODUCTION	139
7.2	METHODS	140
7.3	X-RAY DIFFRACTION (XRD) ANALYSIS	141
7.3.1	Air-dried oriented mount peak pattern	141
7.3.2	Expandable smectite layers	144
7.3.2A	Presence of expandable smectite layers	144

7.3.2B	Peak shape related to the % expandables calculated from potassium content	148
7.3.2C	% expandables from glycolated samples	149
7.3.3	Ordering and structure	154
Chapter 8	GEOCHEMISTRY OF GLAUCONITE	155
8.1	INTRODUCTION	155
8.2	METHODS	156
8.3	X-RAY FLUORESCENCE (XRF) RESULTS	157
8.3.1	Major elements	160
8.3.2	Trace elements	163
8.4	GRAIN SPECIFIC MAJOR ELEMENTS	168
8.4.1	Bottle green ovoidal grains	169
8.4.2	Brown grains	171
8.4.3	Fibroradiated oriented rims	172
8.4.4	Foraminiferal infills	175
8.4.5	Glaucinitised phosphatic grains	177
Chapter 9	AGE OF GLAUCONITE	181
9.1	INTRODUCTION	181
9.2	METHODS	181
9.3	K-AR GLAUCONITE AGE RESULTS	183
Chapter 10	ECONOMIC POTENTIAL OF GLAUCONITE	187
10.1	INTRODUCTION	187
10.2	USES OF GLAUCONITE	187
10.2.1	Fertiliser	188
10.2.2	Water treatment	189
10.2.3	Other uses	190
10.3	RESOURCE ESTIMATE	191
Chapter 11	DISCUSSION OF GLAUCONITE	195
11.1	INTRODUCTION	195
11.2	NATURE OF GLAUCONITE	195
11.2.1	Occurrence and distribution of glauconite	195
11.2.2	Physical properties	198
11.2.3	Mineralogy	203
11.2.4	Geochemistry	204
11.2.5	Age	211
11.3	ORIGIN(S) OF GLAUCONITE	211
11.3.1	Conditions and place of formation	212
11.3.2	Glaucinitisation process	214
11.3.3	Smectite source(s) for glauconitisation	215
11.3.3A	Alteration of volcanic glass into smectite	218
11.3.3B	“Neoformation” of carbonate substrates as smectite source	221
11.3.4	Potassium and iron source(s)	222
11.3.5	Allogenic versus authigenic glauconite	223
11.3.6	Chatham unconformity	226
11.4	ECONOMIC POTENTIAL OF GLAUCONITE	227
11.5	ONLAND NEW ZEALAND TERTIARY GLAUCONITE	231
11.5.1	Physical and morphological comparison	232
11.5.2	Geochemical comparison	235

Chapter 12	SUMMARY AND CONCLUSIONS	239
12.1	ECHO CHARACTER	239
12.2	BULK SEDIMENT FACIES	239
12.3	NATURE OF GLAUCONITE	240
12.4	AGE AND ORIGIN	240
12.5	<i>IN SITU</i> VERSUS ALLOGENIC	241
12.6	“CHATHAM UNCONFORMITY”	241
12.7	ECONOMIC POTENTIAL	242
12.8	ONLAND NEW ZEALAND TERTIARY GLAUCONITE	242
12.9	FUTURE RESEARCH	242
REFERENCE LIST		245
APPENDICES		
Appendix I:	Sample list	255
Appendix II-A:	Munsell colours, glauconite abundance and % blackness	259
Appendix II-B:	Samples used in various laboratory techniques	262
Appendix II-C:	Bulk sample texture	263
Appendix II-D:	% gravel, sand and mud fractions	264
Appendix II-E:	XRD mineralogy	265
Appendix II-F:	Geochemistry	266
Appendix II-G:	CaCO ₃ % acid digestion results	267
Appendix II-H:	Bulk surficial sample photos	268
Appendix III:	Glauconite physical properties	269
Appendix IV:	XRD raw results	270
Appendix V:	Glauconite geochemistry	271
Appendix VI:	Age data	277
Appendix VII:	Economics	278

LIST OF FIGURES

Figure 1.1:	Chatham Rise location off southeastern New Zealand.	3
Figure 1.2:	Flow chart demonstrating the main practical and analytical procedures adopted in carrying out this study.	6
Figure 2.1:	Topography of Chatham Rise in relation to New Zealand.	11
Figure 2.2:	Location of six bathymetric transects (A-F).	14
Figure 2.3:	Topographic profiles along transect A-F.	16
Figure 2.4:	Geological stratigraphic sequence, compared to geology of Chatham Islands.	21
Figure 2.5:	Key for the geological sections in Figure 2.4.	22
Figure 2.6:	Oceanographic setting of Chatham Rise.	25
Figure 3.1:	Location of 137 sediment samples.	30
Figure 3.2:	Simplified Munsell colours across all 137 bulk samples.	31
Figure 3.3:	Pie chart displaying the relative abundance of glauconite visually estimated in the dried 137 bulk samples.	32
Figure 3.4:	Visual estimate of % blackness in each of the 137 bulk samples.	32
Figure 3.5:	Relationship between Munsell colour and visually estimated glauconite content in all 137 bulk samples.	33
Figure 3.6:	Percentages of Folk's (1968) sediment textural classes for all 137 bulk samples.	34
Figure 3.7:	Percent textural size classes in surficial sediments from central Chatham Rise. A: Sand, B: Silt, C: Clay.	35
Figure 3.8:	A: Percent gravel, B: Median sediment texture, C: Folk's (1968) sediment sorting classes for surficial sediment.	36
Figure 3.9:	Distribution of Folk's (1968) sediment textural classes.	37
Figure 3.10:	Relationship between percent glauconite and percent sand sized grains in 39 glauconitic sediment samples.	39
Figure 3.11:	XRD scan of G36 bulk powdered sediment sample.	41
Figure 3.12:	XRD scan of A897 bulk powdered sediment sample.	42
Figure 3.13:	XRD scan of Q356 bulk powdered sediment sample.	43
Figure 3.14:	Movement of the clay mineral (001) XRD peak under different treatments.	45
Figure 3.15:	Air-dried untreated oriented mount XRD scan of mud fraction from Q356.	47
Figure 3.16:	Glycolated oriented mount XRD scan of mud fraction from Q356.	48
Figure 3.17:	Heated oriented mount XRD scan of mud fraction from Q356.	49
Figure 3.18:	Average amount of major elements in the three main surficial sediment textural classes.	55
Figure 3.19:	Average amounts of trace elements in the three main surficial sediment textural classes.	55
Figure 3.20:	Correlation between % CaCO_3 from acid digestion and the XRD calcite $29.4^\circ 2\theta$ peak counts in 10 bulk samples.	57
Figure 3.21:	Distribution of the CaCO_3 content.	59
Figure 3.22:	Average abundance of glauconite, carbonate material, siliciclasts and phosphatic grains across all 15 detrital sand thin sections.	63

Figure 3.23:	Photomicrographs of six different bulk sand thin sections of sediments.	65
Figure 3.24:	Photomicrographs of six different bulk sand thin sections of sediments.	66
Figure 3.25:	Photomicrographs of selected grains in six different bulk sand thin sections of sediments.	67
Figure 3.26:	Relationship between percent carbonate grains and percent glauconite in 15 detrital thin sections.	68
Figure 3.27:	SEM images of some grain types in the bulk mud fraction from sample A891.	70
Figure 3.28:	SEM images of some grain types in the bulk mud fraction from sample Q328.	71
Figure 3.29:	McDougall's (1982) legend for Bounty Sediments map of Chatham Rise.	72
Figure 3.30:	Surficial sediment map for central Chatham Rise extracted from the Bounty Sediment map of McDougall (1982).	73
Figure 3.31:	Surficial sediment facies map for central Chatham Rise developed in this study.	74
Figure 3.32:	Thickness of the surficial sediment deposits in 26 cores.	75
Figure 3.33:	Location of the surficial sediment deposits in 26 cores.	76
Figure 3.34:	XRD scan result for Oligocene chalk sample at Q317.	78
Figure 3.35:	XRD scan result for Oligocene chalk sample at G228.	79
Figure 3.36:	SEM image of Oligocene chalk sample Q317.	80
Figure 3.37:	SEM image of Oligocene chalk sample Q317.	81
Figure 3.38:	SEM image of sample Q317 Oligocene chalk following acid digestion and removal of carbonate material.	81
Figure 4.1:	Location of 3.5 kHz echogram profiles.	85
Figure 4.2:	Example of an echo-type A.	86
Figure 4.3:	Example of an echo-type B.	87
Figure 4.4:	Example of an echo-type C.	87
Figure 4.5:	Example of an echo-type D.	88
Figure 4.6:	Echo-character map of central Chatham Rise.	89
Figure 4.7:	Example of flat-lying seafloor morphology.	90
Figure 4.8:	Example of irregular seafloor morphology.	90
Figure 4.9:	Seafloor morphology of central Chatham Rise.	91
Figure 4.10:	Sediment thickness map of central Chatham Rise.	93
Figure 6.1:	Photomicrographs of examples of the various types of glauconite.	114
Figure 6.2:	Distribution of glauconite in the <2 mm fraction.	121
Figure 6.3:	A: Dark green to black glauconite grains. B: Light to bottle green glauconite grains.	122
Figure 6.4:	A: Photomicrograph of bottle green glauconite pellets. B: Photomicrograph of yellow-brown green glauconite pellets.	123
Figure 6.5:	Abundance of colour types within the 21 glauconite thin sections.	123
Figure 6.6:	Spread of the abundance of colour assemblages within all 21 glauconite thin sections.	124
Figure 6.7:	A and B: Photomicrographs of limonitised grain. C and D: Photomicrographs of opaque inclusions within glauconite pellets.	124

Figure 6.8:	Average abundance of limonitised glauconite grains (A) and glauconite with opaque inclusions (B) across all 21 glauconite thin sections.	125
Figure 6.9:	Abundance of size modes (A), minimum sizes (B) and maximum sizes (C) of the glauconite pellets within the 21 glauconite thin sections.	126
Figure 6.10:	Estimate of the abundance of the different morphological types of glauconite on central Chatham Rise.	127
Figure 6.11:	Glauconite showing ovoidal morphologies.	128
Figure 6.12:	Glauconite showing lobate morphologies.	129
Figure 6.13:	Average abundance of lobate glauconite based on the occurrence of expansion cracks in glauconite pellets across all 21 glauconite thin sections.	130
Figure 6.14:	SEM images of sample A891.	130
Figure 6.15:	Average abundance of composite glauconite i.e. glauconitised phosphatic grains, across all 21 glauconite thin sections.	131
Figure 6.16:	Average abundance of glauconitised infilled skeletal grains across all 21 analysed glauconite thin sections.	131
Figure 6.17:	Average abundance of glauconite pellets within rock fragments across all 21 analysed glauconite thin sections.	132
Figure 6.18:	SEM image of a tabular/discoidal glauconite grain.	132
Figure 6.19:	A and B: Cross-section photos of pigmentary glauconite rims on slabbed phosphorite nodules. C (PPL) and D (CL), and E (PPL) and F (CL): Photomicrographs representing a cross-section of pigmentary glauconite rims on phosphorite nodules.	133
Figure 6.20:	Average abundance of glauconite pelletal shapes across all 21 analysed glauconite thin sections.	134
Figure 6.21:	The three types of internal fabrics within glauconites on central Chatham Rise.	135
Figure 6.22:	Average abundance (%) of various types of internal fabrics within the glauconite grain across all 21 analysed thin sections.	135
Figure 6.23:	Average abundance of oriented fibroradiated rims on glauconite grains across all 21 analysed glauconite thin sections.	136
Figure 6.24:	Average abundance of skeletal infilled grains in glauconite grains across all 21 analysed glauconite thin sections.	137
Figure 7.1:	Air-dried untreated oriented mount XRD scan of glauconite concentrate from G136.	142
Figure 7.2:	Air-dried untreated oriented mount XRD scan of glauconite concentrate from G137.	143
Figure 7.3:	Heated oriented mount XRD scan of glauconite concentrate from G136.	146
Figure 7.4:	Heated oriented mount XRD scan of glauconite concentrate from G137.	147
Figure 7.5:	Abundance of samples with different (001) peak shape classes, K ₂ O contents and % expandable smectite layers.	148
Figure 7.6:	Curve for determining the % expandables based on the 10Å spread in a glycolated sample.	149
Figure 7.7:	Glycolated oriented mount XRD scan of glauconite concentrate from A891.	151
Figure 7.8:	Glycolated oriented mount XRD scan of glauconite	152

	concentrate from G136.	
Figure 7.9:	Glycolated oriented mount XRD scan of glauconite concentrate from G217.	153
Figure 7.10:	Example of an alleverdite-like ordering that may be present in the stacking in central Chatham Rise glauconites.	154
Figure 8.1:	Correlation between Fe_2O_3^* and K_2O in 24 of the analysed glauconite concentrates.	162
Figure 8.2:	Relationship between % expandables calculated using Compton's (1989) method based on K_2O values and the total Fe_2O_3^* content in central Chatham Rise glauconites.	163
Figure 8.3:	Photomicrographs representative of the different glauconite varieties and features investigated by microprobe to determine their major element geochemistry.	169
Figure 8.4:	Average geochemistry of microprobed individual green glauconite grains, compared to average bulk XRF glauconite analysis.	171
Figure 8.5:	The average microprobe results for major oxides in typical green glauconite grains compared to brown glauconite grains.	172
Figure 8.6:	Comparison between the major oxide geochemistry of glauconite in the rim and inner pellet of four samples.	174
Figure 8.7:	Average wt% of the major oxides in the inner core of glauconite grains compared to their surrounding brown rims.	174
Figure 8.8:	Comparison of the average major element geochemistry of glauconite between ovoidal green pellets and foraminiferal infills.	176
Figure 8.9:	Locations 1 and 2 in a glauconite filled fracture were microprobed within a glauconitised phosphatic fragment in sample Q325.	178
Figure 8.10:	A: backscattered image and B: topographic image of the glauconitised phosphatic grain Q325-1.	178
Figure 9.1:	Dark green to black ovoidal (0.2 mm) pellets that were selected for age dating	182
Figure 10.1:	Glauconite fertiliser purifying techniques.	189
Figure 10.2:	Glauconite resource estimates in the four most concentrated areas across central Chatham Rise.	193
Figure 11.1:	Surficial sediment facies map for central Chatham Rise.	197
Figure 11.2:	Schematic diagram showing how lobate grains can transform into ovoidal grains, due to mechanical breakdown (A) or by abrasion and reworking (B).	199
Figure 11.3:	Examples of internal mold (A) versus fossil cast (B) morphologies.	201
Figure 11.4:	Glauconitisation of a phosphorite nodule by a rim of pigmentary glauconite.	202
Figure 11.5:	Redrawn illustrative version of Table 8.1.	203
Figure 11.6:	Schematic illustration of the progressional development of glauconite being oxidised into brown and then reddish brown (limonite) colours.	209
Figure 11.7:	Schematic diagram of an oriented rim development about a	

	glaucinite pellet.	210
Figure 11.8:	Evolution of a glauconite grain, showing the four stages of evolution.	215
Figure 11.9:	Clay mineral assemblage profile from the Middle Miocene to Quaternary at DSDP Site 594 off southwestern Chatham Rise.	217
Figure 11.10:	Location of possible “local” sources of Miocene-including volcanic ash, their composition (rhyolitic or basaltic) and age ranges of volcanism having that composition.	219
Figure 11.11:	Schematic illustration showing the Neogene evolution of glauconite and phosphorite formation on central Chatham Rise.	225
Figure 11.12:	Three potential mining methods for seafloor glauconite and phosphate deposits.	231
Figure 11.13:	Map of New Zealand with the five main onland areas which contain Cenozoic glauconite deposits outlined, as well as the central Chatham Rise glauconites of the present study.	233

LIST OF TABLES

Table 2.1:	Depth profile transects across the central Chatham Rise.	12
Table 3.1:	Tabulation of mineral types in XRD scans of 50 XRD bulk samples.	40
Table 3.2:	XRF elemental data correlation matrix for all 49 bulk powdered samples.	52
Table 3.3:	% CaCO ₃ values in bulk sediment samples determined using acid digestion and XRD.	57
Table 3.4:	Key to notations used for the petrographic data.	60
Table 3.5:	Thin section petrographic data for the bulk sand fraction of samples.	61
Table 3.6:	Acid digestion % CaCO ₃ results for five Oligocene chalk samples.	77
Table 4.1:	Definition of the echo-types which were used as a starting point for echo-types seen in the present study.	84
Table 4.2:	General features of the four echo-types (A to D) observed on 3.5 kHz profiles.	86
Table 5.1:	Major element positions within the crystallographic structure of glauconite.	105
Table 5.2:	Glauconite types and structure based mainly on potassium content.	107
Table 6.1:	Various glauconite types and their descriptions.	113
Table 6.2:	Key for the glauconite petrographic sheets.	116
Table 6.3:	Petrographic data for pure glauconite concentrates.	117
Table 6.4:	Morphological varieties of glauconite.	127
Table 7.1:	(001) peak spread in the 34 air-dried sample mounts determined from XRD scans.	144
Table 7.2:	The % expandables in all 34 analysed glauconite samples.	150
Table 8.1:	Glauconite types and structure based mainly on potassium content.	155
Table 8.2:	Chemical analysis of glauconite from Stn 287.	156
Table 8.3:	Correlation matrix between the major and trace elements in 30 analysed glauconite samples.	158
Table 8.4:	Major elemental composition of the 25 glauconite samples.	160
Table 8.5:	Comparison of XRF major element average results for 25 samples from central Chatham Rise, with the one sample previously analysed by Kudrass and Cullen (1982).	161
Table 8.6:	Average amounts (ppm) of the main trace elements within 39 glauconite concentrates.	164
Table 8.7:	Correlations (r values) between group 1 trace elements in glauconites.	165
Table 8.8:	Microprobe results (wt%) for individual bottle green ovoidal glauconite pellets.	170

Table 8.9:	Microprobe analysis (wt%) of brownish glauconite grains.	171
Table 8.10:	Microprobe analysis (wt%) of the inner and rim portions of several glauconite grains.	173
Table 8.11:	Geochemistry of average aggregate inner glauconite cores and their oriented fibroradiated rims in Odom (1976) compared to the central Chatham Rise glauconites.	175
Table 8.12:	Microprobed analysis (wt%) of glauconite infilling planktic foraminiferal chambers within a large glauconitised phosphatic grain (i.e. composite glauconite).	176
Table 8.13:	Microprobe analysis (wt%) of glauconitised phosphatic grains.	177
Table 8.14:	Major oxide composition of two glauconite filled fractures probed within a glauconitised phosphatic grain in sample Q325.	178
Table 8.15:	Glauconite pellets and glauconite foraminiferal infills within glauconitised phosphatic grains.	179
Table 9.1:	Age results for the five glauconite samples, calculated using K-Ar dating.	184
Table 10.1:	Glauconite resource estimates different sectors of central Chatham Rise, based on wt% glauconite, density, area and volume.	192
Table 11.1:	Outline of the four groups of trace elements within central Chatham Rise glauconites, based on their associated crystallographic position.	206
Table 11.2:	Major oxide geochemistry for glauconite from the five main areas within New Zealand.	236

Chapter 1

INTRODUCTION

1.1 BACKGROUND

Glaucinite, an iron potassium phyllosilicate green mineral belonging to the mica group, is widespread in uplifted Tertiary deposits in New Zealand, but its nature, origin and significance are generally poorly understood and simply inferred from overseas studies. Glaucinite is especially abundant in the modern surficial sediments covering central Chatham Rise off eastern South Island (Figure 1.1) where it is associated with authigenic carbonate-phosphate surficial deposits. Glaucinite is particularly concentrated on the Rise between 177° and 180° longitudes in 200-500 m water depths, forming 10 – >80% of the sediment content. The glauconite occurs as dark-green well-rounded sand-sized grains, as foraminiferal test infills, and as coatings on phosphorite nodules. Moreover, the glauconite on the Rise occurs in close association with other authigenic mineral deposits that involve phosphate- and/or carbonate-rich materials. A detailed study of the nature and origin of the glauconite on Chatham Rise should help elucidate the significance of glauconite in the New Zealand onland Tertiary sedimentary record, and may also advance a better understanding of the genesis and significance of glauconite-rich deposits in general.

The Chatham Rise phosphorites have well known economic significance as a potential agricultural fertiliser (von Rad, 1984; Cullen, 1987). Less well recognised is the potential for glauconite to similarly have economic importance, especially as a soil conditioner with its ability for slow release of potassium (K) and other nutrients, for retention of soil moisture, and for breaking up clayey soils (McRae, 1972; McConchie, 1978; Odin & Fullagar, 1988).

The distribution of the surficial sediments across Chatham Rise has been previously mapped broadly by McDougall (1982), and of glauconite by Norris (1964). However, their maps are based on limited data and the specifics are not well documented. The various glauconite varieties on central Chatham Rise have not been fully documented, with only a few varieties recognised by Norris (1964),

Bell and Goodell (1967) and von Rad and Rösch (1984). The mineralogy of the Chatham glauconites remains unexplored, and only one major elemental geochemical analysis has been previously undertaken by Kudrass and Cullen (1982), and no trace elemental analyses. The age of the glauconite on Chatham Rise has not been fully analysed, with only a few possible ages obtained by Cullen (1967) and Kreuzer (1984), and the origin of the glauconite has never been fully understood and explained. Finally, a resource size estimate of the Chatham glauconites has not been previously attempted, nor has there been a full economic discussion in relation to the potential benefits for New Zealand. This thesis endeavours to address the above shortcomings of our knowledge data for the central Chatham Rise glauconite deposits.

1.2 STUDY AREA

The Chatham Rise is an elongated submarine ridge-like platform or micro-continent, a part of New Zealand's Plateau, extending from about 100 km east of Banks Peninsula for about 1100 km eastwards past the Chatham Islands into the Southwest Pacific Ocean. The Rise is approximately 150 km wide and submerged to an average water depth of 400 m (Figure 1.1) (Norris, 1964; Heath, 1981; Kudrass & Cullen, 1982; Wood *et al.*, 1989). The area of the Rise is actually about the same as two thirds of the South Island land area (Pasho, 1976). The Chatham Rise is separated at its western end from the South Island continental shelf by the Mernoo Saddle, which is about 580 m deep. The eastern end of the Chatham Rise abuts at the northwest to southeast-trending Louisville Ridge (Heath, 1981). This thesis concentrates on the surficial glauconitic sediments upon central Chatham Rise, from 177-180°E longitude and 43-44°S latitude, giving a study area of approximately 40,000 km².

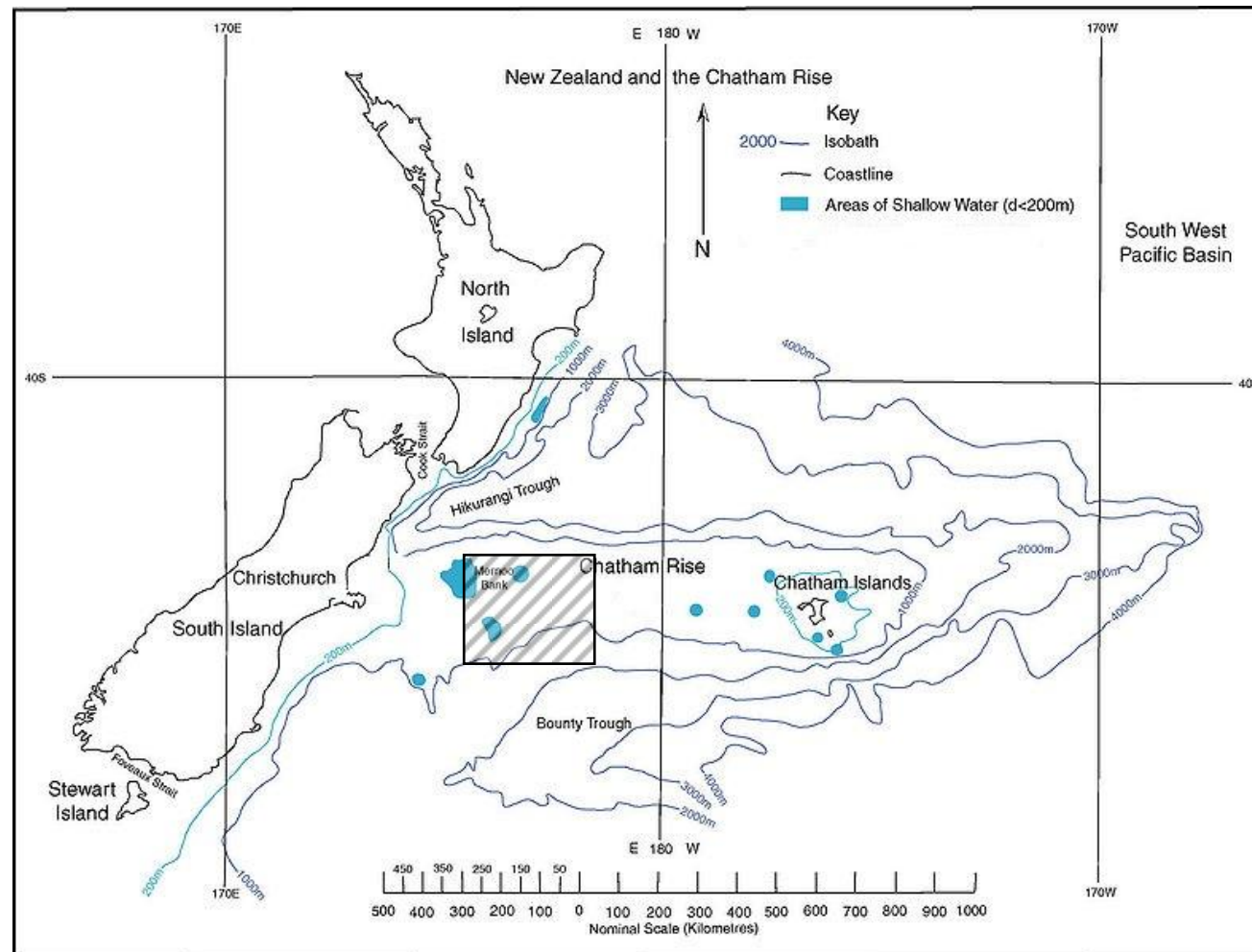


Figure 1.1: Chatham Rise location off southeastern New Zealand (from Ngatimozart, 2001). The hatched box outlines the study area on central Chatham Rise.

1.3 AIMS OF THIS STUDY

The general objectives/aims of this thesis are as follows.

1. The main objective is to document the physical properties, mineralogy and geochemistry of the glauconite within the central Chatham Rise surficial sediments.
2. Document the nature of the bulk surficial sediment facies containing the glauconite, including Munsell colour, texture, bulk and clay mineralogy, bulk geochemistry, calcium carbonate content, the distribution of the various sediment types, the short core stratigraphy, and characterisation of the underlying Oligocene chalk deposits.
3. Create an echo-character map of the sub-bottom stratigraphy of the glauconitic and phosphatic deposits on central Chatham Rise by examining and compiling all existing 3.5 kHz profiler data available at NIWA, Wellington.
4. Elucidate the age(s) and origin(s) of the glauconite in relation to the associated widespread phosphatisation processes that have occurred on the Rise.
5. Determine whether the glauconite on Chatham Rise is an authigenic *in situ* mineral or whether it has been redistributed by ocean bottom currents or other mechanisms such as mass flows, and is therefore allogenic.
6. To provide a fuller geological context to the study, the carbonate-phosphate-glauconite mineral association on Chatham Rise is briefly compared with some onland New Zealand occurrences of equivalent Tertiary ancient deposits which could ultimately lead to the development of an improved conceptual paleoenvironmental model for such authigenic mineral facies in the rock record.
7. Provide an economic summary of the glauconite resource on central Chatham Rise, outlining the potential benefits for New Zealand.

1.4 GENERAL PROCEDURES ADOPTED IN THIS STUDY

Sediment splits come from existing NIWA (Wellington) dredge pipe, grab, piston core and trawl samples, as well as a suite of new samples collected from *RV Tangaroa* (TAN1103 Leg 2) on transects across central Chatham Rise. The textural and petrological properties of the host sediments and the glauconite are analysed using facilities at The University of Waikato, including the laser particle sizer (grain size), binocular and petrographic microscopes (morphology, fabrics, mineralogy), SEM (micro-fabrics), XRD (mineralogy), and XRF (major and trace element bulk geochemistry). Individual grain major elemental geochemistry has been analysed using the electron probe micro-analyser at The University of Auckland, and K-Ar isotopic age dating of glauconite was undertaken by Dr Horst Zwingmann at the CSRIO in Perth, Australia.

The shallow sub-bottom stratigraphy of the glauconitic and phosphatic deposits on the Rise, linked to cores, has been assessed from a compilation of all existing 3.5 kHz profiler data at NIWA, enabling assessment of the geometry and thickness of the deposits by creating an echo-character map, sediment thickness map and a seafloor morphology map over central Chatham Rise.

As appropriate, the above analytical results have been related to published and in house NIWA physical, chemical and biological oceanographic data available for the Chatham Rise. Likewise, comparisons of the Chatham Rise deposits with selected onland geological occurrences of the carbonate-phosphate-glauconite mineral association utilises available publications and university theses. Figure 1.2 shows a flow chart of the practical and analytical techniques carried out for this study.

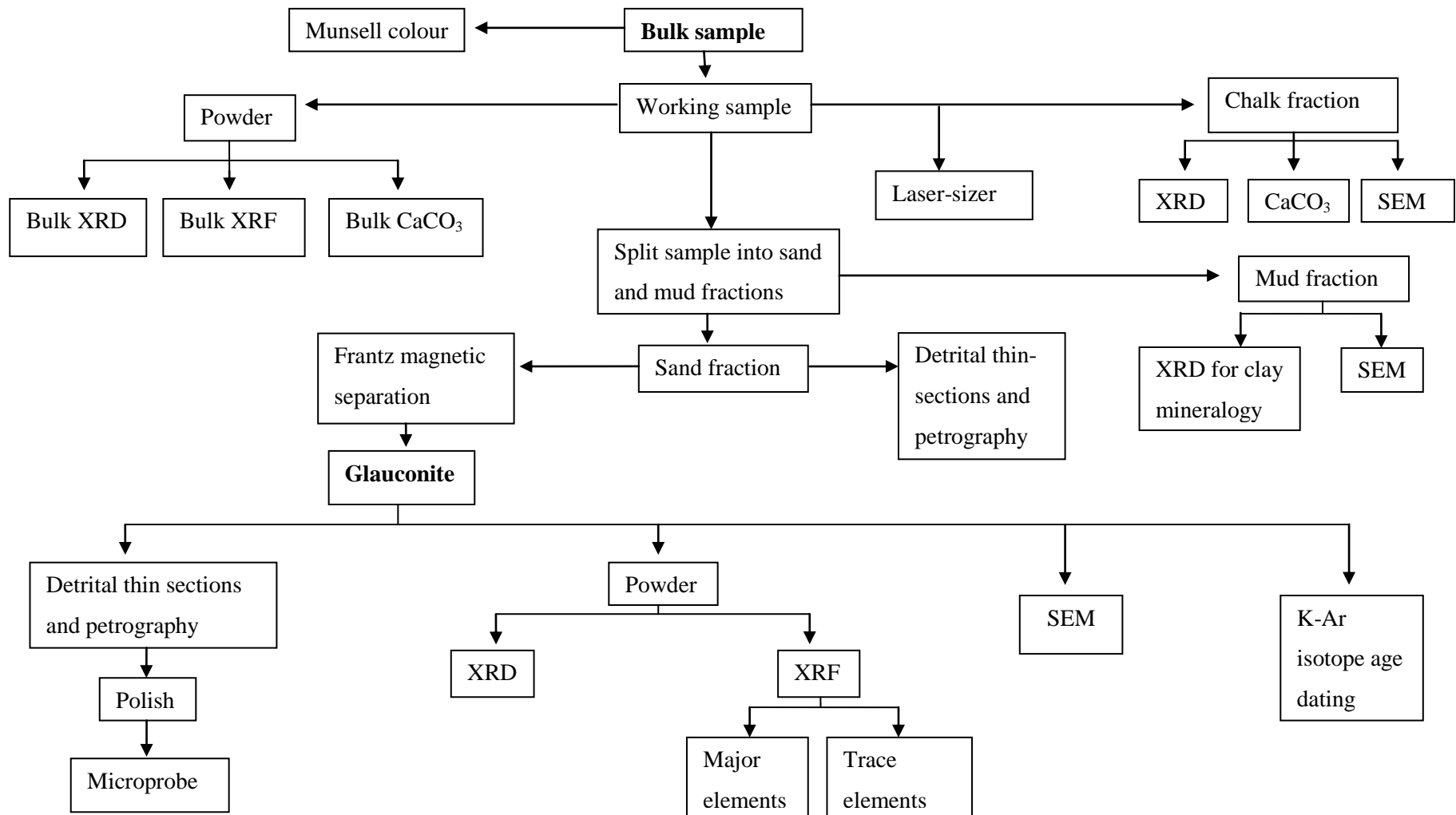


Figure 1.2: Flow chart demonstrating the main practical and analytical procedures adopted in carrying out this study of the central Chatham Rise glauconitic sediments.

1.5 THESIS CHAPTER FORMAT

Chapter 2 summarises the physical and geological setting and history of the Chatham Rise. Chapter 3 introduces the reader to the sediment facies across central Chatham Rise, analysing the physical properties, mineralogy and geochemistry of 137 sediment samples. Chapter 4 investigates the echo-character facies of central Chatham Rise using 3.5 kHz seismic profiles. Chapter 5 presents a literature review of the properties of the mineral glauconite. Chapters 6, 7 and 8 describe respectively the physical properties, mineralogy and geochemistry of glauconite on central Chatham Rise, gained from laboratory analysis of sub-samples from the 137 bulk surficial sediment samples, and represent the main analytical focus of this thesis study. Chapter 9 investigates the age(s) of glauconite on central Chatham Rise. Chapter 10 explores the economic potential of the glauconite on the Rise, including resource size maps and estimates, and glauconite uses. Chapter 11 discusses the results of all the previous chapters, including the nature of the glauconite (physical properties, mineralogy, geochemistry and age), the overall origin(s) of the glauconite, the economic potential of the glauconite for New Zealand, and a comparison of the glauconite with some onland New Zealand Tertiary occurrences.

Chapter 2

GEOLOGICAL AND PHYSICAL SETTING

2.1 INTRODUCTION

The location and some other general features of the Chatham Rise were noted in Chapter 1, and in this chapter I discuss further specifics of the physical and geological setting of the Rise, including topography, structure, geological setting, stratigraphic record, geological history, current circulation patterns and oceanic climate, as well as introducing the general nature of the surficial bulk sediments.

2.2 TOPOGRAPHY AND STRUCTURE

The Chatham Rise is a submarine ridge-like platform that extends 1100 km out into the Southwest Pacific from c.110 km east of Banks Peninsula on South Island to east of the Chatham Island. It is approximately 150 km wide (N to S) and lies in an average water depth of 400 m (Figure 2.1) (Norris, 1964; Heath, 1981; Kudrass & Cullen, 1982; Wood *et al.*, 1989). According to Pasho (1976) the Chatham Rise covers an area equivalent to two thirds that of the South Island. The Chatham Rise has steeply sloping flanks to the north and south into Hikurangi and Bounty Troughs respectively, descending to water depths of up to 3000 m (Kudrass & Cullen, 1982). The slope of the northern flank into Hikurangi Trough is rather abrupt and much steeper than the southern flank into Bounty Trough and most likely represents a pre-break up margin of Gondwanaland on the south of the Rise (Norris, 1964; Heath, 1981). The Chatham Rise crest has an irregular seafloor that slopes broadly in an easterly direction from 390 m to 370 m water depth and supports regular occurrences of small elevations and depressions which Kudrass and Cullen (1982) suggest represent a karstic landscape that may have formed from submarine solution.

Norris (1964) divided Chatham Rise into three main topographic units:

1. The only land emergent area, Chatham Islands, in the east.
2. West of this is the central part of Chatham Rise which consists of an undulating crest that has a slightly irregular seafloor but low relief, in water depths of no more than 500 m. This second unit contains the majority of the present study area.
3. The third topographic unit is the western portion of Chatham Rise which extends from about 177° 30'E to Banks Peninsula and supports three pedestals or banks, including Mernoo Bank, Verman Bank and Reserve Bank.

Alternatively, Pasho (1976) described the topographic divisions of Chatham Rise from a slightly different view and notes that the main topographic features that make up the Rise are four banks – Mernoo Bank, Verman Bank, Reserve Bank and Matheson Banks – and Chatham Islands (Figure 2.1). The westernmost bank on the Rise, Mernoo Bank, is the largest of the four banks and also has the shallowest water depths of about 50-55 m. This dome-shaped feature supports channels and ridges suggesting it has been exposed to subaerial erosion. The valleys and ridges can be traced down to about 100 m water depth, which is consistent with a sea level lowering of about 120 m at times during the Pleistocene ice ages (Norris, 1964; Pasho, 1976). Verman Bank is considered to be a truncated volcanic cone on the basis of its small steep-sided shape and dredged volcanic rock occurrences (Pasho, 1976). Verman Bank has a minimum water depth of 145 m (Norris, 1964). Reserve Bank (contained in the present study area) is an isolated topographic high reaching a minimum water depth of 200 m. It is mostly circular in shape with low relief and a slight east-west elongation (Norris, 1964; Pasho, 1976). Matheson Bank has the same minimum water depth as Reserve Bank of 200 m, but is much smaller and appears to rise rapidly from the north and south (Pasho, 1976).

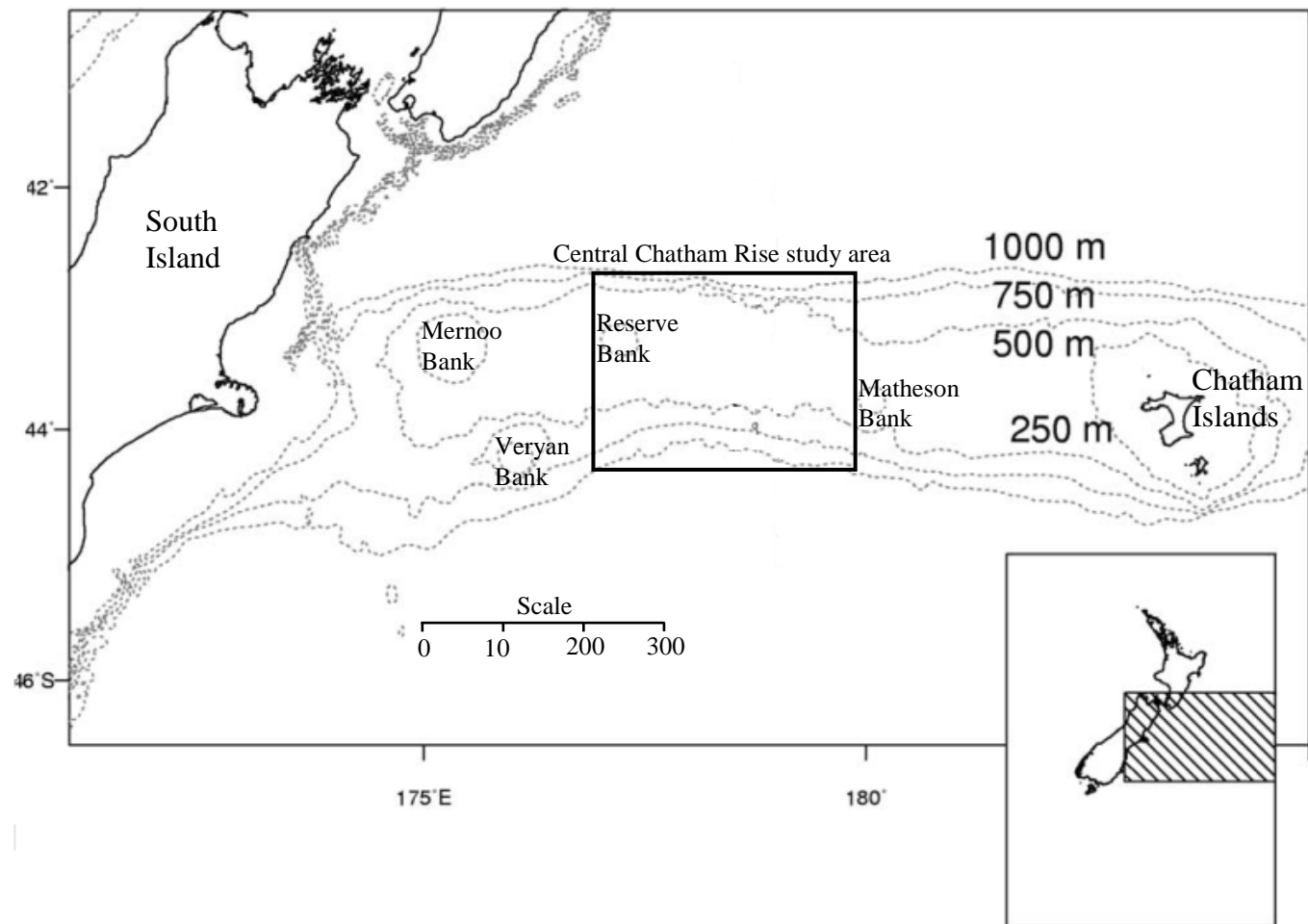


Figure 2.1: Topography of Chatham Rise in relation to New Zealand, showing the locations of Chatham Islands and the four banks on the Rise (modified after McClatchie *et al.*, 2004., p.3). The present study area of central Chatham Rise is outlined.

Structurally, the Chatham Rise is considered to be broadly anticlinal about an east – west axis, evident from the upper surface of the Rise being convex with an undulating surface (Norris, 1964; Pasho, 1976). The general structural properties of the Rise have been identified using seismic reflection profiles (Pasho, 1976). The four banks described above are claimed by Pasho (1976) to have formed due to normal faulting, suggested for example by 50 m vertical offsets on Matheson Bank. The structural setting of Chatham Rise as seen today is thought to have not changed much since early Tertiary time, apart from some uplift accounting for the emergence of the Chatham Islands (Norris, 1964; Wood *et al.*, 1989).

The central portion of the Chatham Rise is the focus of the present study, from approximately 177-180° E longitude (Figure 2.1), and so a more detailed analysis of the topography and structure is relevant for this area. Six transects were constructed using the interpolate line tool from the 3D Analyst toolbox from an elevation raster using the suite of ArcGIS 10 software. Three transects were oriented west – east (transects A-C) and three south – north (transects D-F) over central Chatham Rise (Figure 2.2). Co-ordinates for these profiles are drawn in Table 2.1 and they are located on Figure 2.2.

Table 2.1: Depth profile transects across the central Chatham Rise, with start and end points given in decimal degrees (transect locations are shown in Figure 2.2).

Transect	A	B	C	D	E	F
Start	176.6879 -43.7514	176.5094 -43.4476	176.4484 -43.1741	177.1321 -45.0694	178.4909 -45.065	179.8236 -45.0527
End	179.1878 -43.7546	179.1311 -43.4222	-179.1703 -43.1582	177.0973 -41.9156	178.4909 -41.9436	179.7757 -41.8525

Transects A-C illustrate topographic profiles across the central Chatham Rise from west to east (Figures 2.3A-C). They clearly show the topographic high known as Reserve Bank in <250 m water depth on the westernmost side of the study area, with a profile that then increases in water depth east from here. This pattern is especially seen in transects B and C (Figures 2.3B and C) while transect A, the southernmost transect, shows a more irregular pattern with repeated highs and lows from west to east (Figure 2.3A).

Transects D-F show topographic profiles across the central Chatham Rise from south to north (Figure 2.3D-F). These profiles illustrate the overall topographic structure of the Rise, with average summit water depths of approximately 400 m and a Rise width of 150-200 km. They also clearly show that the northern flank of the Rise descending into Hikurangi Trough has a much steeper and abrupt entry into water depths exceeding 2500 m than does the southern flank that enters Bounty Trough, which is rather more gradual and irregular.

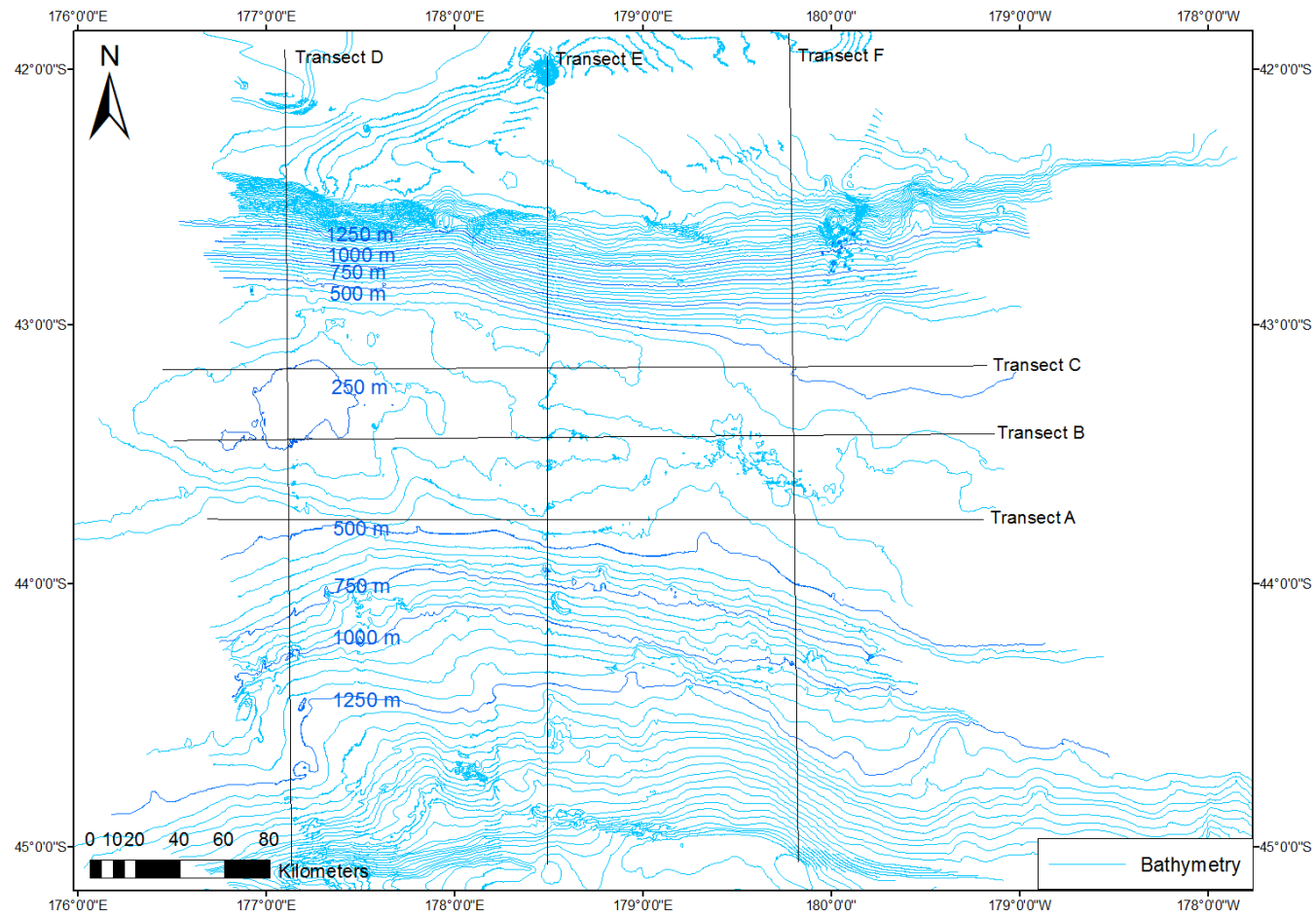
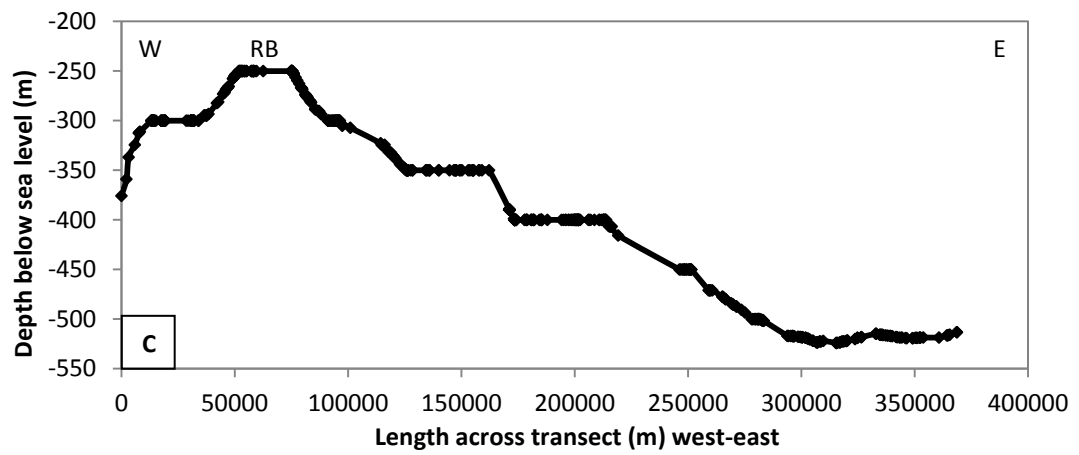
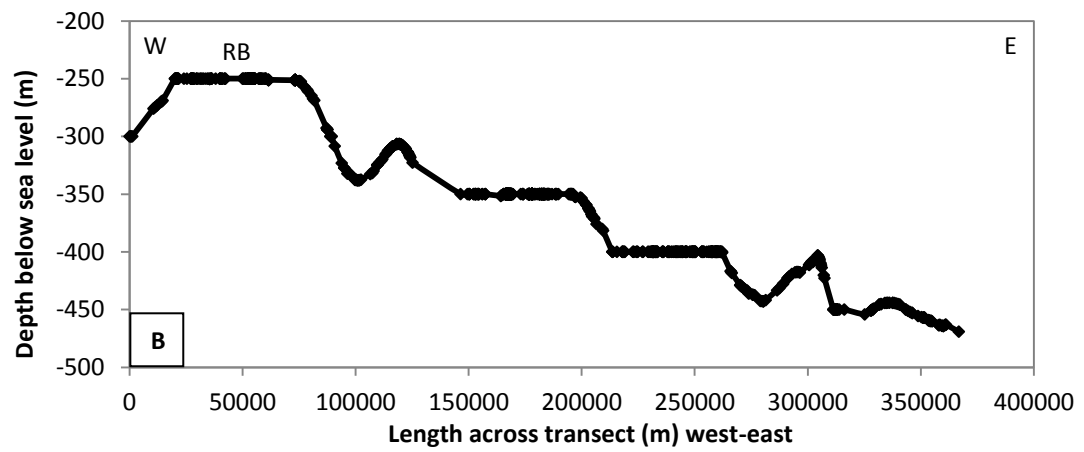
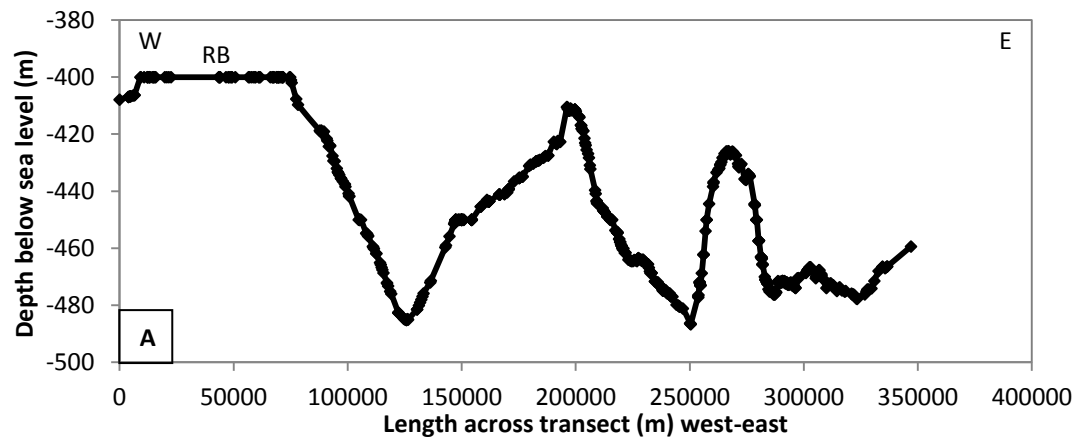


Figure 2.2: Location of six bathymetric transects (A-F) over central Chatham Rise, reproduced in Figure 2.3.



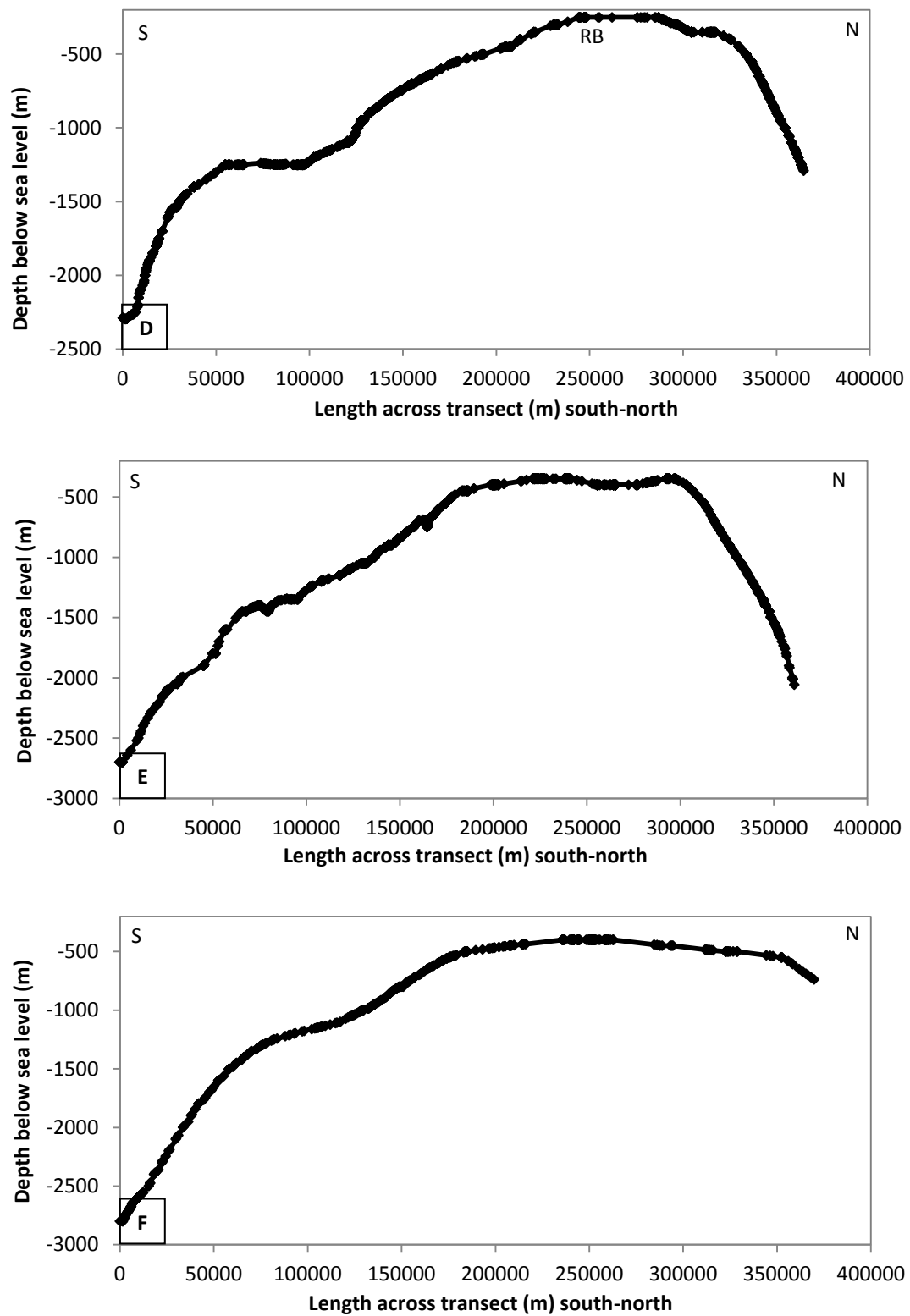


Figure 2.3: Topographic profiles along transects A-F (RB=Reserve Bank, E=east, W=west, N=north, S=south).

2.3 BEDROCK GEOLOGY AND GEOLOGICAL HISTORY

The bedrock geology and stratigraphic history of Chatham Rise are poorly understood. Most direct information comes from the exposed geology on the Chatham Islands, but is also surmised from the results of seismic sections obtained over the Rise (Norris, 1964; Falconer *et al.*, 1984; Wood *et al.*, 1989).

Geologically, Chatham Rise can be regarded as an extension of the South Island as part of New Zealand's continental plateau (Zealandia) and represents east-west striking half-graben rift structures formed in the Middle to Late Cretaceous (Wood *et al.*, 1989). Near the close of the Cretaceous, the Rise was considered to be a dry land peninsula that extended from east of South Island out to Chatham Islands, albeit not in its present geographic configuration. During the Mesozoic the land was dominated by gymnosperm forests, with some angiosperms (Stilwell *et al.*, 2006).

Latest Paleozoic and Mesozoic basement rocks of indurated greywackes, argillites and schists of Permian-Early Cretaceous age are the oldest rocks underpinning Chatham Rise (Kudrass & Cullen, 1982; Wood *et al.*, 1989). They are exposed sporadically on the Chatham Islands and share similarities with the age equivalent Otago Schist and Torlesse "greywackes" in South Island. The basement rocks are overlain by a stratigraphic sequence of Late Cretaceous and Cenozoic volcanic and sedimentary deposits whose distribution and character are generally poorly known. This sequence includes Middle Eocene foraminiferal limestone and Early Oligocene chalk, portions of which were subsequently phosphatised in the Late Miocene, overlain by Miocene foraminiferal ooze that was mostly removed by erosion to leave phosphate nodules now embedded in unconsolidated muddy glauconitic sand and silt (Norris, 1964; Kudrass & Cullen, 1982). The unconsolidated muddy glauconitic sand and silt is especially concentrated on the central portion of the Rise, and is the deposit that is the focus of the present study.

Falconer *et al.* (1984) and Wood *et al.* (1989) have produced the most comprehensive assessment of the geological history of Chatham Rise since the Permian. Armed with this knowledge, along with insights from Norris (1964) and Pasho (1976), I have attempted to summarise the geological history of Chatham Rise in a series of time periods and rock/sediment units (Figure 2.4, a key for the

diagram summarised in Figure 2.5). Figure 2.4 also includes a schematic diagram of the geological succession on Chatham Islands (James *et al.*, 2011) which can be compared to the inferred geology beneath Chatham Rise (Falconer *et al.*, 1984; Wood *et al.*, 1989).

Permian to Jurassic: On Chatham Islands, deformed and indurated greywacke, schist and argillite similar to the Torlesse Supergroup and Otago Schist in South Island were deposited on the active margin of Gondwanaland and now most likely make up the basement rocks of Chatham Rise. These Permian-Jurassic schists and greywackes have also been sampled in dredge hauls at three of the four banks on Chatham Rise, thus further supporting the assumption that these rocks make up the basement rocks of the Rise (Falconer *et al.*, 1984; Wood *et al.*, 1989). The Permian-Jurassic basement rocks represent Unit 1 on Figure 2.4.

Early Cretaceous: Normal faulting associated with the breakup of eastern Gondwanaland produced half graben structures during the Cretaceous that became infilled with some 500-2000 m or more of marine sediments and alluvium shed from upstanding fault blocks and volcanoes (Falconer *et al.*, 1984; Wood *et al.*, 1989). These Cretaceous deposits are illustrated in Figure 2.4 as Unit 2.

Late Cretaceous: By Late Cretaceous the filling of grabens had ceased and was followed by eastwards drift of Zealandia out into the paleo-Pacific Ocean, thermal subsidence, peneplanation and alkaline basalt eruptions from few but large volcanic complexes. The landmass occupying the position of the crest of Chatham Rise was now low-lying, and during this time the western side was covered with lagoonal and marginal marine sands, muds and coal measures (represented as Unit 3 in Figure 2.4). These sediments, along with others that accumulated during this time, led to thickening towards the Bounty Trough which suggests that Chatham Rise had an arch-like form as far back as the Late Cretaceous (Wood *et al.*, 1989).

Paleocene: During the Paleocene Chatham Rise continued to be relatively low-lying with very stable tectonic conditions that prompted the formation of unconformities. These two factors allowed shallow marine greensands (glauconite-rich), sandstones and limestones to be deposited over large areas of Chatham Rise, recorded as Unit 4 in Figure 2.4. In the Late Paleocene and Early

Eocene basaltic volcanism occurred, which was mostly confined to the Chatham Islands and east of 180° longitude on the Rise (Wood *et al.*, 1989).

Eocene: During the Eocene, towards the western end of Chatham Rise, a small increase in tectonic tempo reactivated the earlier Cretaceous normal faults which in turn led to the sudden reintroduction of clastic sedimentation (Unit 5 in Figure 2.4). In contrast, on the eastern portion of the Rise relatively stable tectonic conditions remained which allowed limestone deposition to continue (Unit 6 in Figure 2.4). In the Late Eocene alkali basaltic volcanism returned on the eastern part of the Rise (Wood *et al.*, 1989). Pasho (1976) believed that truncation of the crest of the Rise indicates it was likely emergent during the immediately post-Eocene period.

Oligocene to Middle Miocene: The sedimentary record is very poor for this period, particularly during the Oligocene. However, it is recognised that in the inferred Oligocene to Early Miocene sections there are prevalent unconformities associated with thin remnants of limestone/chalk and greensand deposits, represented by Unit 7 in Figure 2.4 (Wood *et al.*, 1989). It is suggested that some of the Oligocene chalk was phosphatised and is the source of the phosphorite nodules on the Rise. Widespread Miocene foraminiferal chalk is inferred to have been deposited during this time, but has now mostly been eroded away, leading to exposure of the phosphorite nodules on the seafloor (Unit 8 in Figure 2.4) (Falconer *et al.*, 1984). Block faulting with throws of 10-65 m occurred during this time (Wood *et al.*, 1989).

Post Middle-Late Miocene: From the Middle Miocene onwards, uplift of the Southern Alps on the transform plate boundary in South Island greatly affected the western side of the Rise. Across the axis of the Rise, a foreland basin was formed (which included the Canterbury plains, shelf and Mernoo Gap). This basin was filled by gravels, sands and silts derived from uplift of the mountains, illustrated as Unit 9 in Figure 2.4. Faulting associated with the present plate boundary then occurred in the northwestern area of the Rise. The pattern of unconformities and associated remnants of depositional greensands, limestones and phosphorites continued throughout the rest of the Neogene (Unit 10 in Figure

2.4). It is most likely that during this period little new sedimentation occurred due to the formation of unconformities (Wood *et al.*, 1989).

Chatham Rise is presently tectonically stable and the main controls currently affecting sedimentation include ocean current changes, water temperature and local volcanism (particularly closer to the Chatham Islands). Thus the sediments which formed during the Neogene consist predominantly of biogenic and authigenic sediments, including limestones, phosphorites and greensands, and also local volcanics (Unit 10 in Figure 2.4) (Norris, 1964; Wood *et al.*, 1989).

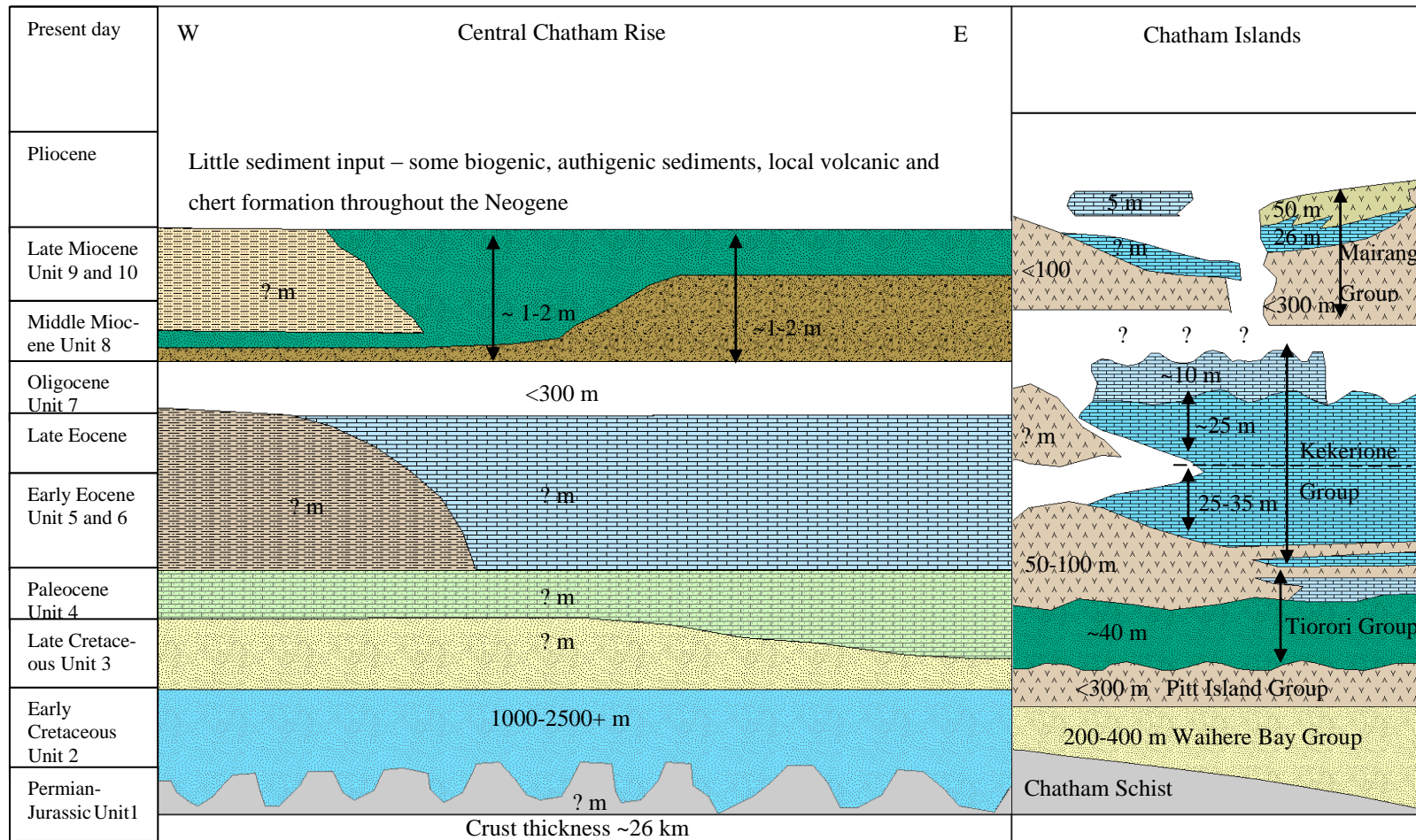
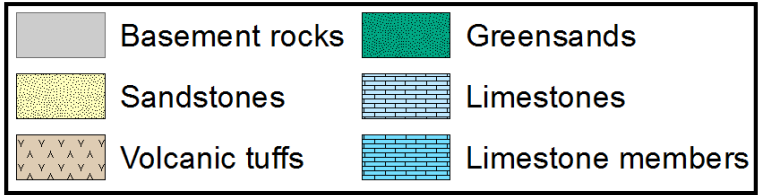


Figure 2.4: Geological stratigraphic sequence (after the geological history summarised by Wood *et al.*, 1989), compared to geology of Chatham Islands (after James *et al.*, 2011). Key in Figure 2.5.

Chatham Islands Key



Chatham Rise Key

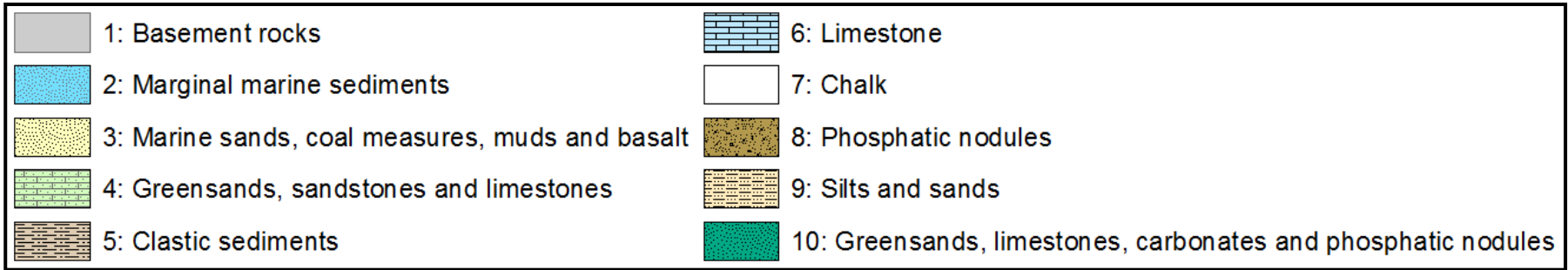


Figure 2.5: Key for the geological sections in Figure 2.4, with unit numbers 1-10 shown for the central Chatham Rise section.

2.4 CURRENT CIRCULATION PATTERNS AND OCEANIC CLIMATE

2.4.1 Current circulation – subtropical front

Chatham Rise is a submarine platform that extends eastwards for about 1100 km off the South Island of New Zealand. The prominent upstanding length and relief of the Rise exerts a major control on the movement of oceanic currents, which consequently powers the physical, biological and sediment processes occurring on the Rise (Heath, 1981; Chiswell, 2001; Grant, 2005). The general flow runs parallel along the Chatham Rise, where warm ($>16^{\circ}\text{C}$) Subtropical water (STW) coming down the southeastern side of the North Island meets cooler ($<14^{\circ}\text{C}$) Subantarctic water (SAW) rising up from the southeast of the South Island to create the Subtropical Front (STF) at shallow (av. 400 m) water depths upon the Rise (Figure 2.6). The STF is a global oceanic front which separates warm, macronutrient-limited STW in the north from cool macronutrient-rich SAW in the south (Chiswell, 2001; Sutton, 2001; Grant, 2005; Nodder *et al.*, 2007; James *et al.*, 2011). The salinity across Chatham Rise changes from more saline ($>34.5\text{‰}$) STW in the north to less saline ($<34.2\text{‰}$) SAW in the south and, more dramatically, there is a $4\text{--}5^{\circ}\text{C}$ temperature drop over 200 km or only 1° of latitude (Kudrass & Cullen, 1982; Chiswell, 2001; Sutton, 2001; Grant, 2005; Stilwell *et al.*, 2006; James *et al.*, 2011). Sutton (2001) suggested that the STF is split into northern and southern fronts separated by a frontal zone (STFZ). The STF also has a strong horizontal gradient in relation to its water properties (Heath, 1981). The position of the STF is controlled by the seafloor topography of the Chatham Rise and also by the surface current strengths (Grant, 2005). The STF plays a large role in ocean dynamics over the Rise, affecting both physical and chemical properties, including momentum, dissipation and heat, as well as the vertical exchange being enhanced. Sea surface temperatures show that there is significant mixing and movement of the various water masses associated with the STF (Chiswell, 2001). The STF is underlain by Antarctic Intermediate Water (AAIW) and Subantarctic Mode Water (SAMW) occurring in water depths of 600–1500 m (Grant, 2005). The position of the STF is determined by the topography of the Rise, as well as the confluence of the East Cape Current (ECC), which runs along the northern edge of the Chatham Rise, and the Southland Current, which runs along the southern edge of the Rise (Figure 2.6) (Grant, 2005).

The STF is recognised as an area of elevated biological productivity, relative to the surrounding waters, and so high amounts of particulate organic matter sink into the deep ocean. This pattern is indicated by the dissolved CO₂ content which is much lower in the surface waters of the STF in comparison to the SAW due to the STF utilising much more CO₂ as a consequence of a stronger biological pump in the upwelling waters (Grant, 2005). High biological activity is also illustrated by the total organic matter being about 1-5% of the sediment, by a bacterial abundance ranging from 2.06×10^8 to 3.46×10^9 cells/g, by a chlorophyll *a*/g value of 0.05-1 g and by a carbonate content ranging from 30-80% (Mass *et al.*, 2009). The values for chlorophyll *a*, organic carbon and biogenic material all peak in spring, but despite this the phytoplankton are dominated by diatoms due to the waters being enriched in nitrate at 5-12 $\mu\text{mol/l NO}_3^-$ (Grant, 2005). The high amounts of organic matter combined with the upwelling that occurs due to the STF foster the formation of authigenic minerals such as glauconite and phosphorite on the Rise (Heath, 1981; Kudrass & Cullen, 1982; Chiswell, 2001; Sutton, 2001).

Despite the general flow in the STF along the Chatham Rise, there is considerable variability in the flow across the Rise. The flow is made even more variable due to the presence of the Mernoo Saddle situated at the western end of Chatham Rise, which causes interactions to occur between the alongshore flows from both the north and south directions (Heath, 1981). The water flow across the Rise also has meridional components typically seen in the STF where STW, which is less dense, warm and salty, overrides the SAW, which is more dense, cold and fresh (Heath, 1981, 1983; Chiswell, 2001; Sutton, 2001).

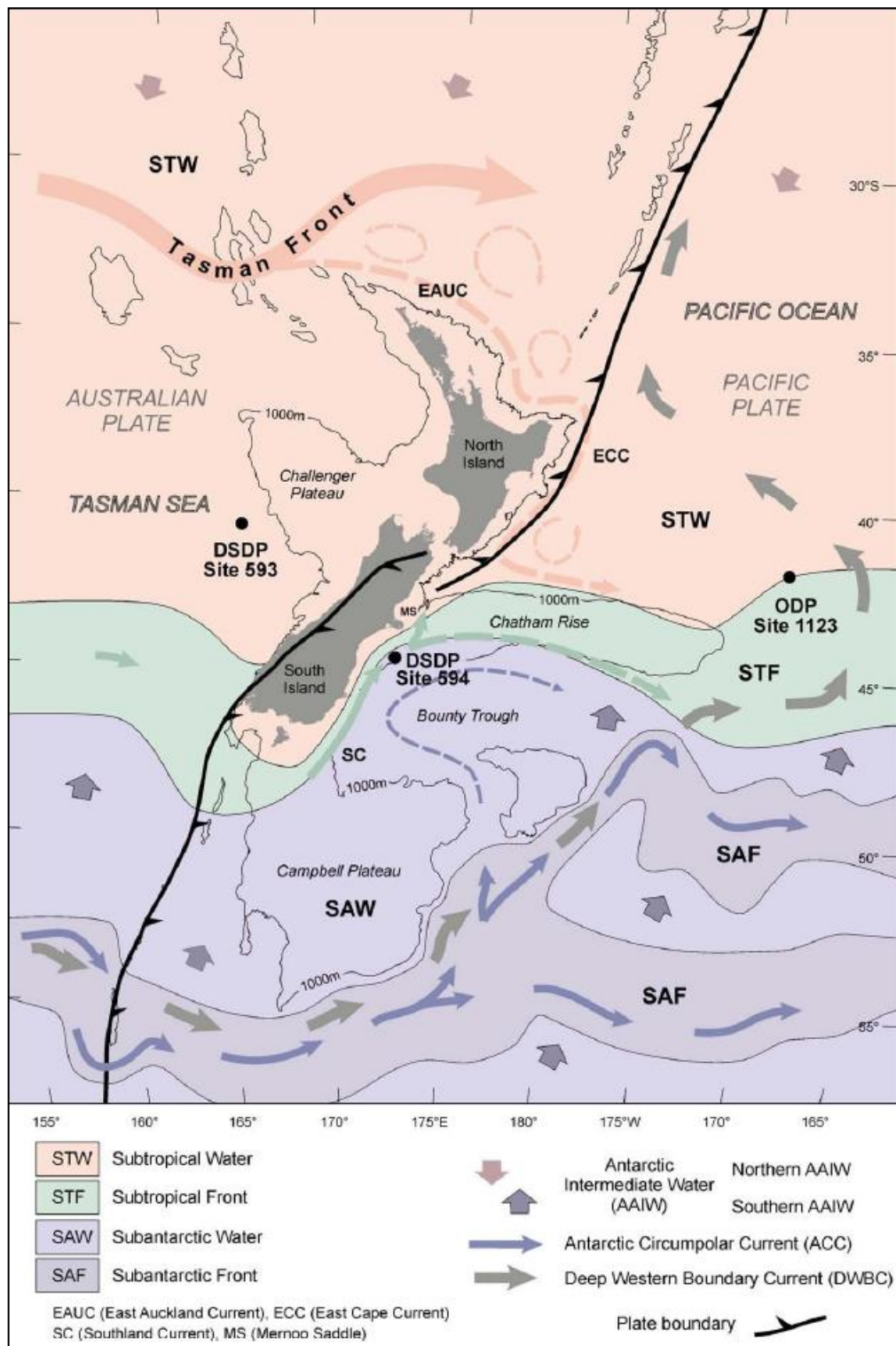


Figure 2.6: Oceanographic setting of Chatham Rise, displaying global fronts, water bodies and currents, as well as major topographic features (after Crundwell *et al.*, 2008).

2.4.2 Water movements and speeds

Considering that Chatham Rise has been stable since at least the Late Miocene (apart from uplift since the Pliocene on Chatham Islands), the water movements across the Rise are of particular interest. This is because water movements are the

biggest factor directly influencing sedimentation patterns, including changes in speed of ocean currents and in the position of sea level. Water movements can control sediment movement and, if velocities are strong enough, minerals such as the phosphorite nodules can be exposed on the seafloor due to sediment erosion (Heath, 1983). Von Rad (1984) found that current velocities close to the seafloor (17 m) over Chatham Rise (measured on the crest of the Rise at 43° 34.4`S and 179° 26.9`E) are in the range of 5 to 24.2 cm s⁻¹, with a mean of 12.5 cm s⁻¹, and that these currents flow predominantly in a south to southeasterly direction. Such current speeds are high enough to enable movement of sands and silts on the seafloor, so that erosion and winnowing would explain the exposure of the phosphorite and glauconite deposits (von Rad, 1984; Sutton, 2001). Current speeds near the seafloor on the Rise have been reported to be much greater in the south at 15 cm s⁻¹, compared to the north at 4.5 cm s⁻¹, and generally the mean flow has an eastwards zonal direction on both the northern and southern flanks of the Rise (Chiswell, 2001).

2.4.3 Tidal currents

Heath (1983) reported that water movement across Chatham Rise is controlled by semi-diurnal and diurnal tides, and is consistent with the lunar semi-diurnal tide (M₂) that is travelling anti-clockwise around New Zealand. The strongest tidal influence on Chatham Rise comes from the M₂ barotropic tide, with a strength of 11 cm s⁻¹, while the M₂ baroclinic tide has a much smaller influence. Chiswell (2000) concluded that the baroclinic tide is phase-locked to the barotropic tide, with a wide range of amplitudes recorded. Vertical displacements of up to 40 m were also measured which confirms a baroclinic tidal phase is present on the Rise, as baroclinic waves generate large vertical displacements of the oceanic thermocline of tens of metres. There is also an unpredictably strong diurnal tidal flow, explained by a continental shelf wave that exists off the Rise, and the solar semi-diurnal tide (S₂) only accounts for a very small elevation (Heath, 1983).

2.4.4 Climate

The STF situated over Chatham Rise, results in a 15°C surface isotherm temperature in summer, and a 10°C isotherm in winter (Wilson *et al.*, 2005). The STF and its connected temperature contrast that exists over Chatham Rise also

affects the local meteorological conditions, in that cloud formation is stimulated due to the surrounding air being cooled by the sea (Heath, 1981). Wind speeds have been recorded in the range of 1-15 ms⁻¹ (von Rad, 1984), and wave heights have been known to reach over 10 m due to the strong currents flowing over the Chatham Rise. At the Chatham Islands the annual rainfall is 800 mm, with the winter months being wetter than in summer.

2.4.5 General bottom sediment facies

The surface of Chatham Rise is dominantly covered in a surficial layer of *Globigerina* ooze, a carbonate-rich sediment consisting of the tiny shells of the planktic foraminifera. In many places this ooze is mixed with glauconitic sand and/or clasts of older Tertiary chalk, often now lithified into hard limestone that was subsequently phosphatised and eroded to generate phosphorite nodules (Norris, 1964). Surficial sediments also include biogenic detritus and smaller amounts of detrital minerals such as feldspar, quartz and volcanic glass (Norris, 1964; Kudrass & Cullen, 1982).

Norris (1964) states that Chatham Rise is blanketed almost entirely with unconsolidated deposits which can be divided into five main sources of sediments as follows:

1. Rock fragments, which have most likely been rafted in on ice (i.e. glacial erratics) or on trees.
2. Authigenic minerals, including glauconite, phosphorite and gypsum.
3. Skeletal materials, including foraminifera, shell fragments of molluscs, echinoderms, bryozoans, and a smaller amount of coccolithophores and siliceous materials such as diatoms, radiolarians and sponges.
4. Faecal pellets and slime-cemented silty aggregates and trails.
5. Monomineralic grains, predominantly derived from North Island volcanic sources.

The sedimentary facies will be discussed more fully in Chapter 3 following my textural, mineralogical and geochemical analyses undertaken on sediment samples from central Chatham Rise, which has produced a new surficial sediment facies map (see Figure 3.31).

Chapter 3

SURFICIAL SEDIMENT FACIES

3.1 INTRODUCTION

The central Chatham Rise seabed is covered by a surficial layer of loose sediments, typically from 40-60 cm thick, composed of *Globigerina* ooze mixed with glauconitic sand, skeletal material, limestone clasts and phosphorite nodules (av. 4 to 6 cm size), corresponding to Unit 10 in Figure 2.2. This deposit overlies an Oligocene chalk deposit (Unit 7 in Figure 2.2) up to 300 m thick (Norris, 1964; Pasho, 1976; Kudrass & Cullen, 1982). Splits of 135 bulk sediment dredge pipe, grab, piston core, and trawl samples from the central Chatham Rise were acquired for this thesis study from the sample archive store at NIWA Wellington, along with two new multi cores obtained during the *RV Tangaroa* (TAN1103 Leg 2) cruise in 2011. In the laboratory a variety of sedimentologic properties were determined for the surficial deposits including their colour, texture, calcium carbonate content, and bulk mineralogy and geochemistry. Techniques used involved the Munsell colour chart, laser-sizer, X-ray fluorescence (XRF), X-ray diffraction (XRD), scanning electron microscopy (SEM), microscope petrography, and CaCO₃ acid digestion. Short core stratigraphy was also analysed using the 26 cores available, as was the nature of the Oligocene chalk underlying the unconsolidated surficial deposits.

3.2 SURFICIAL SEDIMENTS

This section describes in detail the surficial sediment deposits on central Chatham Rise. Figure 3.1 shows the locations of the 137 dredge pipe, grab, piston core and trawl samples analysed and should be referred back to when mentioning the results for particular samples both in this chapter and elsewhere in the thesis.

Figure 3.1: Location of 137 sediment samples from central Chatham Rise (grid co-ordinates and other sample locality information are given in Appendix I).

3.2.1 Munsell colour

The Munsell colours of all the dried bulk sediment samples from central Chatham Rise were determined using the “Standard soil colour chart” booklet (Oyama & Takehara, 1970), and recorded in Appendix II-A. Results are summarised in Figure 3.2 which shows a predominance (48%) of light grey colours associated with carbonate-rich samples, followed by 36% of light grey samples including at least 10% black grains, which are those containing some to moderate amounts of glauconite. The remainder of samples (16%) involve grey, olive and black colours in various proportions and contain the most glauconite grains (Figure 3.2).

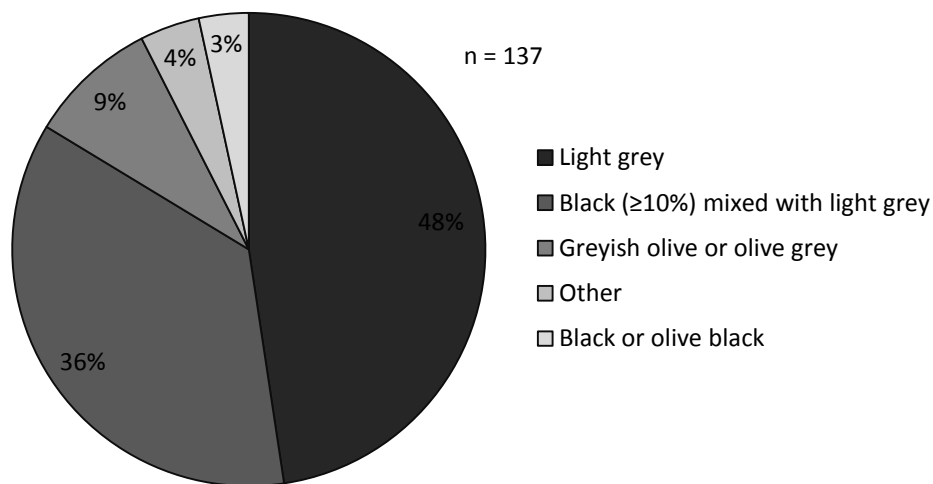


Figure 3.2: Simplified Munsell colours across all 137 bulk samples from the central Chatham Rise.

The relative abundance of glauconite was visually estimated for each sample (Figure 3.3). About one third of samples contain little or no glauconite, another third include at least some glauconite, and the final third are conspicuously rich in glauconite. This assessment aided in the subsequent choice of samples for more specific glauconite analysis. The glauconite content could also be gauged from the percentage blackness within each sample (Figure 3.4) (see Appendix II-A for estimated relative abundance of glauconite and % blackness in all samples).

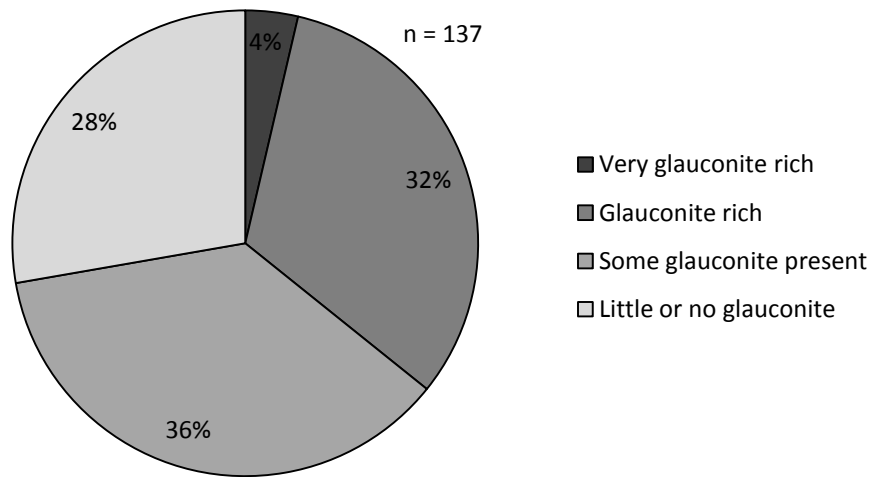


Figure 3.3: Pie chart displaying the relative abundance of glauconite visually estimated in the dried 137 bulk samples from central Chatham Rise.

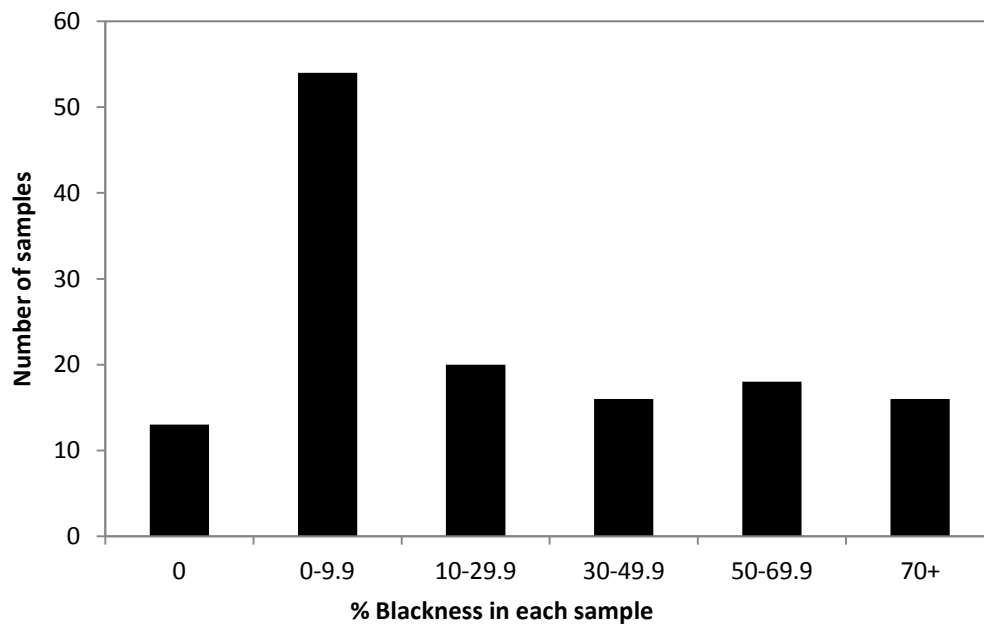


Figure 3.4: Visual estimate of % blackness in each of the 137 bulk samples from central Chatham Rise.

By comparing Munsell colour (Figure 3.2) with the estimated percentage of blackness (Figure 3.4) in each sample an indirect correlation is derived between sample colour and glauconite content (Figure 3.5). This validates the general relationship that the darker the colour of the bulk surficial sediment samples from central Chatham Rise, the higher the glauconite content.

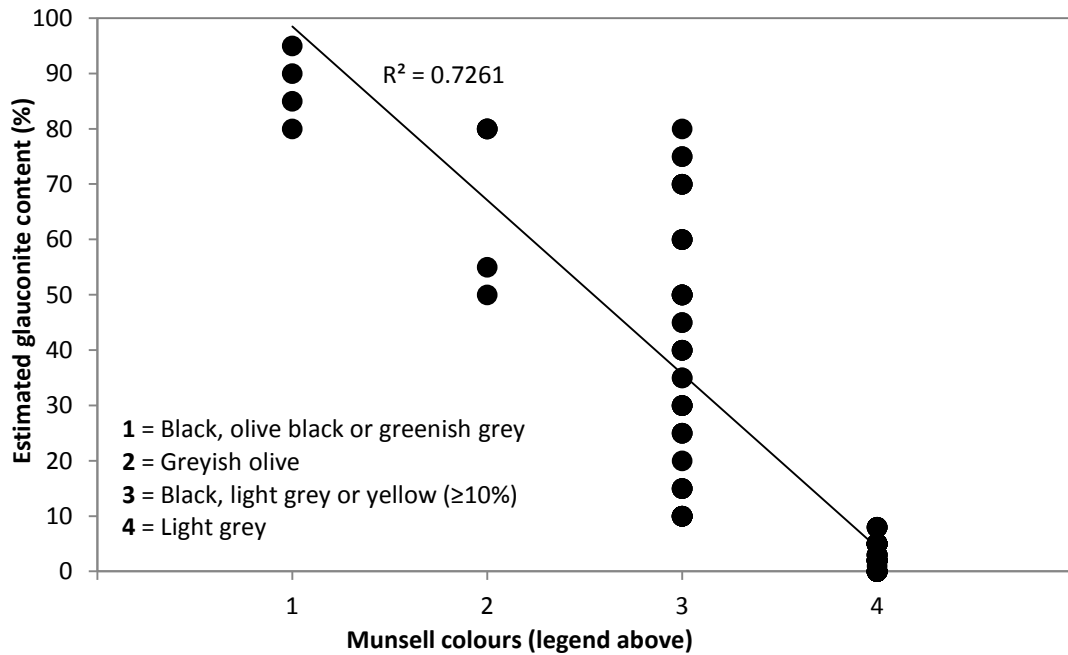


Figure 3.5: Relationship between Munsell colour and visually estimated glauconite content in all 137 bulk samples from central Chatham Rise.

3.2.2 Texture

The Malvern laser-sizer at The University of Waikato was used to gather textural information for the bulk surficial sediment samples. For the coarser samples (fine to medium sand) 1-2 g of sample was used, while for muddier samples 0.1-0.3 g of sample was used. The sediment samples were mixed with four to six drops of calgon to help disperse the silt and clay-sized grains in the mud fraction. The samples were introduced into the Malvern laser particle sizer one at a time and analysis was started once the obscuration value was in the range of 10-20%. Figure 3.6 shows the overall Folk (1968) sediment textural classes for all 137 samples (see Appendix II-B for samples chosen and Appendix II-C for all laser-sizer and textural results). The ternary plot shows that the textures of the bulk surficial samples on central Chatham Rise range from sand to silty sand to sandy silt, with the majority (68%) being silty sand (Figure 3.6).

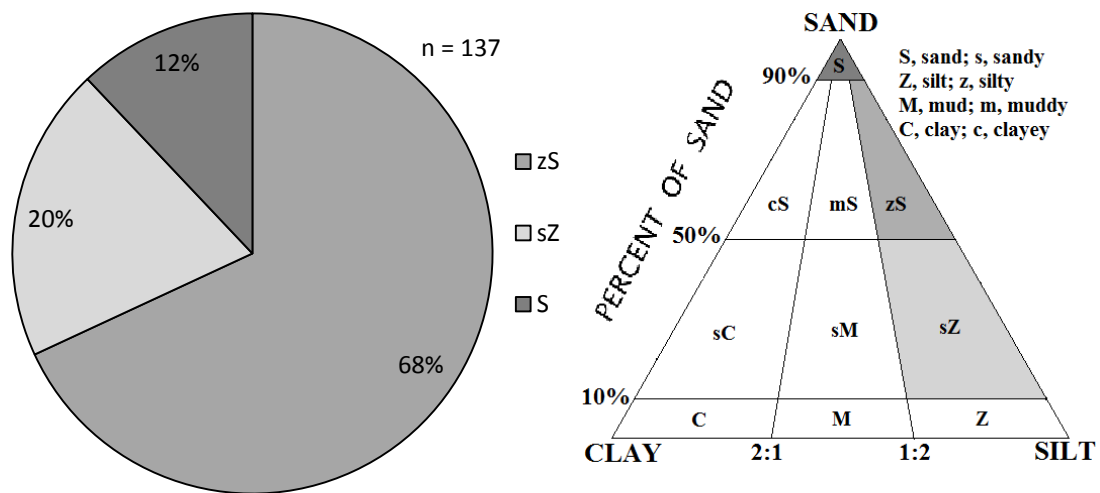


Figure 3.6: Percentages of Folk's (1968) sediment textural classes for all 137 bulk samples from central Chatham Rise.

Figure 3.7 illustrates the distribution of the individual sand, silt and clay sized grains in the surficial sediments on central Chatham Rise, and Figure 3.8 the gravel content, median sediment size and the Folk (1968) sorting class for the same samples. The areal distribution of Folk's (1968) sediment textural classes on central Chatham Rise is displayed in Figure 3.9.

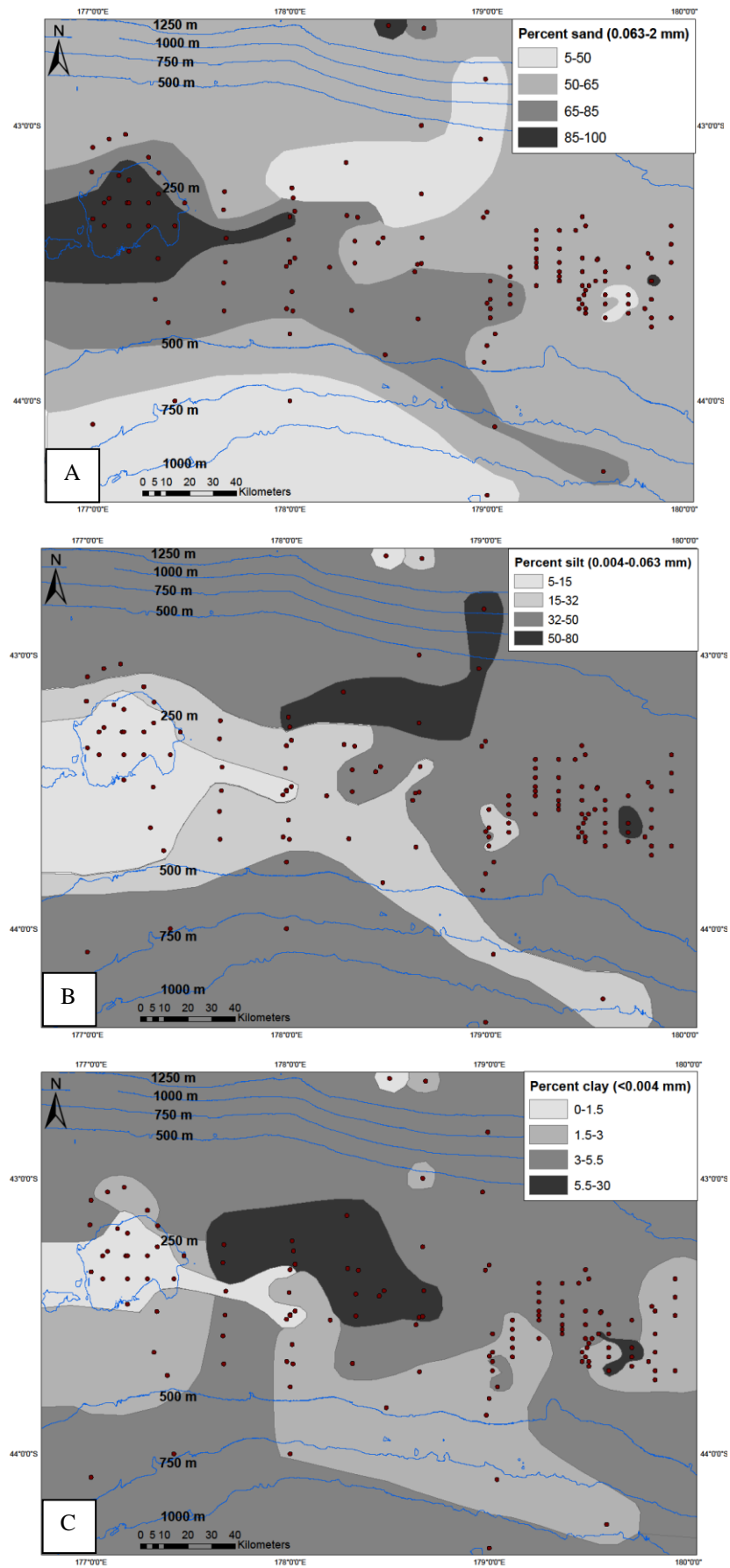


Figure 3.7: Percent textural size classes in surficial sediments from central Chatham Rise. A: Sand (0.063-2 mm), B: Silt (0.004-0.063 mm), C: Clay (<0.004 mm).

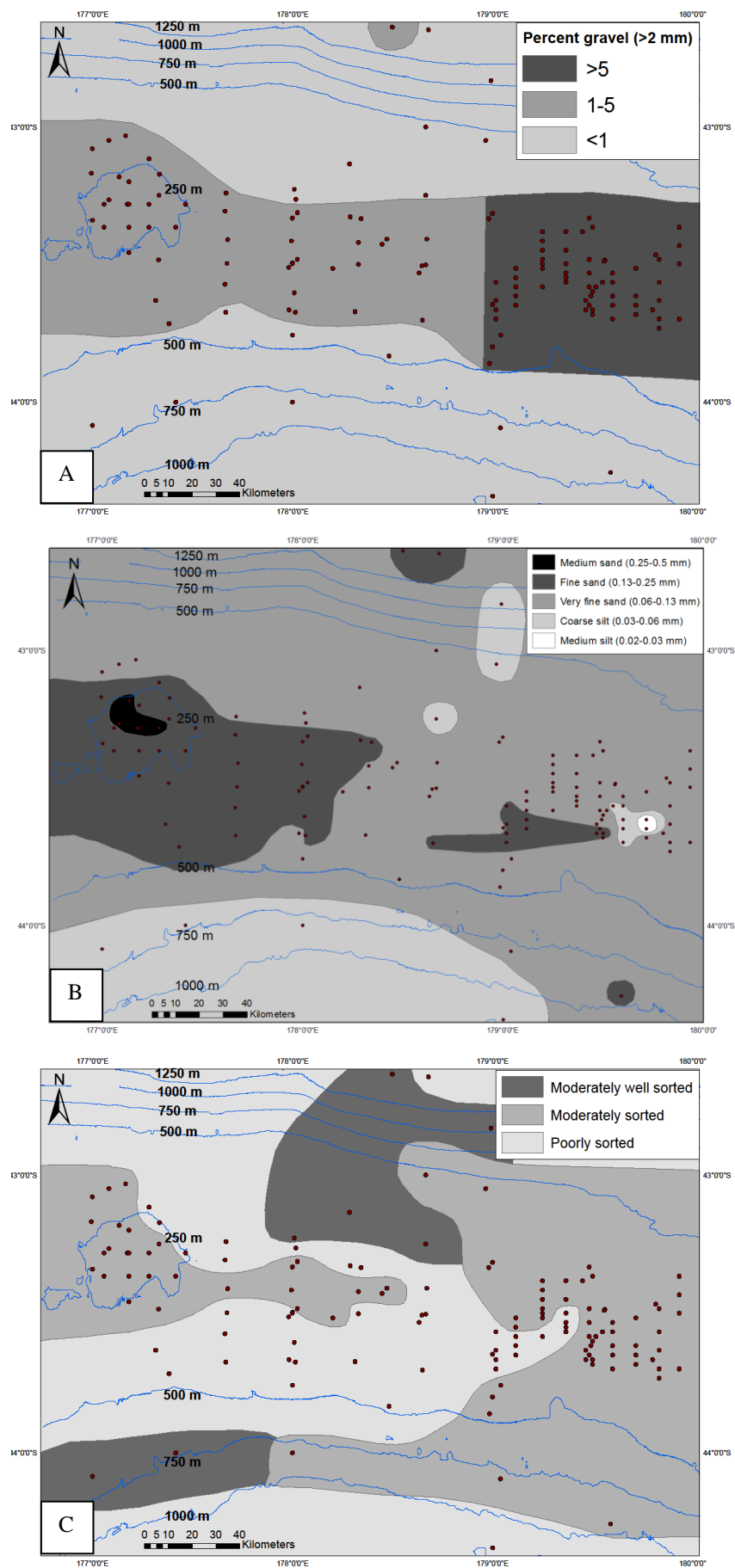


Figure 3.8: A: Percent gravel (>2 mm), B: Median sediment texture, C: Folk's (1968) sediment sorting classes for surficial sediment on central Chatham Rise.

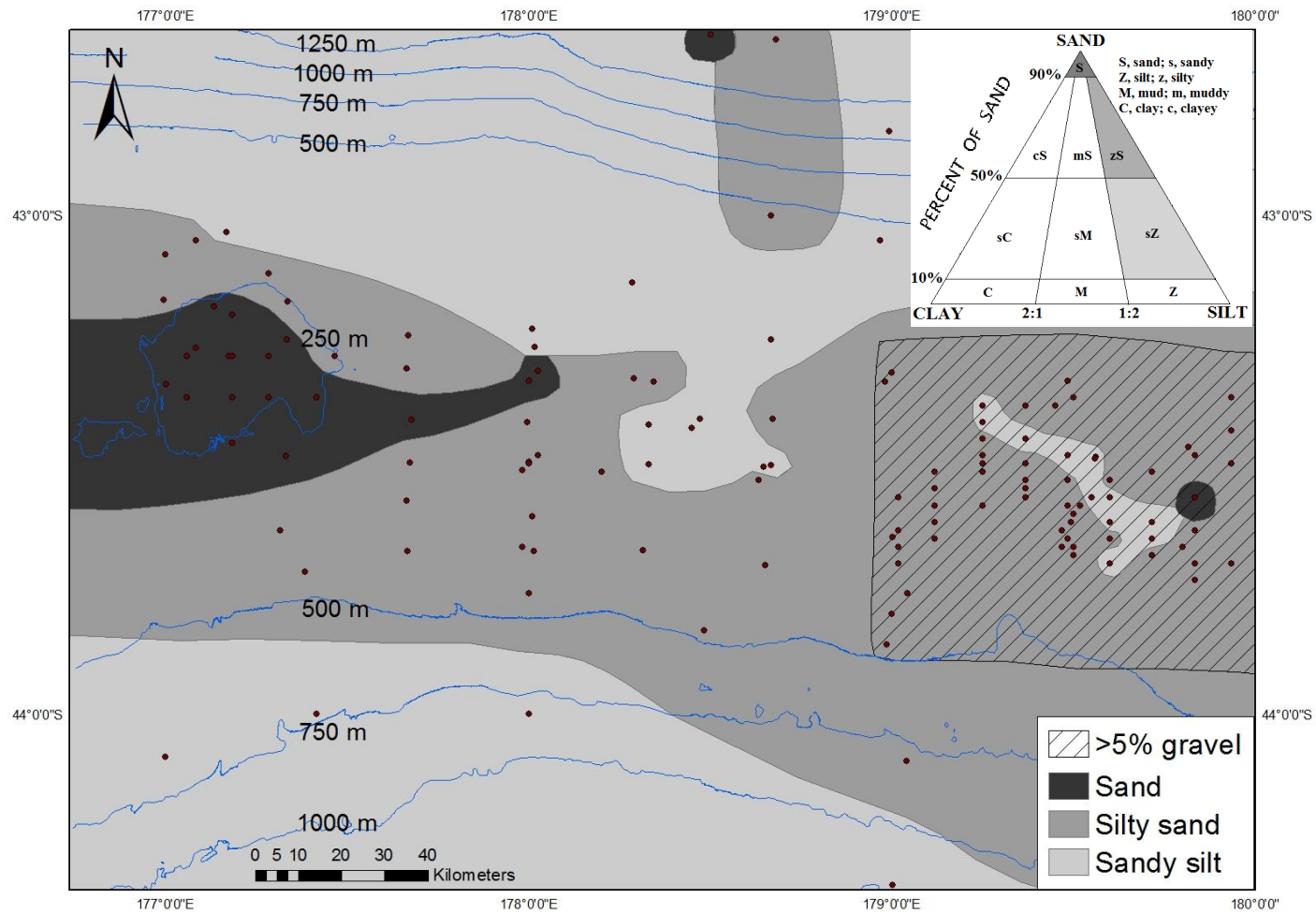


Figure 3.9: Distribution of Folk's (1968) sediment textural classes over central Chatham Rise.

Figure 3.7 illustrates some clear patterns between the percent size classes and water depth over central Chatham Rise. The highest sand content and the lowest clay content occur in the least water depths associated with Reserve Bank, a topographic high rising to 250 m depth (Norris, 1964; Pasho, 1976). The highest percentages of clay and silt are mostly in water depths greater than 500 m, where the sand contents are typically low to moderate. The percentage of sand decreases away from a very high content on Reserve Bank (Figure 3.7). The gravel content is highest on the eastern side of central Chatham Rise, an area known to be especially rich in phosphorite nodules (Figure 3.8A), and is lowest (<1%) in water depths greater than 500 m.

The distribution of median sediment size also broadly relates to water depth (Figure 3.8B), increasing with decreasing water depth. Thus medium to fine sands are constrained to water depths less than 500 m while very fine sands to medium silts occupy depths greater than 500 m. Medium and fine sands are particularly abundant on Reserve Bank (Figure 3.8B). A similar pattern is evident in Figure 3.9, where using Folk's (1968) textural classes sand dominates the shallowest (<300 m) portions of the Rise on Reserve Bank, silty sand dominates in <500 m water depths and sandy silt in the deeper (>500 m) areas of central Chatham Rise. This textural class map (Figure 3.9) also shows a "saddle" along the 178° 30'E longitude line where there exists a band of finer textured sediments of predominantly sandy silts, compared to silty sands to the east and west of this position. This "saddle" pattern is also evident in the sorting classification map (Figure 3.8C), with poorly sorted sediments within the longitudinal band in <500 m water depths compared to mainly moderately sorted values elsewhere on the Rise at comparable depths.

Following the bulk sediment size analysis the sand fraction of 39 selected samples was separated into a glauconite fraction and a non-magnetic siliciclast and carbonate fraction using a Frantz magnetic separator (see Appendix II-D for wt% of each fraction in all samples). Separation was achievable due to the magnetic nature of glauconite owing to its high iron content (McConchie, 1978; Compton, 1989) (the separation technique is fully explained in Section 6.2). The analysis expectedly shows that there is a good positive relationship ($r^2=0.675$) between

glauconite content and percent sand sized material in the surficial sediments on central Chatham Rise (Figure 3.10).

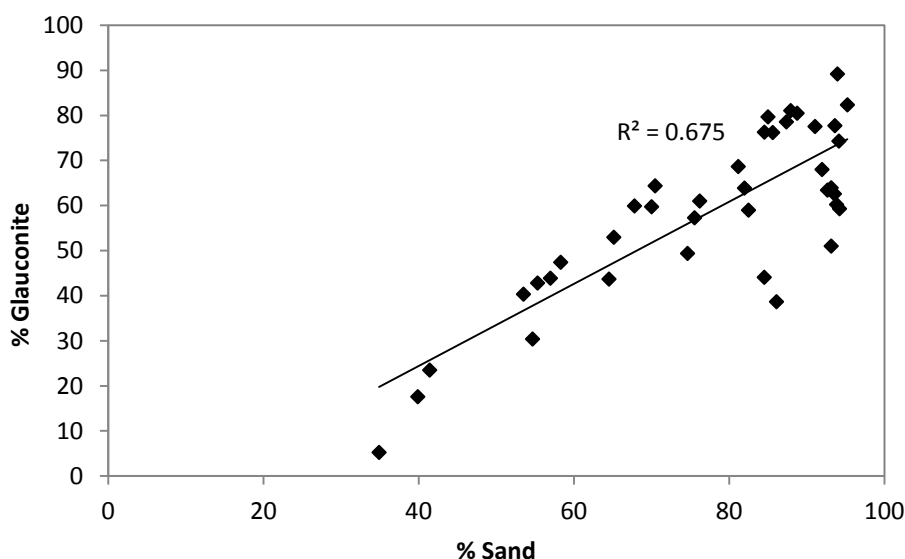


Figure 3.10: Relationship between percent glauconite and percent sand sized grains in 39 glauconitic sediment samples on central Chatham Rise.

3.2.3 XRD mineralogy

The mineralogy of surficial sediment samples from central Chatham Rise was studied using XRD, both for the bulk samples and the clay fraction. 50 bulk samples representative of the range of echo-types, water depths (north to south), and Munsell colours present over central Chatham Rise were powdered in a tungsten carbide ring mill for the bulk XRD (and XRF: see Section 3.2.4A) analysis (see Appendix II-B for samples used).

3.2.3A Bulk mineralogy

Bulk powdered samples were analysed on a Philips X'Pert X-Ray Diffraction machine (XRD) with X'Pert Highscore computer software to determine the mineralogy of the bulk sediments and also to confirm which samples were rich in glauconite. To use the XRD machine it was necessary to first become an approved user, which involved training by the XRD technician Indar Singe, as well as undergoing a safety test run by Associate Professor Alan Langdon in the Chemistry Department at The University of Waikato.

Each sample was pressed into a small metal disc to provide unoriented powder mounts. Machine settings were configuration 2, scans from 2-40° 2 θ angle, 0.03 step size and 1.0 step time, and a scan rate of 1.8° 2 θ /min. The XRD scans of all 50 bulk powdered samples generally gave similar mineralogical assemblages involving predominantly calcite, quartz, plagioclase feldspar, glauconite/illite and some other clays minerals. Examples of XRD graphs produced for three different bulk samples are shown in Figures 3.11, 3.12 and 3.13. Appendix II-E contains all the XRD scan results.

All XRD scans showed quartz and calcite peaks, while plagioclase feldspar occurred in three quarters of the scans. In all cases the calcite peak position (29.4° 2 θ , or 3.03Å) is consistent with the calcite being low-Mg calcite. Glauconite and other clay mineral peaks showed up in the glauconite-rich samples, glauconite being positively detected in one third of samples and other clays in about two thirds of the samples (Table 3.1). In these bulk sample XRD scans the phyllosilicate peaks were mostly weak due partly to the unoriented nature of the powder mounts.

Table 3.1: Tabulation of mineral types in XRD scans of 50 XRD bulk samples from central Chatham Rise.

Mineral	Main peak	Number of samples	Percent of samples (%)
Quartz	26.6° 2 θ	50	100
Calcite	29.4° 2 θ	50	100
Plagioclase	27.9° 2 θ	37	74
Clay minerals	19.6° 2 θ	34	68
Glauconite	8.6° 2 θ	17	34

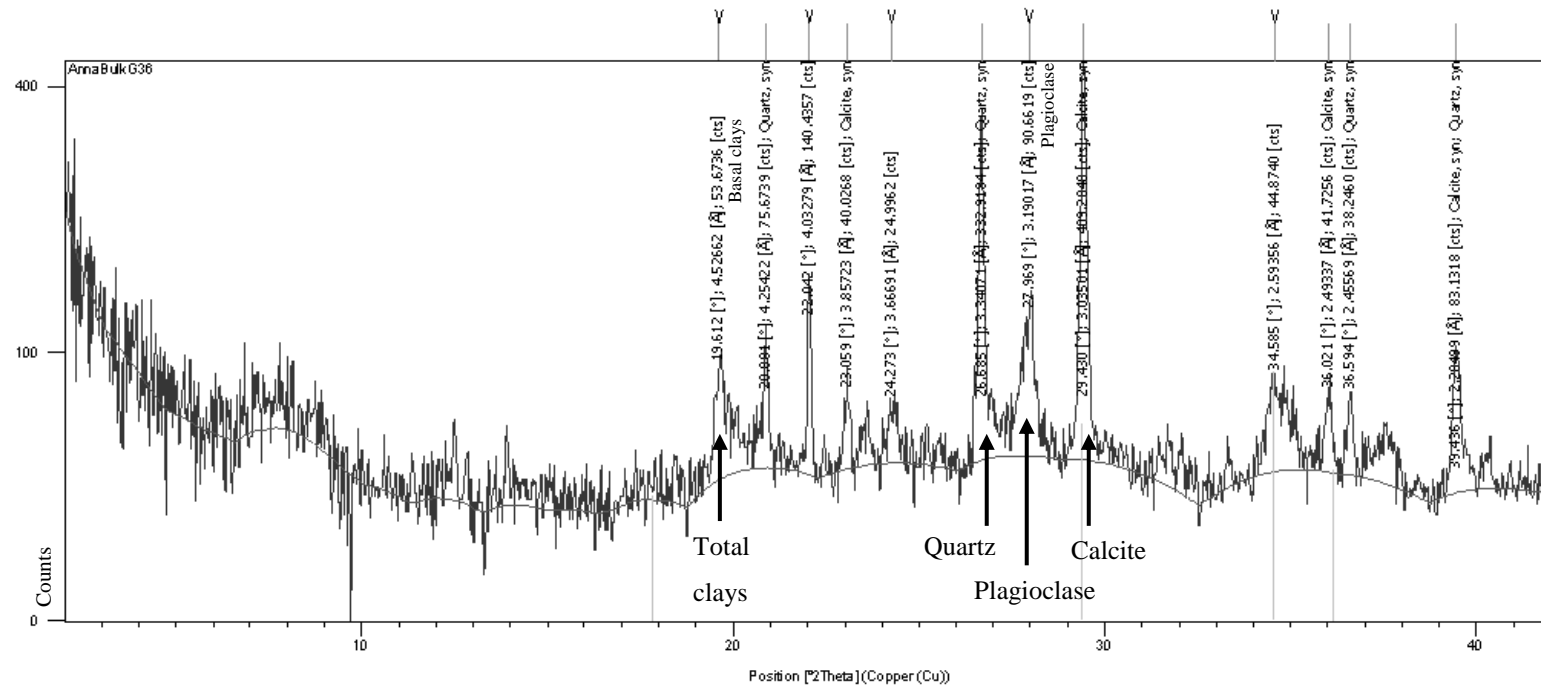


Figure 3.11: XRD scan of G36 bulk powdered sediment sample.

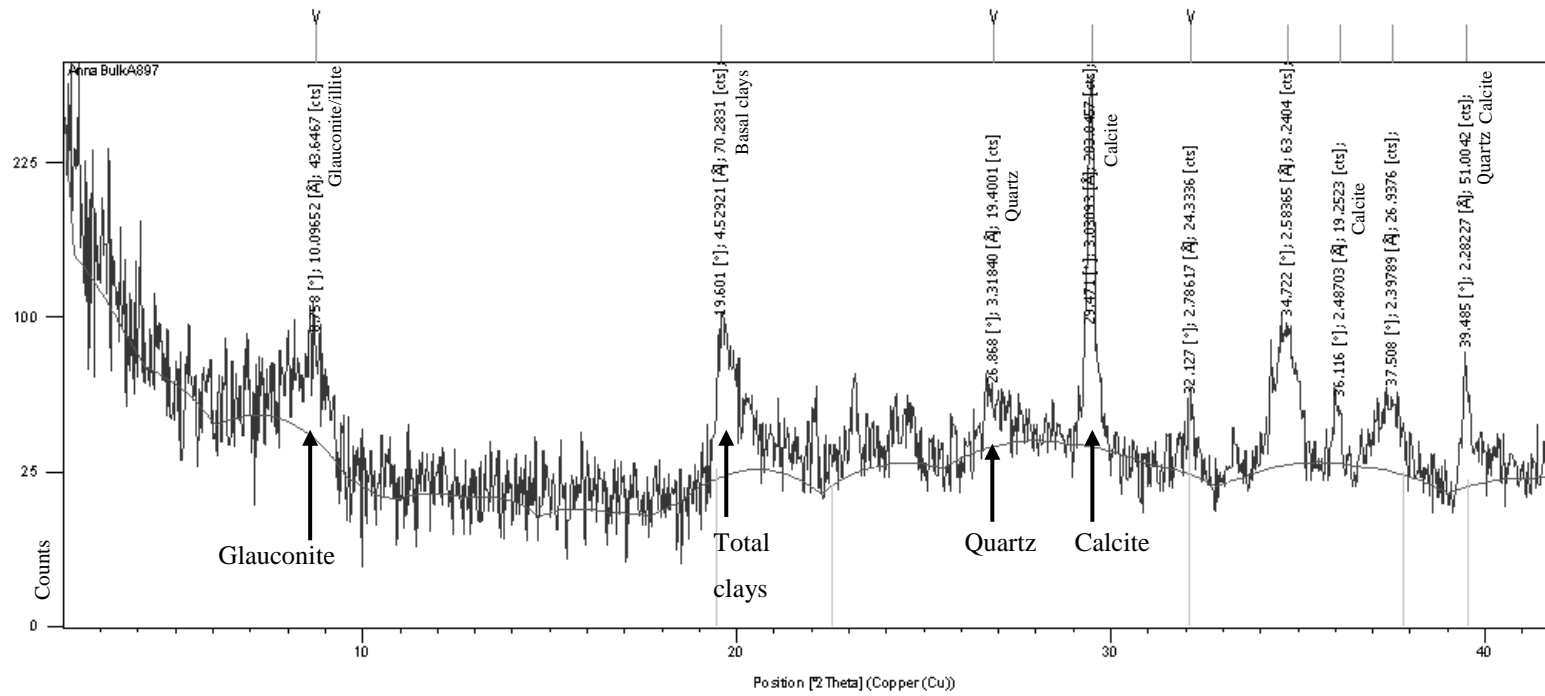


Figure 3.12: XRD scan of A897 bulk powdered sediment sample.

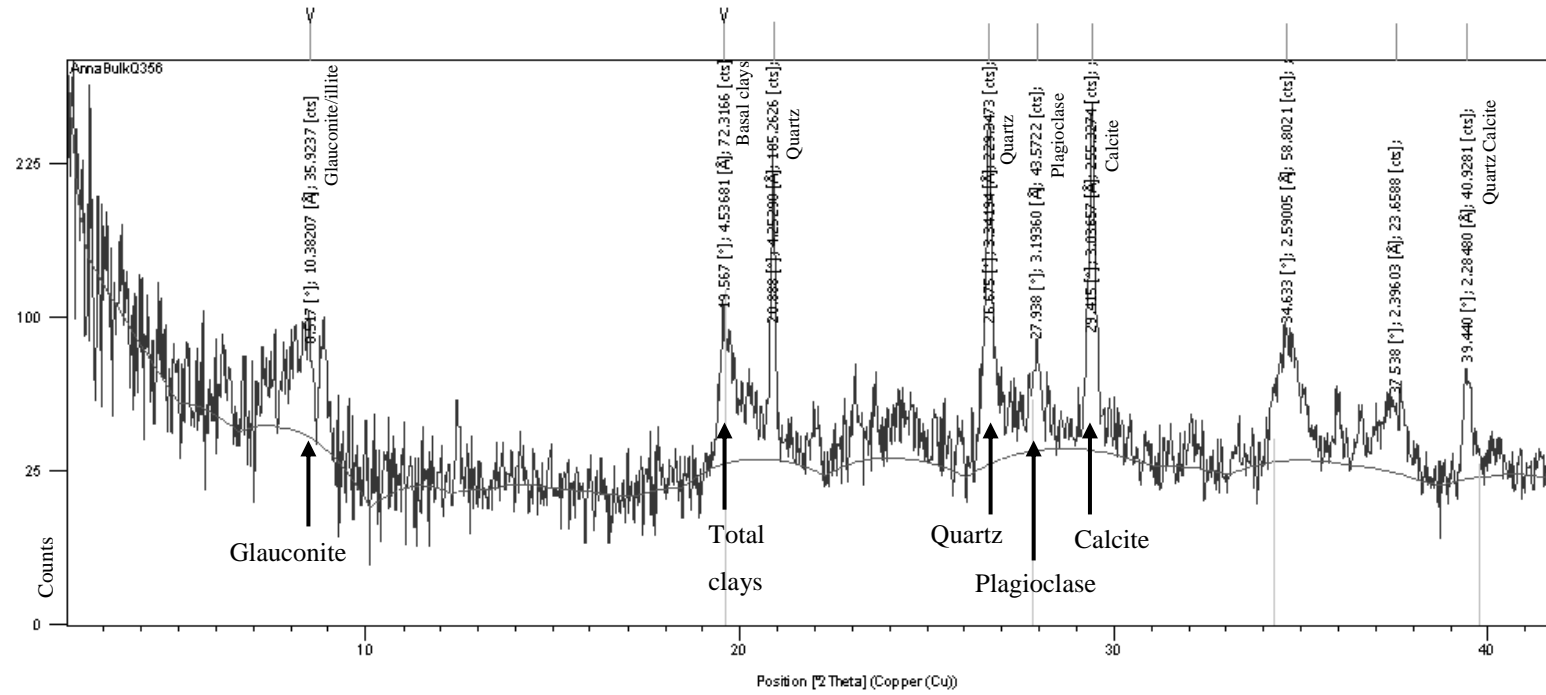


Figure 3.13: XRD scan of Q356 bulk powdered sediment sample.

3.2.3B Clay mineralogy

Apart from CaCO_3 determinations (see Section 4.2.5) the remainder of the laboratory analysis carried out in this thesis required the samples to be separated into their gravel, sand and mud fractions (Figure 1.2). The mud fraction ($<63\ \mu\text{m}$) of each sample was obtained by wet sieving over a bucket through a $63\ \mu\text{m}$ mesh screen using a low pressure water pump and working with a soft baking spatula. The mud fraction was left to settle in the bucket overnight before draining off most of the water and transferring the mud into a small labelled pottle. The $>63\ \mu\text{m}$ sand plus gravel fraction was transferred into an aluminium tray and placed in an oven set at 50°C to dry overnight. The dried sample was put through a 2 mm mesh sieve to separate the gravel and sand fractions, each of which was weighed and transferred into labelled plastic bags (raw results in Appendix II-D).

The mineralogy of the potted mud fraction was analysed using XRD. Mud-rich samples were pipetted onto glass slides and left to settle and dry for 3-4 hours to yield an oriented sample mount. Samples were then run through the XRD machine using the same settings as before (Section 3.2.3A). Following the air-dried scans, the oriented sample mounts were placed in a desiccator containing ethylene glycol for 48 hours, principally to positively detect the presence of any swelling smectite clay (McConchie, 1978; Hume & Nelson, 1982). After glycolation the samples were rescanned by XRD using configuration 2 settings from $2\text{-}15^\circ\ 2\theta$, a 0.02 step size and a 1.0 step time, a slightly slower scan over a shorter 2θ interval compared to the air-dried mounts. Lastly, XRD scans were then made of the sample mounts following heating in a furnace at 550°C for 1 hour using the same settings as for the glycolated scans. The heating enabled further characterisation of the clay minerals present by collapsing any smectite/montmorillonite present to illite (McConchie, 1978; Hume & Nelson, 1982). Figure 3.14 illustrates the movements of the (001) peak position of different clay minerals under various XRD treatments: air-dry untreated slides, glycolation, and heating (Hume & Nelson, 1982), which aids identification of the clay minerals present within samples from the central Chatham Rise.

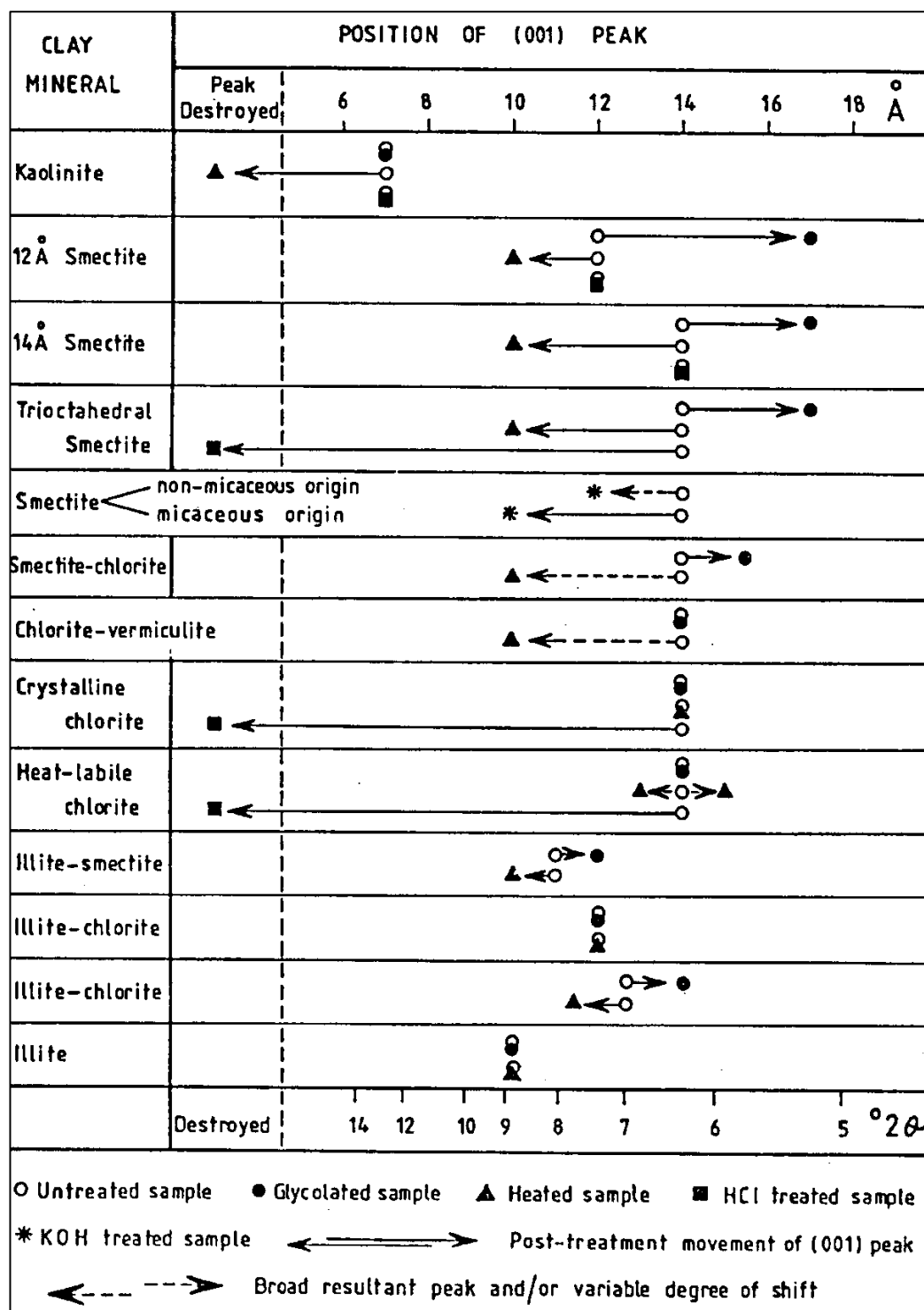


Figure 3.14: Movement of the clay mineral (001) XRD peak under different treatments, in which the relevant ones for this study are untreated, glycolated and heated (from Hume & Nelson, 1982).

The clay mineral peaks in the 35 air-dried oriented samples analysed yielded very similar results, and so only 13 samples were chosen to undergo the full three step analytical process (see Appendix II-B for samples chosen and Appendix II-E for all XRD scans). These were those samples with more clay present, as determined from the Malvern laser-sizer and XRF data.

The clay mineralogy results for the 13 samples are overall very similar and so one sample has been selected here to display the clay mineralogy of the mud fraction of the surficial sediments on central Chatham Rise (Figures 3.15, 3.16 and 3.17). The traces show three dominant clay mineral peaks that are unaltered in position following glycolation and heating. The 13.8Å peak at approximately 6.5° 2θ is according to Figure 3.14 either the 14Å peak of smectite or of chlorite, but because this peak does not change under glycolation or heating (Figures 3.16 and 3.17) smectite is ruled out. The next peak, occurring at 9.1° 2θ or 9.7Å (Figure 3.15), is due to illite (Figure 3.14) because it does not shift with glycolation or heating (Figures 3.16 and 3.17); this illite/mica peak in fact corresponds to the main (001) glauconite peak. The last main peak is an approximately 7Å peak at 12.7° 2θ (Figure 3.15), which could be an (001) peak of kaolinite or the (002) peak of chlorite (Figure 3.14). Because this peak does not shift with glycolation or subsequent heating (Figures 3.16 and 3.17) it likely represents the (002) peak of the chlorite present within the bulk mud sample (Hume & Nelson, 1982). In summary, the XRD results demonstrate the clay mineralogy of the bulk samples on central Chatham Rise comprises illite/glauconite and chlorite. The asymmetry on the high-angle side of the illite/glauconite peak will be addressed when discussing the mineralogy of the glauconite (Section 7.3.1), but is basically due to a variable but small amount of mixed-layer smectite within the overall glauconite structure.

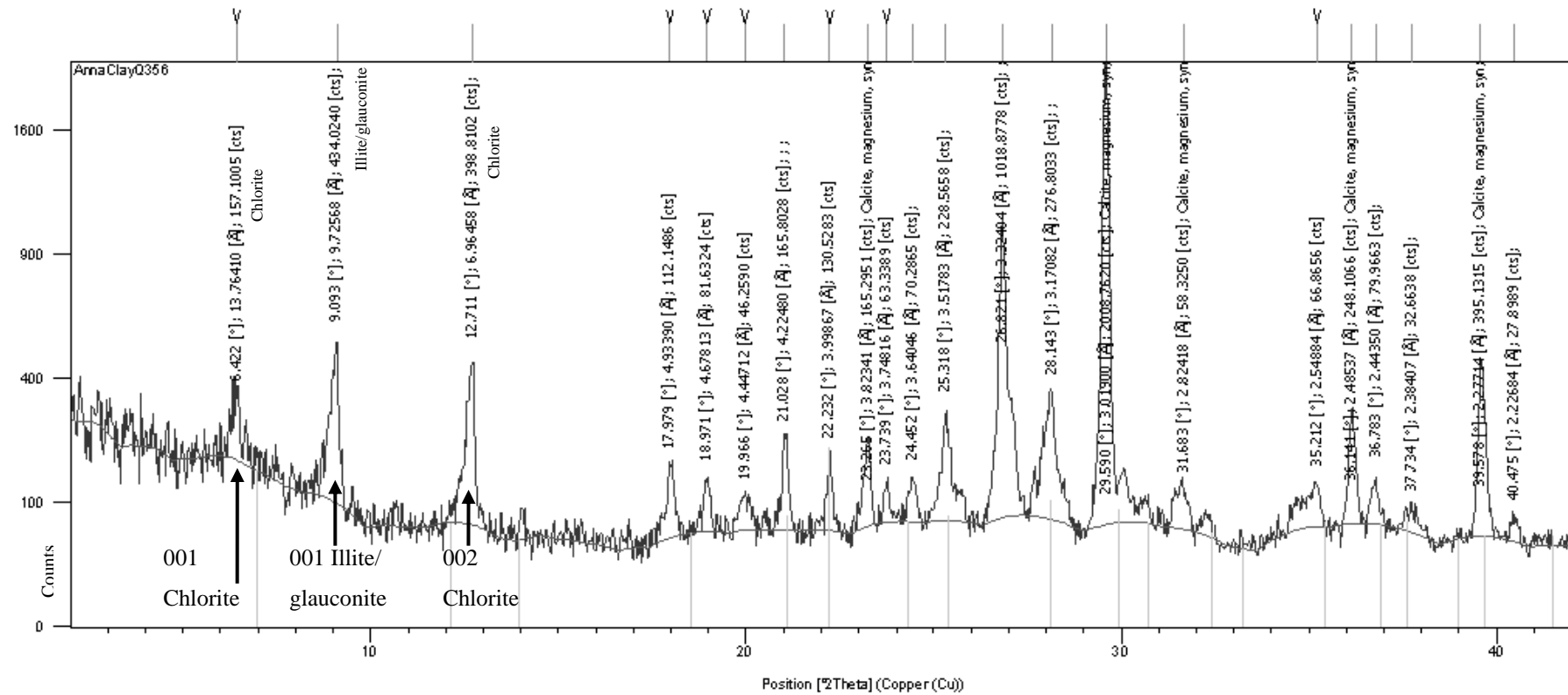


Figure 3.15: Air-dried untreated oriented mount XRD scan of mud fraction from Q356.

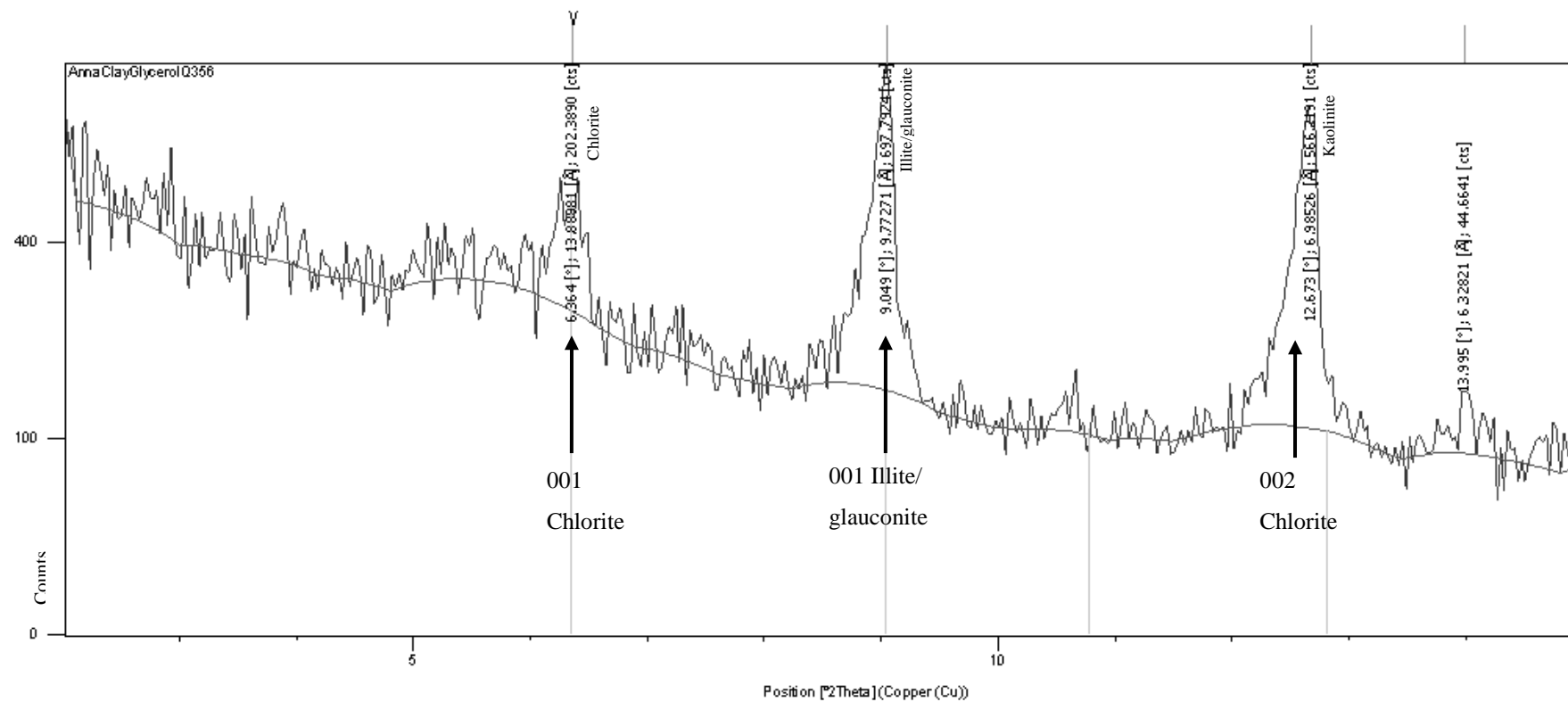


Figure 3.16: Glycolated oriented mount XRD scan of mud fraction from Q356.

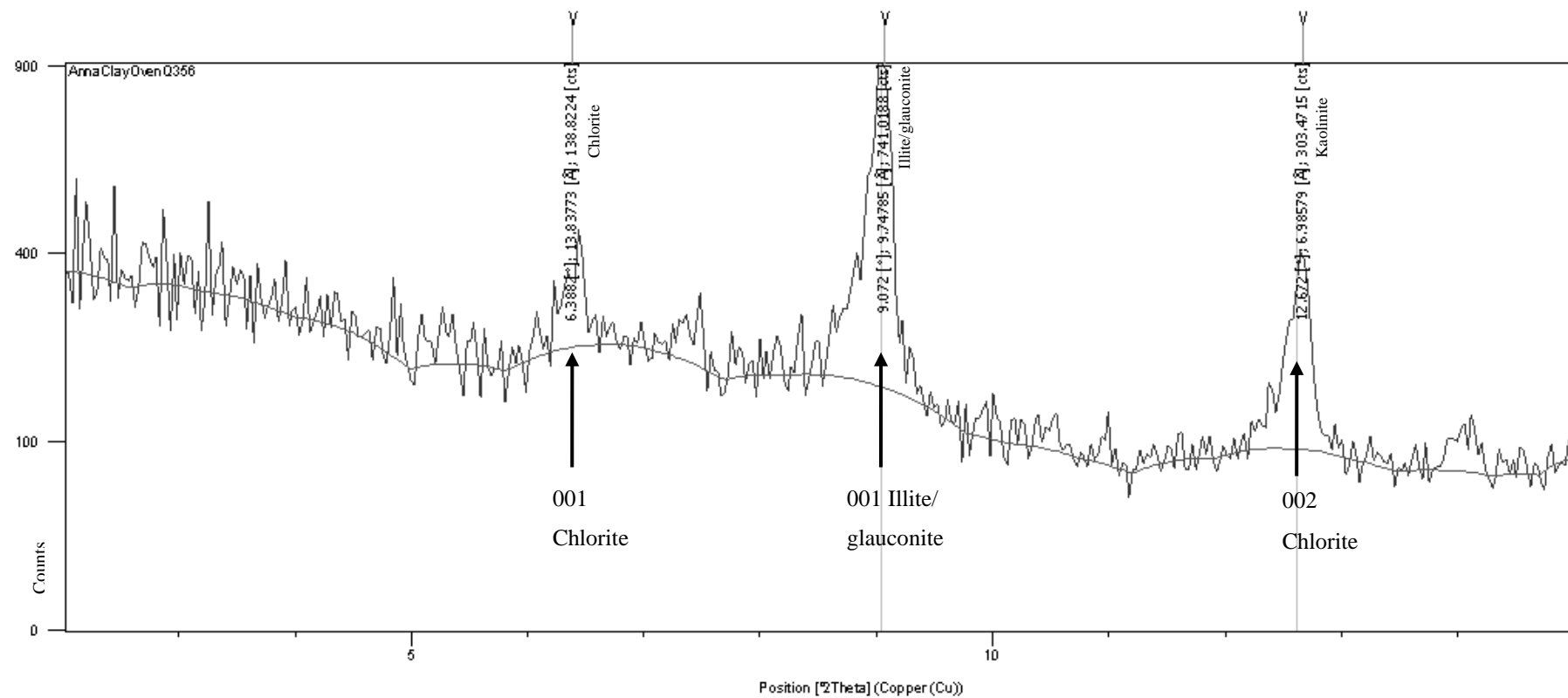


Figure 3.17: Heated oriented mount XRD scan of mud fraction from Q356.

3.2.4 Geochemistry

The geochemistry of 49 of the bulk surficial sediment samples from central Chatham Rise mentioned in Section 3.2.3 was studied using XRF and their CaCO_3 content was analysed by acid digestion and bulk XRD scans.

3.2.4A XRF elemental composition

X-ray fluorescence is a technique used to analyse the major and trace element content of samples via the fused glass disc and pressed pellet methods, respectively. Analyses were made using the SPECTRO X-LAB 2000 XRF instrument at The University of Waikato. XRF analysis was undertaken on pressed pellets which is very accurate for trace elements but less so for major elements. Nevertheless, the K_2O and Fe_2O_3^* (* = total Fe, i.e. Fe_2O_3 and FeO) values were sufficiently good to identify those samples rich in glauconite for subsequent more detailed analysis of glauconite concentrates. Moreover, the same bulk major element analyses provided general information about clay mineral and carbonate contents from the Al_2O_3 and CaO values, respectively (see Appendix II-B for samples chosen and Appendix II-F for raw XRF results).

In order to analyse the trace elements using the XRF machine, pressed pellets were prepared. Using a paper cup, approximately 5 g of sample was added along with 10 drops of PVA binder, and mixed thoroughly using a wooden spatula. The sample was then added into a pre-recorded weight aluminium cup and pressed down slightly. This cup was then put onto a raised metal base, with a cylinder over it, followed by inserting a plunger on top of the cup. The entire base, sample in the cup, cylinder and plunger was then loaded into a hydraulic press to about 90 bars. The cup with the now pressed sample in it was then put into a 70°C oven for 2 hours in order to evaporate the binder. Once the sample is cooled, it was weighed again, after taring an empty aluminium cup, so that the exact sample weight can be recorded. The last step was to insert the sample into the carousel in the XRF machine.

Table 3.2 summarises the XRF geochemical data into a correlation matrix for all major and trace elements for the 49 bulk powdered samples from central Chatham Rise. The moderate to strong correlations are highlighted in grey (Table 3.2) and

some of these are mentioned briefly here. Al_2O_3 and SiO_2 have a strong positive correlation (0.95), presumably reflecting the content of clay minerals and/or feldspar in the sediments. There is also a positive correlation (0.70) between Al_2O_3 and TiO_2 , likely tied to the siliciclastic clay mineral content. There is also a strong positive correlation (0.95) between K_2O and Fe_2O_3^* , undoubtedly due to the glauconitic component of bulk samples. A negative relationship occurs between CaO and both K_2O (-0.69) and Fe_2O_3^* (-0.95) (Table 3.2), presumably because as the glauconite component in bulk samples increases (as represented by K_2O and Fe_2O_3^*), the carbonate (CaO) fraction decreases, and vice versa.

Table 3.2: XRF elemental data correlation matrix for all 49 bulk powdered samples from central Chatham Rise (Note: Fe₂O₃* is total Fe, i.e. Fe₂O₃ and FeO).

	Na ₂ O	MgO	Al ₂ O ₃	SiO ₂	P ₂ O ₅	K ₂ O	CaO	TiO ₂	MnO	Fe ₂ O ₃ *	S	Cl	V	Cr	Co	Ni	Cu	Zn
MgO	-0.59
Al₂O₃	-0.65	0.63
SiO₂	-0.60	0.71	0.95
P₂O₅	-0.32	0.18	-0.02	0.05
K₂O	-0.31	0.94	0.45	0.56	0.10
CaO	-0.20	-0.54	-0.44	-0.58	0.21	-0.69
TiO₂	-0.20	-0.02	0.70	0.62	-0.18	-0.15	-0.27
MnO	-0.06	-0.52	0.29	0.17	-0.13	-0.68	0.24	0.79
Fe₂O₃*	-0.22	0.85	0.23	0.36	0.10	0.95	-0.60	-0.31	-0.79
S	0.19	0.14	-0.26	-0.14	0.51	0.27	-0.17	-0.36	-0.43	0.33
Cl	0.99	-0.66	-0.66	-0.63	-0.32	-0.40	-0.13	-0.18	0.01	-0.31	0.13
V	-0.41	0.90	0.45	0.58	0.34	0.92	-0.58	-0.06	-0.58	0.89	0.31	-0.49
Cr	-0.32	0.90	0.43	0.54	0.11	0.95	-0.65	-0.11	-0.65	0.95	0.27	-0.42	0.91
Co	0.09	0.06	0.12	0.11	0.30	0.12	-0.28	0.16	0.01	0.15	0.35	0.11	0.19	0.24
Ni	-0.29	0.56	0.24	0.30	0.74	0.56	-0.25	-0.16	-0.42	0.53	0.57	-0.34	0.67	0.61	0.50	.	.	.
Cu	0.01	-0.32	0.26	0.09	0.10	-0.41	0.11	0.54	0.66	-0.52	-0.03	0.06	-0.32	-0.41	0.27	0.01	.	.
Zn	-0.08	0.50	0.28	0.31	0.08	0.56	-0.48	0.10	-0.31	0.59	0.18	-0.16	0.62	0.69	0.29	0.50	-0.08	.
Ga	-0.06	0.64	0.58	0.61	-0.21	0.74	-0.84	0.32	-0.23	0.68	0.15	-0.14	0.66	0.77	0.37	0.37	-0.01	0.64
Ge	0.02	0.69	0.28	0.39	0.02	0.84	-0.77	-0.08	-0.59	0.85	0.31	-0.07	0.75	0.85	0.33	0.51	-0.30	0.61
As	-0.27	0.55	-0.02	0.13	0.77	0.58	-0.16	-0.46	-0.63	0.64	0.66	-0.32	0.70	0.56	0.27	0.79	-0.30	0.23
Br	0.67	-0.82	-0.55	-0.66	-0.34	-0.73	0.36	-0.08	0.33	-0.71	-0.17	0.72	-0.84	-0.75	-0.10	-0.50	0.31	-0.39
Rb	-0.12	0.83	0.32	0.42	0.02	0.96	-0.74	-0.19	-0.72	0.97	0.34	-0.22	0.87	0.96	0.25	0.55	-0.39	0.64
Sr	-0.04	-0.68	-0.41	-0.53	0.24	-0.82	0.92	-0.08	0.46	-0.79	-0.17	0.04	-0.68	-0.81	-0.25	-0.30	0.29	-0.54
Y	-0.16	0.42	0.08	0.11	0.45	0.47	-0.20	-0.29	-0.44	0.52	0.48	-0.20	0.52	0.55	0.51	0.73	-0.07	0.49
Zr	0.00	-0.31	0.40	0.43	-0.14	-0.41	-0.14	0.83	0.84	-0.54	-0.29	0.03	-0.33	-0.39	0.06	-0.32	0.44	-0.23

Ba	-0.31	-0.54	-0.40	0.36	-0.70	0.53	-0.33	0.71	0.89	0.25	0.39	0.42
La	0.27	0.16	0.30	-0.22	0.18	-0.19	0.63	0.19	0.19	0.46	-0.03	0.39	0.19
Ce	0.56	0.33	0.11	-0.44	0.32	-0.50	0.23	0.55	0.41	0.13	-0.35	-0.03	0.16	0.53
Hf	0.15	0.00	-0.32	0.30	-0.19	-0.13	-0.23	0.65	0.54	-0.03	0.04	0.18	0.46	0.14	0.47
Tl	-0.57	-0.62	-0.35	0.66	-0.77	0.63	-0.33	0.44	0.60	0.26	0.62	0.38	0.78	0.07	-0.14	0.37
Pb	-0.26	-0.25	0.09	0.11	-0.33	0.28	-0.01	0.39	0.50	0.48	0.05	-0.03	0.42	0.17	0.27	0.39	0.43	.	.	.
Bi	-0.48	-0.52	-0.27	0.21	-0.60	0.50	-0.48	0.31	0.34	0.01	0.14	0.19	0.38	-0.22	-0.25	0.04	0.48	0.10	.	.
Th	-0.54	-0.77	-0.67	0.66	-0.91	0.69	-0.48	0.62	0.75	0.00	0.59	0.28	0.82	-0.07	-0.11	0.42	0.79	0.38	0.51	.
U	-0.21	0.03	0.77	-0.28	0.01	0.24	0.43	-0.16	0.08	0.90	-0.12	-0.05	0.18	0.35	-0.01	-0.19	0.21	0.32	0.00	-0.12

Figures 3.18 and 3.19 illustrate the relationship between the main surficial sediment textural classes on central Chatham Rise (Figure 3.9) and the content of selected major and trace elements respectively within each textural class (see Appendix II-F for the textural classes and geochemistry of all samples).

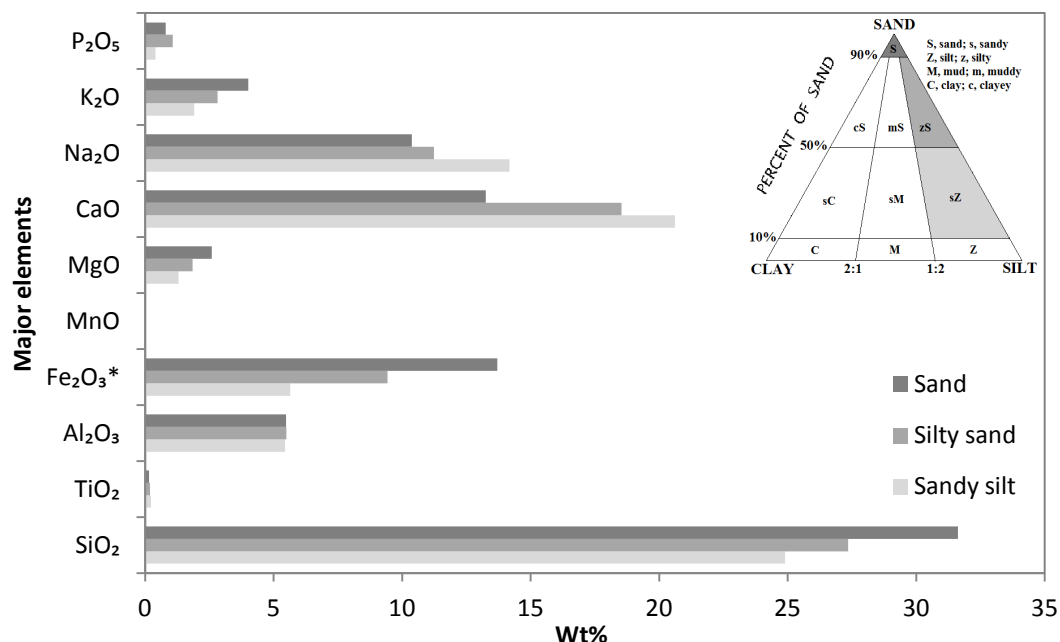


Figure 3.18: Average amount of major elements in the three main surficial sediment textural classes (sand, silty sand and sandy silt) on central Chatham Rise.

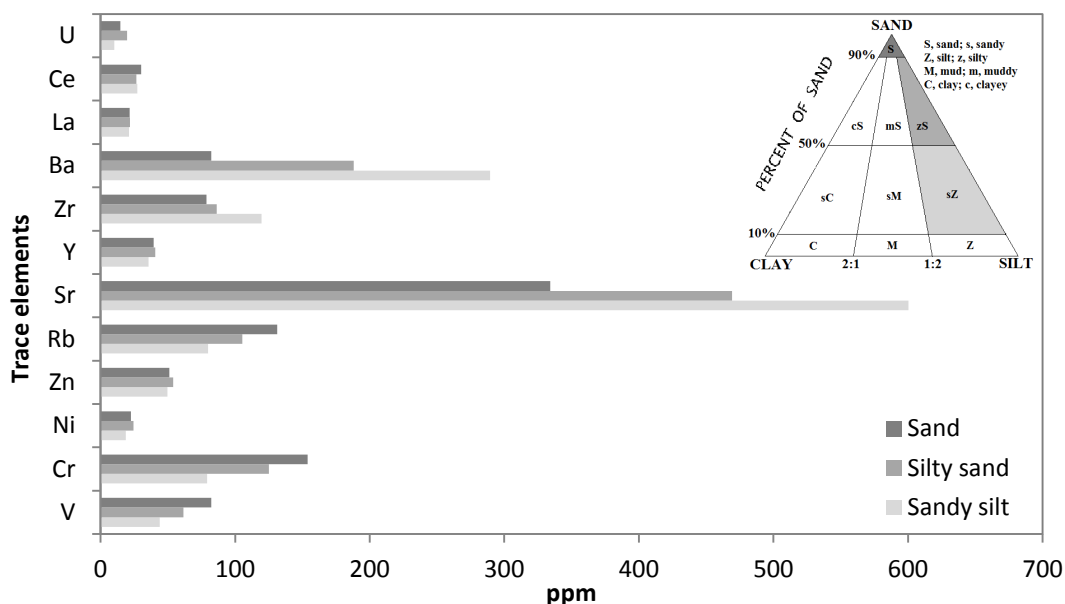


Figure 3.19: Average amounts of trace elements in the three main surficial sediment textural classes (sand, silty sand and sandy silt) on central Chatham Rise.

K₂O, MgO, Fe₂O₃* and SiO₂ all have the greatest concentration in the sand samples (Figure 3.18), most likely reflecting a high content of glauconite grains which are mainly of sand size. CaO on the other hand is highest in the sandy silt

samples, most likely due to a preponderance of mud-sized calcareous material. Na₂O is also highest in the sandy silt class. MnO, TiO₂, Al₂O₃ and P₂O₅ do not seem to change much between the three different textural classes (Figure 3.18).

Figure 3.19 shows that Rb, Cr and V are most concentrated in the sand textural class. Glauconite is typically enriched in these elements (McConchie, 1978; Compton, 1989) and so they are probably mainly tied up in the sand-sized glauconite fraction within the bulk samples. Sr, Ba and Zr are highest within the sandy silt textural class and are presumably mainly associated with the mud-sized siliciclastic and calcareous material. Ce, La, Y, Zn, Ni and V do not vary much between the three textural classes (Figure 3.19).

3.2.4B CaCO₃ content

The bulk sediments forming the surficial deposits covering the central Chatham Rise typically contain a significant amount of carbonate material, and so knowing the calcium carbonate (CaCO₃) percentage of the bulk samples is an important aspect of this study. Determination of the CaCO₃ content can come from acid digestion, petrographic analysis, XRD and XRF.

Subsamples from 10 bulk powdered samples were chosen for acid digestion on the basis of their distribution across the area of central Chatham Rise and from their estimated calcium carbonate content from petrographic analysis. The reason only 10 samples was chosen for acid digestion was to investigate the relationship between the acidified ‘actual’ carbonate percentage and the height/counts of the main XRD calcite 29.4° 2θ peak in the same samples. If a significant relationship exists then the % CaCO₃ could be determined from the calcite peak counts for all 50 samples analysed by XRD. Samples were placed in an oven overnight at 105°C to remove any moisture and then into a pre-weighed 150 ml beaker, and again weighed before adding acid. 10% HCl acid was added to the beakers in periods until the samples ceased effervescing. Samples were left overnight in the acid to ensure all the carbonate was dissolved. Samples were then washed 5 times with distilled water before being put onto a hot plate set at 105°C for 12 hours to dry out before reweighing to determine the % CaCO₃ (see Appendix II-G for all data). The CaCO₃ results are summarised in Table 3.3. The acid digestion results were

then compared to the carbonate values obtained from XRF analysis, petrographic data and XRD scans (see Appendix II-G for data).

Table 3.3: % CaCO₃ values in bulk sediment samples determined using acid digestion and XRD (X-ray diffraction).

Sample	Acid digestion % CaCO ₃	XRD calcite 29.4° 2θ counts
A899	33.5	536.4
C605	27.3	352.6
C606	38.0	760.1
D116	32.5	667.8
G34	19.2	223.3
G113	13.1	155.7
G136	46.7	976.4
G217	41.5	785.9
Q325	17.5	209.8
Q356	17.4	255.3

The acid digestion CaCO₃ values are plotted against the XRD calcite 29.4° 2θ peak counts in Figure 3.20. XRD was chosen over XRF and thin section analysis because results were available for 50 XRD plots compared to 26 thin sections, and the XRF major element values were based on pressed pellets rather than glass discs. The correlation between XRD calcite 29.4° 2θ peak counts and the % CaCO₃ of the ten acid digested samples is excellent (Figure 3.20).

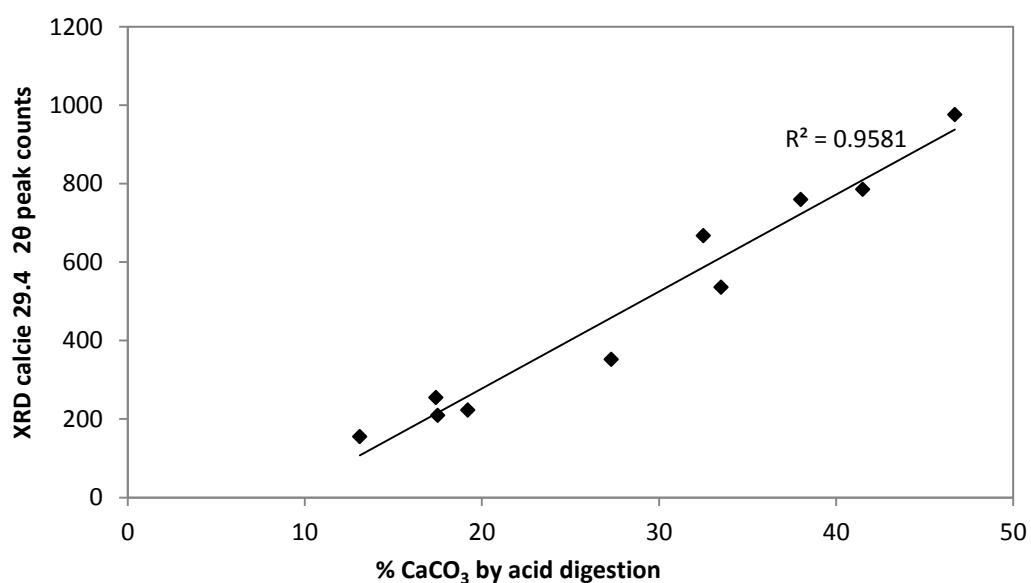


Figure 3.20: Correlation between % CaCO₃ from acid digestion and the XRD calcite 29.4° 2θ peak counts in 10 bulk samples.

The high r^2 value (0.9581) therefore enabled determination of the theoretical % CaCO_3 value in all 50 XRD bulk samples (see Appendix II-E for results). As a result it has been possible to produce a map displaying the distribution of CaCO_3 content across the entire central Chatham Rise (Figure 3.21).

Figure 3.21 shows that the calcium carbonate content is lowest (<30%) on and near Reserve Bank, a topographic high (<250 m) upon central Chatham Rise (Norris, 1964; Pasho, 1976). Reserve Bank is an isolated upstanding feature so that any terrigenous input is very low (Norris, 1964) making it an ideal setting for the formation of glauconite. The calcium carbonate content increases as water depth increases (>500 m) towards the northern and southern flanks of the Rise, and also increases between 179° and 180°E longitude, the area referred to as being 'phosphatic-rich' (Pasho, 1967; Kudrass & von Rad, 1984a, 1984b; von Rad, 1984).

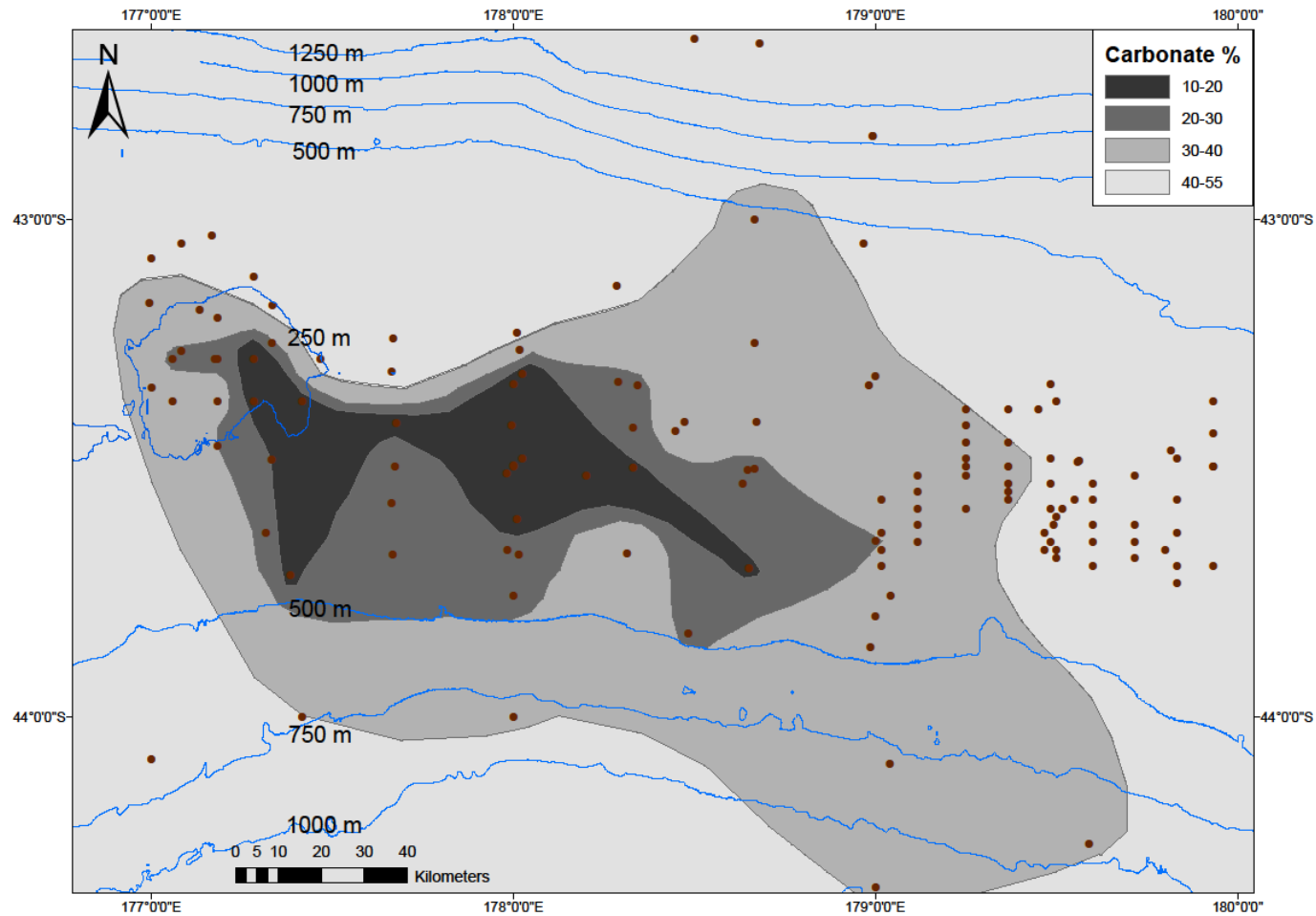


Figure 3.21: Distribution of the CaCO_3 content across the central Chatham Rise, based on both acid digestion and XRD calcite $29.4^\circ 2\theta$ peak counts (see Figures 3.20 and 3.31).

3.2.5 Petrography

The sand-sized fractions separated from bulk samples were used to make detrital thin sections. 15 sand fractions representative of the spread of facies across central Chatham Rise were chosen (see Figure 3.1 for sample locations and Appendix II-H for all photomicrograph results).

Detrital thin sections were made using an aluminium foil bath containing resin and admixed sand, and the heated sample was left to dry for about an hour. The resin plugs were then ground down on a grinding plate to remove the foil and leave a flat surface on the plugs which was further smoothed on a glass plate with 600 grade carborundum powder. The next step was to frost the mounting glass slides and to dry these and the sediment blocks overnight, after which the two could be glued together using resin and left overnight to dry on a cool surface. Using the Struers Discoplan-TS, a thin slice was cut off the sediment block, and then ground down until the mineral grains were at a thickness suitable for petrographic study, typically when quartz showed pale yellow to grey interference colours.

Two petrographic data sheets were designed, one for the sand thin sections and the other for the glauconite thin sections (see Chapter 6). The results of the sand thin section analysis are recorded in Table 3.5, and the key for the petrographic information is contained in Table 3.4.

Table 3.4: Key to notations used for the petrographic data shown in Table 3.5.

Abundance		Sorting		Shape	
R: <1%	Rare	VW	Very well	WR	Well rounded
S: 1-5%	Some	W	Well	R	Rounded
M: 5-15%	Most	M	Moderate	SR	Subrounded
C: 15-25%	Common	P	Poor	SA	Subangular
VC: 25-50%	Very common	VP	Very poor	A	Angular
A: 50-75%	Abundant				
VA: >75%	Very abundant				

Table 3.5: Thin section petrographic data for the bulk sand fraction of samples from central Chatham Rise.

		A898	A899	A900	C606	C961	G34	G36	G113
Calcioclasts	Total skeletal %	40	35	30	45	27	10	15	3
	Bryozoans	M	S	S	S	S	R	S	
	Echinoderms	S	S	R	R	S		R	R
	Benthic forams	C	S	S	M	M	S	M	R
	Planktic forams	VC	C	C	C	M	M	M	S
	Bivalves	S	S	S	M	S	R	R	
	Brachiopods	S	M	R		R			R
	Calcite fragments	C	M	M	C	M	S	S	S
	Chert	R							
	Radiolarians (SiO ₂)	S		S					
	1° size mode mm	0.1	0.1	0.1	0.25	0.25	0.15	0.15	0.1
	2° size mode mm	0.5	0.2	0.35	0.1	0.15	0.05	0.05	0.3
	Shape/abrasion	2	2	3	3	2	2	3	1
	Microborings	M	S	S	S	M	M		
	Sorting	M	M	M	M	M	P	P	M
Glauconite	Glauconite %	50	60	65	50	70	87	75	90
	Size mode mm	0.2	0.25	0.3	0.15	0.2	0.15	0.2	0.2
	Shape	SR-R	SR-R	SA-SR	SA-SR	SR-R	SR-R	SR-SA	SR-SA
	Sorting	W	W	M	M	W	W	M	P
	Glauconite pellets	VC	A	A	VC	A	VA	A	VA
	Glauconite infills	S	R	M	M	S		S	R
	Glauconitised rock fragments	M	R	R	R	S	M	C	S
	Glauconitised carbonate	M	S	S	R	S		R	
	Glauconitised phosphatic grains	S	R			R		M	S
	Size range mm	0.8-2.0	0.5-2	0.5	0.5-1	1.25	0.8-1.5	1-2	1-1.5
Other authigenics	Pyrite %	yes			yes		yes		
	Phosphate %	2	1						2
	Phosphatised frags	S	R						
	Phosphate grains	S	R	R	R				S
Siliciclasts	Total siliciclasts %	8	4	5	5	3	3	5	5
	Quartz	M	S	S	S	R	S	S	S
	Feldspar	R	R				R	R	R
	Opakes	R	S	R	R	R	R	R	R
	Size mode mm	0.1	0.15	0.1	0.05	0.1	0.1	0.05	0.15
	Shape	SA	SA	SA	A	A	A	A	SA
	Rock fragments	M	S	S	S	S	R	S	R
	Size mode mm	0.75	0.35	0.3	0.25	0.2	0.15	0.2	0.4
	Shape	SA	SA	SA	SA	A	SR	SR	SR
	Sorting	P	P	M	P	W	W	M	M

Table 3.5 (continued).

		G135	G136	H959	Q328	U160 2A	U6866 10- 13cm	U6872 10- 15cm
Calciclasts	Total skeletal %	25	55	10	25	45	13	85
	Bryozoans	S	R	R	S	S	R	S
	Echinoderms	S	R		S	M	R	S
	Benthic forams	S	M	S	C	S	S	C
	Planktic forams	M	VC	S	M	C	M	VC
	Bivalves	S	R	R	S	R	R	S
	Brachiopods	R	R					
	Calcite fragments	S	S	S	S	S	S	C
	Chert					R	R	
	Radiolarians (SiO ₂)		R					R
	1° size mode mm	0.3	0.1	0.1	0.1	0.05	0.1	0.05
	2° size mode mm	0.8	0.25	0.2		0.5	0.25	0.15
	Shape/abrasion	1	2	3	3	3	2	2
	Microborings	S	S				S	
	Sorting	P	M	M	M	P	P	W
Glauconite	Glauconite %	70	40	83	60	45	80	5
	Size mode mm	0.25	0.1- 0.2	0.1- 0.25	0.15	0.1- 0.25	0.15	0.1
	Shape	SR-R	SA- SR	SR- SA	SR-R	SA- SR	SR-R	SR-R
	Sorting	M	M	P	M	P	W	M
	Glauconite pellets	A	VC	A	A	VC	VA	S
	Glauconite infills	S	R				R	
	Glauconitised rock fragment	S	R	C	M		S	
	Glauconitised carbonate	S	S	S				
	Glauconitised phosphatic grain	M	S	S		R	S	
	Size range mm	1-2.5	0.5-1	0.5- 1.5	0.2- 0.5	0.7	0.5-1	
Other authigenics	Pyrite %			Yes	Yes	Yes	Yes	
	Phosphate %	1	2	1	3	2	2	1
	Phosphatised frags				S			
	Phosphate grains	R	S	R		S	S	R
Siliciclasts	Total siliciclasts%	4	3	6	7	8	5	9
	Quartz	S	S	S	S	S	S	S
	Feldspar			R	S			
	Opakes				R	S	S	R
	Size mode mm	0.1	0.2	0.15	0.15	0.1	0.15	0.05
	Shape	A	SA	A	SA	A	SA	A
	Rock fragments	S	S	R	M	S	S	S
	Size mode mm	0.5	0.3	0.25	0.35	0.25	0.3	0.4
	Shape	SR	SR	SR	SA	SR	SR	SR
	Sorting	M	P	P	P	P	P	P

The petrographic results show that glauconite is the main component in the sand fraction of the 15 bulk surficial sediments analysed from central Chatham Rise. Overall, on average, glauconite comprises 62%, carbonate material about 31%, siliciclasts 5%, and phosphatic grains 2% (Figure 3.22). Illustrations of the bulk sand fractions are shown in Figure 3.23.

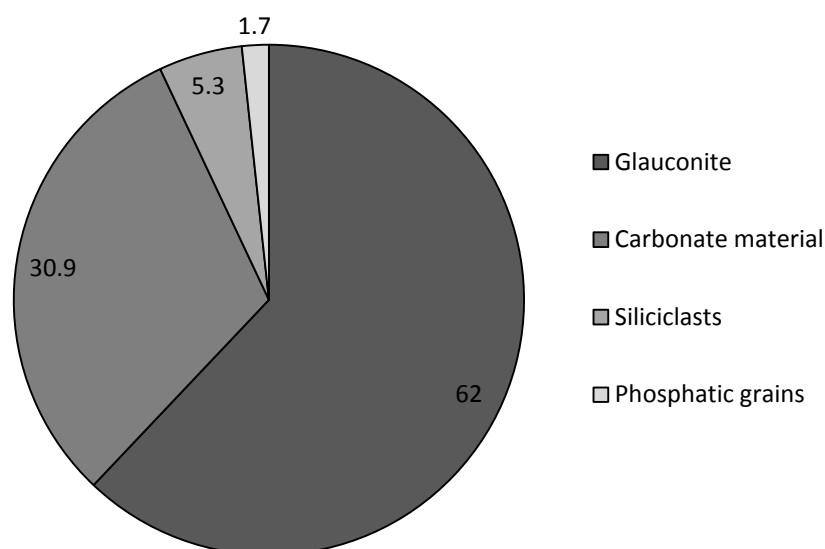


Figure 3.22: Average abundance of glauconite, carbonate material, siliciclasts and phosphatic grains across all 15 detrital sand thin sections (data from Table 3.5).

The glauconite in samples is predominantly (>75%) present as ovoidal and sometimes lobate pellets (Figure 3.23), but also occurs (1-15%) within skeletal grains, typically as foraminiferal chamber infills (Figure 3.23D), as pellets within rock fragments (Figure 3.25F), and as much larger sized (0.5-2.5 mm) glauconitised phosphatic grains (Figure 3.23E and F). The average size of the glauconite pellets is 0.15-0.2 mm, or fine sand (Table 3.5 and Figure 3.23). Glauconite may also occur within or on many other grains. For example, Figure 3.25B shows glauconite occurring in fractures within a quartz grain, while in Figure 3.25C the glauconite is forming within a biotite grain.

The main carbonate material evident in thin section is planktic foraminifera (Figure 3.24E and F), benthic foraminifera (Figure 3.24A and F), and unidentified carbonate fragments. There is also typically some echinoderm fragments/spines (Figure 3.24A, C and D), brachiopod detritus (Figure 3.24B), and occasional bivalve and bryozoan material. Radiolarians, although siliceous, are added into the calciclast category on the petrographic data sheets (Table 3.5), but are rare, as are occasional chert fragments. The average size of carbonate grains is typically in the

0.1-0.3 mm range (fine sand), but they may be as large as 1.25 mm or more (Figure 3.24).

Quartz (Figure 3.25B) makes up most of the siliciclast fraction, but there are also glauconitised rock fragments (Figure 3.25F), micrite rock fragments (Figure 3.21D), opaque grains, feldspar (Figure 3.25A) and biotite (Figure 3.21C). Siliciclasts are mostly angular to subangular and range in size from 0.05-0.15 mm, or very fine to fine sand (Figure 3.25A and B), while rock fragments are usually larger in the range 0.25-0.4 mm, or medium sand, and are mostly subangular to subrounded (Figure 3.25F). The rock fragments can contain glauconite pellets, quartz and planktic foraminifera.

Phosphatic minerals occur rarely in the sand thin sections as very small rounded grains (Figure 3.25E), identified by their virtually isotropic nature under cross-polarised light. However, as mentioned earlier, phosphorite is present sometimes (1-15%) as much larger (0.5-2.5 mm) glauconitised phosphatic grains (Figure 3.23E and F). These glauconitised phosphatic grains may also include glauconite veins/fractures, and some contain small glauconite pellets that appear to resemble the shape of foraminiferal casts (further discussed in Chapter 8).

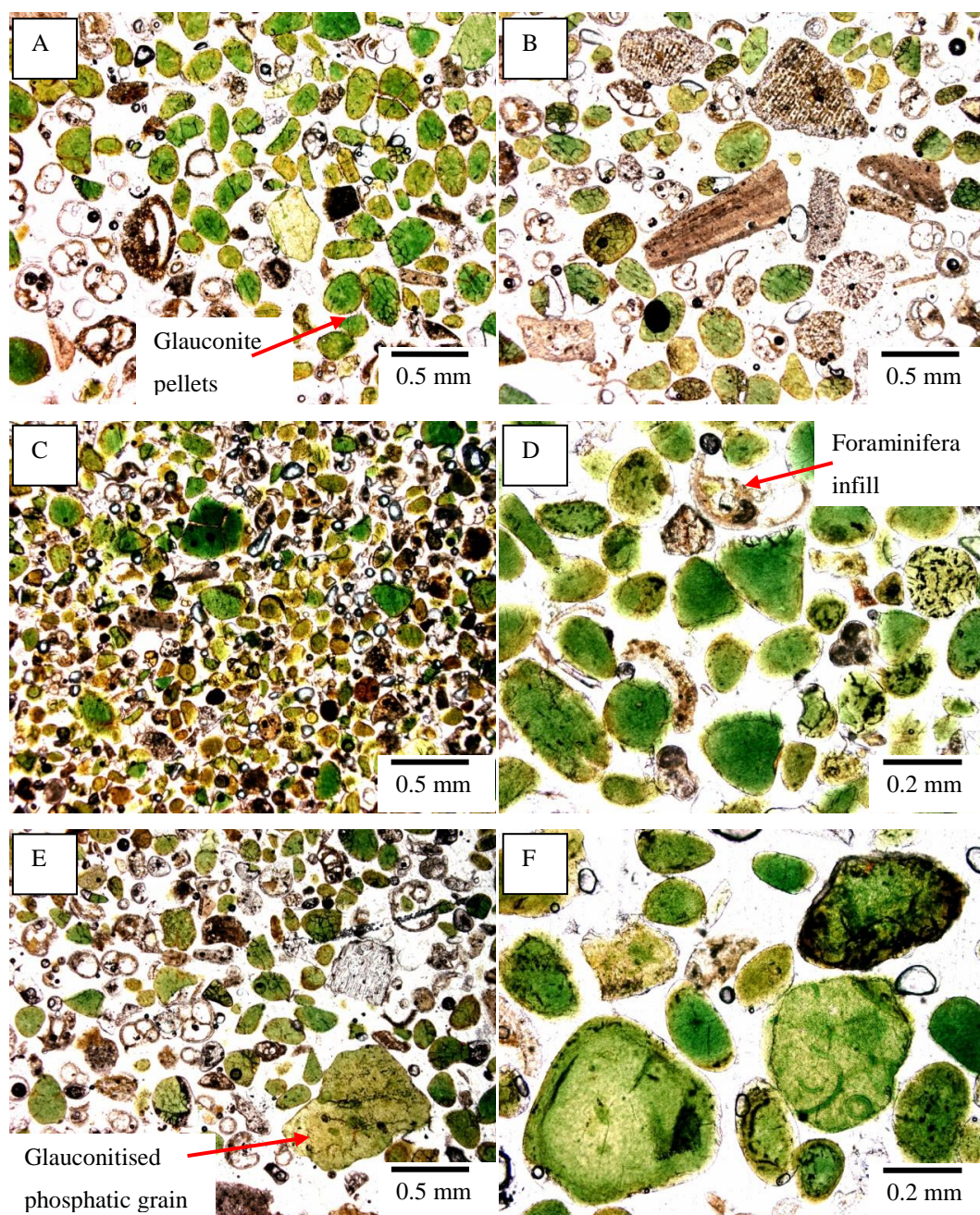


Figure 3.23: Photomicrographs of six different bulk sand thin sections of sediments from central Chatham Rise. A: glauconite pellets from C961, B: glauconite pellets and carbonate grains from G135, C: glauconite pellets from A900, D: glauconite pellets and foraminifera infill from U6866 10-13 cm, E: glauconite pellets, foraminifera infills and glauconitised phosphatic grains from A898, F: glauconite pellets and glauconitised phosphatic grains from U6866 10-13 cm.

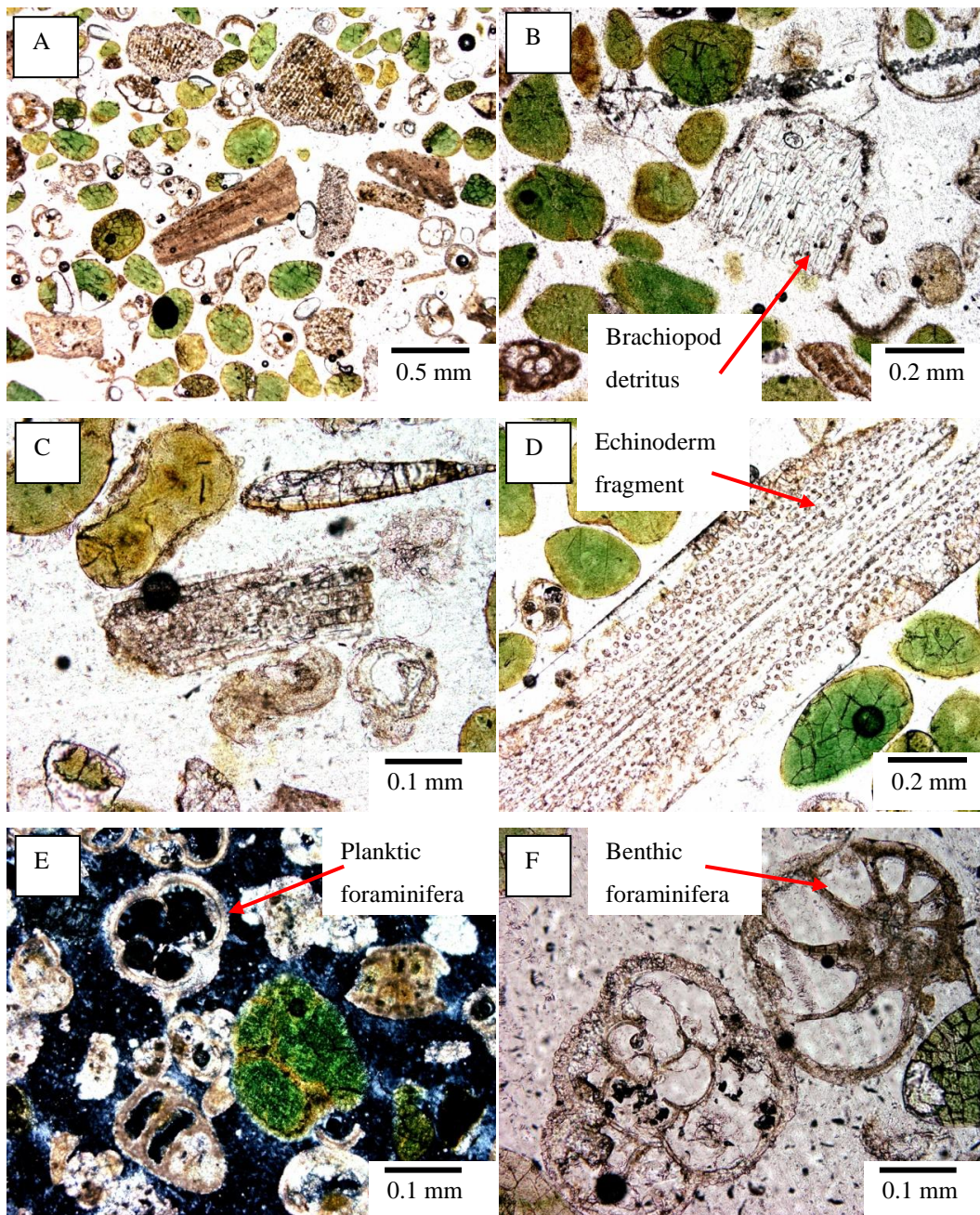


Figure 3.24: Photomicrographs of six different bulk sand thin sections of sediments from central Chatham Rise. A: carbonate and glauconite grains from G135, B: Brachiopod detritus and glauconite pellets from A898, C: echinoderm fragment from G36, D: echinoderm fragment and glauconite pellets from G135, E: planktic foraminifera under cross-polarised light from G136, F: planktic and benthic foraminifera from G135.

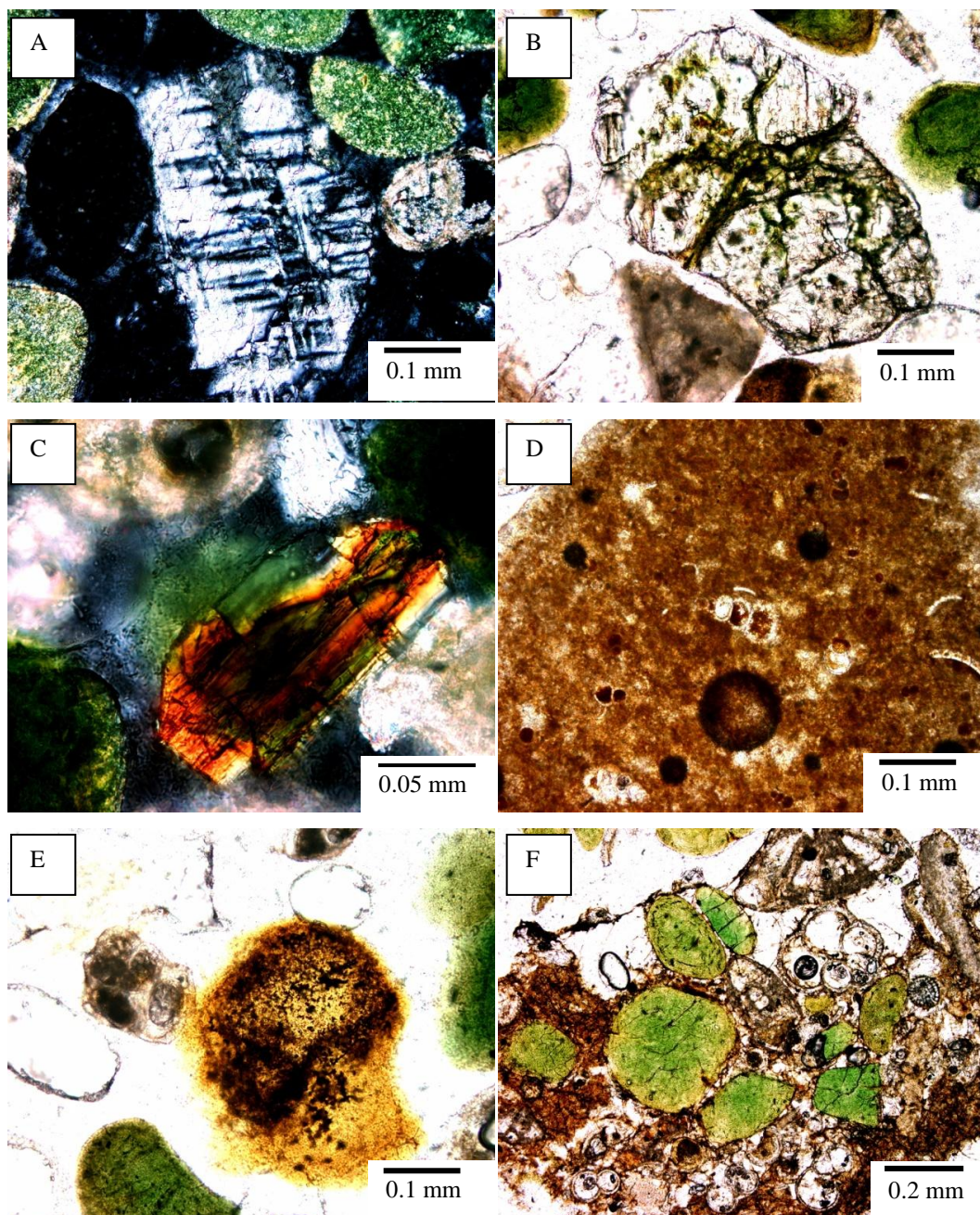


Figure 3.25: Photomicrographs of selected grains in six different bulk sand thin sections of sediments from central Chatham Rise. A: feldspar under cross-polarised light from G34, B: glaucinitised quartz grain from G136, C: biotite grain under cross-polarised light from A899, D: micrite fragment from G135, E: phosphatic grain from U6866 10-13cm, F: glaucinite pellets within a rock fragment from C961.

Figure 3.26 illustrates there is a strong inverse relationship between the abundance of carbonate material and glauconite in the central Chatham Rise sediments: the higher the carbonate content the lower the glauconite content and vice versa. This relationship was also mentioned in Section 3.2.3, in which there was a negative correlation between CaO (indicative of calcite) and both K₂O and Fe₂O₃ (indicative of glauconite). The relationship described here could be due to glauconite forming via infilling of carbonate grains (i.e. foraminiferal test infills), therefore would mean that as the grain becomes infilled with more glauconite, the carbonate fraction would have to consequently decrease (Norris, 1964; Kudrass & Cullen, 1982; von Rad & Rösch, 1984).

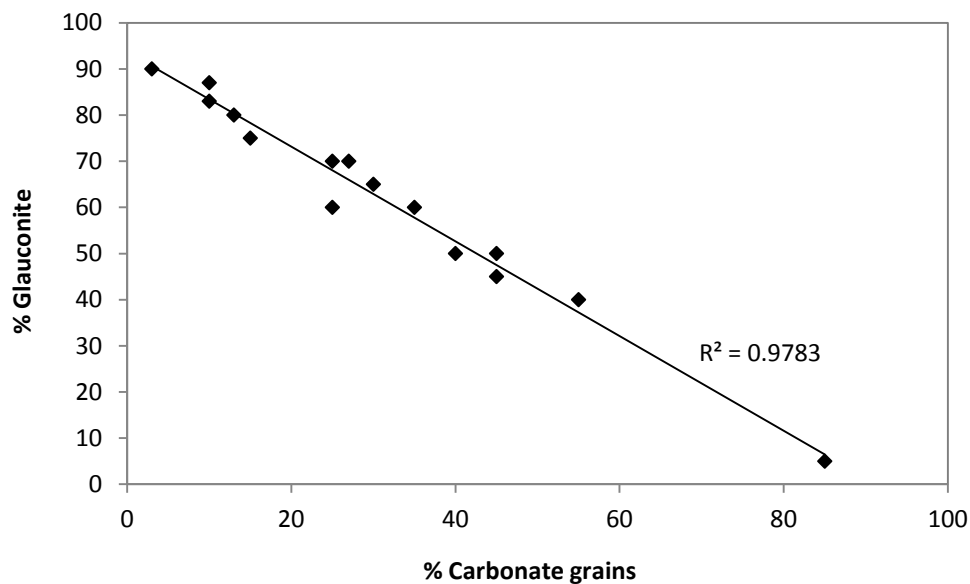


Figure 3.26: Relationship between percent carbonate grains and percent glauconite in 15 detrital thin sections analysed under the petrographic microscope.

3.2.6 SEM

An electron microscope uses a high-energy beam of electrons in a raster scan pattern to take an image of a sample. The SEM at The University of Waikato was used for this analysis. The mud fractions from two bulk samples (A891 and Q328) were analysed for their component particles (see Appendix II-H for all photos). These consist of predominantly foraminiferal and other calcareous and siliceous micro-taxa, as well as rare clay minerals.

Figure 3.27A is a low power SEM view of a typical mud fraction, showing comminuted skeletal carbonate material. Figure 3.27B and D show the planktic foraminifera *Orbulina universa* d'Orbigny, known to range in age from the Middle Miocene to Recent. Other foraminiferal species within the mud fraction include common *Globoconella* (Figure 3.27C), benthic biserial species (Figure 3.27G), benthic fragments (Figure 3.27H), planktic coccoliths (Figure 3.28H), and occasional planktic *Discoaster* (Figure 3.28C) which ranges throughout the Neogene. Other carbonate taxa within the mud fraction include echinoderm debris and spines (Figure 3.28B). Whole or fragmented siliceous diatoms (Figure 3.28G), calcite crystals (Figure 3.28A) and radiolarians and sponge spicules are also reasonably common in the mud fraction of the surficial sediments on central Chatham Rise (R. Hansen, personal communication, September, 2011; Hayward & Gross, 2011).

Only one suspected clay mineral was noted under SEM in the mud fraction, possibly a chlorite particle (Figure 3.27E). However, XRD scans of the mud fraction indicated the presence of both chlorite and illite/glaucinite, so that clay minerals should be present under SEM. Figure 3.28E, although appearing organic, could actually be the inside of a glauconite or smectite-rich grain.

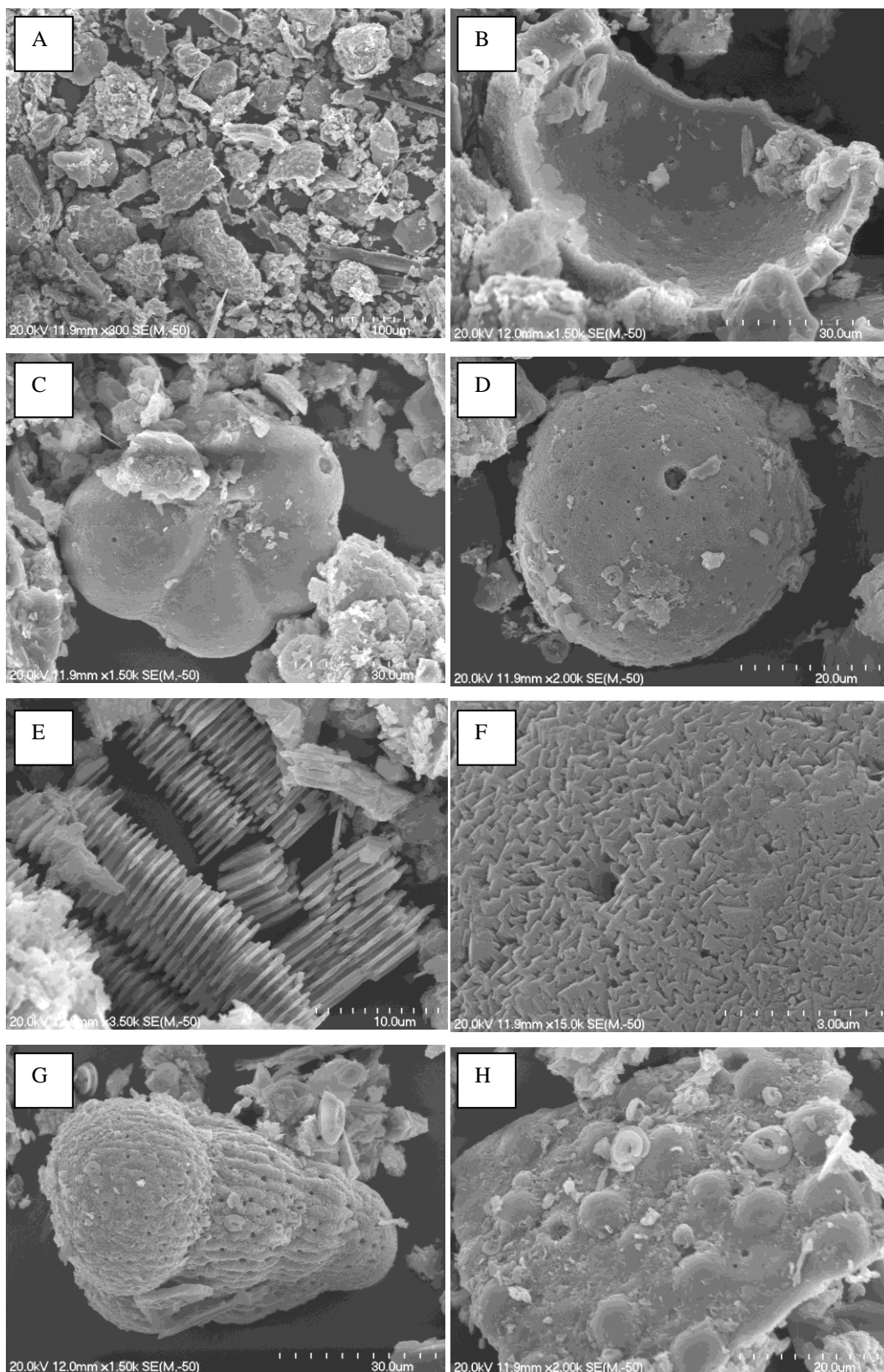


Figure 3.27: SEM images of some grain types in the bulk mud fraction from sample A891. A: comminuted carbonate material, B and D: *Orbulina universa* d'Orbigny, C: *Globoconella*, E: possible chlorite grain, F: benthic foraminifera test close-up, G: benthic biserial species, H: benthic fragments.

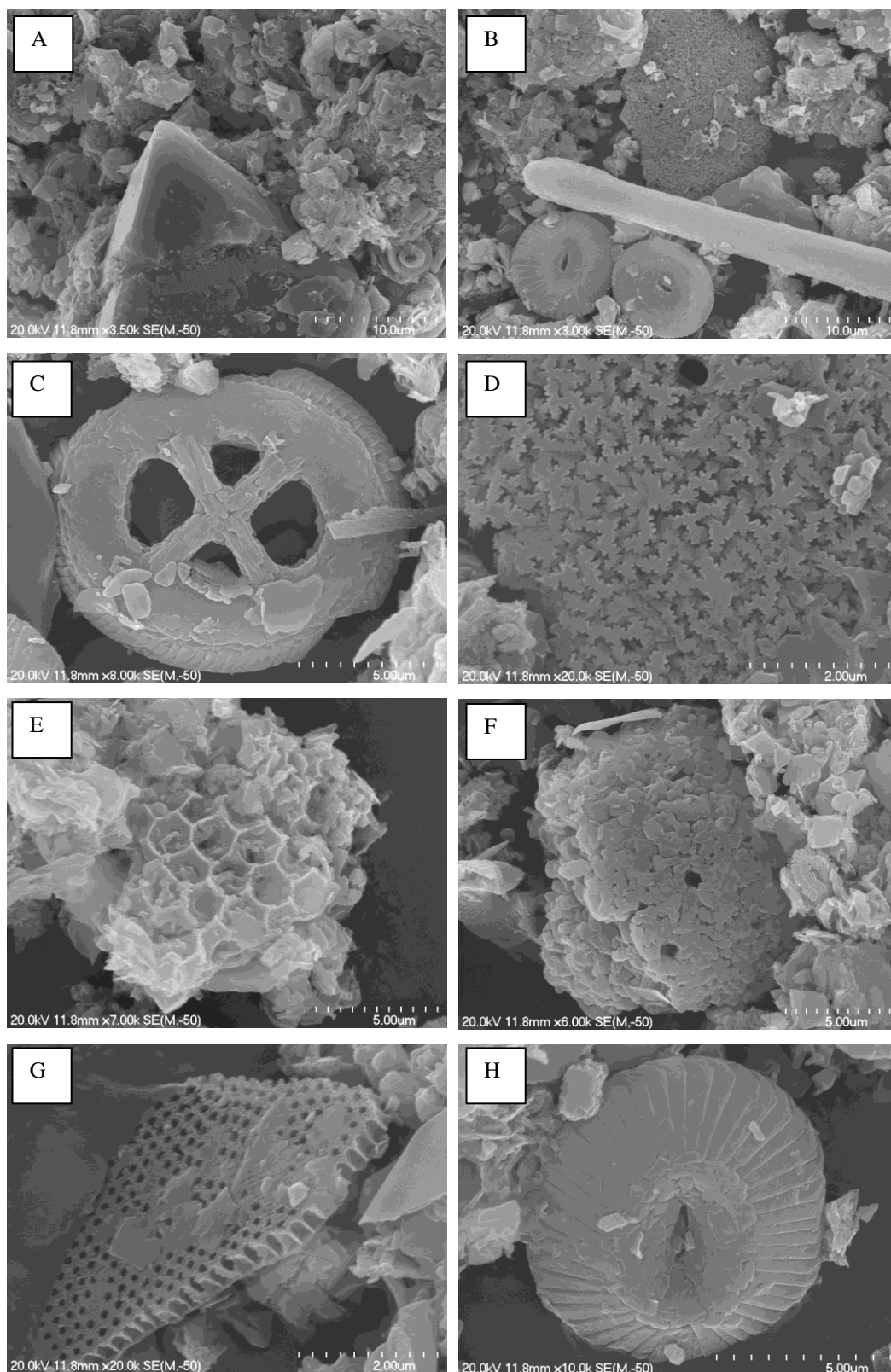


Figure 3.28: SEM images of some grain types in the bulk mud fraction from sample Q328. A: calcite crystal, B: echinoderm debris and spine, C: *Discoaster*, D: unknown, E: glauconite or smectite, F: unknown, G: siliceous diatoms, H: coccolith.

3.2.7 Surficial sediment facies map

Surficial sediment analysis can lead to production of a sediment facies map for the study area. One previous and mainly rather generalised map for the entire Chatham Rise was created by McDougall (1982). The portion of this map which represents the central Chatham Rise has been scaled down to the map coverage of the present study (Figure 3.29: legend and Figure 3.30: map). It shows the general sediment types, but does not however recognise the relative contents of glauconite, carbonate and phosphorite in samples.

Using the surficial sediment results presented here in Section 3.2 (i.e. textural analysis, CaCO_3 content and petrography), as well as the percent glauconite results (see Chapter 6), has enabled the construction of an updated and more precise version of a surficial sediment facies map for the central Chatham Rise (Figure 3.31). It also summarises the relative percentage of glauconite and carbonate, as well as the predominant sediment textural classes. It also recognises, in contrast to what was proposed in the McDougall (1982) map, that much of the glauconite and phosphorite on the Rise is probably not strictly authigenic, but rather detrital (see Section 9.3).

DOMINANT PARTICLE COMPOSITION	SIZE OF PARTICLES (mm)	TERRIGENOUS		VOLCANIC		RED CLAY		AUTHIGENIC		BENTHIC CARBONATE		PLANKTONIC CARBONATE		SILICEOUS	
		Dominant fraction	Subsidiary fraction >20%	Dominant fraction	Subsidiary fraction >20%	Dominant fraction	Subsidiary fraction >20%	Dominant fraction	Subsidiary fraction >20%	Dominant fraction	Subsidiary fraction >20%	Dominant fraction	Subsidiary fraction >20%	Dominant fraction	Subsidiary fraction >20%
Boulders	>256	†	†	†	†	†	†	†	†	†	†	†	†	†	†
Cobbles and pebbles	4–256			†		†	†	†				†	†	†	†
Granules and coarse sand	0.5–4			†	†	†	†	†	†			†		†	†
Medium and fine sand	0.063–0.5			†	†	†	†							†	†
Mud	<0.063			†	†	†	†	†	†	†	†			†	†

† These do not appear on this chart

Figure 3.29: McDougall's (1982) legend for Bounty Sediments map of Chatham Rise (see Figure 3.30).

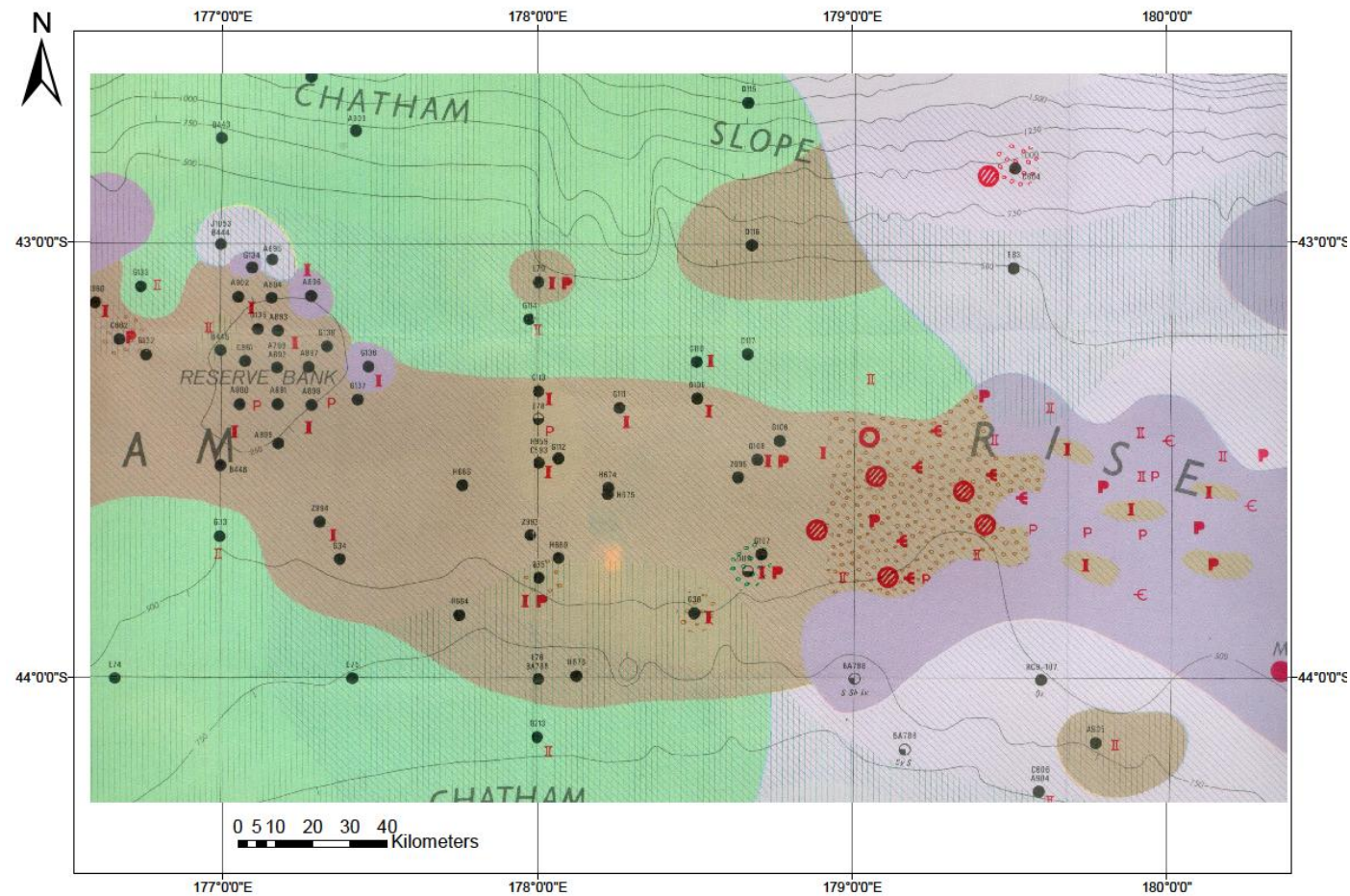


Figure 3.30: Surficial sediment map for central Chatham Rise extracted from the Bounty Sediment map of McDougall (1982). Key in Figure 3.29.

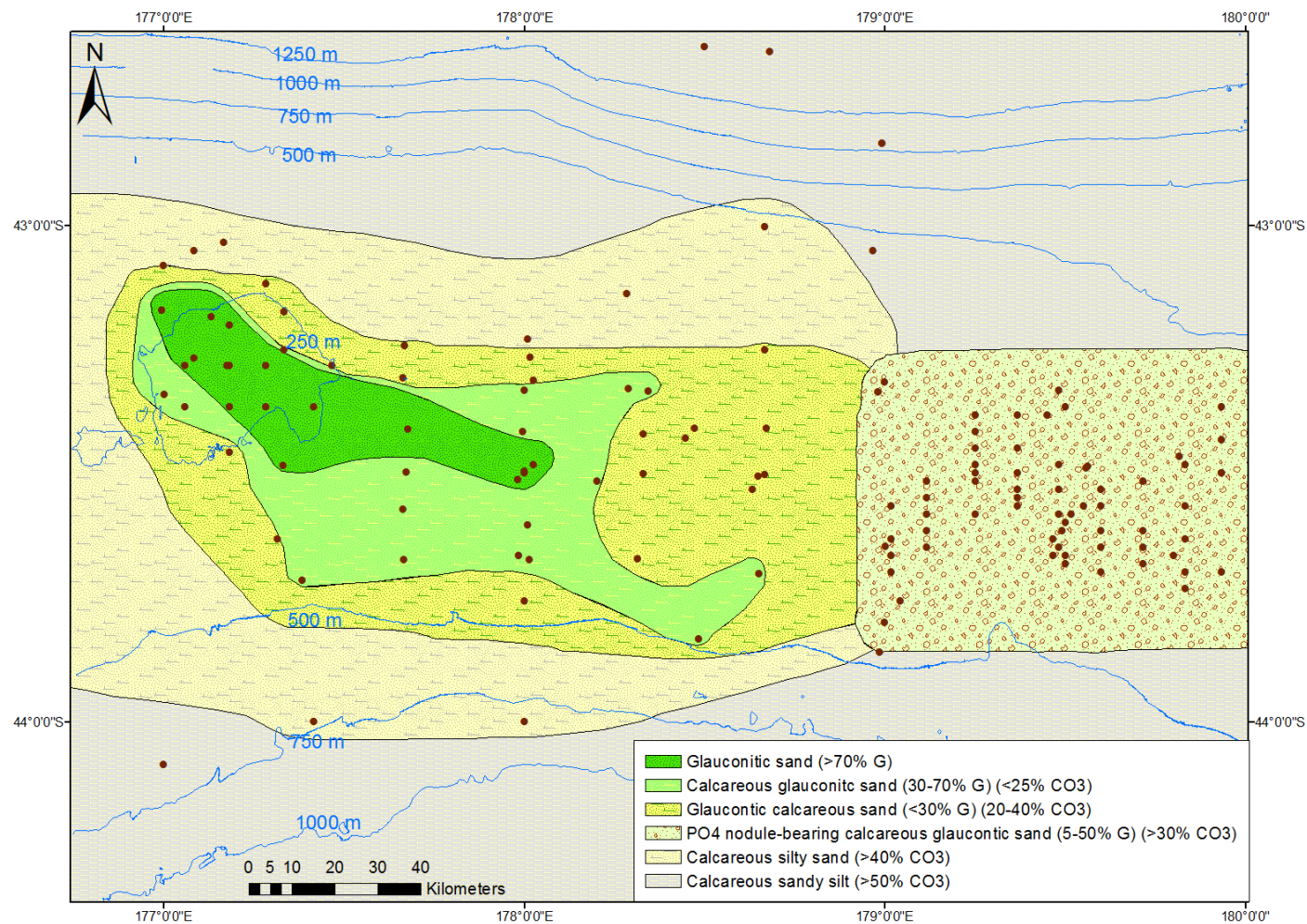


Figure 3.31: Surficial sediment facies map for central Chatham Rise developed in this study. G=glauconite, CO3 = carbonate, PO4=phosphate.

3.3 SHORT CORE STRATIGRAPHY

Unfortunately there is relatively little information available on core stratigraphy on central Chatham Rise and only one glauconite-rich core from the two acquired, was available for direct analysis in this study. However, an examination of some old cores housed at NIWA Wellington shows that the bulk glauconite-carbonate rich surficial deposits on central Chatham Rise overlie Oligocene age chalk.

The thickness of the surficial sediment deposits in 26 cores varies from about 6-135 cm (Figure 3.32) with an overall average of about 60 cm. Figure 3.33 shows the locations of the cores which were analysed for the surficial sediment depth. Between 177 and 178° 30E longitude the thickness averages 40-60 cm, while from 179 to 180°E longitude Kudrass and Cullen (1982) suggested the surficial sediment thickness averages only 17 cm. The one glauconite-rich core sample (U6866) that I obtained on the *Tangaroa* cruise (TAN1103 Leg 2) was analysed at 2 cm increments down to 13 cm and demonstrated that the bulk sediments mainly have the same mineralogy, geochemistry and physical properties down core, until the Oligocene chalk begins. More information on the stratigraphy/bedrock geology is described in Section 2.3.

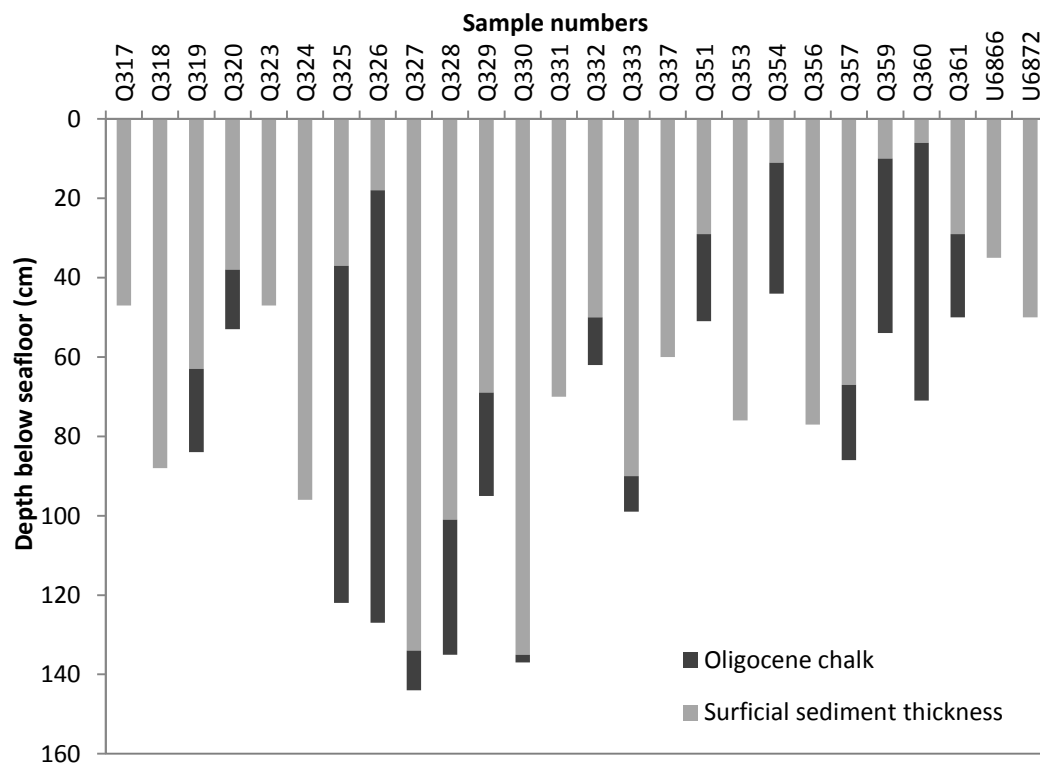


Figure 3.32: Thickness of the surficial sediment deposits in 26 cores from central Chatham Rise. The topmost part of the underlying Oligocene chalk is also shown for most cores.

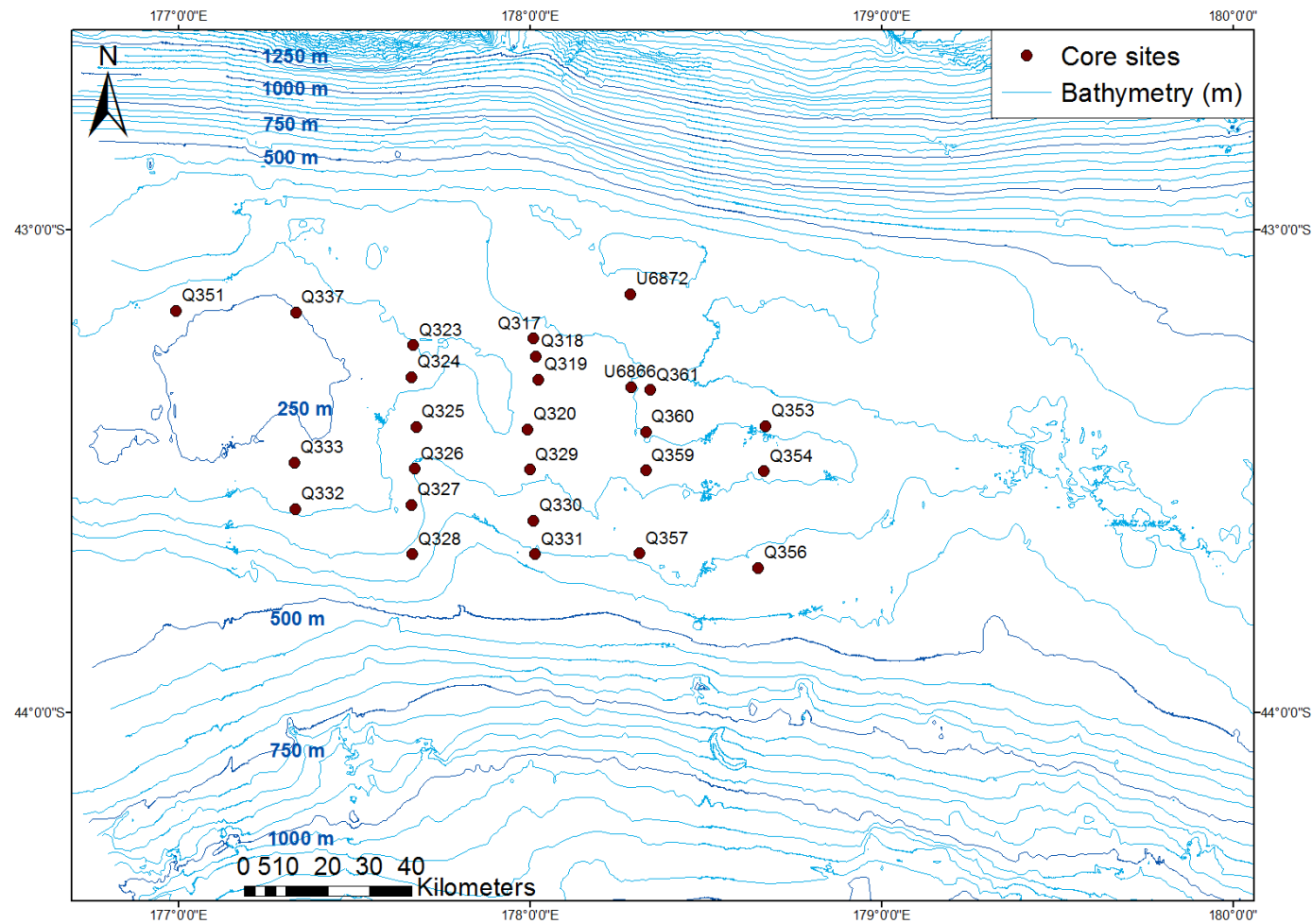


Figure 3.33: Location of the surficial sediment deposits in 26 cores from central Chatham Rise.

3.4 OLIGOCENE CHALK

Beneath the unconsolidated surficial bulk sediment cover is a relatively consolidated Oligocene chalk deposit (Kudrass & Cullen, 1982; Falconer *et al.*, 1984; Wood *et al.*, 1989) in which a subset of chalk samples was analysed using XRD, % CaCO₃ acid digestion and SEM.

The mineralogy of five chalk samples was investigated using XRD (Figures 3.34 and 3.35; all scans in Appendix II-E). The scans show the Oligocene chalk is overwhelmingly dominated by low-Mg calcite. Acid digestion confirms the carbonate-rich (>75% CaCO₃) nature of most samples (Table 3.6), the lower values probably reflecting some admixture with the bulk surficial sediment materials (see Appendix II-G for acid digestion results). Otherwise clay minerals, not readily detected in unoriented bulk sediment mounts, may account for much of the non-calcite material, and perhaps some amorphous silica.

Table 3.6: Acid digestion % CaCO₃ results for five Oligocene chalk samples.

Sample name	CaCO ₃ %
G228	84.6
Q317	95.9
Q318	82.0
Q359	48.8
Q360	76.5

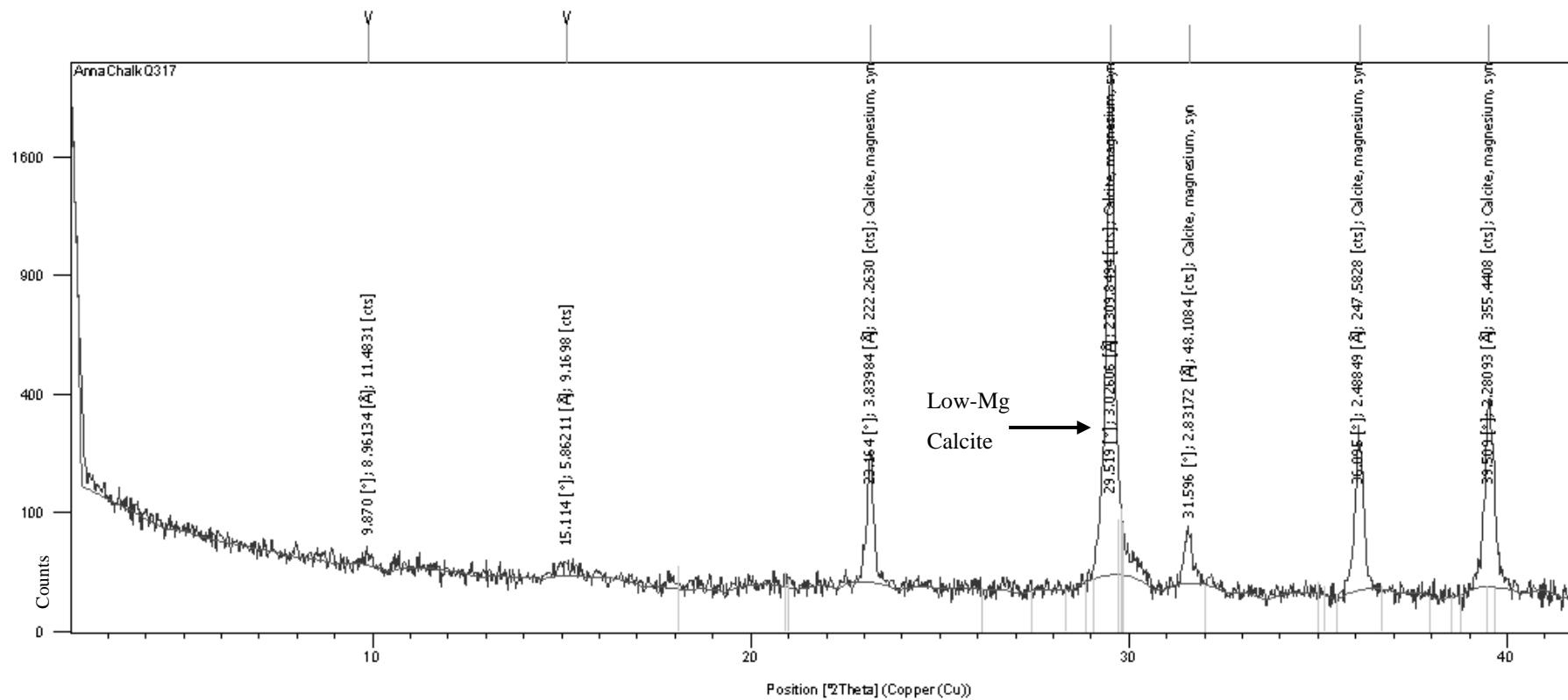


Figure 3.34: XRD scan result for Oligocene chalk sample at Q317.

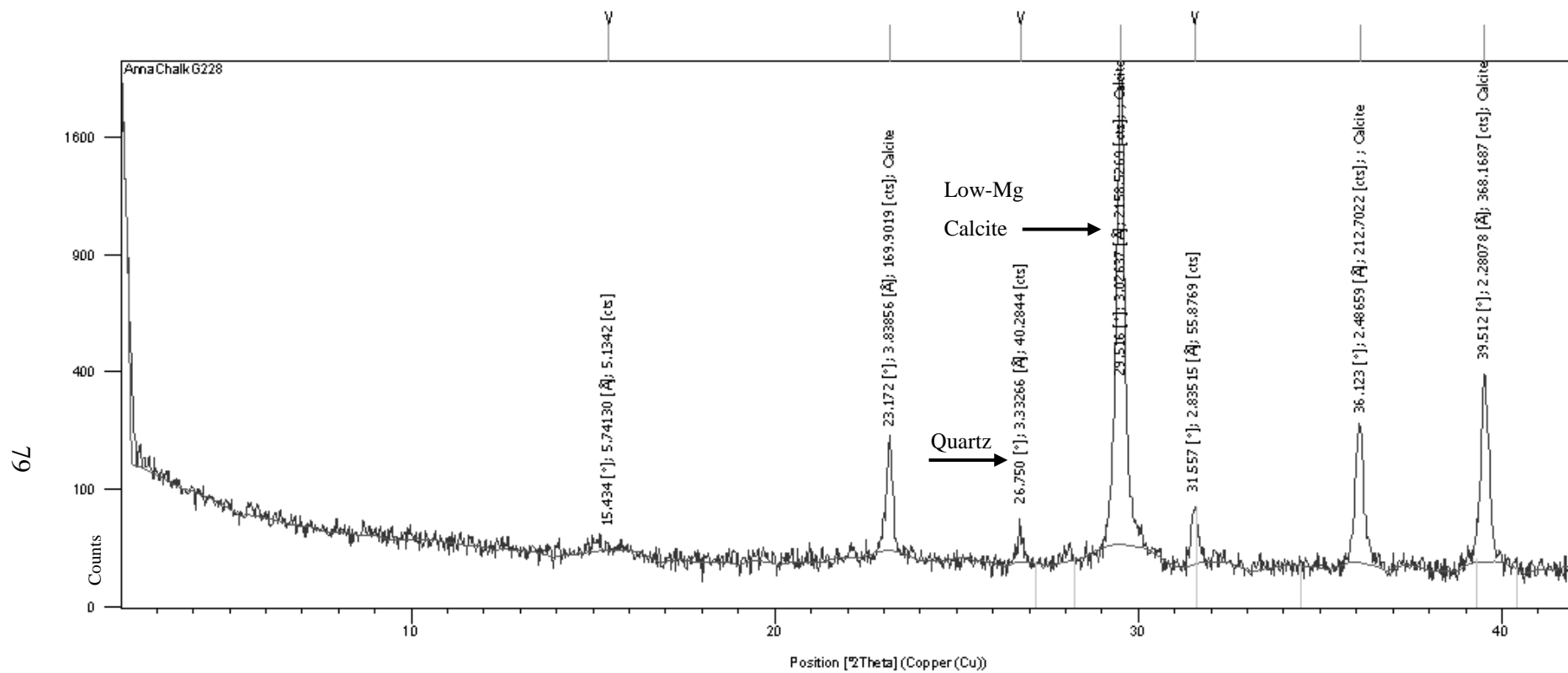


Figure 3.35: XRD scan result for Oligocene chalk sample at G228.

A sample (Q317) of the Oligocene chalk was also viewed under the SEM to reveal the contents of the chalk. A fraction of this sample was scraped onto a small circular disc covered in double sided tape, then coated with platinum in order to make the sample conductive. SEM results show that the Oligocene chalk is predominantly made up of coccolith plates and fragments (>99%), as illustrated in Figures 3.36 and 3.37 (see Appendix II-H for all photos). An SEM image of the decalcified sample (Q317) shows a variety of unidentified siliceous silt and clay sized debris (Figure 3.38).

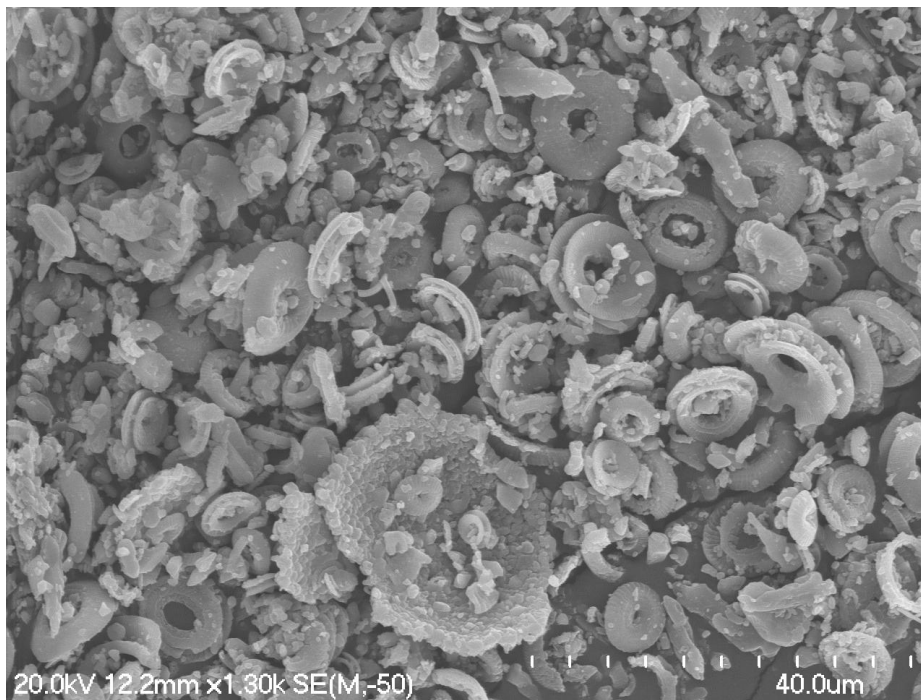


Figure 3.36: SEM image of Oligocene chalk sample Q317 illustrating abundant coccolithophores and a broken foraminiferal shell.



Figure 3.37: SEM image of Oligocene chalk sample Q317, illustrating a coccolithophore and adhering micritic carbonate.

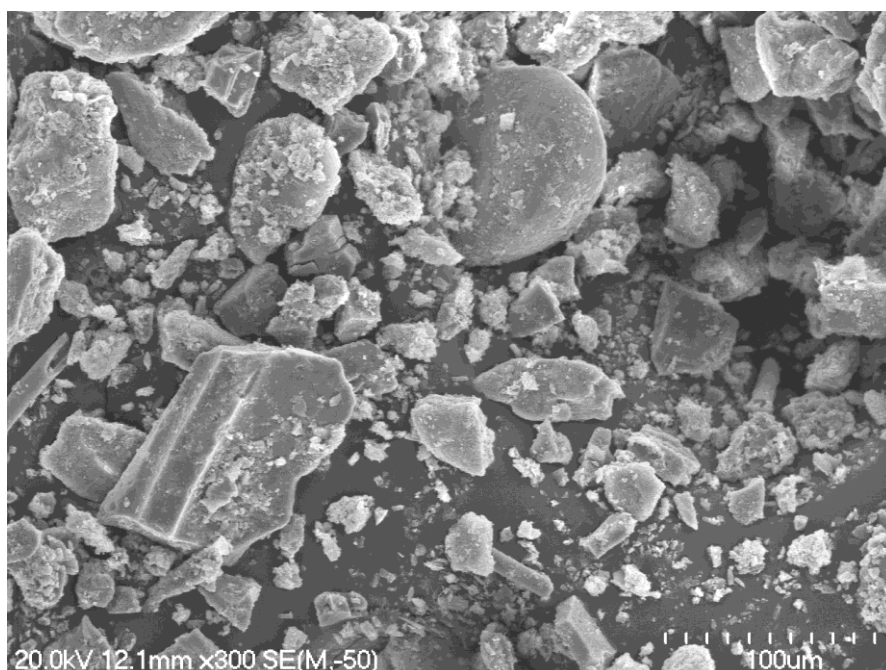


Figure 3.38: SEM image of sample Q317 Oligocene chalk following acid digestion and removal of carbonate material.

Figure 3.38 indicates that the decalcified Oligocene chalk sample contains mostly siliceous material, in which some large organic fragments can be seen, as well as small silt and clay material.

Chapter 4

ECHO-CHARACTER OF BOTTOM SEDIMENTS

4.1 INTRODUCTION

Echograms recorded using high frequency signals (3.5-12 kHz) on board ships can be a very useful tool to examine the seafloor morphology, sediment thickness and sub-bottom stratigraphy (Damuth, 1980). The sound waves penetrate the seafloor sediments and the echograms obtained on different cruises can be combined to construct an echo-character map of a study area.

The aim of this chapter is to produce an echo-character map of central Chatham Rise between 177° and 180° E longitudes in water depths down to 1250 m, and also to produce maps illustrating the seafloor morphology and sediment thickness for this region. The echo-character map should enlighten the shallow sub-bottom stratigraphy beneath the glauconitic and phosphatic deposits over the crest of central Chatham Rise, and provide some inferences about their internal textural make up and the associated seafloor morphology. The echo-character map could potentially enable the distribution of glauconite-rich deposits to be defined.

4.2 METHODS

To create an echo-character map the methodology and classification scheme established by Damuth (1978, 1980) have been followed. Damuth's (1978, 1980) scheme was actually based on work done by Hollister (1967) who constructed an echo-character map for the continental rise off Nova Scotia, Canada, from sound waves which revealed different types of echoes. For the present study only 3.5 kHz data were used because the acoustic energy penetrates quite deep below the seafloor, to about 20 to >110 m (Damuth, 1980).

The first step in creating an echo-character map for central Chatham Rise was to produce a base map that contains the tracks of all the 3.5 kHz echogram profiles available from past cruises within the study area (Figure 4.1). This was created

using GIS for me by Kevin Mackay, a GIS technician at NIWA, Wellington, and includes the following cruise numbers: 2023, 2053, 3013, 3029, and TAN0705. The base map (Figure 4.1) also shows the bathymetry and the positions of all the sediment, rock and core samples that have been collected within the study area.

The next step was to devise a classification scheme for the different types of bottom echoes observed, which was based on the classification terminology established by Damuth (1978) and Damuth (1980) (Table 4.1). From examination of all the available 3.5 kHz echograms I entered onto the base map along the various cruise tracks the types of bottom and sub-bottom echoes, their thickness/sediment depth (in terms of μ s), parallel echoes, the contrast (opaque versus transparent) and strength of signals, the seafloor morphology (irregular versus flat-lying), and any other features of interest (e.g. inclined reflectors, synclinal structures, landslides, etc.).

The last step was to map the distribution of the various echo-types on the base map, as well as the associated sediment thicknesses (i.e. the surficial sediments and semi-consolidated Oligocene chalk described in Chapter 4) and underlying seafloor morphologies. The final echo-character map was produced as a GIS map (see Figure 4.6). In addition, two other maps were prepared, one illustrating the nature of the seafloor morphology (see Figure 4.9) and another showing sediment thicknesses (see Figure 4.10).

Table 4.1: Definition of the echo-types which were used as a starting point for echo-types seen in the present study; as defined by Damuth (1978) and Damuth (1980).

Echo-type	Definition
IIA	“Indistinct, semi-prolonged bottom echoes with intermittent indistinct, discontinuous sub-bottoms”. Contain moderate amounts of silt/sand beds.
IIB	“Very prolonged echoes with no sub-bottoms”. Contains high amounts of bedded silts/sands and the thickest deposits.
IB	“Distinct, continuous sharp bottom echoes with several sharp, parallel sub-bottoms”. Contains little amounts of sand/silt beds.
IIIA	“Large, irregular, overlapping or single hyperbolae with widely spaced varying vertex elevations above the sea floor”.

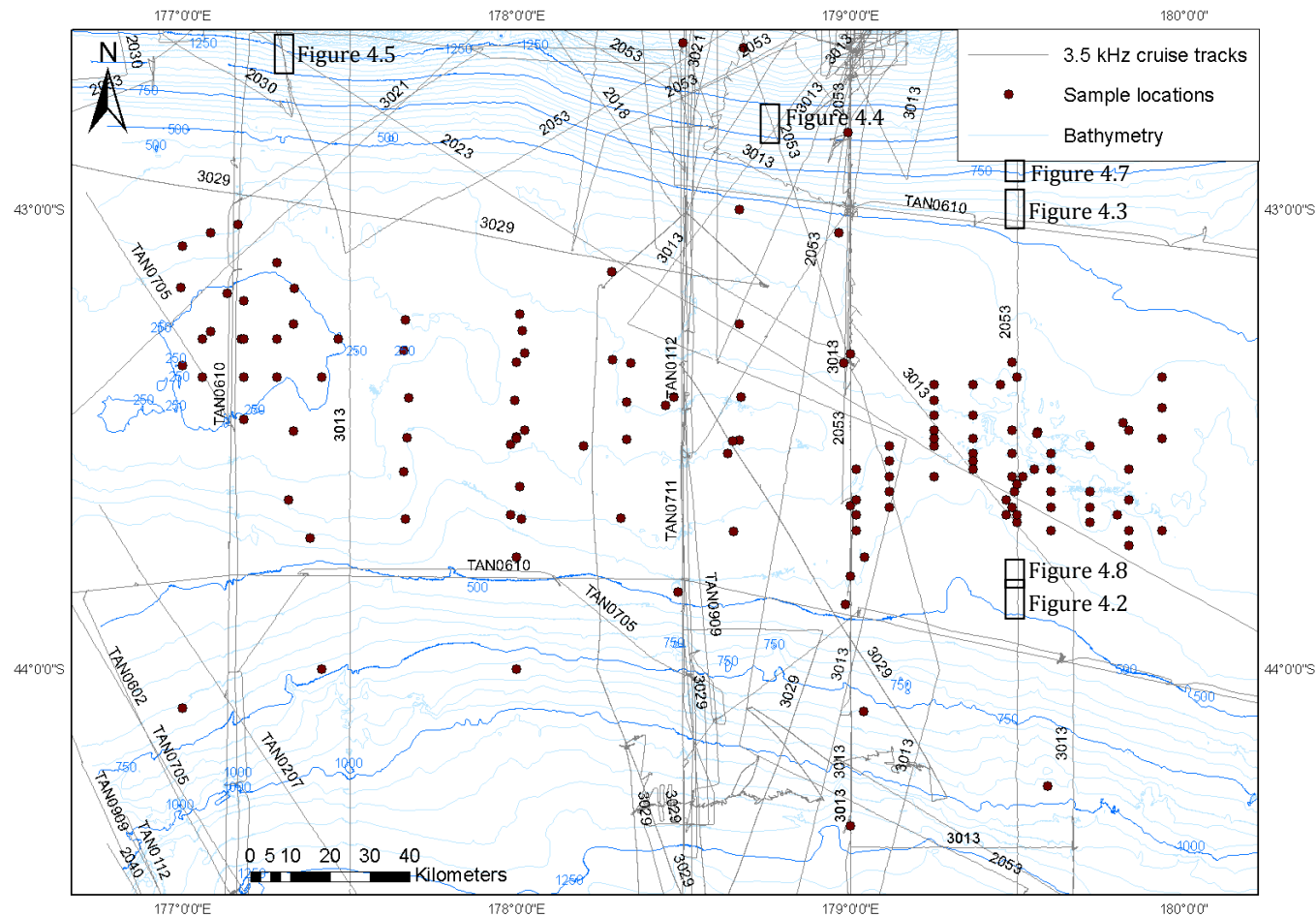


Figure 4.1: Location of 3.5 kHz echogram profiles used in this study to compile echo-character, sediment thickness and seafloor morphology maps. The small rectangular boxes on some of the tracks show the location of Figure examples provided in this chapter.

4.3 CLASSIFICATION TERMINOLOGY

The adopted echo-type classification scheme for central Chatham Rise is based on the classification terminology proposed by Damuth (1978, 1980). Damuth (1978, 1980) described various types of echo-sounds that are seen in high-frequency (i.e. 3.5-12 kHz) echograms. Four main echo-types are defined for the central Chatham Rise (Table 4.2) - types A, B and D are indistinct echoes, while type C is a distinct echo. Indistinct echoes can be further divided into prolonged echoes, which occur in types A and B, and hyperbolic echoes, which occur in type D. The four established echo-types are described below.

Table 4.2: General features of the four echo-types (A to D) observed on 3.5 kHz profiles for central Chatham Rise, defined on a basis of Damuths' (1978, 1980) echo-types defined in Table 4.1 (as contained within the brackets under echo-types).

Echo-types	Definition/features
A (IIA)	Indistinct prolonged echoes, with discontinuous sub-bottom signals
B (IIB)	Indistinct prolonged echoes, with no sub-bottom signals
C (IB)	Distinct echoes, with continuous sharp parallel sub-bottom signals
D (IIIA)	Indistinct hyperbolic echoes

4.3.1 Echo-type A

Echo-type A is similar to the IIA echo-types defined by Damuth (1978, 1980) and it is more or less intermediate between the B and C echo-types in Table 4.2 (described below). They have semi-prolonged indistinct bottom echoes that may be opaque or transparent, and sub-bottom signals are present but are discontinuous, irregular and semi-transparent to transparent (Figure 4.2).

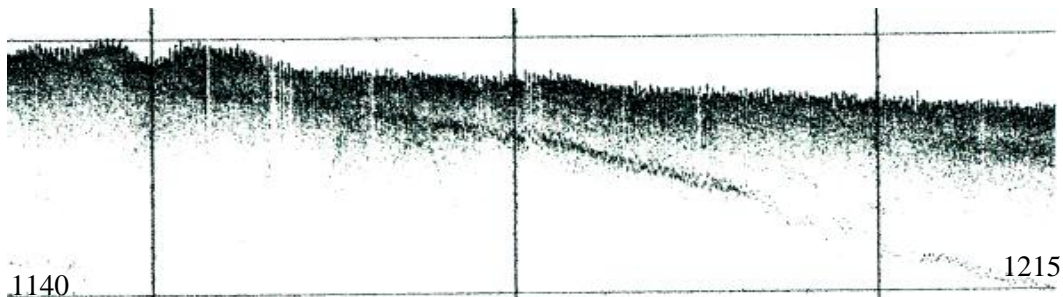


Figure 4.2: Example of an echo-type A from cruise track 2053 on central Chatham Rise on April 6th 1992 from 1140-1215 (see Figure 4.1 for location).

4.3.2 Echo-type B

Echo-type B is based on the IIB echo described by Damuth (1978, 1980). B echoes have a very prolonged opaque bottom echo, show no sub-bottom signals and typically a thick semi-transparent to transparent layer beneath the bottom echo (Figure 4.3). According to Damuth (1980), the average thickness of the deposits increases significantly compared to A and C echo types, which may be true in the present study.

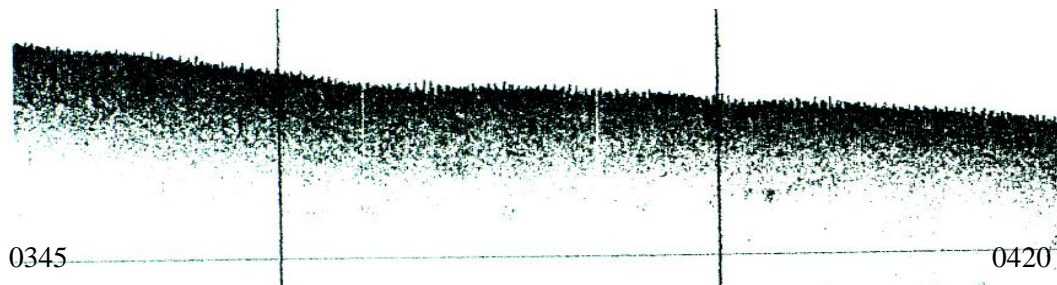


Figure 4.3: Example of an echo-type B from cruise track 2053 on central Chatham Rise on April 6th 1992 from 0345-0420 (see Figure 4.1 for location).

4.3.3 Echo-type C

Echo-type C is based on the IB echo-type of Damuth (1978, 1980). C echoes are distinct echoes that produce a prolonged continuous sharp bottom echo that is opaque, with several continuous relatively opaque and sharp parallel sub-bottom reflectors that typically continue over long distances of many km (Figure 4.4).

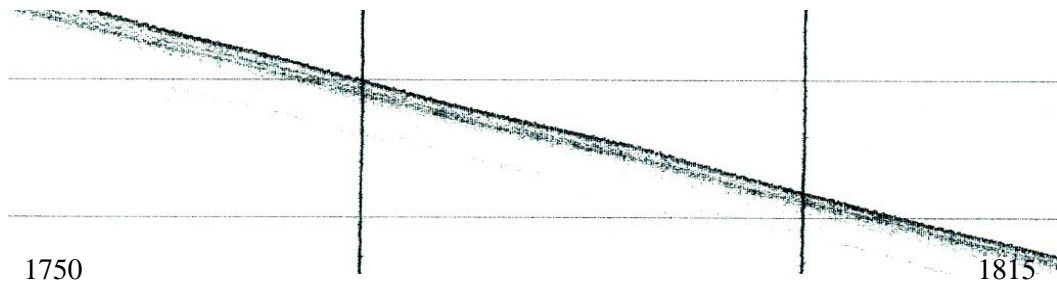


Figure 4.4: Example of an echo-type C from cruise track 2053 on central Chatham Rise on April 6th 1992 from 1750-1815 (see Figure 4.1 for location).

4.3.4 Echo-type D

Echo-type D is based on the IIIA echo in Damuth's (1978) classification scheme. D echoes are hyperbolic and have large irregular hyperbolae that may be singular or overlapping, with various heights and shapes of vertex elevations above the seafloor. They show few or no sub-bottom reflectors (Figure 4.5).

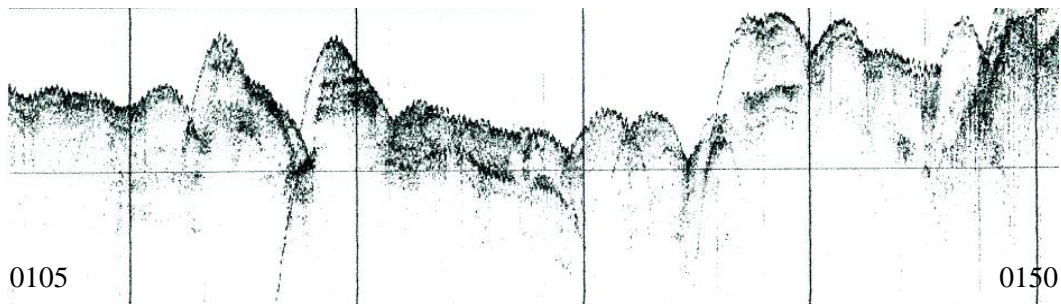


Figure 4.5: Example of an echo-type D from cruise track 2053 on central Chatham Rise on April 12th 1992 from 0105-0150 (see Figure 4.1 for location).

4.4 ECHO-CHARACTER MAPS

4.4.1 Echo-character

The echo-character map for the central Chatham Rise shows relatively little variation, with A type echoes completely dominating (Figure 4.6). These A echoes are especially widespread in waters shallower than c.500 m, whereas B, C and D echoes are more common in waters deeper than 500 m. Damuth (1980) suggested for his IIA echoes, equivalent to A echoes in the present study, that they are associated with moderate amounts of bedded silts and sands. However, analysis of cores in the Chatham study (Section 3.3) reveals no clear bedding present within the surficial sediment deposit, and it is unlikely that the underlying Oligocene chalk deposit would be well bedded.

Overall, the echo-character map for the central Chatham Rise provides little new information about the nature of the bottom sediments, other than a relative monotony of echo-type A character.

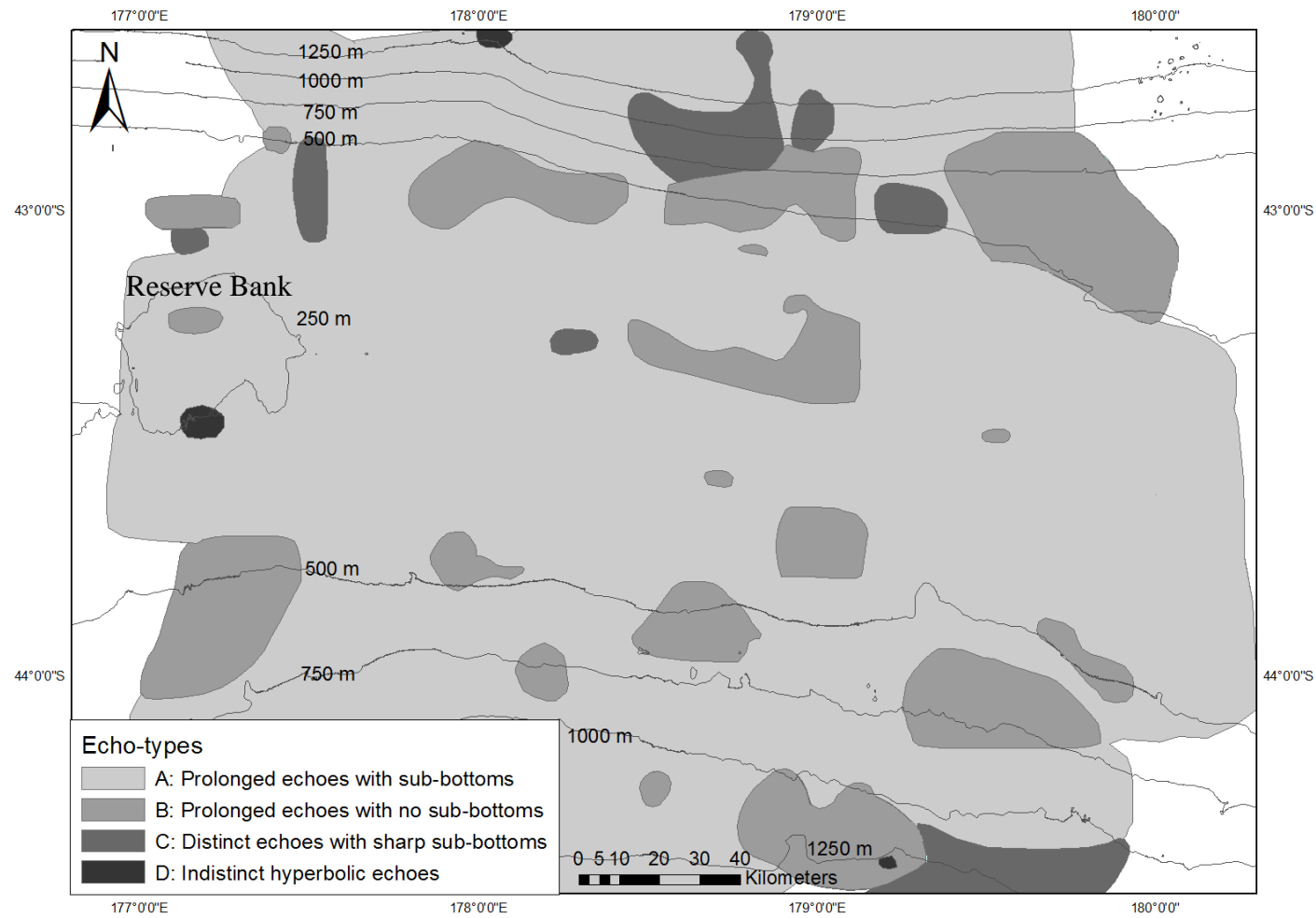


Figure 4.6: Echo-character map of central Chatham Rise (Table 4.1).

4.4.2 Seafloor morphology

The seafloor morphology corresponds to the shape of the sediment-water interface at the seafloor. The seafloor morphology reveals some interesting features in relation to the surficial sediment types present on the seafloor. Figures 4.7 and 4.8 display examples of flat-lying and irregular seafloor morphologies on central Chatham Rise, respectively. The seafloor morphology map in Figure 4.9 shows that the seafloor is mainly flat-lying (Figure 4.7) at water depths from 400 – 1100 m, and is rather more irregular (Figure 4.8) at shallower depths (<400 m). Figure 4.9 also shows that the area where many samples have been previously collected to investigate the prospectivity of mining phosphorite nodules, namely between 179°E and 180° 0' E longitude and 43° 0' S and 43° 50' S latitude, the seafloor is much more irregular due to the high content of gravel-sized phosphorite nodules. In the area to the west of here, from 177°E to 178° 30' E longitude and 43° 0' S to 43° 50' S latitude, the seafloor morphology is rather less irregular and relatively flat-lying, suggestive of few phosphorite nodules and a significantly increase content of sandy materials, likely to be predominately glauconite.

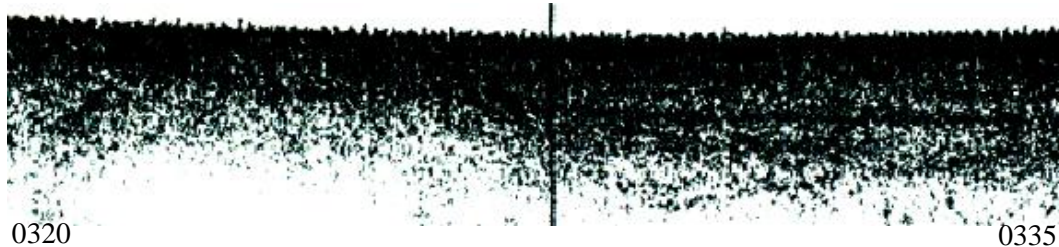


Figure 4.7: Example of flat-lying seafloor morphology from cruise track 2053 on central Chatham Rise on 6th April 1992 from 0320-0335 (see Figure 4.1 for location).



Figure 4.8: Example of irregular seafloor morphology from cruise track 2053 on central Chatham Rise on 6th April 1992 from 1125-1145 (see Figure 4.1 for location).

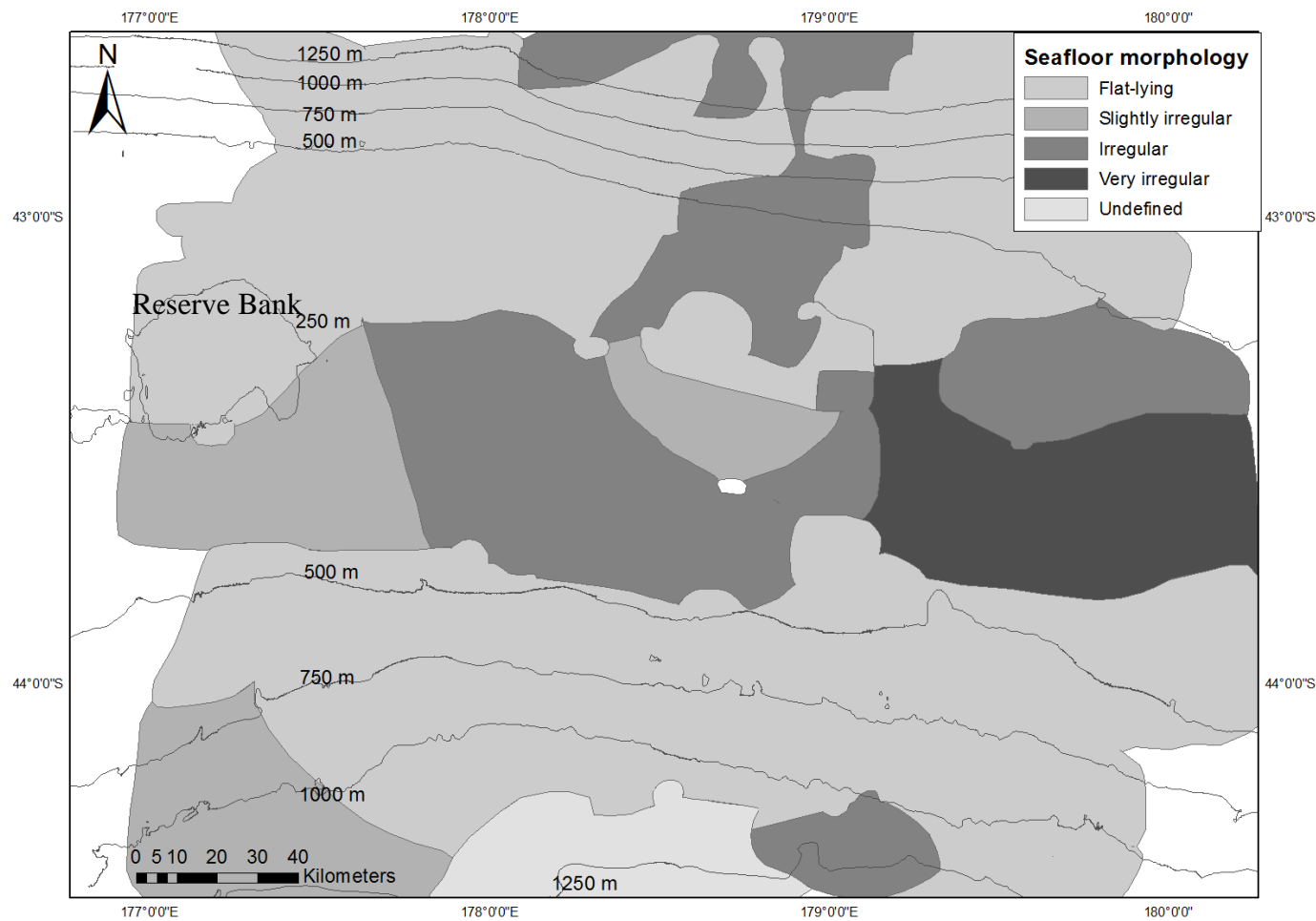


Figure 4.9: Seafloor morphology of central Chatham Rise (see Figures 4.7 and 4.8 for morphology examples).

4.4.3 Sediment thickness

Given that in cores the surficial unconsolidated sediment deposit involving foraminiferal and glauconitic sands and phosphorite nodules showed thicknesses ranging from 6 to 135 cm (Section 3.3), it is clear that the sediment thickness analysed here from 3.5 kHz seismic data (Figure 4.10) must include also the underlying weakly indurated Oligocene chalk (Section 3.4). This would encompass seismic Units 7, 8 and 10 in Figure 2.4. However, the 3.5 kHz penetration signal has not revealed a clear sub-bottom horizon that might demarcate the lower boundary of the Oligocene chalk upon some harder local basement rock. Thus the sediment thickness map shown here may simply record the depth penetrated only partially through the Oligocene chalk deposit and not its full thickness. It is noted that Falconer *et al.* (1984) suggested that the combined thickness of seismic Units 7, 8 and 10 in Figure 2.2 – the Late Tertiary surficial sediments involving chalk, glauconitic sand and phosphorite nodules – ranged from 0 to 300 m thick across Chatham Rise.

The sediment thickness variations in Figure 4.10 appear to be related to water depth and bottom gradient. Sediment thickness increases with decreasing water depth and decreasing gradient (i.e. sediment is thickest (>60 m) in flat areas with a water depth of <500 m). In contrast, the sediment thickness is much less (<60 m) on the steeply sloping flanks of the Chatham Rise to the north and south in much deeper water (>500 m) (Figure 4.10). The thicker sediment and underlying chalk deposit on the flat crest (<500 m) may correspond to areas with greater amounts of glauconite and/or phosphorite (Units 8 and 10 in Figure 2.2), which typically do not form in any abundance in deep (>500 m) well beyond shelf depths (e.g. McRae, 1972; McConchie, 1978; Odin & Letolle, 1980).

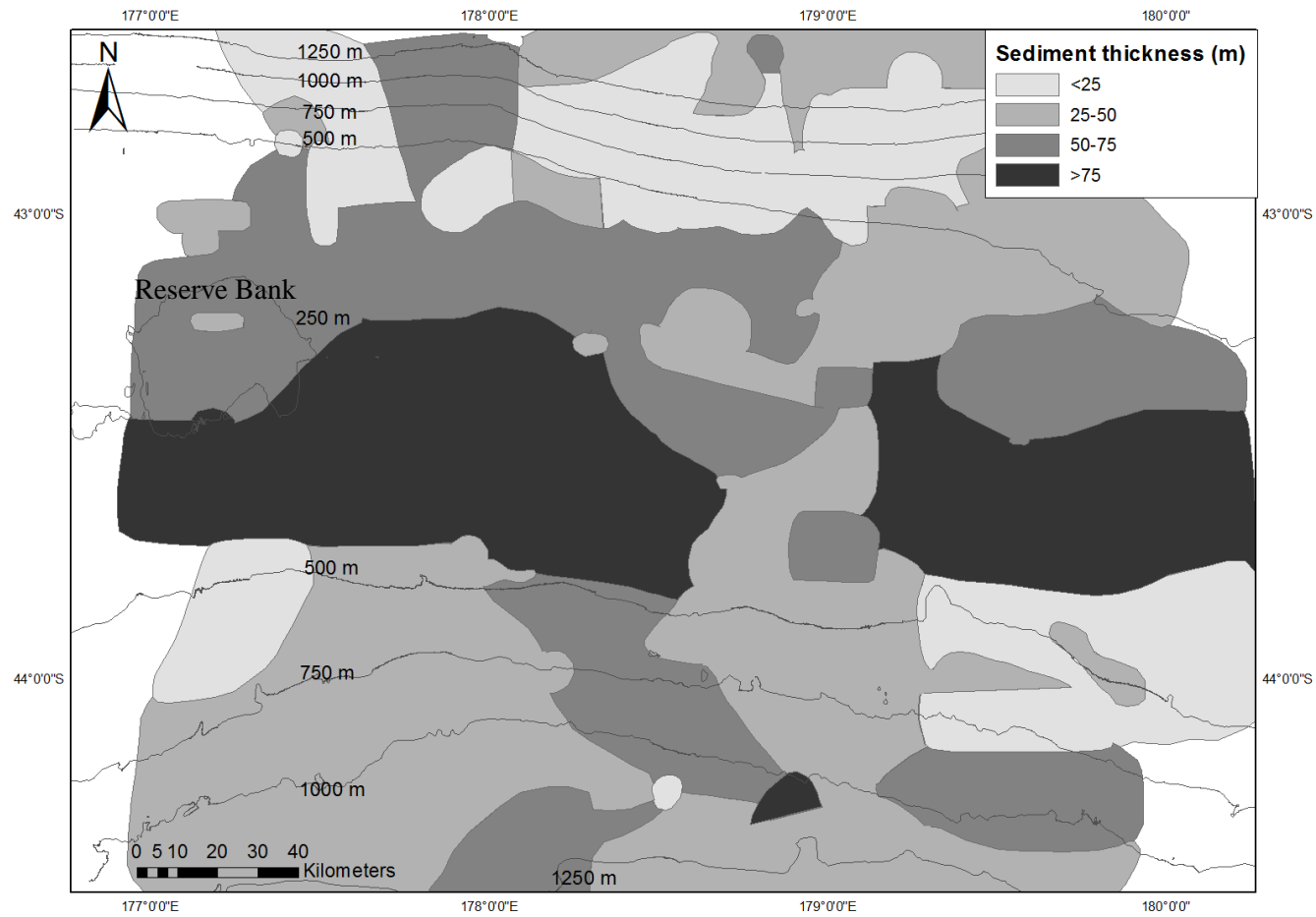


Figure 4.10: Sediment thickness map, likely including the surficial sediment deposits and the underlying Oligocene chalk deposit of central Chatham Rise (i.e. Units 7, 8 and 10 in Figure 2.2).

Chapter 5

LITERATURE REVIEW OF GLAUCONITE

5.1 INTRODUCTION

This chapter is a literature review of the mineral glauconite. The mineral glauconite (on central Chatham Rise) is the main focus of this thesis and so a discussion of it is essential. The history of naming and classifying glauconite is outlined followed by descriptions of its general and physical properties, external morphological varieties, internal fabrics, mineralogy/structure, geochemistry, origin(s) and conditions of formation.

5.2 GLAUCONITE DEFINITION

A century ago scientists knew very little about clayey rocks and minerals, which were often differentiated on the basis of the colour of deposits. Glaucony (or the French spelling glauconie) was a deposit of green grains. However, with more research, colour was recognised to be a superficial property and that the structure of minerals was needed to be known in order to classify the nature of the various types of clay minerals and rock deposits (Millot, 1970). Millot (1970) refers to the structure of various clay mineral species as their “genetic signature”.

The names glauconite and glaucony originate from the Greek “glaucos” for blue green colour (McRae, 1972; Compton, 1989), although some others believe the origin is from a mythical fisherman who turned into a sea-god named Glaucos, and had green hair (Cloud, 1955, p. 484 in Compton, 1989). It is unclear whether the historical (pre-1900) meanings of glauconite defined the actual mineral or whether the name was simply applied to green deposits found in sedimentary rocks (McRae, 1972; McConchie, 1987; Compton, 1989). Contradictions and various meanings of the word glauconite have persisted in the literature until today where glauconite is globally recognised as a greenish iron potassium hydrous phyllosilicate mineral that is positively identified only by X-ray diffraction (XRD) and geochemical analysis.

It needs to be pointed out that glaucony and glauconite have different meanings. Glaucony, or the French spelling glauconie, is defined by Millot (1970) as deposits or facies composed of green grains, which are typically glauconite, and require mineralogical analysis to be recognised. Previous names have included glaukonit, greensand, greenearth, grunerde, terra verte, and others (McRae, 1972; McConchie, 1978). This brings us to the term Glauconite (la glauconite), which is a French word, or glauconitic mica, which was first proposed by Brongniart in 1823 (Millot, 1970; McRae, 1972), but sometimes credit is given to Keferstein (1928). Glauconite, or mineral glauconite (McRae, 1972), is defined as an iron potassium hydrous phyllosilicate greenish mineral which also contains various amounts of calcium, aluminium, and magnesium, has a 2:1 dioctahedral illite-like structure and belongs to the mica group (Hoskins, 1895; Hower, 1961; McRae, 1972; McConchie, 1978; Bailey, 1980). Millot (1970) further defined glauconite as a ferric mineral that is a homeotype of illite. However, there are many variations of this definition (McConchie, 1978). Hower (1961), McRae (1972) and Brindley (1980) add into this definition that mineral glauconite consists of random interstratification of non-expanding 10Å micaceous/illite layers and expanding montmorillonitic/smectite layers, which can be recognised using XRD techniques.

Glauconite as seen in the field typically appears as rounded, greenish to blue-green to yellow-green, mostly sand-sized earthy grains in sedimentary rocks and/or as surface coatings on particles, hardgrounds or fossils (McRae, 1972; McConchie, 1978).

5.3 GENERAL AND PHYSICAL PROPERTIES

The colour of glauconite is typically green, but the shade of green can differ from light green to yellow-green to blue-green to dark green to almost black. Very rarely glauconite grains can actually be close to red, white or grey (McRae, 1972; McConchie, 1978; Compton, 1989). McRae (1972) states that the variation in colour of glauconite grains is related to the amount of iron and aluminium they contain, particularly the ratio of ferrous to ferric iron. Glauconite seen in thin section appears much more vividly green than the colour seen in detrital grains,

and it may also be pleochroic (McRae, 1972). Glauconite has a low weathering resistance, is very friable and has a hardness of 2 on Moh's scale (Milner, 1962, p. 111 in McRae, 1972), although hardness can be variable. Cleavage is perfect, lustre is dull, and specific gravity ranges from 2.3-2.9 (av. 2.64), which depends on the mineral composition as well as the amount of drying the glauconite has been subjected too. The magnetic susceptibility of glauconite is some-what high and will differ depending on the iron content. The grain size of glauconite ranges from clay to coarse sand, but is typically fine to medium sand (i.e. 100-500 μm) (McRae, 1972; McConchie, 1978). McRae (1972) noted that glauconite has a refractive index that ranges from 1.56 to 1.64 and that this optical property can be of diagnostic value. Glauconite can either be authigenic (formed *in situ*) or perigenic (locally redeposited) or allogenic (transported elsewhere after it has formed), which can usually be recognised by the morphology, mineralogy and age of grains (McRae, 1972; Lewis & McConchie, 1994).

5.4 EXTERNAL MORPHOLOGY VARIETIES

There is a large variety of glauconite (and glaucony), both in terms of its mineralogical and geochemical structure and its morphology (Triplehorn, 1966; McRae, 1972; McConchie, 1978).

In general, glauconite occurs as sand-sized grains ranging from 100-500 μm in a wide variety of morphological forms, and glauconite samples typically contain more than one morphological type (McRae, 1972; McConchie, 1978). Many authors have described the various classes of glauconite external morphology and, despite some subtle differences, overall the main groups are similar. Cayeux (1897-1932) was the first to attempt to classify glauconite into different morphological classes, but Triplehorn (1966) provided the most representative classification that is the basis for subsequently quoted schemes (McRae, 1972). I describe briefly below ten morphological forms of glauconite based mainly on the scheme of Triplehorn (1966).

1. Ovoidal and spheroidal: Round, smooth-surfaced pellets that sometimes have small shallow cracks but there is no evidence of breakage. These grains are the

most common type and are typically about 0.2 mm in size. Ovoidal pellets may indicate transportation/reworking and therefore would most likely be allogenic glauconite. Due to reworking and abrasion other morphological types could also be included as ovoidal pellets (Triplehorn, 1966; Konta, 1967; McRae, 1972; McConchie, 1978; Compton, 1989; Payne, 2009).

2. Capsule-shaped: These grains are thought to have formed from faecal pellets due to their cylindrical shapes and circular nature in cross-section. Their colour ranges from brown to earthy to dark green depending on the maturity of grains (Triplehorn, 1966; McRae 1972; Compton, 1978).

3. Fragmentary: According to McConchie (1978) fragmentary glauconites are divided into two types. The first involves irregular grains showing evidence of breakage along weaker sides. They are less than 0.3 mm in size and have a roundness value less than 0.5 on the roundness scale of Powers (1953). The second subdivision is similar to the first, but the roundness value is greater than 0.5 and surface polish may be apparent (McConchie, 1978; Payne, 2009).

4. Tabular or discoidal: These grains appear as flattened plate-like discs, which may look elongated or even bowl-shaped. This type of morphology is very rare and is not a result of compaction/flattening. They may have formed from clay shale flakes or chips, or represent cleaved platelets from vermicular pellets (Triplehorn, 1966; Konta, 1967; McRae, 1972; McConchie, 1978; Compton, 1989; Payne, 2009).

5. Lobate: Lobate grains may be any size and are made up of rounded lobes that are separated by desiccation or deep radial expansion cracks that are triangular in cross-section and infilled with white crystalline material (Triplehorn, 1966; Konta, 1967; McRae, 1972; McConchie, 1978; Compton, 1989; Payne, 2009). According to McConchie (1978), lobate glauconite can look like popcorn, and McRae (1972) states that lobate grains are common. Abrasion and reworking of lobate grains could alter them to ovoidal pellets, which may be smaller in size (Triplehorn, 1966). This group also included Triplehorn's (1966) mammillated grains, which are similar to lobate grains but their cracks are much shallower and the lobes are thought to have formed due to shrinkage or aggregation of smaller rounded pellets.

6. Vermicular: Vermicular grains are elongated and appear to look like a worm or concertina. They are typically made up of flattened disc-like platelets that may have different shapes including coiled, twisted, straight or curved. On some of the cleavage planes, a different colour may be present (Triplehorn, 1966; Konta, 1967; McRae, 1972; McConchie, 1978; Compton, 1989; Payne, 2009). Triplehorn (1966) and McRae (1972) stated that the origin of vermicular glauconite is often the alteration of detrital micas, typically biotite, although various origins have been suggested by others. Triplehorn (1966) states that it would be unlikely for vermicular grains to retain their shape if subjected to abrasion/reworking.

7. Fossil casts and internal molds: Replacement or infilling of organic materials, where grains resemble the internal or external features of organic detritus, such as foraminifera, echinoderms, sponge spicules and other shell fragments (Triplehorn, 1966; Konta, 1967; McRae, 1972; McConchie, 1978; Payne, 2009). McRae (1972) suggested that this morphology can be present as replacement structures or as the end product of the transformation of detrital materials which then infills empty tests and shells.

- Internal molds form due to the infilling of glauconite into the internal cavities of fossil shells in which the organic enclosing shell can later be destroyed; therefore these pellets will reflect the internal shape of the shell.
- Fossil casts on the other hand form due to the replacement of skeletal material as opposed to infilling. These grains will therefore reflect the external shape of the skeletal organism.

8. Composite: Composite pellets are composed of a mixture of glauconite and other mineral grains that are implanted in a glauconitic matrix that is often pale in colour (Triplehorn, 1966; Konta, 1967; McRae, 1972; McConchie, 1978; Payne, 2009). Typically composite pellets are large, up to 3-4 mm in size, but they are relatively uncommon (Triplehorn, 1966; McRae, 1972). Triplehorn (1966) argued that the small pellets within composite grains may have formed earlier prior to incorporation into the larger composite grains.

9. Corroded: A corroded morphology of glauconite was recognised by McConchie (1978) who divided it into two subgroups. He states that corroded glauconite

forms during diagenesis and may have been another morphological form prior to diagenesis.

- **Cauliflower:** Cauliflower morphology of glauconite has been defined by McConchie (1978) and Compton (1989) as grains which are earthy and porous in their surface texture, are often pale red in colour, have no sharp crystals present and are more easily crushed than other glauconite morphologies.
- **Irregular:** The irregular morphology of glauconite has been recognised by Konta (1967), McRae (1972) and McConchie (1978) and is defined as grains that are similar to cauliflower ones except that they display irregular arrays of subangular crystallites.

10. Pigmentary: A pigmentary form of glauconite appears as tiny spots on the surface of detrital grains as coatings, and may look like bacterial colonies. Pigmentary glauconite can also form as infillings of cracks and along cleavages, and is sometimes associated with corroded glauconite (McRae, 1972; McConchie, 1978). Pigmentary glauconite can either be formed by replacement or as a surface coating of very fine glauconite formed from precipitation or alteration of detritus (McRae, 1972).

Burst (1958), Hower (1961), McRae (1972) and McConchie (1978) found that there is no relation between glauconite morphology and chemistry, with the exception of corroded glauconite. Nor is there a relationship between glauconite morphology and % expandables or the disorder coefficient (see Section 5.6). McRae (1972), however, suggested that the morphology of glauconite may be a guide to its origin.

5.5 INTERNAL FABRICS

Like external morphology, there are many different varieties of internal fabric of glauconite grains. Six different types have been described by Triplehorn (1966) which have been further added to by McRae (1972) and McConchie (1978). I describe these internal fabrics below.

1. Random microcrystalline glauconite: Overlapping tiny micaceous crystals/flakes are present in a homogeneous mass and the orientation is completely random. This is the most common type of glauconite internal texture, although it provides little information about the specific origin of the glauconite (Triplehorn, 1966; McRae, 1972; McConchie, 1978).

2. Orientated microcrystalline glauconite: Minute crystals as in the random category, but here the crystallites are orientated to give a near-uniform or parallel mass extinction (Triplehorn, 1966; McRae, 1972; McConchie, 1978). McRae (1972) suggested this class may be monocrystalline, while Triplehorn (1966) suggested it may be more common in older glauconites as a result of recrystallisation of random microcrystalline pellets into single crystals.

3. Semi- orientated microcrystalline glauconite: This class is between random and orientated, so that it has an overall random microcrystalline texture but with some patches showing a well-ordered, near uniform orientation (McConchie, 1978).

4. Micaceous or vermicular structure: Similar to orientated microcrystalline glauconite, due to unit extinction, but the extinction is seen at a much smaller angular rotation of the stage of a petrographic microscope and these grains also have a micaceous cleavage (Triplehorn, 1966; McRae, 1972; McConchie, 1978).

5. Glauconite coatings on grains: Glauconite present as coatings typically has a random microcrystalline texture, and can be about detrital or other glauconite grains. Coatings of glauconite have a wide range of thicknesses, several coatings may be present and there is typically a well developed concentric layering. Glauconite coats also typically occur on heavy minerals and often appear like oolites (Triplehorn, 1966; McRae, 1972). Triplehorn (1966) suggests that coatings may occur as continuous or discontinuous rims, or in isolated patches or irregular networks.

6. Glauconite fibroradiated rims: This is where the glauconite rims comprise elongated microcrystals that are radially orientated and typically have a wavy extinction. They also have a much higher birefringence than the bulk of the affected glauconite grains/pellets and may or may not form continuous rims

around the grains, or they can occur as cracks or spots within a grain (Triplehorn, 1966; McRae, 1972; McConchie, 1978). These rims must have formed due to accumulation or precipitation on a pre-existing grain, as opposed to post-depositional alteration of the grain (Triplehorn, 1966).

7. Organic glauconite replacement structures: In their internal structure they mimic organic structures or the internal structure of organisms, and appear as a variety of fibrous, perforate or lamellar structures (Triplehorn, 1966; McRae, 1972; McConchie, 1978). Triplehorn (1966) suggests that the organic origin is typically destroyed by abrasion and recrystallisation; therefore many pellets could have an organic origin which has subsequently been destroyed.

Like morphology, there is often more than one internal texture in a glauconite assemblage/sample and there appears to be no clear relationship with glauconite chemistry, % expandables, disorder coefficient, or crystallographic class (McConchie, 1978).

5.6 MINERALOGY AND STRUCTURE

Clay minerals like glauconite can display regular (ordered) or irregular (disordered) mixed layers so that different clay mineral layers alternate, and mixed crystals can also exist. Glauconite has a 2:1 dioctahedral structure, characterised by random layer interstratification, where the structure is composed of potassium bearing micaceous non-expanding interlayers and montmorillonite/smectite expanding layers in which the % expandables has a negative correlation with potassium content (Burst, 1958; Hower, 1961; McRae, 1972; Brindley, 1980). Glauconite grains evolve; therefore there is a range of types between smectitic and micaceous end members, where classification is based predominantly on potassium content, as well as the theoretical proportion of smectite and the position of the XRD (001) diffraction peak (Burst, 1958; Hower, 1961; Millot, 1970; McConchie, 1978; Odin & Matter, 1981).

Burst (1958) was the first to recognise that glauconite could be divided into various structural classifications, and he proposed four different categories.

McConchie (1978) redefines Burst's categories, suggesting that the disorder coefficient (DC) should be used, particularly in relation to the category of 'disordered glauconite', as it would avoid problems of worker bias. I will define the four categories below, mainly based on Burst (1958) but also including McConchie's (1978) additions and suggestions by Millot (1970).

1. Ordered glauconite (mineral glauconite): Reflections of the dioctahedral layer are both sharp and symmetrical, similar to a micaceous lattice, with a regular 1 M structure which is essentially non-swelling and has a high potassium content. Well defined peaks at 10, 5 and 3.3Å on XRD scans are a clear diagnosis for ordered glauconite (Burst, 1958). McConchie (1978) adds that there must be a $DC \leq 0.25$, allowing glauconites with less than 10% expandables to be in this category, in agreement with both Burst (1958) and Hower (1961) for ordered glauconite.

2. Disordered glauconite: Peaks are low/subdued and asymmetrical, despite this group being monomineralic and micaceous like group 1, still essentially non-swelling but with a lesser potassium content compared to ordered glauconite. The structure is 1 Md, the d meaning the monoclinic stacking is disordered (Burst, 1958; Millot, 1970; McConchie, 1978). Burst (1958) and Hower (1961) state that disordered glauconite contains 10-20% expandable layers, while McConchie (1978) further subdivides this group into two subgroups: (a) moderately disordered glauconite that has a DC of 0.25-0.5, with less than 40% expandables, and (b) extremely disordered glauconite, that has a $DC > 0.5$ and less than 40% expandables. Thompson and Hower (1975) suggested that disordered glauconite (i.e. glauconite with 10-25% expandable smectite layers) has an alleverdite-like stacking, where the 14Å smectite layers are separated by at least one 10Å illite layer.

3. Interlayered glauconite: Comprises glauconite which is extremely disordered, highly expandable, low in potassium, and has a montmorillonite type lattice (Burst, 1958; Millot, 1970). Burst (1958) and Hower (1961) state that there must be greater than 20% expandable layers, while McConchie (1978) suggests a higher value at more than 40% expandables.

4. Mixed mineral glauconite: Mixture of two or more clay minerals (Burst, 1958). McConchie (1978) states that this group must contain two distinct mineral species on XRD traces, where only one of these is glauconite and the expandables may or may not be high. Burst (1958) records that the most common mixed mineral glauconites are a mixture of illite with montmorillonite and illite with chlorite.

McConchie (1978) suggests that it would be much more suitable to base the classification of glauconite purely on measurements made using XRD methods, as this would eliminate the need for chemical analysis. Burst (1958) emphasised that while the XRD classification system is reasonable, there is often considerable overlap between the various groups, so that the classification approach is limited.

According to Compton (1989), glauconite can be divided into three basic structural types identified using XRD. The three structural categories are much the same as the first three categories described by Burst (1958), but he drops the fourth category as it is not specific to the mineral (only to deposits of green grains, i.e. glaucony).

1. Well ordered 1M structure: Basal 10Å spacing, sharp symmetrical peaks, 112 reflectors always present, with a smectite (expandable) component of <10%. This structure is moderately abundant in glauconites.

2. Disordered 1Md structure: Symmetrical basal peaks, 112 reflectors absent, smectite component of 10-50%. A disordered structure is the most abundant glauconite form.

3. Unstable 2M₁ structure: Structure unclear and is possibly an unstable intermediary formed from octahedral layer charge anomalies.

5.7 GEOCHEMICAL COMPOSITION

Glauconite does not have a specific formula; therefore it has a range of compositions where major elements and trace elements vary, as well as their interdependences (McRae, 1972; McConchie, 1978). Greensand contains

substrate minerals (e.g. kaolinite, illite, chlorite, quartz, mica, pyrite and calcium carbonate) which progressively disappear during glauconite genesis. Glauconite is composed of authigenic clay which replaces substrate and the clay type changes during genesis. Thus there is a range of compositions between an iron-rich and potassium-poor smectite starting member and an iron-richer and potassium-rich micaceous finishing member.

Glauconite belongs to the mica group and is thus classified as a non-expandable 2:1 iron potassium rich phyllosilicate that also contains various amounts of Ca, Si, Al, and Mg, as well as many trace elements. The 2:1 structure refers to the crystallographic structure of the mineral, where two tetrahedral sheets alternate with one octahedral sheet and each of the major elements fall into their specific positions within these sheets, as well as in interlayer positions (Table 5.1).

Table 5.1: Major element positions within the crystallographic structure of glauconite.

Position	Major elements
Tetrahedral	Si, Al
Octahedral	Al, Mg, Fe
Interlayer	K



McRae (1972) and Brindley (1980) suggest that the tetrahedral and octahedral layers contribute relatively equally to the overall charge of glauconite, as shown by the distribution of ions between the two different sheets. However the octahedral sheet often has a slightly higher charge than the tetrahedral layer, due to Al replacing Si in one of the four tetrahedral sheets. This leads to an overall net negative charge, referred to as the cation exchange capacity, which can be of economic importance (Worrall, 1968; McRae, 1972; McConchie, 1978). However, this net negative charge is usually balanced by large interlayer cations, usually K^+ but also others such as Na^+ , Ca^{2+} , Rb^+ , Sr^+ or Cs^+ (Milot, 1970; McRae, 1972; Odin & Letolle, 1980). Once the interlayer cation is in place it is thought to be locked and therefore non-exchangeable (Worrall, 1968; Milot, 1970; McConchie, 1978). The cation exchange capacity thus changes depending on the amount of potassium (i.e. an inverse relationship) and therefore also on the % expandable layers (Hower, 1961; McRae, 1972). Grim (1968) also states that there is an overall decrease in the index of refraction of glauconite when there is an increase in the % expandable layers.

There are many correlations or relationships between the major elements within glauconite, the main ones being noted below. Iron typically replaces aluminium in the octahedral sheet, which as a consequence gets replaced by tetrahedral silicon, so that if glauconite has an increased iron content, the relative abundances of both aluminium and silicon will become reduced (Worrall, 1968; McConchie, 1978). A proportion of magnesium can occupy the lattice sites that are typically occupied by iron (McConchie, 1978). Thus McConchie (1978) has suggested that glauconite containing a high amount of iron (and sometimes aluminium) will actually restrict magnesium to enter into the octahedral position. As the % expandable layers within glauconite increases, this will result in an increase in the overall water content, due to the negative correlation between potassium and water, while the % expandables will decrease if the potassium content increases which will also decrease the water content (Hower, 1961; McConchie, 1978). Calcium and sodium, unlike potassium, does not notably alter the water content (McConchie, 1978).

A dominant correlation is the positive one between iron and potassium, in which both elements increase with increasing glauconite maturity (Compton, 1980; Odin and Matter, 1981). McConchie and Lewis (1980) and Odin and Letolle (1980) state that the iron content in glauconite must be at least 15% Fe_2O_3 and Odin and Letolle (1980) state that the potassium (K_2O) content must be greater than 8%, although McConchie and Lewis (1980) set the minimum at 4%.

As described in Section 5.6, glauconite can be classified into various types based on mineralogy. Odin and Matter (1981), however, suggested that glauconite can be classified into various evolved types, or maturity levels, in which classification is based on potassium content, as well as the mineralogical structure, colour and XRD (001) peak position. In this scheme glauconite ranges from a potassium-poor (<4%) smectite nascent form into an end member involving a highly evolved potassium-rich (>8%) illite mineral (Table 5.2) (Odin & Matter, 1981; Udgate, 2007).

Table 5.2: Glauconite types and structure based mainly on potassium content (after Odin & Matter, 1981; Udgata, 2007).

Glauconite types	Maturity	Mineralogical structure	Colour	K ₂ O %	XRD (001) peak position
Nascent	Low	Smectitic glauconite  Micaceous glauconite	Pale green	<4	14Å
Slightly evolved	Moderate		Light green	4-6	 10Å
Evolved	High		Green	6-8	
Highly evolved	Very high		Dark green	>8	

5.8 THEORIES OF ORIGIN(S)

Glauconite is one of few clay minerals that almost always has a marine origin in a specific microenvironment at the sediment-water interface (Millot, 1970; Velde, 1985; Odin and Fullagar, 1988). However, there is considerable debate concerning the specifics of the origin and development of glauconite.

Glauconite is restricted to sedimentary rocks and is mostly found in marine sediments, although very rarely also in lacustrine and various alluvial deposits in which case it could well have been transported (i.e. detrital or allogenic). Glauconite may be generated *in situ* where it is found, in which case it is authigenic, or it may be transported elsewhere by water or wind, in which case it is allogenic or detrital (McRae, 1972; Lewis & McConchie, 1994; Payne, 2009). To determine whether glauconite is authigenic or allogenic typically involves analysing the petrology of the rock, the morphology of the glauconite grains, the mineralogy and geochemistry of the grains and associated sediment, and the ratio of ferrous to ferric iron and the amount of interlayer ions (McRae, 1972). Radiometric dating of glauconite grains may indicate a detrital origin. Detrital glauconite may originate from a nearby area in a basin where authigenic glauconite is being formed, particularly where there are alkaline pH conditions, or it can be derived from outcrops of pre-existing submarine rocks (McRae, 1972).

It was originally suggested that foraminifera needed to be present for glauconite to form, and also that organic sulphides were essential which became oxidised to H₂SO₄ which turned clays into a gel of aluminium and silica which then reacted with iron hydroxides and K⁺ to allow glauconite development (McRae, 1972;

McConchie, 1978). The theory arose because dredged up sediment samples from ships contained many foraminifera and had a strong H₂S smell. However, the idea was soon disregarded when it was criticised by Prather (1905) who suggested that multiple types of parent materials could form glauconite, thereby explaining the large variations in glauconite morphology and chemistry (McRae, 1972). Triplehorn (1966) suggested the following diverse origins of glauconite: chemical precipitation; chemical replacement; mechanical aggregation; alteration of faecal pellets; expansion and alteration of detrital mica; and the alteration of clay infillings of fossil tests. Most workers now recognise that there are many varieties of parent materials which can be altered to glauconite and so it can have multiple origins, including organic fossil remains, rock fragments, faecal pellets, micas, clay minerals, volcanic glass, opaline silica, alumino silicate gels and even direct chemical precipitation (Triplehorn, 1966; McRae, 1972; McConchie, 1978). McConchie (1978) concluded that the various theories of formation of glauconite are dependent on the parent material that is involved.

Odin (1988) disregarded the theory of formation believed by many authors in the 1960s in which glauconite was “formed by a progressive transformation of an inherited illitic degraded layer” (Odin, 1988, p. 222). Odin and Matter (1981) and Odin and Fullagar (1988) instead believed that glauconite forms through ‘neof ormation’ (i.e. new or recent formation), involving crystal growth and recrystallisation processes. His ideas are compatible with those suggested earlier by Millot (1970) that glauconite formation can be entirely neoformed through epitaxial growth of pre-existing clay minerals or from the transformation of micas.

Despite this, McRae (1972) and McConchie (1978) state that the ‘layer lattice theory’ of glauconite formation developed by Burst (1958) is generally accepted by most workers. Burst (1958), McRae (1972) and McConchie (1978) acknowledge that this theory requires three important factors: (1) the presence of a degraded layer silicate lattice; (2) the availability of iron and potassium; and (3) appropriate Eh (redox potential) and pH (measure of acidity or basicity) conditions which are typically met due to organic matter decay. If all these three factors are met then glauconitisation may proceed with the degraded silicate lattice absorbing both potassium and iron which, given the correct chemical and

environmental conditions and especially time, results in a reduction in the percentage of expandable layers.

There are also other theories of glauconite formation in specific cases, such as the transformation of biotite (Gallagher, 1935 in McRae, 1972) and weathered mica layers acting as templates for glauconite development (Ehlmann *et al.*, 1963 in McRae, 1972).

Odin and Matter (1981) reported that the process of glauconitisation is a two-fold evolutionary process involving the authigenic growth of automorphous crystallites in the pores of the substrate, as well as the progressive alteration and replacement of the substrate. This process results in the verdissement (i.e. act of turning green) of granular substrates, hardgrounds and fossils. Glauconitic smectite forms in the substrates, and then new smectite grows inside any remaining pore space at the same time as the earlier smectites are being modified by incorporation of potassium, so leading to a decrease in the amount of expandable minerals with non-expandable glauconitic mica as the end member of formation. Such a process inherently means that there is likely to be large variations in the mineralogical composition, chemistry and physical appearance of glauconite grains. Due to the glauconitisation evolution process described by Odin and Matter (1981), they suggest four categories for the evolution/formation of glauconite, namely nascent, slightly-evolved, evolved and highly-evolved (Table 5.2).

5.9 SEDIMENTARY CONDITIONS OF FORMATION

As already noted, glauconite forms almost always in a marine environment associated with a variety of conditions or controls within that environment, including water temperature, water depth, Eh, pH, sediment accumulation rate and turbulence (Triplehorn, 1966; Millot, 1970; McRae, 1972; McConchie, 1978; Compton, 1989). Each of these is briefly described in the following sections.

Generalising, glauconite forms during marine diagenesis in relatively shallow open marine environments under mildly reducing conditions, in the presence of some bottom current activity, in all except the coldest of oceans, and in areas

where there is a low sedimentation rate and exposure to the sediment-water interface for long periods of time (up to several million years). Other conditions include 4-20°C water temperatures, pH 8, water depths between 60 and 1000 m, and formation at the boundary between oxidising sea water and reducing interstitial fluid. Glauconite is mostly found forming on continental shelves, which is controlled by the water depth (McRae, 1972). Glauconite formation must also have an appropriate substrate size and porosity, as well as grain movement on the sea floor. For these reasons glauconite is typically found in shallow marine sedimentary rocks such as limestones, shales and sandstones, occurring in both modern and ancient sediments (McRae, 1972; McConchie, 1978). Glauconite is the dominant component in greensand deposits (>50% glauconite) and is often found associated with phosphatic material (McRae, 1972; Odin & Letolle, 1980).

5.9.1 Water temperature

The seawater temperature typically associated with glauconite formation ranges from 15-20°C, but it can form at both colder and warmer temperatures. However, authigenic glauconite is rare or absent in cold polar and the warmest tropical regions. A geochemical reason for why temperature alone controls glauconite formation has not yet been discovered, but temperature on its own seems to control the rate of glauconitisation (Porrenga, 1967; McConchie, 1978). Temperature may control the amount of organic matter which in turn affects the Eh conditions; for example, if there is insufficient organic matter then the Eh may be too high for glauconite to form and vice versa (McConchie, 1978). McRae (1972) further states that glauconite formation is best suited to areas where cold and warm water meet which results in a high amount of organic productivity.

5.9.2 Eh conditions

The Eh control on glauconite formation is not well known, with a variety of ranges being suggested in the literature from moderately anaerobic to strongly oxidising. However, the majority of authors recognise that for glauconite to actively form the environment must be slightly reducing (i.e. $Eh \leq 0$) (Burst, 1958; Hower, 1961; McConchie, 1978). McRae (1972) considered the redox potential to be the most critical controlling factor in the formation of glauconite, with slightly

reducing conditions being common in sediments where bacteria are slowly decomposing organic matter (McRae, 1972).

5.9.3 pH conditions

Glaucinite typically forms in a pH that is slightly alkaline, between about 7 and 8, which is typical of seawater (Fairbridge, 1967; McRae, 1972; McConchie, 1978).

5.9.4 Water depth

Depth itself does not directly control glauconite formation, but it does however affect several other conditions of formation, such as temperature, Eh, turbulence and sedimentation rate. It is unlikely that glauconite would form in depths shallower than about 15 m, as wave activity would cause too much turbulence and the temperature would likely be too warm (McRae, 1972; Odin & Letolle, 1980). Middle to outer shelf depths appear to be optimal, including over the shelf margin down to about 500 m, but apparently glauconite can rarely form as deep as about 2000 m (Porrenga, 1967; McRae, 1972; McConchie, 1978; Odin & Letolle, 1980). Of course glauconite grains can be transported from shallower into deeper waters.

5.9.5 Turbulence

The limit of the amount of turbulence controlling glauconite formation is uncertain, but appears to be inhibited by strong currents while requiring at least some bottom current activity (McConchie, 1978). McRae (1972) suggested that where glauconite occurs in high energy areas or deposits it is likely to be allogenic. Odin and Letolle (1980) favoured a lack of agitated water conditions for glauconite formation.

5.9.6 Sediment accumulation rate

Sediment accumulation rate is considered to be the most important controlling factor of glauconite formation according to McConchie (1978), and must be very low. This is why glauconite is often associated with unconformities, linked to the fact that it forms at the sediment-water interface (Burst, 1958; Hower, 1961; McRae, 1972; McConchie, 1978; Odin & Letolle, 1980). McRae (1972) suggested

that even a negative sedimentation rate is needed for glauconite formation, and that any relatively high influx of siliciclastic detritus will result in a higher % of expandable smectite layers in glauconite, whereas a lower rate would yield monomineralic glauconite with a low % of expandable layers.

5.9.7 Organic matter

The presence of organic matter is important as it controls the Eh conditions. Apart from the naturally present marine organic material, organic matter could also be provided from inundated terrestrial soils during marine transgressions that glauconite formation is commonly associated with (McRae, 1972).

5.9.8 Age preferences

Glauconite found today has ages ranging from Precambrian to Recent, but according to McRae (1972) it is particularly associated with Cretaceous and Tertiary age deposits. Odin and Letolle (1980) reported some evidence that suggested glauconite formation was particularly associated with Middle Cretaceous and Early Miocene strata, but rarely so with Permian and Early Jurassic deposits.

Chapter 6

PHYSICAL PROPERTIES OF GLAUCONITE

6.1 INTRODUCTION

The surficial sediment deposits on central Chatham Rise contain from 10 to over 80% glauconite, making it a major sediment component and therefore in need of full documentation.

This chapter gives a detailed account of the physical properties of the glauconite varieties on central Chatham Rise. The information is fundamental to gaining an in-depth knowledge concerning the nature, origin and economic potential of the glauconite, a major focus of this thesis. The typical physical properties of glauconite globally were reviewed in Chapter 5, and this aids the analysis and discussion of the physical properties of the glauconite on central Chatham Rise.

The different types of glauconite that occur on central Chatham Rise have been previously noted by Norris (1964), Bell and Goodell (1967), and von Rad and Rösch (1984). These have been observed and described in the present study (Table 6.1) with examples illustrated by photomicrographs in Figure 6.1.

Table 6.1: Various glauconite types and their descriptions on central Chatham Rise.

Glaconite type	Description
1. Pelletal	Sand-sized dark green to black smooth and polished grains (Figure 6.1A).
2. Precipitated	a) Skeletal chamber infills e.g. foraminiferal infill (Figure 6.1B).
3. Replacement	a) Skeletal grains. b) Other grains e.g. margins of glauconitised phosphatic nodules (Figure 6.1C) and glauconitised phosphatic grains (Figure 6.1D).
4. Rock fragments	Glauconite pellets within a rock fragment, along with foraminifera, and siliciclastic minerals (Figure 6.1E).

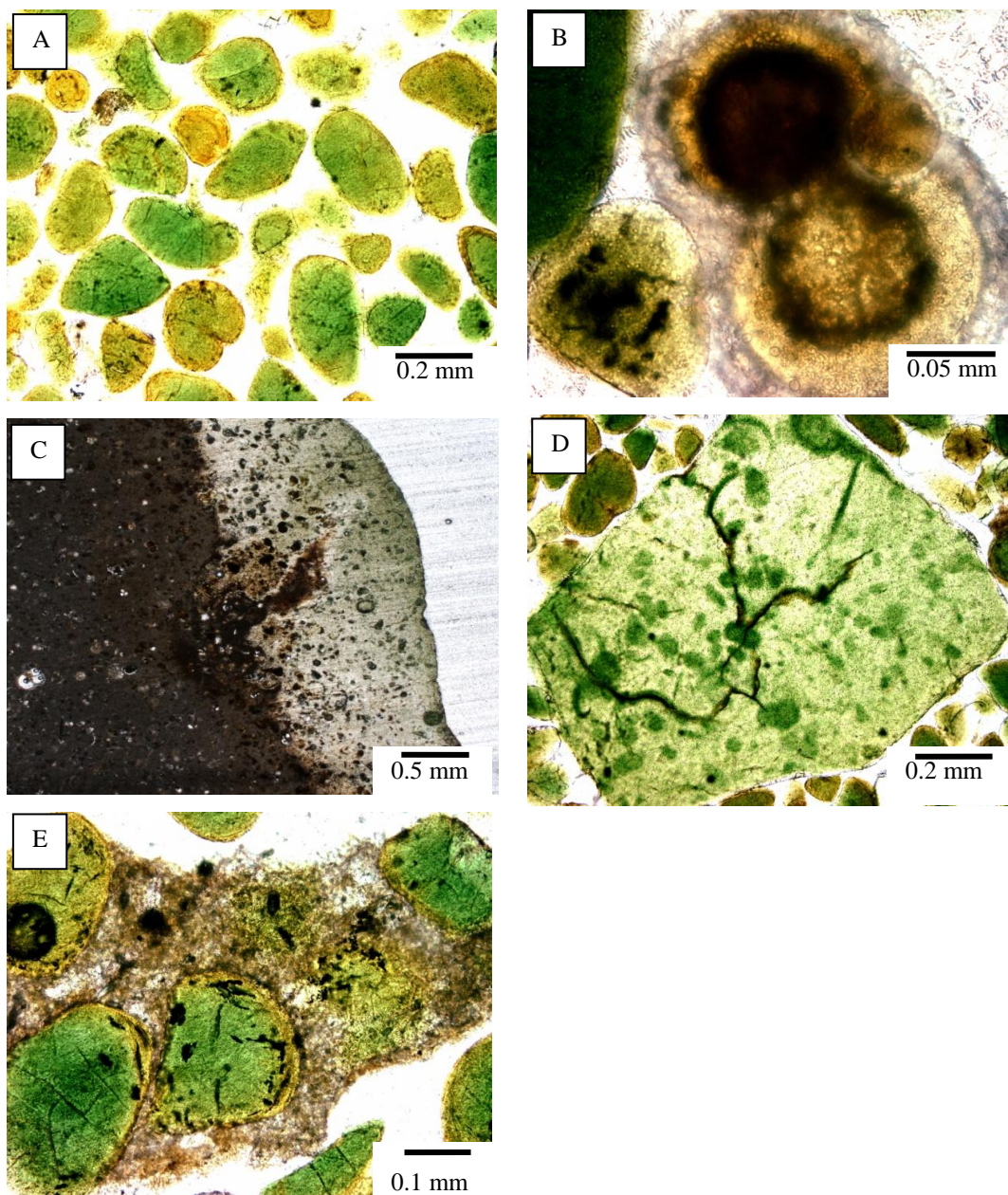


Figure 6.1: Photomicrographs of examples of the various types of glauconite that occur on central Chatham Rise as described in Table 6.1. A: pelletal glauconite grains (A897), B: foraminiferal glauconite infill (A891), C: glauconite rim on a phosphorite nodule, D: glauconitised phosphatic grain (Q325), E: glauconite pellets within a rock fragment (Q356).

6.2 METHODS

In order to fully describe the physical properties of the glauconite a variety of laboratory methods were undertaken, including use of the Frantz magnetic separator to concentrate glauconite grains from the bulk sand samples, binocular microscope to observe their 3-d morphology, and thin section analysis and SEM (Appendix III) to record petrographic features. The analysis of 34 surficial samples plus 6 down-core sample (U6866) provided information about the

distribution, content, colour, size, morphology, and fabric of the glauconite grains. When sample numbers are referred to throughout this chapter, see Figure 3.1 for their location.

The first step was to separate the glauconite fraction from the sand samples. Glauconite is paramagnetic and so can be separated from a non-magnetic sand sample using a Frantz magnetic separator to an approximately 99% pure glauconitic sample (Bell & Goodell, 1967; McConchie, 1978, Compton, 1989). Each sample was put through the separator three times and settings were chosen based on the previous work on Tertiary glauconites by McConchie (1978) and Compton (1989), as well as by trial and error. The first setting used was 0.5 amps, a 15° sideways tilt and a 20° forwards tilt. The magnetic fraction was then re-run again at the same settings in order to remove any non-magnetic contaminants, except that the sideways tilt was changed to 20° if there were few non-magnetics, or 25° if there appeared to be many. Some samples were run through a third time at the same settings, and even then most samples still contained a tiny amount of non-magnetic material. The various fractions of the original bulk samples (i.e. gravel, glauconite sand, non-magnetic sand and mud) were each weighed to determine wt% content (raw results in Appendix III).

Individual glauconite grains were handpicked from two subsamples (A891 and Q325) into various morphological, size and colour categories, and analysed under the binocular microscope and recorded photographically. Some handpicked grains were also chosen for the SEM analysis of morphology, size and fabric (Appendix III).

The petrography of 26 pure glauconite detrital thin sections is documented in Table 6.3 in which the abbreviation codes are defined in Table 6.2. Photomicrographs of samples have also been taken (Appendix III). Note that sample U6866 involves the downcore analysis of glauconite at roughly 2 cm intervals, which revealed essentially no differences.

Table 6.2: Key for the glauconite petrographic sheets (Tables 6.3).

Abundance		Sorting		Shape		Morphology	
R: <1%	Rare	VW	Very well	WR	Well rounded	O	Ovoidal
S: 1-5%	Some	W	Well	R	Rounded	L	Lobate
M: 5-15%	Most	M	Moderate	SR	Sub rounded	C	Composite (glauconitised phosphatic grains)
C: 15-25%	Common	P	Poor	SA	Sub angular	F	Fossil cast/internal mold
VC: 25-50%	Very common	VP	Very poor	A	Angular	T	Tabular/discoidal
A: 50-75%	Abundant					P	Pigmentary
VA: >75%	Very abundant					RF	Glauconitised rock fragments

Internal fabric		Colour	
Rx	Random microcrystalline	Bg	Bottle green
Fr	Oriented fibroradiated rims	Yg	Yellow – brown green
Or	Organic replacement structures		

Table 6.3: Petrographic data for pure glauconite concentrates from central Chatham Rise (Key for abbreviations in Table 6.2).

	A891	A892	A897	A899	C605	C606	C961	G34	G36	G112
Pellet	VA	VA	VA	VA	VA	VA	VA	VA	VA	VA
Grain size - max	1.1	2.7	2.1	1.1	2.4	1.15	1.2	0.9	0.7	1.0
(mm) - min	0.05	0.05	0.05	0.05	0.025	0.04	0.1	0.1	0.05	0.05
- mode	0.2	0.2	0.15	0.2	0.15	0.15	0.2	0.2	0.2	0.15
Shape	SR-R	SR-R	SR-R	SR-R	SR-SA	SR-SA	SR-SA	SR-R	SA-SR	SR-R
Main morphology	O	O	O	O	O	O	O	O	O	O
Sorting	M	M	P	M	P	P	M	M	M	M
Colour 1	Bg: A	Bg: A	Bg: VA	Bg: A	Bg: A	Bg: C	Bg: VA	Bg: VC	Bg: VC	Bg: A
Colour 2	Yg: VC	Yg: VC	Yg: C	Yg: VC	Yg: C	Yg: A	Yg: M	Yg: C	Yg: VC	Yg: C
Expansion cracks	C	M	M	VC	VC	M	S	C	VC	C
Opaque inclusions	M	M	C	S	VC	S	M	M	M	S
Limonitisation	M	M	M	C	M	C	R	S	S	R
Main internal fabric	Rx	Rx	Rx	Rx	Rx	Rx	Rx	Rx	Rx	Rx
Fr: Fibroradiated rims	C	VC	VC	M	C	C	M	S	M	S
Or: Foraminiferal infill	S	S	S	M	S	M	R	S	S	
Other morphologies/types										
F: Carbonate/skeletal grain	M	S	S	M	S	S	R	R	R	
RF: Rock fragment				R	S			M	M	
- Size range (mm)	0.5-1	0.2-0.5	0.1-0.3	0.15-0.3	0.5-1.9	0.1-0.2	0.25	0.5-1.5	0.5-1	
- Shape	SR	SA	SA	SR	SA	SA	SR	SA	SA	
C: Glauconitised phosphatic	S	S	S	R	S	S	M	M	S	S
- Size range (mm)	0.3-0.7	0.15-1.1	0.5-2.1	0.2	0.6-2.4	0.3-0.7	0.35-0.8	0.25-0.4	0.3	0.3-0.5

Table 6.3 continued.

	G113	G135	G137	G138	H959	Q325	Q328	Q356	U2582F	V381
Pellet	VA	VA	VA	VA	VA	VA	VA	VA	VA	VA
Grain size - max	0.5	0.4	0.5	0.5	0.4	0.5	0.6	0.35	0.35	0.5
(mm) - min	0.05	0.05	0.05	0.05	0.04	0.05	0.05	0.05	0.04	0.08
- mode	0.2	0.2	0.2	0.15	0.2	0.15	0.2	0.15	0.15	0.2
Shape	SR-SA	SR-SA	SR	SR-SA	SR-SA	SR-SA	SR-SA	SR	SR-SA	SR-R
Main morphology	O	O	O	O	O	O	O	O	O	O
Sorting	P	M	P	P	P	P	P	M	P	M
Colour 1	Bg:A	Bg:A	Bg:A	Bg:VC	Bg:A	Bg:A	Bg:A	Bg:A	Bg:A	Bg:VC
Colour 2	Yg:C	Yg:VC	Yg:C	Yg:VC	Yg:VC	Yg:C	Yg:C	Yg:C	Yg:C	Yg:VC
Expansion cracks	M	M	C	S	M	M	S	M	C	M
Opaque inclusions	S	R	R	R	R	M	VC	C	C	S
Limonitisation	M	M	S	C	M	S	S	S	S	S
Main internal fabric	Rx	Rx	Rx	Rx	Rx	Rx	Rx	Rx	Rx	Rx
Fr: Fibroradiated rims	M	M	S	M	S	S	M	C	S	S
Or: Foraminiferal infill	R	S	R	S		R	S	R	R	S
Other morphologies/types										
F: Carbonate/skeletal grain	R	S	R	R			R		R	S
RF: Rock fragment	R		S		S	M	S	S	R	
- Size range (mm)	0.6	0.3	0.5-1.2	0.25	0.5-1.7	0.3-0.6	0.4-0.7	0.3-1.25	0.15-0.4	0.2-0.6
- Shape	SA	SR	SA	SA	SA	SA	SA	SA	SA	SA
C: Glauconitised phosphatic	M	M	S	S	R	M	R	S	M	S
- Size range (mm)	0.3-0.8	0.4-1.8	0.2-0.7	0.3-1.4	0.2-0.25	0.3-1.6	0.8	0.2-0.4	0.3-2.0	0.25-0.65

Table 6.3 continued.

	U6866 0-2 cm	U6866 2-4 cm	U6866 4-6 cm	U6866 6-8 cm	U6866 8-10 cm	U6866 10-13 cm
Pellet	VA	VA	VA	VA	VA	VA
Grain size - max	0.5	0.4	0.4	0.5	0.6	0.35
(mm) - min	0.08	0.08	0.08	0.05	0.05	0.05
- mode	0.2	0.2	0.2	0.2	0.2	0.2
Shape	SR-R	SR-R	SR-R	SR-R	SR-R	SR-R
Main morphology	O	O	O	O	O	O
Sorting	M-P	M-P	M-P	M-P	M-P	M-P
Colour 1	Bg:VA	Bg:VA	Bg:VA	Bg:VA	Bg:VA	Bg:VA
Colour 2	Yg:S	Yg:M	Yg:M	Yg:M	Yg:M	Yg:M
Expansion cracks	S	S	S	S	S	S
Opaque inclusions	C	M	C	C	M	M
Limonitisation	R	R	R	R	S	R
Main internal fabric	Rx	Rx	Rx	Rx	Rx	Rx
Fr: Fibroradiated rims	S	S	S	S	S	S
Or: Foraminiferal infill		R	R	R	R	R
Other Morphologies/types						
F: Carbonate/skeletal grain				R		R
RF: Rock fragment	S	R	R	R	R	S
- Size range mm	0.3	0.4	0.4	0.4	0.3	0.75
- Shape	SA	SA	SA	SA	SA	SA
C: Glauconitised phosphatic	S	S	S	S	S	S
- Size range (mm)	0.4-1.0	0.25-1.25	0.2-0.6	0.3-0.9	0.25-0.75	0.2-0.7

6.3 DISTRIBUTION

The abundance and distribution of glauconite in the <2 mm fraction over central Chatham Rise is shown in Figure 6.2 (Appendix III).

The highest concentration of glauconite (50%-80+%) occurs on or near the topographic high forming Reserve Bank. Reserve Bank is in less than 250 m water depth, and was considered by Norris (1964) as too deep for the accumulation of mollusc shells and sufficiently isolated from land sources for terrigenous input to be low, both requirements for glauconite formation. The glauconite content then gradually decreases in a southeastwards direction, possibly the direction in which the grains have been reworked and redistributed.

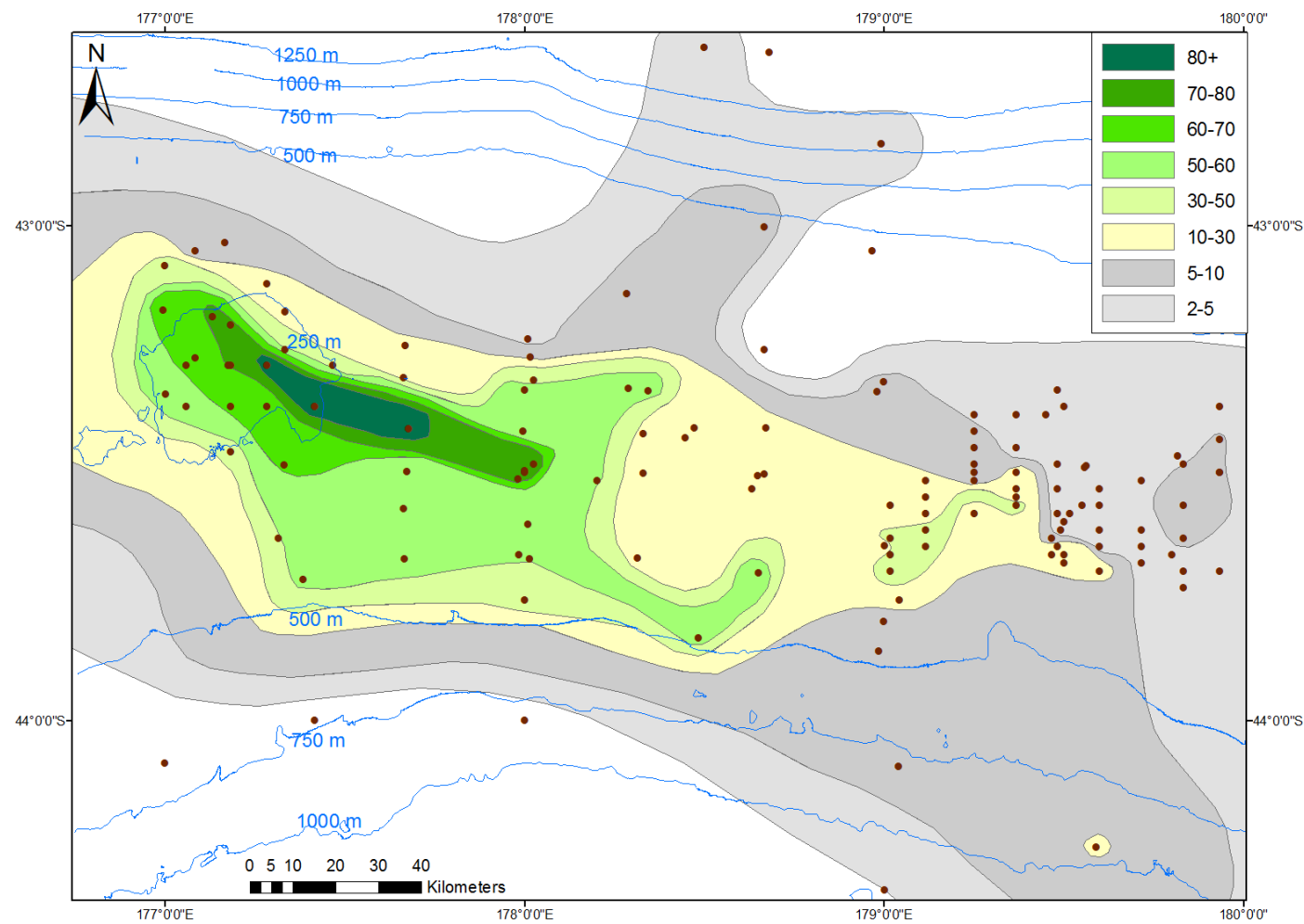


Figure 6.2: Distribution of glauconite (weight%) in the <2 mm fraction over central Chatham Rise.

6.4 COLOUR

The colour of glauconite grains on central Chatham Rise was analysed under a binocular microscope for the loose detrital grains, and under the petrographic microscope in thin sections (Appendix III). The colour of glauconite is mainly controlled by its chemical composition, predominantly the amount of Fe and Al and the ratio of $\text{Fe}^{2+}/\text{Fe}^{3+}$ (McRae, 1972). The loose detrital glauconite grains on central Chatham Rise mainly (>90%) have a very dark green to almost black colour (Figure 6.3A), which is consistent with other studies (Norris, 1964; Pasho, 1976). Such a dark green to black colour typically reflects glauconite having a high maturity (i.e. a high Fe and K content). Most remaining grains (<10%) are light green and not as smooth or ovoidal as the dark green to black varieties (Figure 6.3B). The abundance of the dark green to black grains can be directly correlated to an increase in the % blackness described in the bulk samples (Figure 3.4), and also to the darker Munsell colours, i.e. black, olive black, greyish olive and olive grey (Figure 3.2). The lighter green colours however, would not be as easily recognised as glauconite in the bulk samples, therefore may not be included in the % blackness and Munsell colours may be lighter, i.e. light grey (Section 3.2.1).

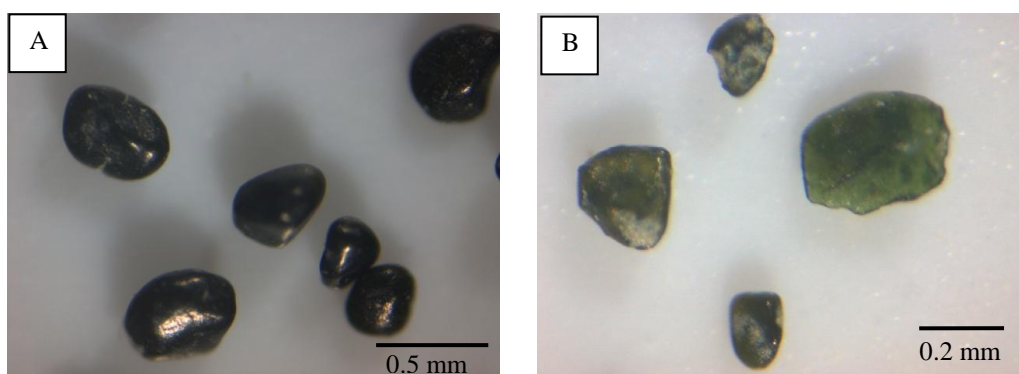


Figure 6.3: A: Dark green to black (10G 1.7/1 greenish black) glauconite grains in sample Q325. B: Light to bottle green (5G 4/1 dark greenish grey) glauconite grains in sample Q325.

In thin section the glauconites range from a bottle green to a lighter yellow-brown green colour (Figure 6.4). Bottle green glauconite is typically very abundant to abundant (>50%) in samples, while yellow-brown green grains are usually common (15-25%) (Figure 6.5).

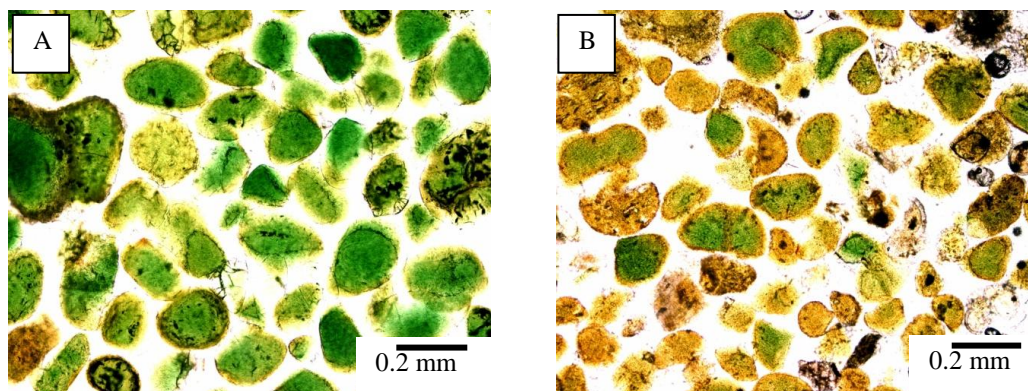


Figure 6.4: A: Photomicrograph of bottle green glauconite pellets (sample U6866 10-13 cm). B: Photomicrograph of yellow-brown green glauconite pellets (sample C606).

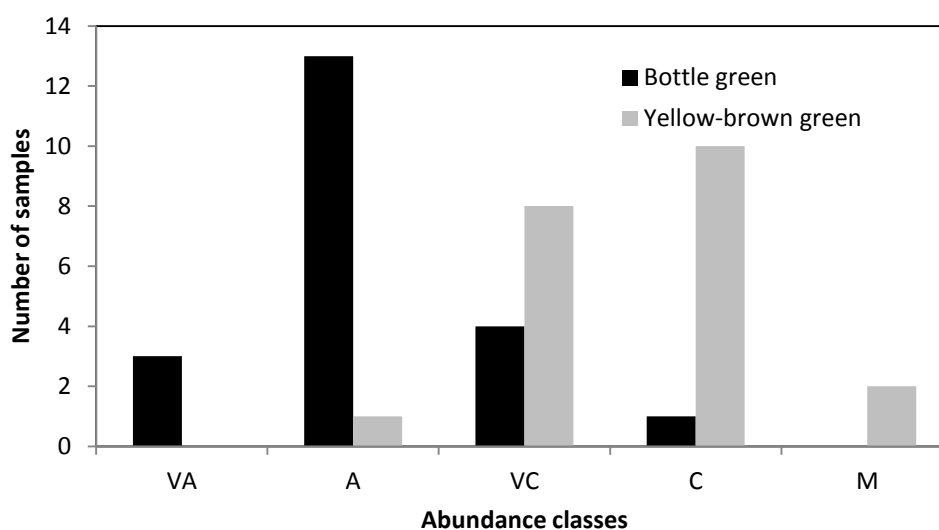


Figure 6.5: Abundance of colour types within the 21 glauconite thin sections from central Chatham Rise (abundance classes defined in Table 6.2).

Figure 6.6 shows the spread of abundance of the two main colours of glauconite (Bg - bottle green; and Yg - Yellow-brown green) within all 21 thin sections. The most common occurrence of colour assemblages is abundant (50-75%) bottle green glauconite pellets, with common (15-25%) yellow-brown green glauconite pellets.

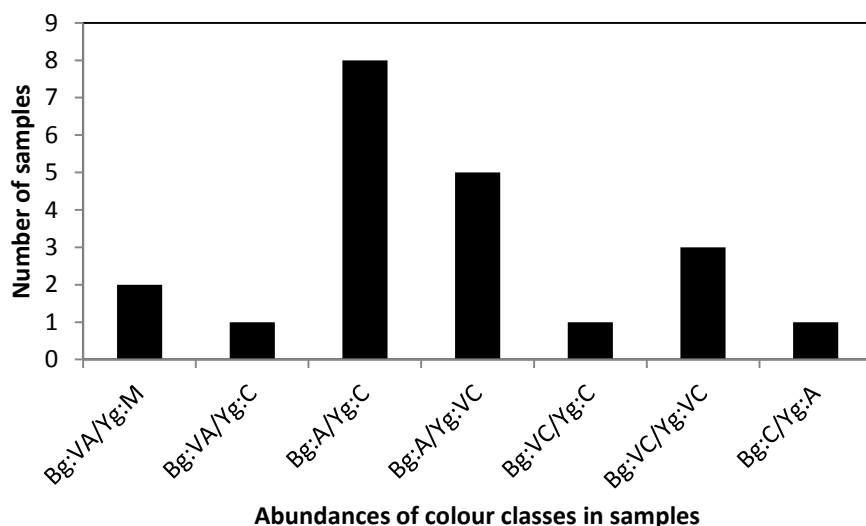


Figure 6.6: Spread of the abundance of colour assemblages within all 21 glauconite thin sections from central Chatham Rise (Bg = bottle green, increases to the left; Yg = yellow-green, increases to the right) (abundance notations defined in Table 6.2).

Other colour variants of the glauconite on central Chatham include limonitised grains (Figure 6.7A and B) and opaque inclusions within the glauconite grains (Figure 6.7C and D). Their abundance in the studied thin sections is shown in Figures 6.8A and B, respectively.

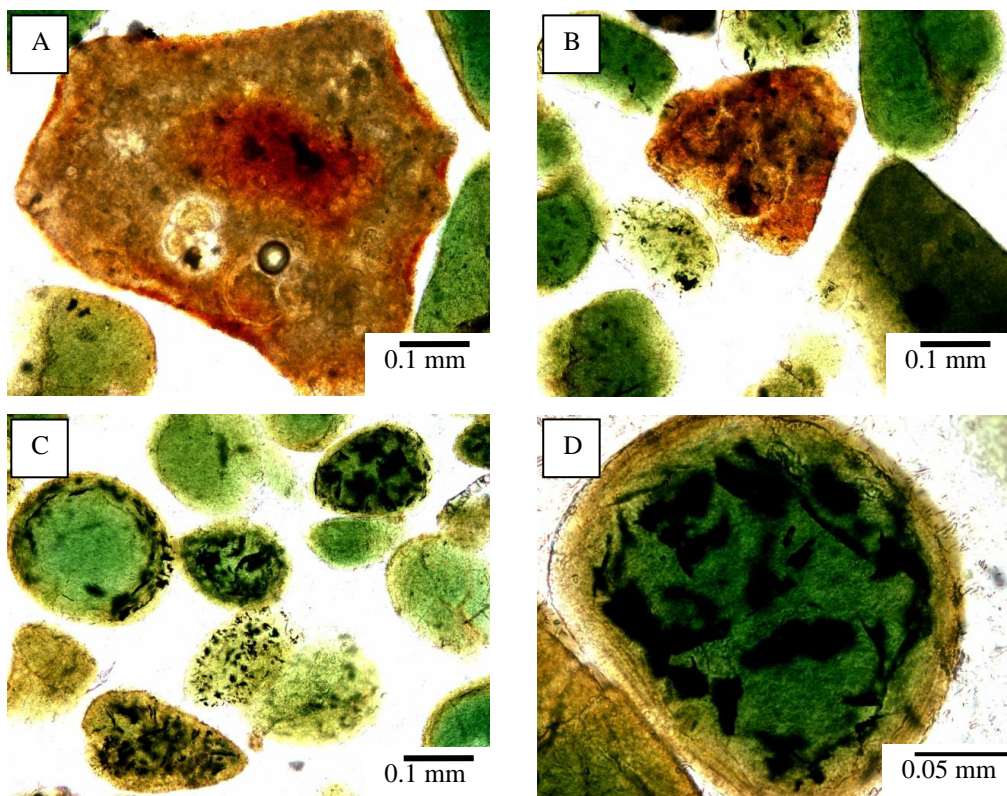


Figure 6.7: A: A892 and B: U6866 10-13 cm: Photomicrographs of limonitised grain. C: U6866 2-4 cm and D: G36: Photomicrographs of opaque inclusions within glauconite pellets.

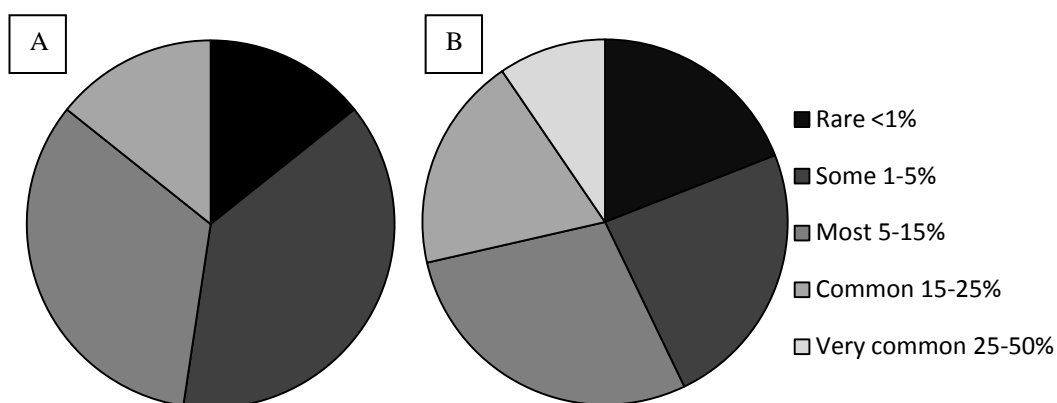


Figure 6.8: Average abundance of limonitised glauconite grains (A) and glauconite with opaque inclusions (B) across all 21 glauconite thin sections from central Chatham Rise.

Limonitised glauconite grains typically occur in 1-15% of samples (Figure 6.8A), and form due to oxidation of the iron in glauconite to rusty red-brown limonite (McRae, 1972). Opaque inclusions have developed within 5-20% of glauconite grains (e.g. Figure 6.8B) and are typically either pyrite or iron oxides (McRae, 1972). Reflected light microscopy reveals a sparkly gold colour so that the opaque inclusions in the Chatham glauconites are pyrite.

6.5 SIZE

As previously reported by others (Norris, 1964; Bell & Goodell, 1967; von Rad & Rösch, 1984) the typical size of the glauconite pellets on central Chatham Rise is medium to fine sand size (0.5-0.125 mm). My microscope measurements show that the average glauconite pellet size is typically of fine sand size, with the majority of pellets being about 0.2 mm size (Figure 6.9). The minimum size of glauconite pellets av. 0.05 mm (coarse silt), but ranges from 0.025 to 0.1 mm (medium silt to very fine sand) (Figure 6.9B). The maximum size av. 0.55 mm (coarse sand) and ranges from 0.3 to 2.7 mm (medium sand to grit/granule) (Figure 6.9C). The largest glauconite grains represent the glauconitised phosphatic grains noted in Table 6.1 and shown in Figure 6.1D, and also the replacement rims about PO_4 clasts shown in Figure 6.1C.

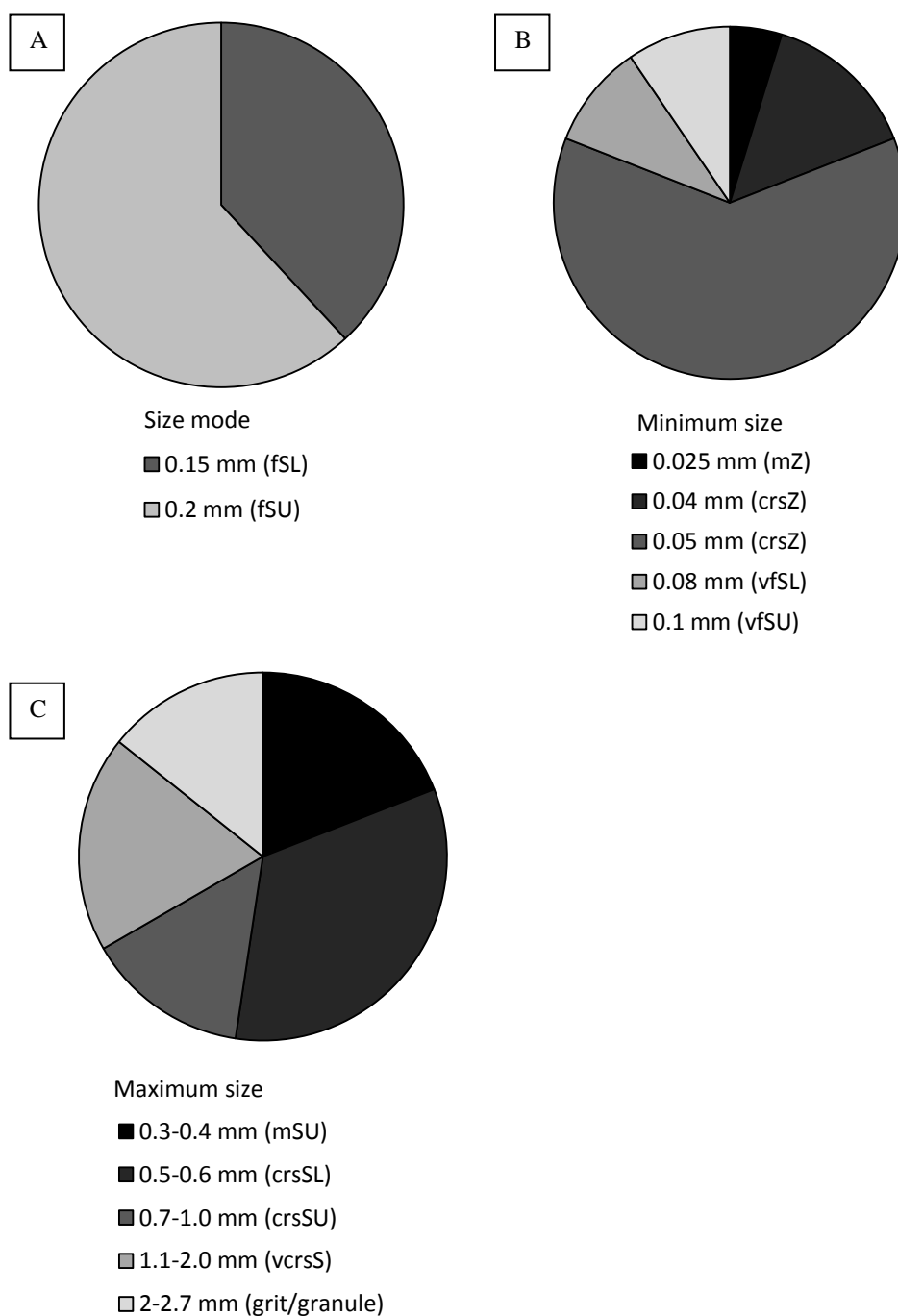


Figure 6.9: Abundance of size modes (A), minimum sizes (B) and maximum sizes (C) of the glauconite pellets within the 21 glauconite thin sections from central Chatham Rise (Z=silt, S=sand, f=fine, m=medium, c=coarse, v=very, U=upper, L=lower).

6.6 MORPHOLOGY

Binocular, petrographic, and scanning electron microscopy (SEM) have been used to describe the many different types of glauconite morphologies occurring on central Chatham Rise. The outcome is summarised in Table 6.4 and the estimated abundance of the morphological types in Figure 6.10.

Table 6.4: Morphological varieties of glauconite occurring on central Chatham Rise.

Morphology	Description
Ovoidal/ spheroidal	Smooth round pellets with no evidence of breakage, although some small surface cracks may be present. These grains are typically c.0.2 mm in size and are very common.
Lobate	Popcorn-shaped irregular grains of any size, comprising rounded lobes separated by deep radial expansion or desiccation cracks that are typically infilled with white crystalline material. These grains are common.
Composite	Large grains, typically 0.6-2 mm size, composed of a mixture of glauconite and other minerals set in a pale green glauconitic matrix (i.e. glauconitised phosphatic grains).
Fossil cast and internal molds	Grains which mimic the internal and/or external features and shape of skeletal grains such as foraminifera.
Tabular/ discoidal	Very rare grains which are flattened elongated discs or bowl shaped.
Pigmentary	Glauconite appearing as small spots on the surface of detrital grains, as coatings, or in cracks and along cleavages.
Glauconite in rock fragments	Glauconite pellets that are contained within rock fragments.

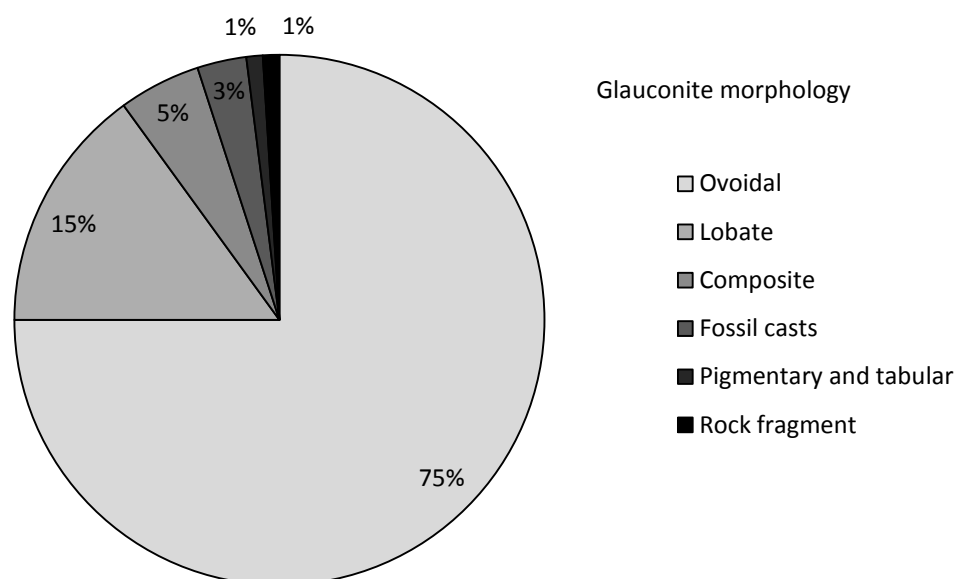


Figure 6.10: Estimate of the abundance of the different morphological types of glauconite on central Chatham Rise.

6.6.1 Ovoidal

By far the dominant morphology of the glauconite on central Chatham Rise is ovoidal varieties (Figure 6.11), forming >75% of the glauconite in the analysed samples (Figure 6.10). These grains are extremely well rounded grains with a smooth polished surface (Figure 6.11B), indicative of reworking.

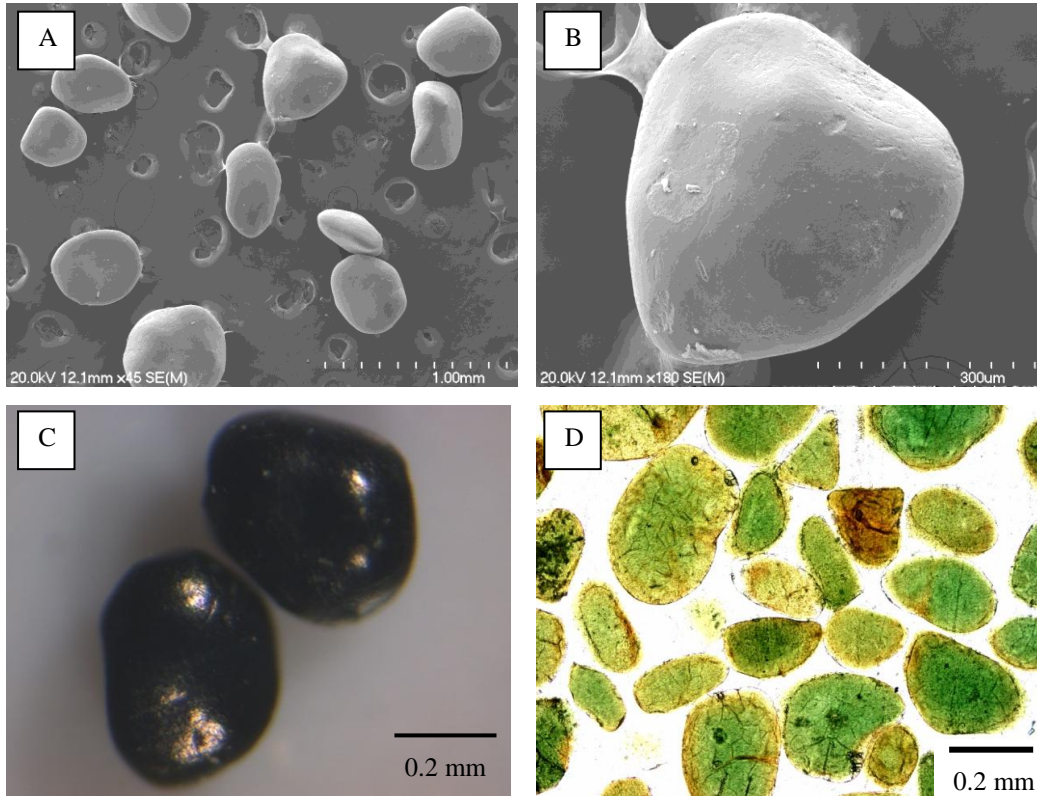


Figure 6.11: Glauconite showing ovoidal morphologies. A and B (A891): SEM images of ovoidal glauconite with distinct round shapes. C (A891): Ovoidal glauconite showing the smooth surface polish. D (G135): Thin section photomicrograph of ovoidal glauconite.

6.6.2 Lobate

The next most common morphological type is lobate glauconite, av. about 15% in samples (Figure 6.10). It is characterised by radial cracks which taper inwards and are often triangular in cross-section and filled with white crystalline material. Examples of the lobate glauconite morphologies in thin section, detrital grains and under SEM are shown in Figure 6.12. The abundance of lobate glauconite in the 21 glauconite thin sections, based on the occurrence of expansion cracks, is plotted in Figure 6.13. It shows that the majority of samples contain 5-15% lobate glauconite, followed closely by the next major occurrence at 15-25%.

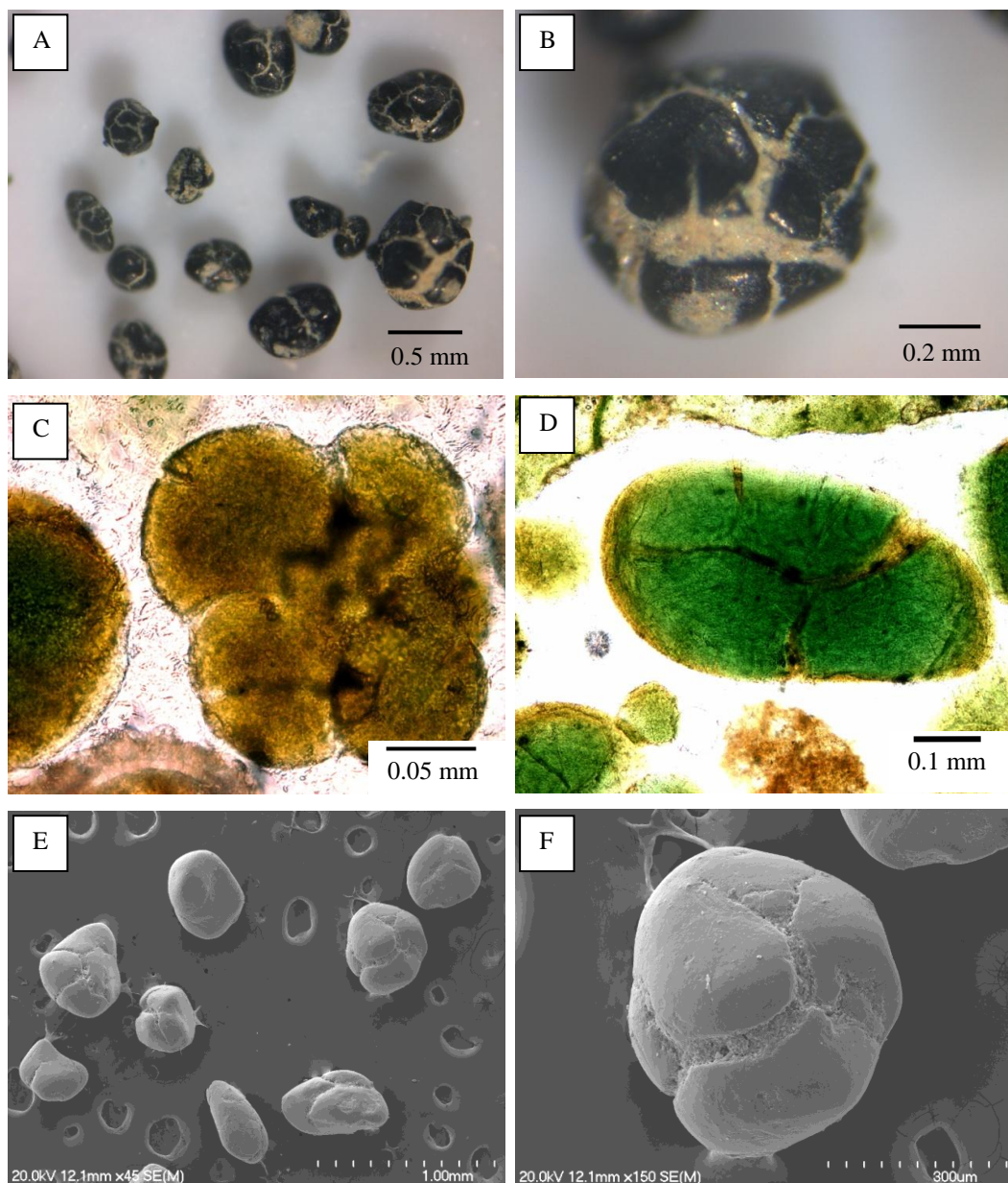


Figure 6.12: Glauconite showing lobate morphologies. A and B (Q325): Lobate glauconite showing the distinctive deep radial cracks infilled with white crystalline material. C (C606): Thin section photomicrograph of lobate glauconite. D (Q325): Thin section photomicrograph of lobate glauconite showing triangular expansion cracks. E and F (A891): SEM images of lobate glauconite with typical deep radial expansion cracks.

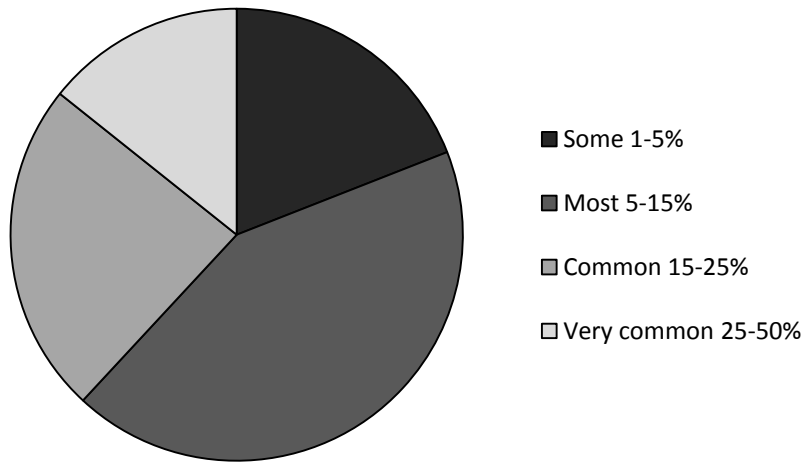


Figure 6.13: Average abundance of lobate glauconite based on the occurrence of expansion cracks in glauconite pellets across all 21 glauconite thin sections from central Chatham Rise.

Under SEM the white crystalline material infilling the expansion cracks of the lobate glauconite is predominantly (>90%) made up of coccolith plates and debris, as well as foraminiferal and other fine skeletal remains cemented together by microcrystalline calcite (Figure 6.14). McRae (1972) suggested that the cracks within lobate glauconite may have formed due to expansion of the pellet itself during mineral growth so that the cracks would develop radially and taper inwards, or alternatively from partial desiccation.

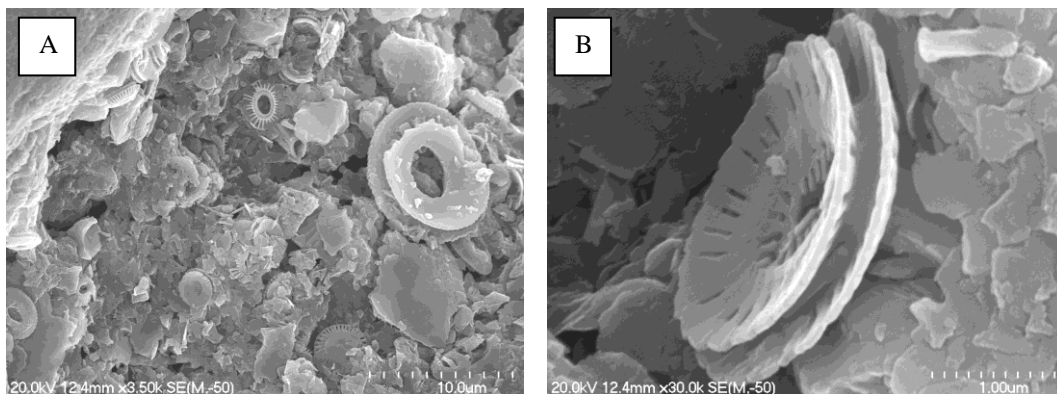


Figure 6.14: SEM images of sample A891. A and B: high powdered images of cracks which have been infilled with a white crystalline material, showing that the main constituent of the white material is coccoliths and coccolith debris.

6.6.3 Composite

The third type of morphology occurring on central Chatham Rise is composite glauconite (Figure 6.15 and Table 6.4). The grains are large (0.6-2 mm) and I have put one of the types of glauconite noted in Table 6.1 within this class:

glaucanitised phosphatic grains. An example of a composite grain is shown in the photomicrograph in Figure 6.1D. Figure 6.14 illustrates that the composite morphology (i.e. glaucanitised phosphatic grains) typically forms 1-5% of the glaucanite morphologies within all 21 thin sections on central Chatham Rise.

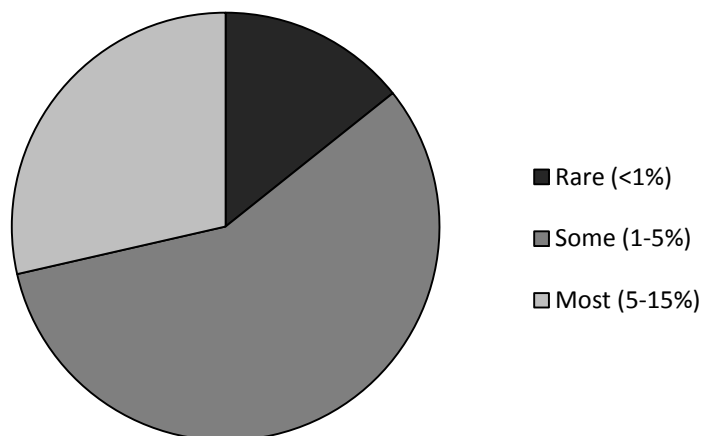


Figure 6.15: Average abundance of composite glaucanite i.e. glaucanitised phosphatic grains, across all 21 glaucanite thin sections from central Chatham Rise.

6.6.4 Fossil casts and internal molds

The fourth type of glaucanite morphology on central Chatham Rise is fossil casts and internal molds. Glaucanite infilled fossil casts and internal molds are grains which mimic the internal and/or external features and shape of skeletal grains, typically foraminifera (Table 6.4). An example is illustrated in Figure 6.1B, which shows a light yellow brown glaucanite inside foraminiferal chambers, i.e. an internal mold. The abundance of glaucanite as fossil casts and internal molds is relatively low, with the majority of samples containing <1%, followed closely by 1-5% abundance (Figure 6.16).

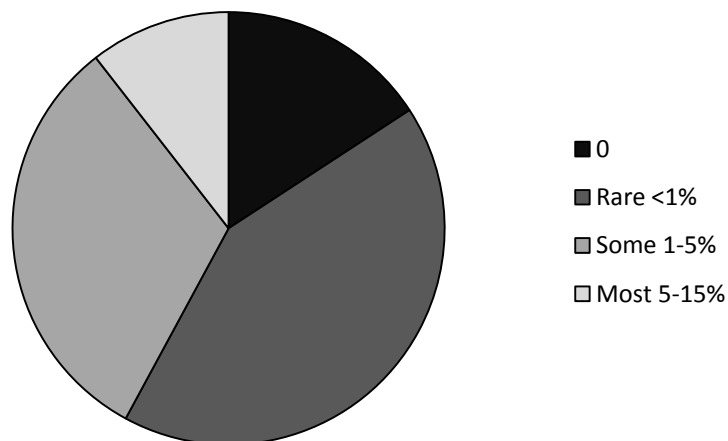


Figure 6.16: Average abundance of glaucanite infilled skeletal grains across all 21 analysed glaucanite thin sections from central Chatham Rise.

6.6.5 Glauconite pellets within rock fragments

Glauconite pellets within rock fragments form only c.1% of the glauconite varieties on central Chatham Rise. As shown in Figure 6.17, these grains are typically not present within samples, but several contain at least 1%. An example of glauconite pellets within a rock fragment is given in Figure 6.1E.

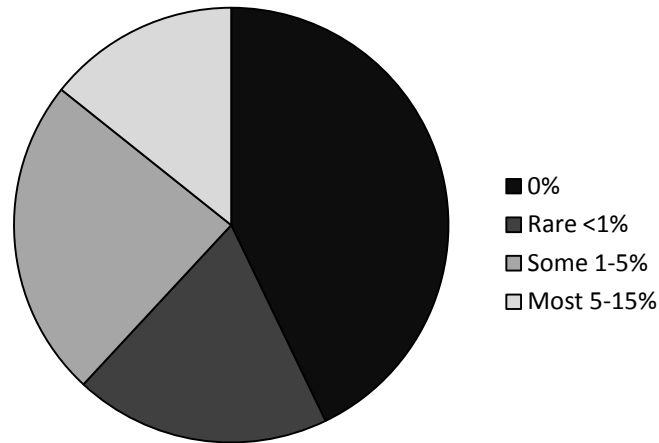


Figure 6.17: Average abundance of glauconite pellets within rock fragments across all 21 analysed glauconite thin sections from central Chatham Rise.

6.6.6 Tabular/discoidal and pigmentary

Tabular/discoidal and pigmentary grains of glauconite are very rare in samples from central Chatham Rise. An example of a tabular/discoidal glauconite grain is shown in Figure 6.18.

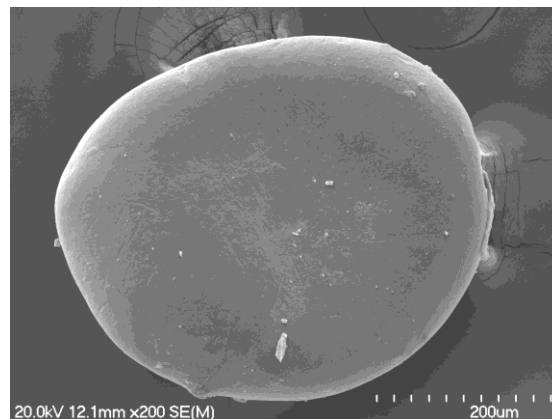


Figure 6.18: SEM image of a tabular/discoidal glauconite grain (Q325).

Pigmentary grains in the central Chatham Rise glauconites are recognised mainly as glauconite coatings on phosphorite nodules (av. 4-6 cm) (von Rad & Rösch, 1984), and therefore were mainly not seen in the sand thin sections. However, some phosphorite nodules with glauconite rims were slabbed in an investigation

carried out by Nelson (2011) (Figure 6.19A and B) and analysed under the binocular microscope in the present study. Some were also made into thin sections and analysed under a petrographic microscope (Nelson, 2001) (Figure 6.19C to F).

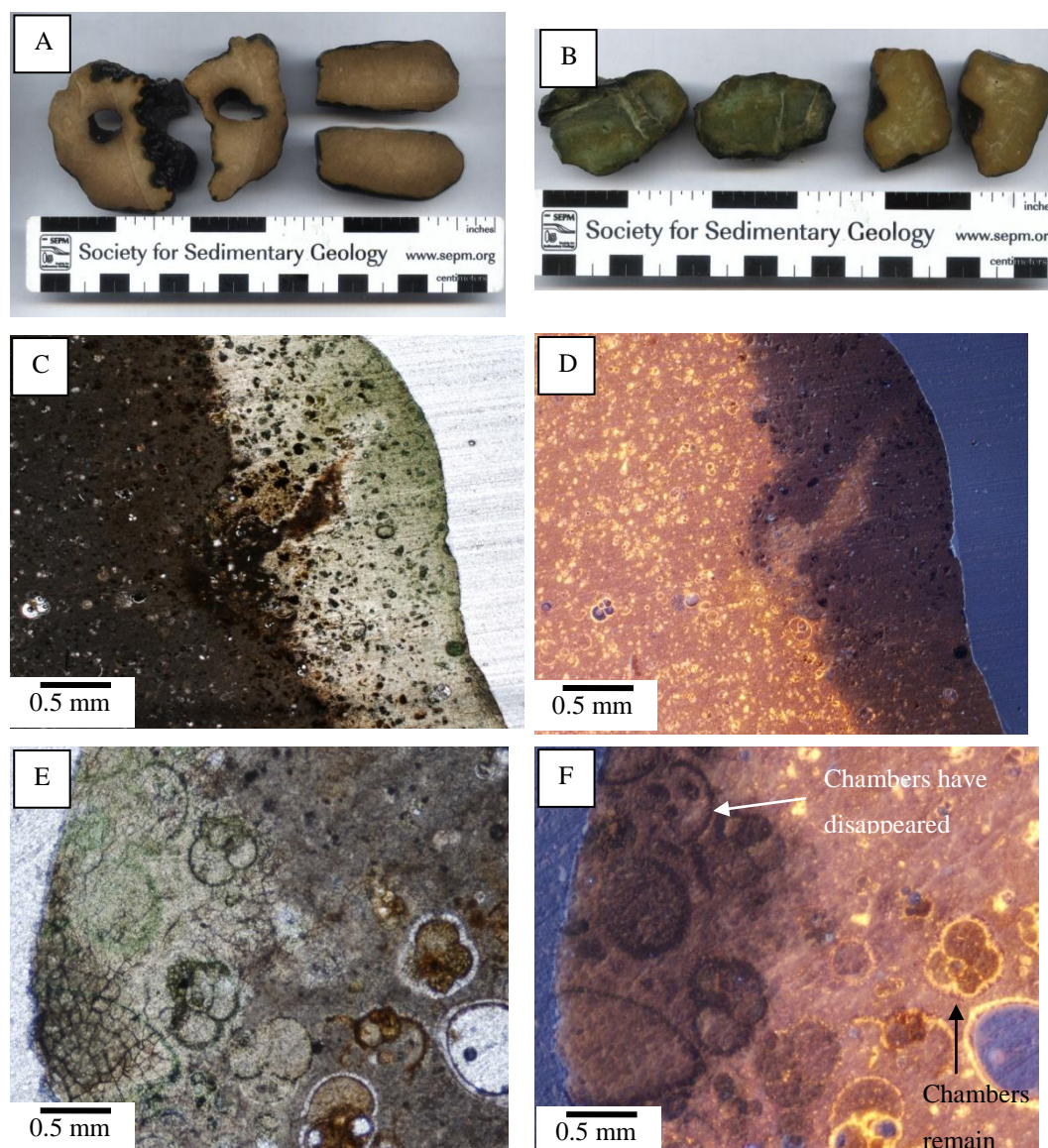


Figure 6.19: A (stn 36 sample J11b) and B (Stn 48 sample J20B): Cross-section photos of pigmentary glauconite rims on slabbed phosphorite nodules. C (PPL) and D (CL), and E (PPL) and F (CL): Photomicrographs representing a cross-section of pigmentary glauconite rims on phosphorite nodules (Nelson, 2011).

The analyses prove that the black rim occurring about many of the phosphorite nodules is in fact glauconite. The rims are not always continuous and some rims are much more apparent than others. Glauconite can also begin to pervade into the clast so that glauconitisation can turn the inside of the phosphorite grain into a slight green colour and thus change the overall geochemistry (Figure 6.19A to D). Glauconite is common inside the foraminifera inside the rim, but also sometimes within the phosphate grain itself. The calcite foraminiferal chambers still mostly

remain, but sometimes even these chambers have been completely glauconitised leaving only the shape of the original foraminiferal grain and no calcite. This is demonstrated when looking at a sample under PPL (Figure 6.19E) and then under CL (Figure 6.19F), where under CL calcite is represented by a bright orange colour and the glauconite shows a darker green-brown colour.

6.6.7 Shape

Although not strictly a morphology, I have included the general shape classes of the glauconite grains within this section (Figure 6.20). This shows that the glauconite grains on central Chatham Rise have an even proportion between subrounded to subangular, and subrounded to rounded. The preponderance of subrounded shapes is anticipated from the abundance of ovoidal glauconite morphologies on central Chatham Rise.

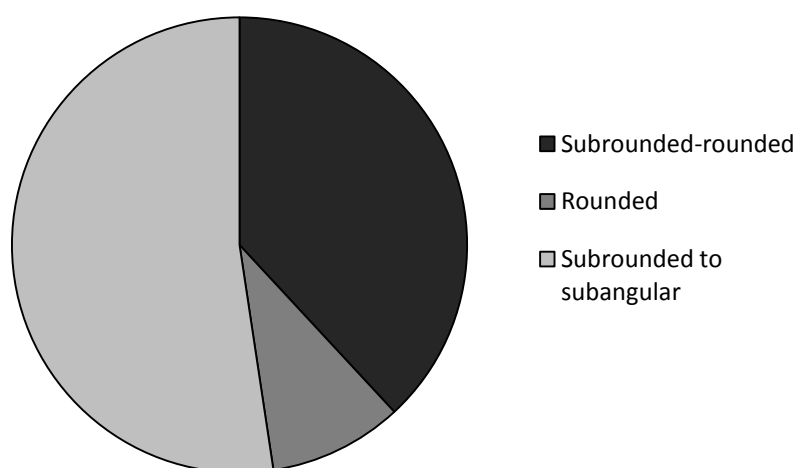


Figure 6.20: Average abundance of glauconite pelletal shapes across all 21 analysed glauconite thin sections from central Chatham Rise.

6.7 INTERNAL FABRICS

Three main internal fabrics characterise the glauconite grains from central Chatham Rise (Figure 6.21). Their abundance across the analysed samples is shown in a pie diagram (Figure 6.22).

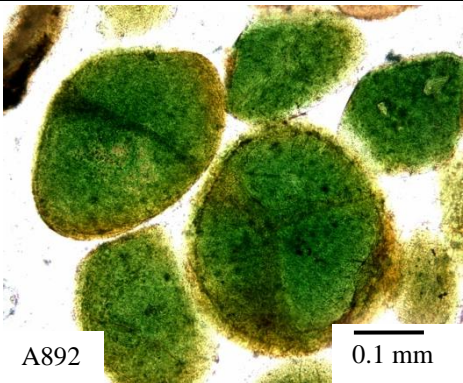
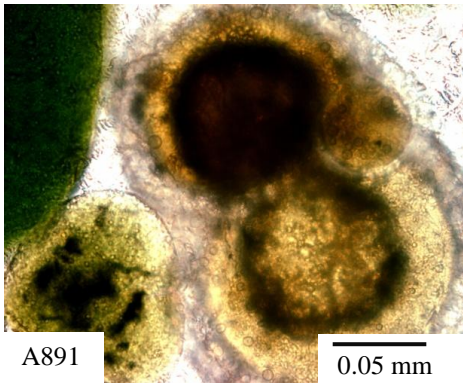
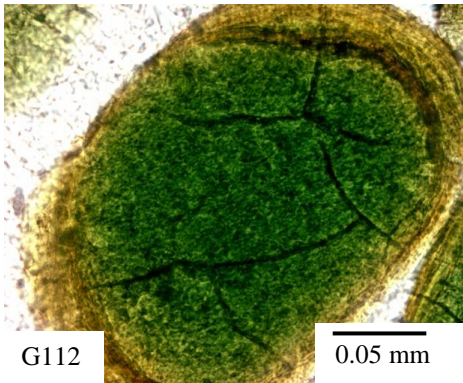
Rx = Random microcrystalline (most common)	An aggregate texture, where homogenous extremely small micaceous crystals overlap with no preferred orientation.	 A892 0.1 mm
Sk = Skeletal infilled grains	These grains reflect the internal structure of the skeletal grain they have infilled, and may show fibrous, lamellar or perforate structures.	 A891 0.05 mm
Fr = Oriented fibroradiating rims	Pellets that have oriented fibroradiating rims which are typically brown, with a higher birefringence than the core of the grain, and exhibit wavy extinction.	 G112 0.05 mm

Figure 6.21: The three types of internal fabrics within glauconites on central Chatham Rise.

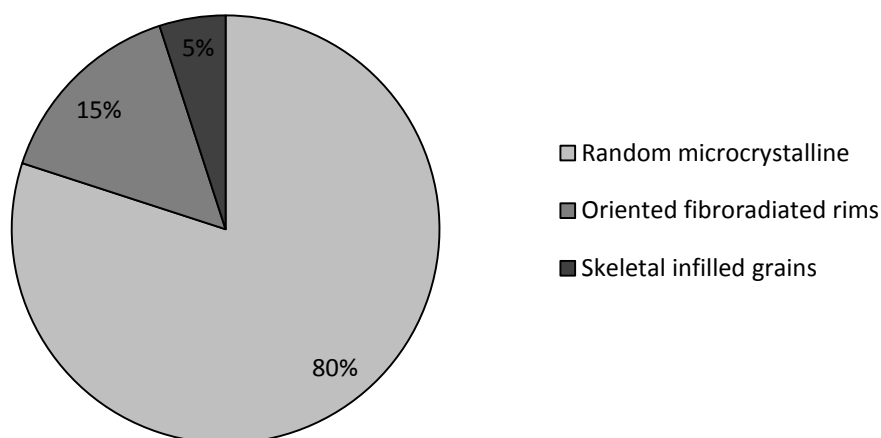


Figure 6.22: Average abundance (%) of various types of internal fabrics within the glauconite grain across all 21 analysed thin sections from central Chatham Rise.

6.7.1 Random microcrystalline

Random microcrystalline grains are by far the most common internal fabric of the glauconites on central Chatham Rise (Table 6.3 and Figure 6.22). The tiny micaceous crystals overlap with no preferred orientation so that a mottled extinction is evident under cross-polarised light. This is the most common internal texture of the mineral glauconite generally (Triplehorn, 1966; McRae, 1972; McConchie, 1978).

6.7.2 Oriented fibroradiating rims

Oriented fibroradiating rims occur within all the 21 analysed thin sections from central Chatham Rise, where they typically occur at 5-15% of the time within samples, followed closely by 15-25% of the time (Figure 6.23). McRae (1972) and Odom (1976) describe these rims as having an oriented fabric, which is somewhat parallel but is wavy in its extinction. They point out that the rims are typically brown in colour and exhibit a much higher birefringence than the inner core, which is also what is observed in the glauconite on central Chatham Rise. The rims on the glauconite pellets of the Rise do not always occur as a complete rim around the grain, as they are also found partially surrounding the grain, as cracks within the grain and in patches, which is consistent with the typical fibroradiated rims described by Odom (1976).

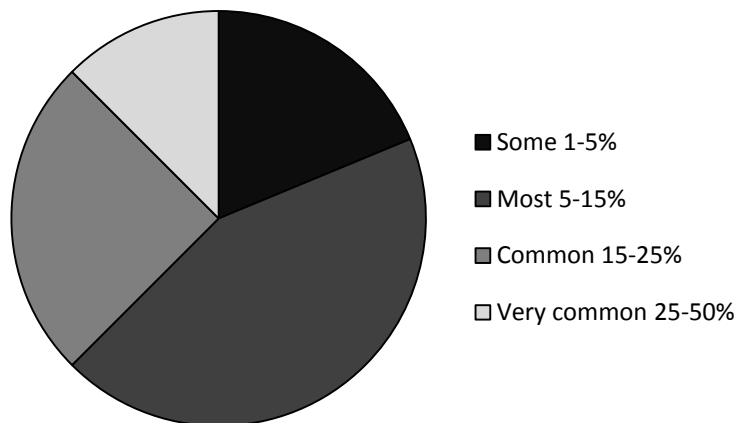


Figure 6.23: Average abundance of oriented fibroradiated rims on glauconite grains across all 21 analysed glauconite thin sections from central Chatham Rise.

6.7.3 Skeletal infilled grains

The abundance of skeletal infilled grains in the 21 glauconite thin sections is plotted in Figure 6.24. The majority of these samples contain 1-5% skeletal infilled grains, followed closely by <1%.

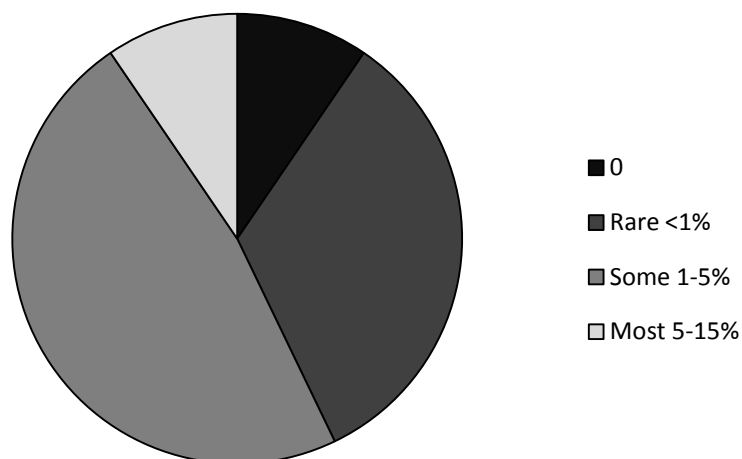


Figure 6.24: Average abundance of skeletal infilled grains in glauconite grains across all 21 analysed glauconite thin sections from central Chatham Rise.

Chapter 7

MINERALOGY OF GLAUCONITE

7.1 INTRODUCTION

Investigating the mineralogy of glauconite on central Chatham Rise is vital to its classification, and can also be used to determine how the glauconite may have formed. The main technique used to classify the mineralogy of glauconite is X-ray diffraction (XRD), a technique based on the unique reflection angles of different minerals. The reflection angle is used to calculate the interplanar spacings (d) in angstroms (\AA).

This chapter fully documents the mineralogy of the glauconite on central Chatham Rise, predominantly based on the classification scheme proposed by Burst (1958) and others (Section 5.5). The mineralogical classification of the glauconite is fundamental to gaining a better understanding of its nature, origin and economic potential.

To date little work has been carried out on the mineralogy of the glauconite on central Chatham Rise, with only one study aiming to classify the glauconite using XRD. This study was undertaken by Bell and Goodell (1967) where they suggested that the glauconite has very little crystallographic structure and is composed of poorly crystallised illite (peak at approximately 10\AA). They also suggested that there is no genetic relationship between the glauconite and clay fraction of the Chatham Rise sediments, due to the large crystallographic differences.

7.2 METHODS

The mineralogy of the glauconite was analysed using a Philips X'Pert X-Ray Diffraction machine (XRD), with X'Pert Highscore computer software at The University of Waikato. Sample numbers mentioned in this chapter are located in Figure 3.1.

Samples were scanned using XRD to classify the mineralogical glauconite class, i.e. ordered, disordered, interlayered or mixed-layer glauconite (Section 5.5), and also to discover the nature and percentage of expandable layers (Burst, 1958; McConchie, 1978; Hume & Nelson, 1982). A three step XRD method was used based on work carried out by McConchie (1978) and others (Hume & Nelson, 1982; Compton, 1989), which is described below.

34 glauconite concentrates were powdered in a tungsten carbide ring mill (see Appendix IV for sample numbers analysed). Note that samples numbered U6866 involve the downcore analysis of several samples at roughly 2 cm intervals, which nevertheless revealed essentially no differences. Approximately 10 mg of the powdered glauconite concentrates were pipetted onto glass slides and left to settle and dry for 3-4 hours to yield an oriented sample mount. Samples were then run through the XRD machine at configuration 2, being scanned from 2-42° 2 θ angle with a 0.03 step size and 1.0 step time, and a scan rate of 1.8° 2 θ /min. Following the air dried scans, the oriented sample mounts were placed in a desiccator containing ethylene glycol for 12 hours. After glycolation the samples were rescanned by XRD using configuration 2 and settings 2-15° 2 θ , 0.02 step size and 1.0 step time, a slightly slower scan rate over a shorter ° 2 θ interval compared to the air-dried mounts. Lastly, XRD scans were then made of the sample mounts following heating in a furnace at 450°C for 1 hour using the same settings as for the glycolated scans (Hower, 1961; McConchie, 1978; Hume & Nelson, 1982; Compton, 1989; Kriaa *et al.*, 2009). Samples are glycolated and heated in order to determine the movement and height of the 10Å peak, which enables the calculation of the expandable smectite layers present in the glauconite concentrates (McConchie, 1978; Kriaa *et al.*, 2009).

All glauconite scans from all samples and treatments are contained in Appendix IV.

7.3 X-RAY DIFFRACTION (XRD) ANALYSIS

The XRD scans showed that the general peak patterns were similar for all 34 samples, but there can be some subtle variations in the spread and shape of the (001) 10Å peak and the % expandables. See Appendix IV for all XRD scan results.

7.3.1 Air-dried oriented mount peak pattern

Because all 34 analysed air-dried oriented mounts yielded similar results, two samples have been selected here to display the peak patterns of the glauconite on central Chatham Rise (Figures 7.1 and 7.2).

Figures 7.1 and 7.2 show that the glauconite on central Chatham Rise is definitely glauconite, with main peaks occurring in air-dried samples at approximately 10Å, 4.5Å and 3.3Å (Compton, 1989; Kriaa *et al.*, 2009). All other peaks within the XRD scans are also attributed to glauconite, apart from the weak peak at ~7.08Å that may reflect an Fe-rich clay mineral known as berthierine, which is commonly associated with glauconite (Figure 7.2) (Udgata, 2007). Since the (001) peak occurs mostly close to 10Å rather than 14Å, this suggests that the glauconite is evolved to highly evolved glauconitic mica (Table 5.2).

All peaks are typically broad and asymmetrical (Figures 7.1 and 7.2) indicating that the glauconite is slightly disordered (1Md). This means that the glauconite must contain some expandable smectite layers (Burst, 1958; Hower, 1961; Millot, 1970; McConchie, 1978; Compton, 1989).

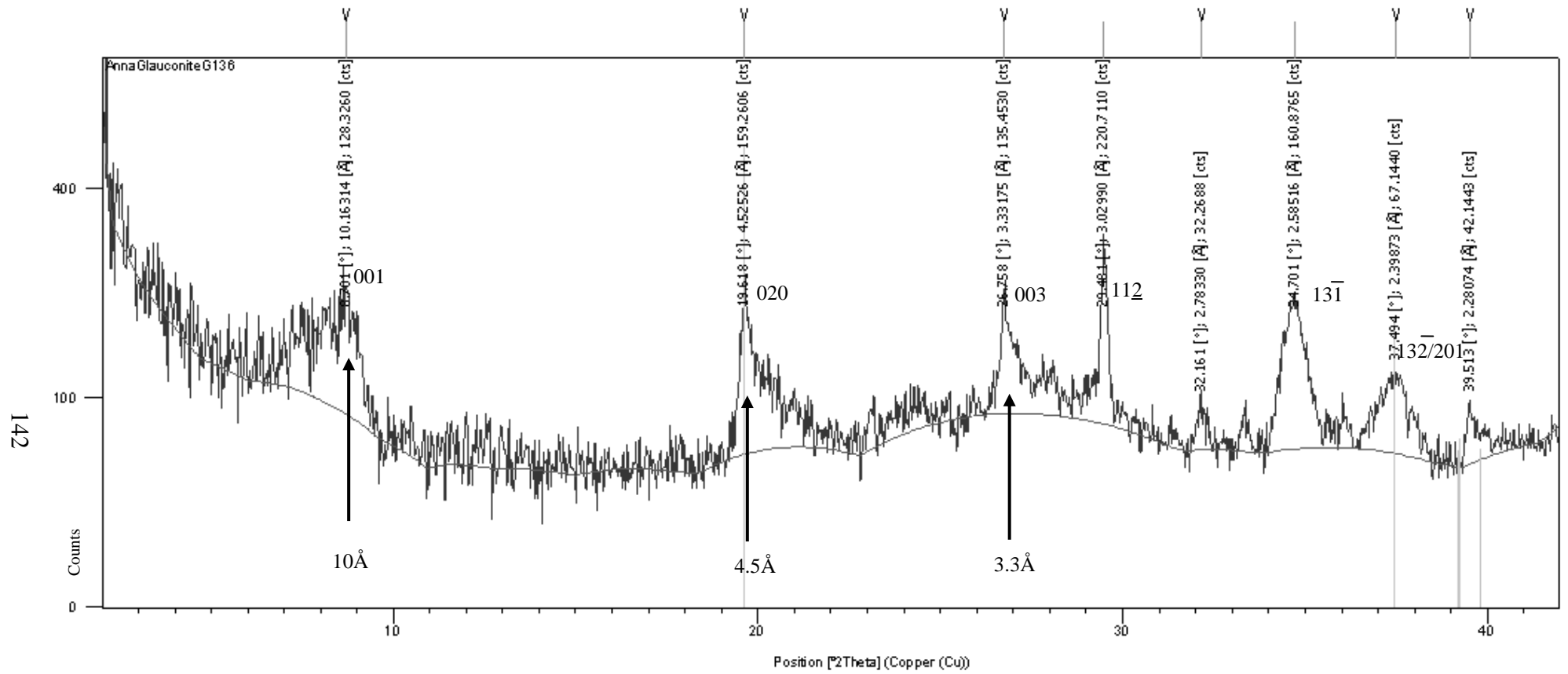


Figure 7.1: Air-dried untreated oriented mount XRD scan of glauconite concentrate from G136.

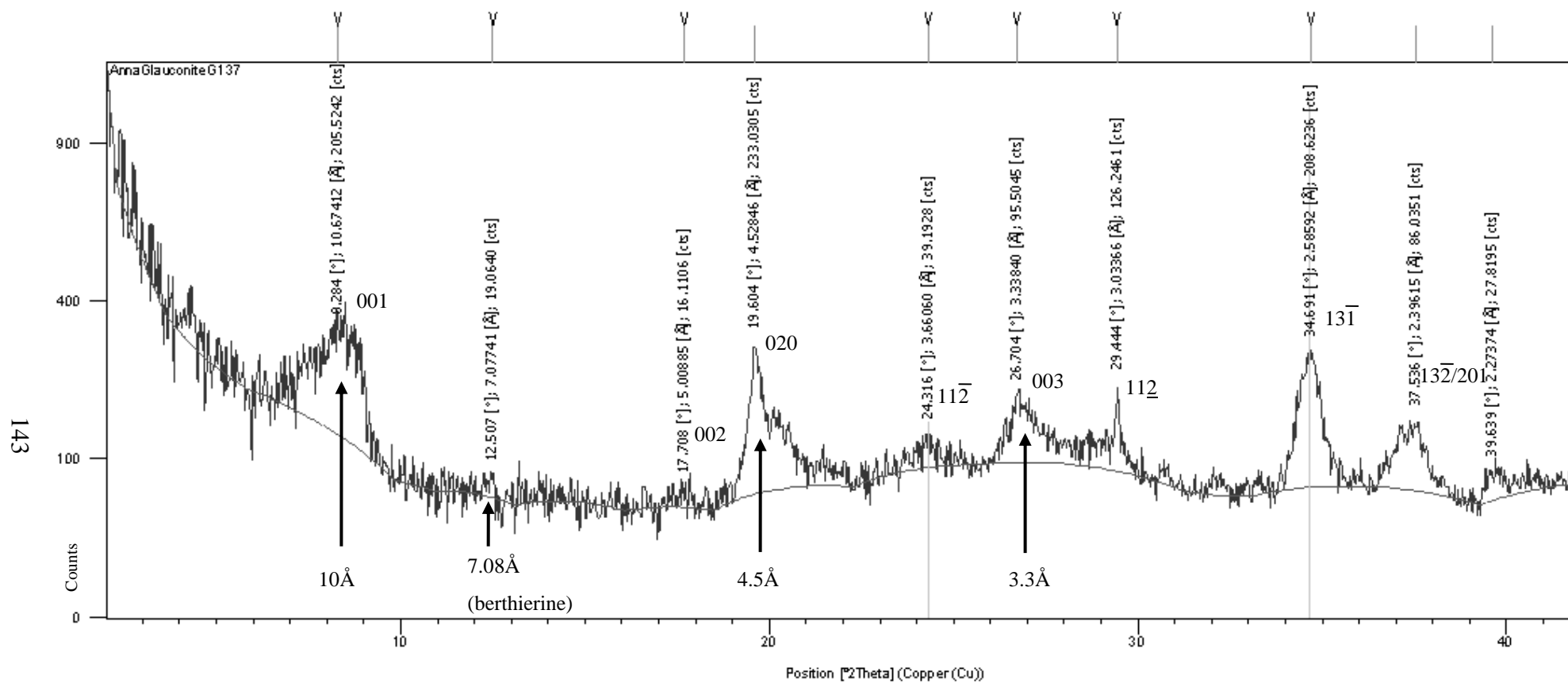


Figure 7.2: Air-dried untreated oriented mount XRD scan of glauconite concentrate from G137.

7.3.2 Expandable smectite layers

Air-dried oriented scans revealed that the glauconite on central Chatham Rise is slightly disordered (i.e. contains some expandable smectite layers). The % expandable smectite layers have been calculated in this study using two different methods. First, by substituting the K₂O wt% calculated by XRF (see Section 8.3.1) into the equation set by Compton (1989): % expandables = -7.79 x K₂O + 68.7. Second, by calculating the (001) 10Å peak spread in the glycolated XRD scans and then using Weaver's (1956) curve (see Figure 7.6).

7.3.2A Presence of expandable smectite layers

In the air-dried oriented scans the spread of the (001) peak indicates the percentage of expandable smectite layers present and also the maturity of the glauconite. High maturity relates to the 10Å glauconitic illite/mica end-member, while low maturity is represented by the 14Å glauconitic smectite end (Table 5.2). The central Chatham Rise glauconite XRD scans do not show a sharp symmetrical peak at 10Å, but rather display a definite peak at 10Å that falls off in an asymmetrical pattern towards higher Å values, ranging from 11 to 14Å (Figures 7.1 and 7.2). This (001) peak spread is summarised in Table 7.1 for the 34 analysed glauconite samples (see Appendix IV for (001) peak spreads for all samples).

Table 7.1: (001) peak spread in the 34 air-dried sample mounts determined from XRD scans.

(001) peak spread	Number of samples	Percentage
10-12Å	11	32
10-12.5Å	14	41
10-13Å	4	12
10-14Å	5	15

The (001) peak spread ranges from 10 out to 14Å, as summarised in Table 7.1. Most commonly the spread for the glauconite on central Chatham Rise is from 10-12.5Å (41% of samples) followed by slightly fewer samples (32%) showing a smaller spread from 10-12Å. This indicates that the majority of the glauconite on central Chatham Rise ranges from slightly evolved glauconitic smectite-illite to highly evolved (10Å) glauconitic illite/mica (Table 5.2). Table 7.1 further shows

that the glauconite on central Chatham Rise must be disordered due to the presence of at least some expandable smectite layers in samples, as shown by the (001) peak spread being greater than 10Å.

Another way to investigate whether glauconite contains any expandable smectite layers is to heat the oriented mounts (after glycolation) to above 450°C then immediately re-run through the XRD machine. This causes expandable layers to collapse producing a much smaller spread of the (001) peak to about 9.4-9.8Å (Weaver, 1956). Following heating, all 34 samples showed a slight decrease in the (001) spread compared to the air-dried state to 9.14-10Å. Two examples of these heated scans are shown in Figures 7.3 and 7.4. Figure 7.3 shows that the (001) peak has collapsed to 10.65Å after heating from 12.45Å in the air-dried mount of sample G136 (Figure 7.1), while sample G137 in Figure 7.4 has collapsed to 10.78 from 12.45Å (Figure 7.2). See Appendix IV for the (001) peak change between air-dried and heated sample mounts in all samples.

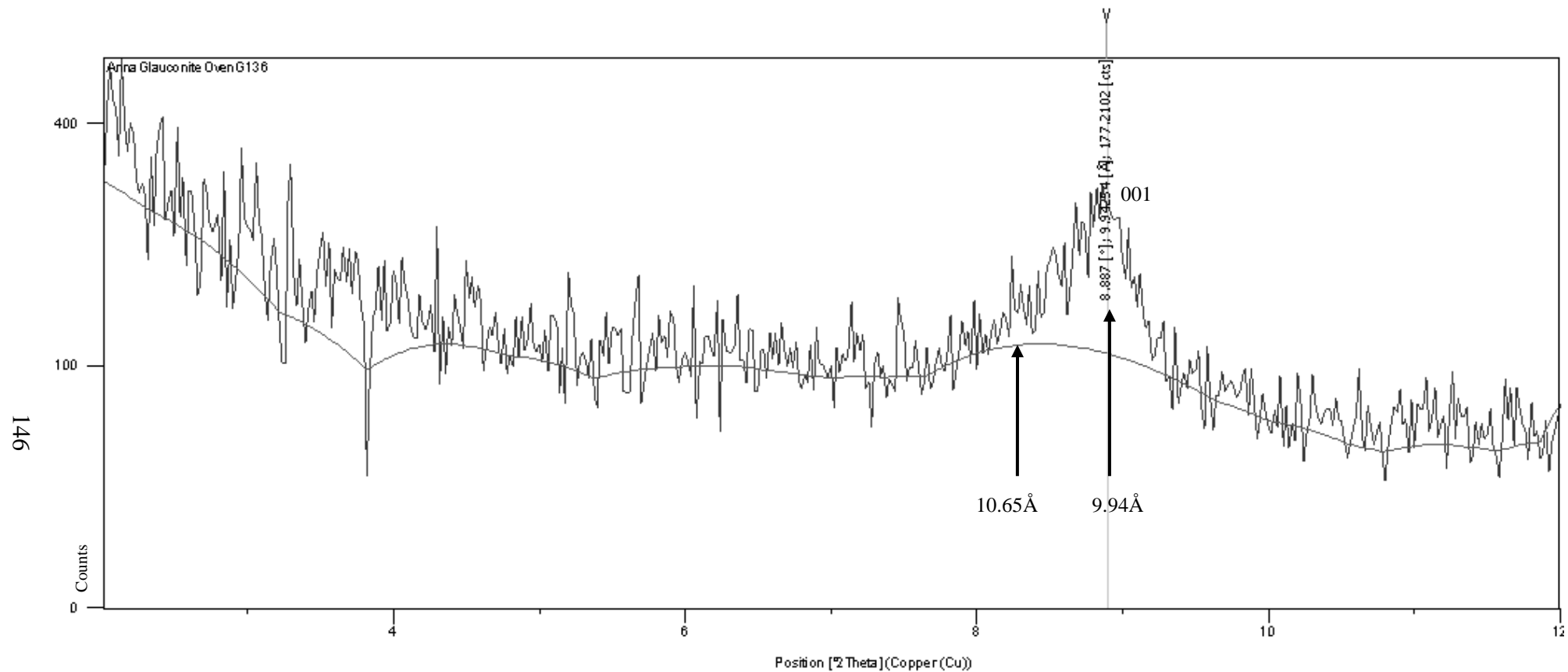


Figure 7.3: Heated oriented mount XRD scan of glauconite concentrate from G136 (cf. Figure 7.1).

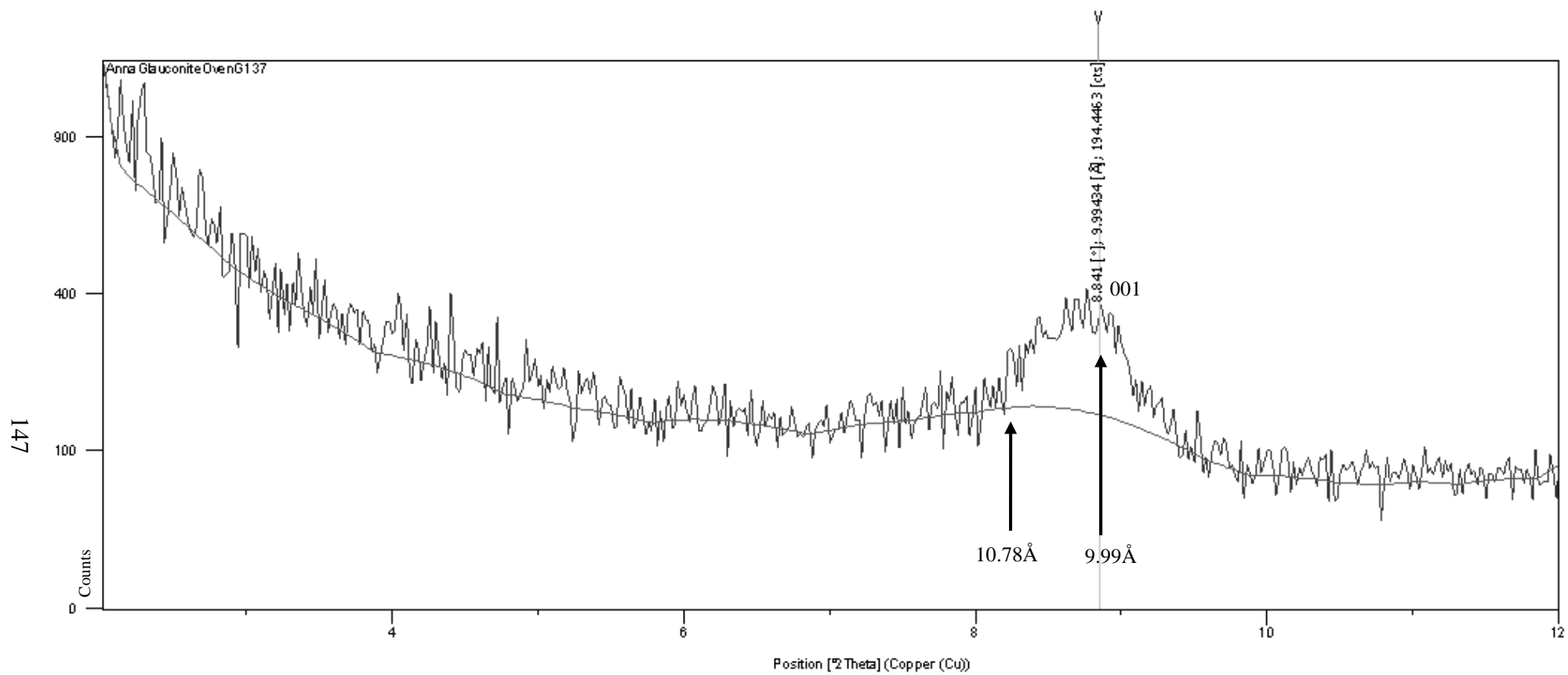


Figure 7.4: Heated oriented mount XRD scan of glauconite concentrate from G137 (cf. Figure 7.2).

7.3.2B Peak shape related to the % expandables calculated from potassium content

As noted already, there are subtle variations in the (001) peak pattern and spread between the 34 analysed air-dried samples. These variations can be directly related to the % expandable smectite layers, as calculated here using the K₂O content of samples (see Section 8.3.1 for K₂O results) (e.g. Compton, 1989). Analysis of the (001) peak shape in the Chatham glauconite traces reveals three general classes of defined (001) peak spreads that can be related to the K₂O % and therefore subsequently the % expandable smectite layers (Figure 7.5). See Appendix IV for all samples (001) peak shape classes and % expandables calculated from potassium contents.

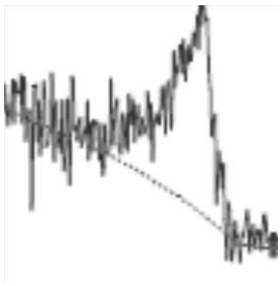
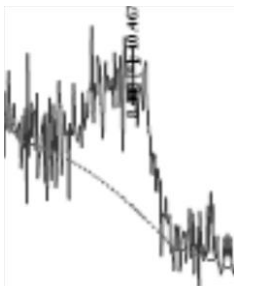
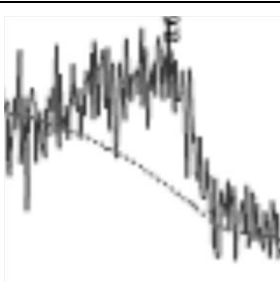
Class	(001) peak shape	Number (%) of samples	Average wt% K ₂ O content	%expandables based on K ₂ O
1: Sharp increase to the 10Å peak		8 (24%)	7.54	10
2: Two peaks at 10Å and ~12.5- 12Å		14 (41%)	7.15	13
3: Relatively flat 10Å peak		12 (35%)	6.77	16

Figure 7.5: Abundance of samples with different (001) peak shape classes, K₂O contents and % expandable smectite layers (as calculated from the potassium content).

Disordered glauconite typically contains 10-20% expandables (Burst, 1958; Hower, 1961; Compton, 1989), therefore Figure 7.5 indicates that the 34 glauconite samples from central Chatham Rise are slightly disordered due to their range of 10-20% expandable smectite layers.

It is known that the % expandable smectite layers decreases with increasing potassium content and so with increasing glauconite maturity illite layers become more dominant (Burst, 1958; Compton, 1989). This is the case for central Chatham Rise glauconites, where the potassium contents of 7-9 wt% are very high (see Section 8.3.1) while the % expandables are relatively low at 10-20% (Figure 7.5). This means that the Chatham glauconite has a high maturity and can be classed as evolved to highly evolved (cf. Table 5.2).

7.3.2C % expandables from glycolated samples

The % expandable smectite layers has also been calculated in the 34 analysed Chatham samples by comparing the (001) 10\AA spread in the glycolated samples with the curve of Weaver (1956) (Figure 7.6). Results are tabulated in Table 7.2. Three main categories of (001) peak spreads have been determined, namely 10\AA , $10\text{-}10.5\text{\AA}$ and $10\text{-}11\text{\AA}$. Figures 7.7, 7.8 and 7.9 respectively display examples of glycolated sample XRD scans for the three categories. See Appendix IV for the glycolated peak spread and the % expandables for all samples calculated using this method.

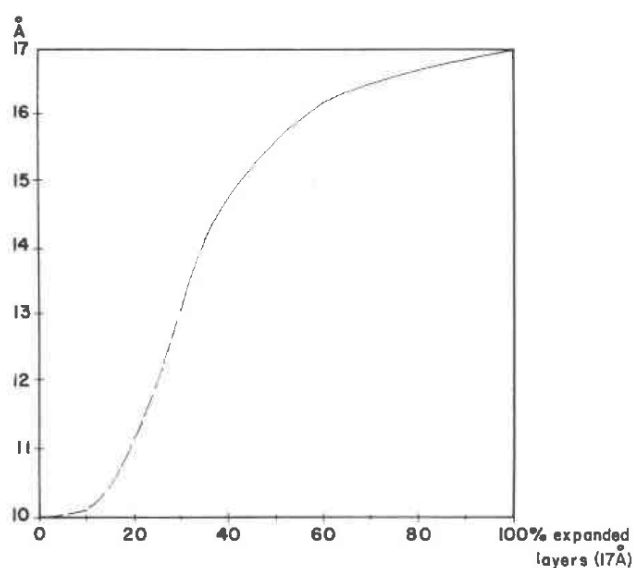


Figure 7.6: Curve for determining the % expandables based on the 10\AA spread in a glycolated sample (after Weaver, 1956).

Table 7.2: The % expandables in all 34 analysed glauconite samples based on the (001) 10Å spread in the glycolated sample, calculated from the Weaver (1956) curve displayed in Figure 7.6.

(001) 10Å spread	% of samples	% expandables
10Å	32.3	0-10
10-10.5Å	41.2	10-15
10-11Å	26.5	15-20

Calculating the % expandables in glauconite using this method (Table 7.2) reveals similar results to Compton's (1989) method (Figure 7.5), with % expandable smectite layers ranging from 0-20%. Again this shows that the glauconite on central Chatham Rise is slightly disordered and evolved. However, about 32% of samples are on the verge of being ordered glauconite, having <10% expandables, but the majority (41%) are slightly disordered having 10-15% expandable layers, and the remainder (27%) are also disordered with slightly higher expandable contents in the range 15-20% (Table 7.2).

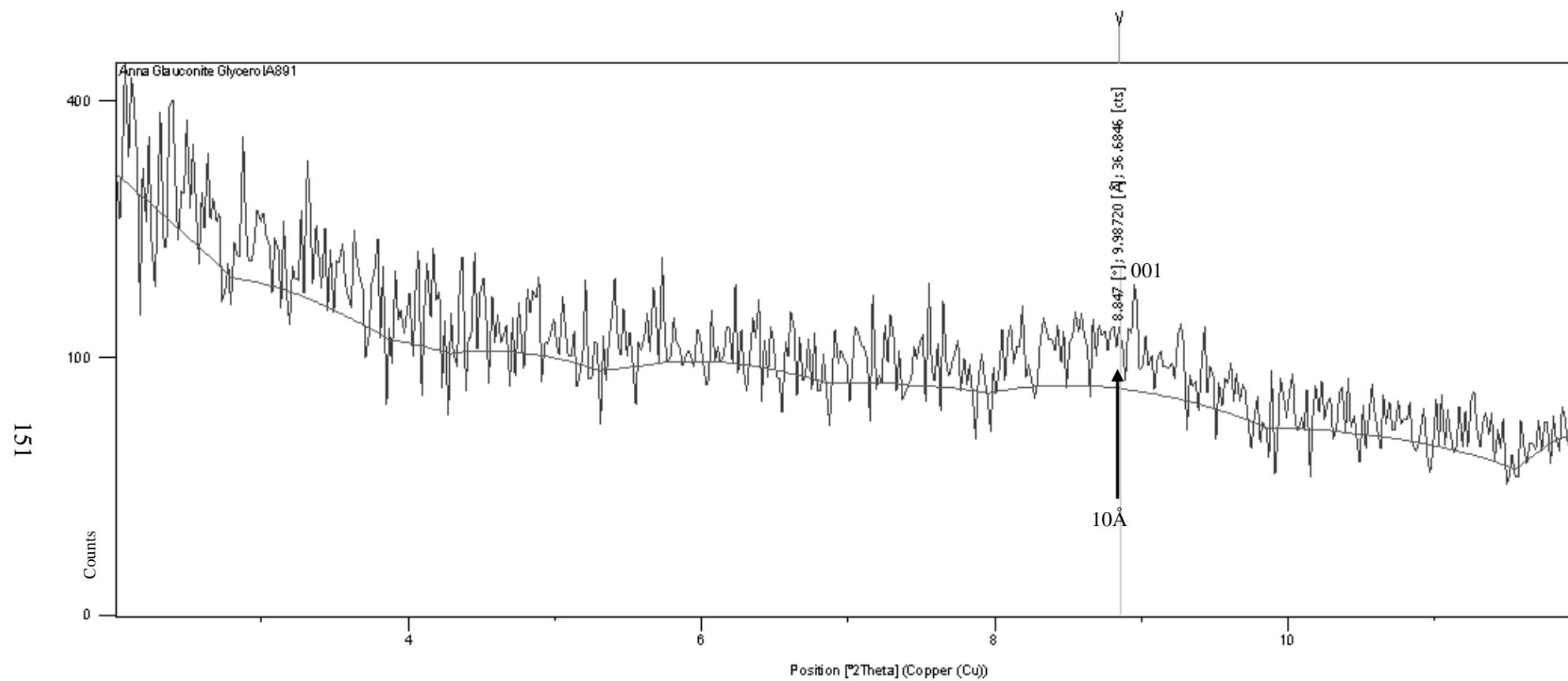


Figure 7.7: Glycolated oriented mount XRD scan of glauconite concentrate from A891 (example of 10 Å spread in Table 7.2).

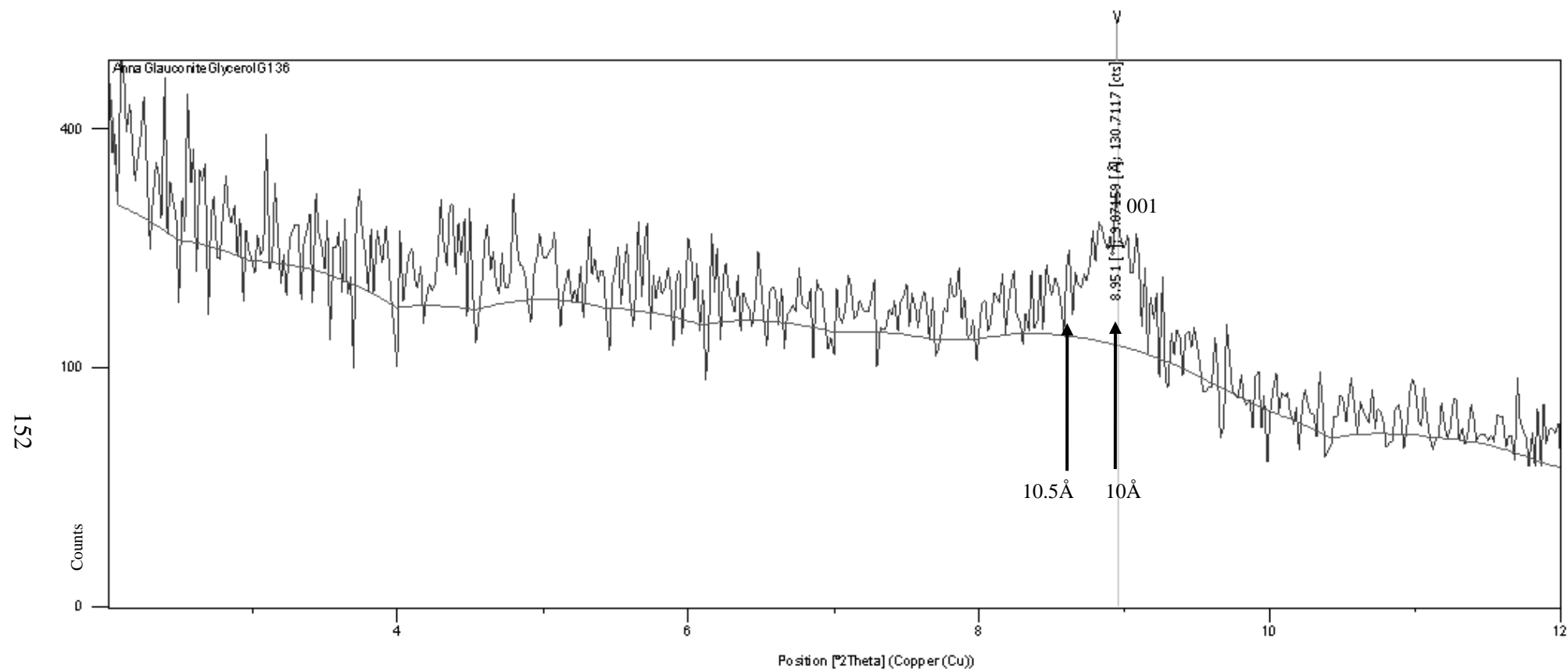


Figure 7.8: Glycolated oriented mount XRD scan of glauconite concentrate from G136 (example of 10-10.5 Å spread in Table 7.2).

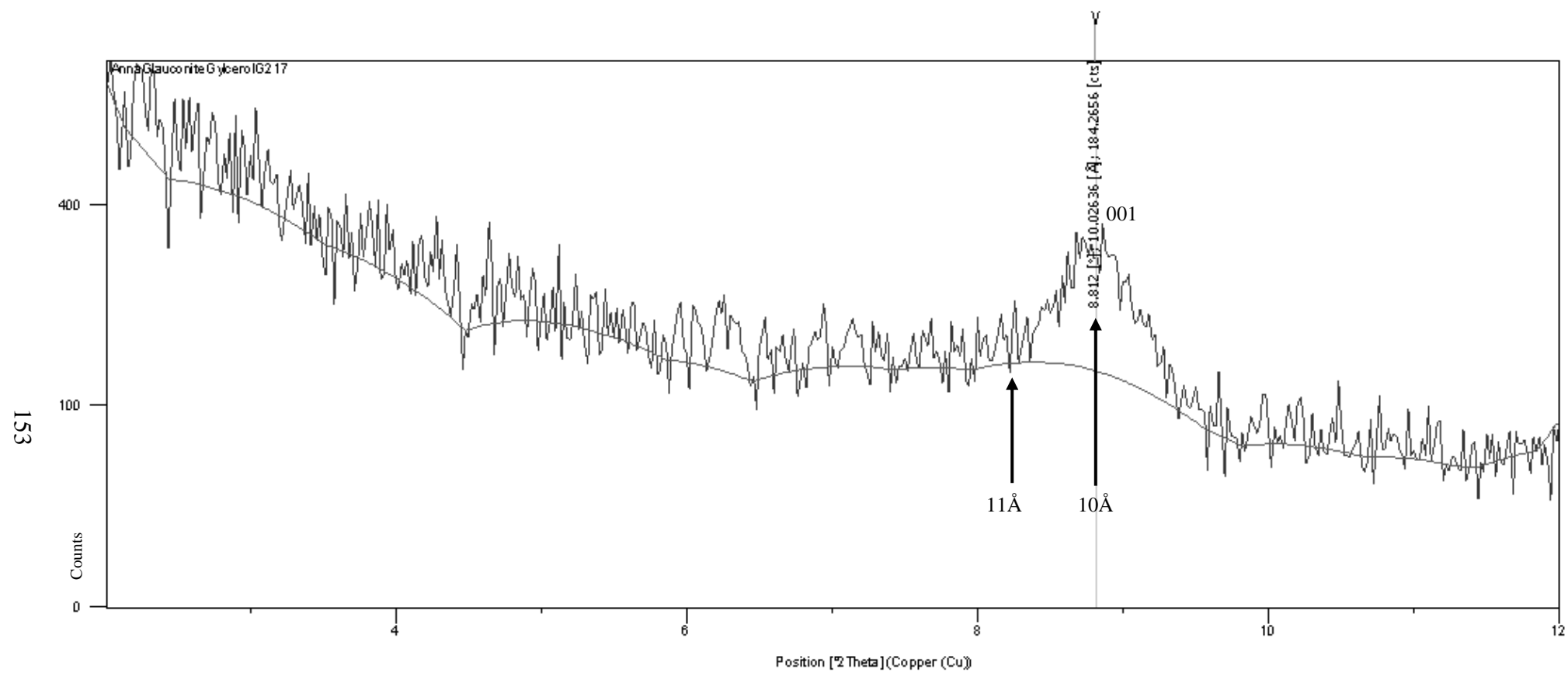


Figure 7.9: Glycolated oriented mount XRD scan of glauconite concentrate from G217 (example of 10-11 Å spread in Table 7.2).

7.3.3 Ordering and structure

As described in Section 5.6, glauconite typically has a 2:1 dioctahedral structure that is characterised by layer interstratification, where the structure is composed of potassium bearing micaceous interlayers and expandable montmorillonite/smectite layers, the amount of the latter decreasing as the potassium content increases (Burst, 1958; Hower, 1961; McRae, 1972).

Thompson and Hower (1975) have suggested that glauconite which contains 10-25% expandable smectite layers, as in the central Chatham Rise glauconites in this study, has an alleverdite-like ordering in which the 14Å smectite layers are separated by at least one 10Å illite layer. So the central Chatham Rise glauconites therefore may show an interstratified stacking in which one 14Å smectite layer is stacked between several 10Å illite layers (e.g. Figure 7.10, after J. Churchman, personal communication, November, 2011).

10Å	illite
14Å	smectite
10Å	illite
10Å	illite
14Å	smectite
10Å	illite
10Å	illite
10Å	illite

Figure 7.10: Example of an alleverdite-like ordering that may be present in the stacking in central Chatham Rise glauconites.

Chapter 8

GEOCHEMISTRY OF GLAUCONITE

8.1 INTRODUCTION

Analysing the chemical composition of glauconite is essential to its classification, and assists in identifying the various types of glauconite, their origins, and their economic potential. The geochemistry of glauconite can be determined on a bulk glauconite concentrate using XRF, or on an individual glauconite grain in thin section using a microprobe.

As alluded to in Chapter 5, the main major element used to classify glauconite into various evolved types based on its maturity is potassium, with glauconite ranging from a nascent potassium-poor (<4%) smectitic form to a highly evolved potassium-rich (>8%) illitic mineral (Table 8.1).

Table 8.1: Glauconite types and structure based mainly on potassium content (after Odin & Matter, 1981; Udgata, 2007).

Glauconite types	Maturity	Mineralogical structure	Colour	K ₂ O %	XRD (001) peak position
Nascent	Low	Smectitic glauconite ↓ Micaceous glauconite	Pale green	<4	14Å ↓ 10Å
Slightly evolved	Moderate		Light green	4-6	
Evolved	High		Green	6-8	
Highly evolved	Very high		Dark green	>8	

This chapter fully documents the geochemistry of the glauconite on central Chatham Rise. The analyses will enable classification of the glauconite based on Table 8.1, which is fundamental to gaining a better understanding of its origin and economic potential. The geochemistry of the different glauconite types, morphologies and internal fabrics will be investigated using single grain geochemical analysis with a microprobe instrument.

To date little work has been done on the geochemistry of the glauconite on central Chatham Rise. Norris (1964) suggested that the glauconite on the Rise has a high

potassium content of approximately 7.9%, which was further implied by Bell and Goodell (1967). Kudrass and Cullen (1982) undertook the first full chemical analysis of one magnetically separated pure glauconite sample (from Stn 287, c.179° 25' E longitude and 43° 29' S latitude) from central Chatham Rise. Their results are shown in Table 8.2.

Table 8.2: Chemical analysis of glauconite from Stn 287 (Kudrass & Cullen, 1982).

SiO ₂	Al ₂ O ₃	Fe ₂ O ₃ *	H ₂ O	CaO	Na ₂ O	K ₂ O	P ₂ O ₅	SO ₃	F	LOI
48.3	8.4	18.8	4.3	1.4	0.2	7.5	0.7	0.1	0	10

8.2 METHODS

The chemical composition of the glauconite was analysed using the SPECTRO X-LAB 200 XRF instrument at The University of Waikato, for trace and major element, and a microprobe housed at The University of Auckland for single grain major element analysis. Sample numbers mentioned in this chapter are located in Figure 3.1.

The 39 glauconite concentrates were powdered in a tungsten carbide ring mill. Trace elements were determined on 39 pressed pellet sample mounts, while major element composition was analysed on 30 sample mounts using fused glass discs. The methods on how to make up pressed pellets for trace element analysis were described in Section 3.2.4A. The method to make fused glass discs is a little more complicated. The first step is to mix approximately 2.5 g of 57:43 flux (57% Li-tetraborate, 43% Li-metaborate) with approximately 0.33 g of powdered glauconite concentrate sample in a platinum-gold crucible, mixing with a metal spatula. The crucibles (five at a time) are then put into a furnace and heated at the following three steps: 700°C for 10-15 minutes, 800°C for 10-15 minutes, and finally 1040°C with the shaker on for 10-15 minutes. A pinch of ammonium iodide is added to each sample, followed quickly by taking one crucible at a time out of the furnace using platinum tongs. The sample is poured into the centre of a graphite disc and flattened gently using a press and left for about 10 seconds to cool. The sample which is now a glass disc is transferred onto a hot plate at 230°C for 2 hours, followed by a second hot plate at 160°C for a further 2 hours.

The glass discs are then taken off the hot plate and left to cool before labelling with a white sticky label on the back side of the disc, which also helps to prevent the discs from breaking or cracking. Each sample weight and flux weight used is entered into the software programme on the XRF instrument, so that the wt% of each major element can be recorded. The loss on ignition (LOI) of all samples was also analysed. This involved strongly heating (igniting) approximately 1 g of each sample in a crucible in a furnace at ~1100 °C for about an hour to allow volatile substances to escape. Samples are then immediately reweighed to record the amount of volatiles which have escaped. In the case of glauconite the LOI is predominately water (H₂O).

The geochemistry of individual glauconite grains was also investigated in eight polished thin sections using the JEOL JXA-840A electron probe micro-analyser at the School of Environment, The University of Auckland, with the assistance of Ritchie Sims. Each polished thin section was coated with a 25 nm carbon film in an Edwards vacuum evaporator. The analysis conditions included an electron gun accelerating voltage of 15 kV, a 1000 pA beam current, and an electron spot diameter of approximately 2 µm. The X-ray analysis system used included a eumeX Si(Li) Be-window detector and Moran Scientific pulse-processor and software. Each spectrum was collected for 100 seconds of live time. Standardisation used a set of Astimex mineral standards (Cook, 2002, p.76 appendices; R. Simms, personal communication, August, 2011).

8.3 X-RAY FLUORESCENCE (XRF) RESULTS

Major and trace element raw results for all analysed samples are given in Appendix V, along with the main major and trace elements. Table 8.3 (also in Appendix V) summarises the XRF data into a correlation matrix for all major and trace elements for the 30 glauconite concentrates from central Chatham Rise. Only 30 samples were able to be analysed in the correlation matrix because both major and trace elements are needed to be known, and only 30 samples were analysed for their major elements, while 39 were analysed for trace elements. The moderate to strong correlations are highlighted in grey in Table 8.3.

Table 8.3: Correlation matrix between the major and trace elements in 30 analysed glauconite samples from central Chatham Rise (Note: Fe₂O₃* is total Fe, i.e. FeO and Fe₂O₃).

	SiO ₂	TiO ₂	Al ₂ O ₃	Fe ₂ O ₃ *	MnO	MgO	CaO	P ₂ O ₅	Na ₂ O	K ₂ O	LOI	Expandables	S	Cl	V
TiO₂	-0.16
Al₂O₃	0.57	-0.08
Fe₂O₃*	0.09	-0.56	-0.23
MnO	-0.27	0.93	-0.17	-0.39
MgO	0.71	0.06	0.61	-0.28	-0.07
CaO	-0.38	0.71	-0.48	-0.46	0.70	-0.15
P₂O₅	-0.16	0.25	-0.36	-0.44	0.23	0.02	0.78
Na₂O	0.09	0.66	0.06	-0.30	0.64	0.03	0.31	-0.09
K₂O	0.32	-0.80	0.35	0.29	-0.73	0.29	-0.56	0.01	-0.63
LOI	-0.40	0.22	-0.19	-0.12	0.34	-0.48	0.26	0.03	0.26	-0.35
Expandables	-0.32	0.80	-0.35	-0.29	0.73	-0.29	0.56	-0.01	0.63	-1.00	0.35
S	-0.59	0.23	-0.34	-0.41	0.21	-0.38	0.29	0.20	0.05	-0.28	0.14	0.28	.	.	.
Cl	-0.05	0.44	0.18	-0.30	0.41	0.02	0.15	-0.10	0.56	-0.29	0.19	0.29	0.35	.	.
V	-0.13	0.79	-0.29	-0.62	0.63	0.01	0.71	0.49	0.50	-0.68	0.17	0.68	0.25	0.07	.
Cr	-0.06	0.63	-0.40	-0.41	0.50	-0.01	0.50	0.28	0.47	-0.66	0.12	0.66	0.17	-0.04	0.90
Ni	-0.10	0.62	0.17	-0.82	0.48	0.27	0.35	0.22	0.33	-0.39	0.01	0.39	0.40	0.18	0.66
Zn	-0.25	0.61	-0.53	-0.17	0.49	-0.17	0.56	0.18	0.27	-0.79	0.05	0.79	0.19	-0.06	0.75
Ga	-0.29	0.59	-0.11	-0.68	0.52	-0.10	0.66	0.55	0.38	-0.42	0.18	0.42	0.36	0.20	0.65
Ge	0.27	0.08	0.07	-0.28	-0.04	0.26	0.08	0.30	0.17	0.07	-0.30	-0.07	0.01	-0.05	0.35
As	-0.24	-0.46	0.21	0.23	-0.28	-0.23	-0.18	-0.01	-0.45	0.46	0.06	-0.46	0.01	-0.22	-0.65
Br	0.03	0.40	0.24	-0.17	0.39	0.11	0.12	-0.19	0.54	-0.30	0.23	0.30	0.17	0.93	-0.01
Rb	0.22	-0.69	-0.13	0.32	-0.75	0.12	-0.47	0.01	-0.56	0.63	-0.47	-0.63	-0.13	-0.43	-0.26
Sr	-0.32	0.65	-0.47	-0.49	0.62	-0.11	0.98	0.86	0.25	-0.48	0.21	0.48	0.29	0.11	0.73
Y	-0.16	0.32	-0.35	-0.52	0.27	0.05	0.78	0.97	-0.03	-0.05	0.03	0.05	0.22	-0.13	0.61
Zr	-0.25	0.90	-0.27	-0.48	0.76	-0.04	0.64	0.17	0.57	-0.87	0.14	0.87	0.36	0.41	0.79
Nb	-0.08	0.73	-0.07	-0.39	0.64	0.12	0.57	0.32	0.35	-0.48	-0.03	0.48	0.26	0.64	0.43
Mo	-0.40	-0.06	-0.35	0.10	-0.04	-0.15	-0.03	-0.05	-0.33	0.08	-0.25	-0.08	0.54	0.19	-0.14
Sb	-0.12	-0.21	-0.18	0.06	-0.02	-0.11	0.18	0.47	-0.27	0.42	0.02	-0.42	0.17	-0.18	-0.10

Ba	-0.19	0.93	-0.22	-0.37	0.90	-0.08	0.66	0.12	0.75	-0.91	0.35	0.91	0.18	0.36	0.74
La	-0.18	0.23	-0.36	-0.44	0.20	0.01	0.74	0.97	-0.08	0.02	0.05	-0.02	0.20	-0.16	0.52
Ce	-0.12	0.01	-0.28	-0.22	0.02	-0.04	0.58	0.89	-0.20	0.23	0.03	-0.23	0.22	-0.06	0.20
W	-0.13	0.43	0.15	-0.30	0.41	0.27	0.36	0.29	-0.03	-0.03	0.00	0.03	0.15	0.39	0.20
Pb	-0.36	0.52	-0.07	-0.25	0.56	-0.15	0.45	0.24	-0.04	-0.29	0.15	0.29	0.33	0.30	0.23
U	0.02	0.04	-0.12	-0.34	-0.04	0.22	0.36	0.62	-0.10	0.20	-0.22	-0.20	0.36	0.26	0.15

	Cr	Ni	Zn	Ga	Ge	As	Br	Rb	Sr	Y	Zr	Nb	Mo	Sb	Ba	La	Ce	W	Pb
Ni	0.54
Zn	0.77	0.36
Ga	0.43	0.57	0.33
Ge	0.37	0.39	0.09	0.28
As	-0.80	-0.40	-0.60	-0.08	-0.38
Br	-0.09	0.02	-0.05	0.09	-0.20	-0.16
Rb	-0.06	-0.25	-0.15	-0.40	0.35	-0.14	-0.50
Sr	0.51	0.35	0.53	0.67	0.17	-0.20	0.06	-0.36
Y	0.41	0.38	0.28	0.61	0.38	-0.14	-0.25	0.04	0.86
Zr	0.70	0.55	0.78	0.47	0.12	-0.59	0.36	-0.52	0.59	0.23
Nb	0.24	0.28	0.37	0.37	0.08	-0.29	0.58	-0.47	0.56	0.28	0.73
Mo	-0.10	-0.02	0.09	-0.20	-0.09	-0.03	0.10	0.27	-0.04	-0.08	0.16	0.29
Sb	-0.12	-0.07	-0.31	0.11	0.31	0.30	-0.27	0.24	0.21	0.42	-0.34	-0.11	0.19
Ba	0.67	0.47	0.66	0.49	0.02	-0.49	0.38	-0.73	0.58	0.18	0.89	0.58	-0.14	-0.26
La	0.33	0.30	0.21	0.53	0.35	-0.07	-0.26	0.07	0.82	0.98	0.14	0.20	-0.12	0.44	0.11
Ce	-0.01	0.06	-0.03	0.36	0.23	0.17	-0.16	0.10	0.66	0.85	-0.09	0.17	-0.05	0.51	-0.11	0.90	.	.	.
W	0.03	0.37	0.13	0.23	0.14	-0.12	0.36	-0.15	0.35	0.31	0.32	0.60	0.34	0.25	0.21	0.29	0.30	.	.
Pb	0.01	0.34	0.26	0.36	-0.06	0.08	0.19	-0.39	0.41	0.25	0.42	0.62	0.30	0.13	0.33	0.19	0.19	0.67	.
U	0.01	0.13	-0.10	0.11	0.25	-0.09	0.14	0.15	0.43	0.53	0.13	0.42	0.39	0.30	-0.08	0.54	0.61	0.32	0.11

8.3.1 Major elements

24 samples plus 6 down-core samples at 2 cm intervals from station U6866, therefore 25 sample stations (with a total of 30 concentrates), were chosen on the basis of being representative across central Chatham Rise. Table 8.4 summarises the range of values for the major elements for the 25 surficial glauconite samples, as well as the overall average value. Note there were essentially no elemental differences between the 6 core samples at U6866, and so they were treated as one.

Table 8.4: Major elemental composition of the 25 glauconite samples from central Chatham Rise (see Appendix V for raw results and sample numbers).

Element	Average wt%	Range wt%
SiO₂	47.7	41.4 – 50.9
TiO₂	0.2	0.1 – 0.3
Al₂O₃	8.2	6.5 – 9.1
Fe₂O₃*	20.3	18.7 – 21.7
MnO	0.01	0.01 – 0.02
MgO	4.0	3.7 – 4.2
CaO	1.9	1.0 – 6.1
P₂O₅	0.9	0.4 – 3.7
Na₂O	0.7	0.5 – 0.9
K₂O	7.2	5.5 – 7.6
LOI	7.5	6.2 – 8.3
Total	98.4	89.4 – 101.4

According to the chemical classification scheme in Table 8.1, Table 8.4 shows that the glauconite on central Chatham Rise on average has a high maturity due to its K₂O content of 7.2 wt%, making it evolved glauconitic mica. This is compatible with the high Fe₂O₃* content, averaging 20.3 wt%. However the range of K₂O values from 5.5-7.6 wt% (Table 8.4) suggests the glauconite on the Rise varies from slightly evolved to almost highly evolved. It is possible that the few samples which had lower K₂O and Fe₂O₃* contents (see Appendix V) included also some contaminant carbonate and/or phosphorite grains not fully separated out by the Frantz magnetic separator.

Table 8.5 compares the average major element composition for the 25 glauconite samples in this study with the single analysis made by Kudrass and Cullen

(1982). There is relatively little difference, apart from the LOI value which is 2.5 wt% higher in the Kudrass and Cullen (1982) analysis.

Table 8.5: Comparison of XRF major element average results for 25 samples from central Chatham Rise, with the one sample previously analysed by Kudrass and Cullen (1982).

Element	Average wt% (this study)	Kudrass and Cullen (1982)	Difference
SiO ₂	47.7	48.3	-0.6
TiO ₂	0.2	-	-
Al ₂ O ₃	8.2	8.4	-0.2
Fe ₂ O ₃ *	20.3	18.8	1.5
MnO	0.01	-	-
MgO	4.0	-	-
CaO	19	1.4	0.5
P ₂ O ₅	0.9	0.7	0.2
Na ₂ O	0.7	0.2	0.5
K ₂ O	7.2	7.45	-0.3
LOI	7.5	10	-2.5

The correlation matrix between all major and trace elements forming Table 8.3 highlights in grey some inter-element correlations noted below.

The expected positive relationship between iron and potassium contents in glauconites from central Chatham Rise yields the highest r^2 value of 0.68 (Figure 8.1; cf. Compton, 1980; Odin & Matter, 1981). However when we look at the correlation coefficient, i.e. r (Table 8.3), compared to the coefficient of determination, i.e. r^2 (Figure 8.1), which is 0.29 compared to 0.68, respectively, we see a marked difference. This is mostly due to the removal of sample C606 in the r^2 determination (cf. Figure 8.1), due to its unusually low potassium content, so that when it is included in the analysis it hides the relationship between these two elements.

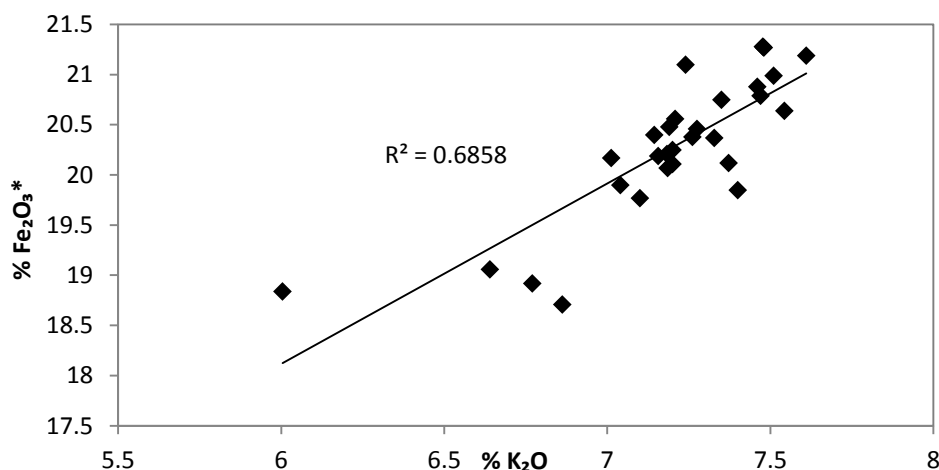


Figure 8.1: Correlation between Fe_2O_3^* and K_2O in 24 of the analysed glauconite concentrates from central Chatham Rise (sample C606 has been taken out of this correlation, due to its unusually low K_2O content; therefore here only 24 out of the 25 samples are analysed).

Typically, as glauconitisation proceeds Fe_2O_3^* should increase at the expense of Al_2O_3 replacement in octahedral sites (McConchie, 1978; Compton, 1989). But the Chatham glauconites show only a weak negative correlation ($r = -0.23$) in this regard. There is also no correlation between Fe_2O_3^* and SiO_2 values ($r = 0.09$).

McRae (1972) suggested that mineral glauconite has a consistent MgO content of c. 4%, which matches the average of 4.0 wt% occurring in the Chatham Rise glauconites (Table 8.4). MgO values show good positive correlations with both SiO_2 ($r = 0.71$) and Al_2O_3 ($r = 0.61$) (Table 8.3).

K_2O and H_2O (in LOI) are expected to have a negative correlation because the higher the K_2O content the lower the % expandables where H_2O resides (McRae, 1972; McConchie, 1978). The relationship is compatible with the $r = -0.35$ value between these components in the Chatham glauconites (Table 8.3).

The % expandable layers in glauconite can be determined using the position of the (001) clay peaks in glycolated XRD scans in conjunction with the curve of Weaver (1956), as outlined in Chapter 7. The % expandables can also be calculated using the K_2O content and Compton's (1989) equation, and because this equation substitutes the K_2O content within each sample, the correlation with the % expandables would subsequently display a perfect relationship (i.e. $r^2 = 1$) with K_2O . Figure 8.2 displays the relationship between % expandables calculated using Compton's (1989) method and the total Fe_2O_3^* content in the Chatham

glaucanites. It shows that as the glauconite becomes more mature (i.e. less expandables) the Fe_2O_3^* content increases. However, when we compare the correlation coefficient, i.e. r (Table 8.3), with the coefficient of determination, i.e. r^2 (Figure 8.2), which is 0.29 compared to 0.72, respectively, we see a marked difference. This is mostly due to the removal of samples C606 and U6872 in the r^2 determination (cf. Figure 8.2) due to their unusual elemental content results; if included in the analysis they tend to hide the true relationship. The % expandables and LOI/water content show a low positive correlation ($r = 0.35$) compared to what might otherwise have been anticipated (Hower, 1961; McConchie, 1978).

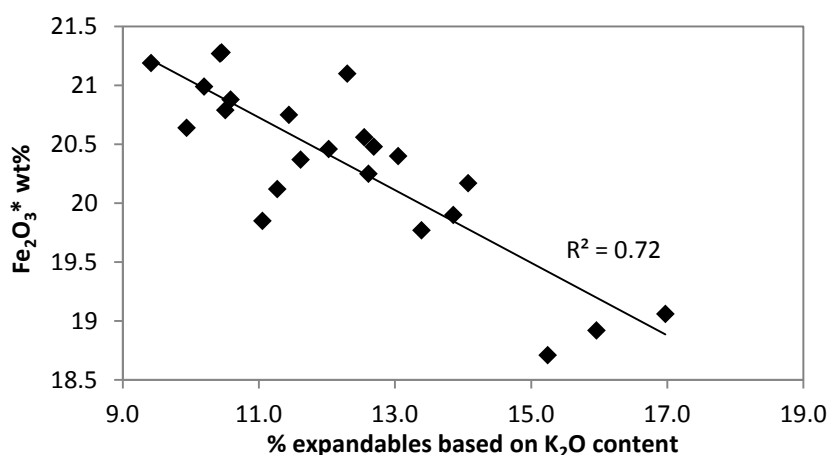


Figure 8.2: Relationship between % expandables calculated using Compton's (1989) method based on K_2O values and the total Fe_2O_3^* content in central Chatham Rise glauconites (note that samples C606 and U6872 have been taken out of this correlation due to unusual elemental compositions; therefore only 23 out of the 25 samples are plotted here).

No other significant correlations were noted amongst the more abundant major elements in the Chatham glauconites (Table 8.3). However some do occur involving CaO , NaO , TiO_2 , MnO and P_2O_5 (Table 8.3), but none of these elements had significant wt% contents within the glauconite (i.e. all <1.86 wt%; Table 8.4) and are not further considered here.

8.3.2 Trace elements

Making up pressed pellets for trace element analysis is a fast and easy technique so that all 33 glauconite samples plus 6 down-core samples (U6866), therefore 34 sample stations but 39 glauconite concentrates, were investigated for their full trace element concentrations in ppm. Average trace element values across all the glauconite samples is shown in Table 8.6 (see Appendix V for results) and the correlation between all trace and major elements is recorded in Table 8.3.

Table 8.6: Average amounts (ppm) of the main trace elements within 39 glauconite concentrates from central Chatham Rise (see Appendix V for all results).

Element	Average concentration (ppm)
S	1018
Cl	973
V	125
Cr	240
Ni	33
Zn	66
Ga	14
Ge	3
As	25
Br	9
Rb	184
Sr	76
Y	37
Zr	36
Nb	5
Sb	4
Ba	26
La	17
Ce	25
W	30
Pb	7
U	15

McConchie (1978) concluded that trace elements within glauconite can be divided into four groups based on both their concentration (in ppm) and the correlations between the trace and major elements. I have used McConchie's (1978) four groups as a framework to describe the trace elements within the central Chatham Rise glauconites.

1. Mn, V, Zr, Ti, (sometimes Y), Ba and Cr (and maybe Zn, Nd and Ni)

McConchie (1978) included in his group 1 the trace elements Mn, V, Ti, Zr and sometimes Y. I have kept these trace elements within group 1, but have added Ba and Cr, as well as possibly Zn, Nd and Ni. Trace elements in group 1 are related in terms of abundance, with the average at about 26 to 125 ppm, with Cr higher at 240 ppm (although Mn and Ti were measured in major oxides therefore given as wt %, at 0.01 and 0.2 respectively, therefore it cannot be analysed whether these two elements are related to other elements within this group based on their

abundance) (Table 8.6). Trace elements within group 1 occupy similar lattice positions, as indicated by their typically strong positive correlations with each other (Table 8.3 and 8.7), although correlations with Y are mainly weaker and perhaps better related to the elements in group 2.

Table 8.7: Correlations (r values) between group 1 trace elements in glauconites from central Chatham Rise (Table 8.3).

Trace elements	Correlation (r)
Ti-Ba	0.93
Ti-Mn	0.93
Ti-Zr	0.90
V-Cr	0.90
Mn-Ba	0.90
Ba-Zr	0.89
Ti-Zr	0.79
V-Zr	0.79
Mn-Zr	0.77
V-Ba	0.75
Cr-Zr	0.70
Cr-Ba	0.67
Ti-Cr	0.63
Mn-V	0.63
Y-V	0.61
Mn-Cr	0.50
Y-Cr	0.41
Y-Ti	0.32
Y-Mn	0.28
Y-Zr	0.23
Y-Ba	0.18

Group 1 trace elements are thought to occupy octahedral lattice sites (McConchie, 1978). Group 1 elements show moderate ($r = -0.37$ to -0.62) negative correlations with Fe_2O_3^* , due to these trace elements being transition metals, and therefore they occupy octahedral positions preferentially over Fe_2O_3^* because Fe_2O_3^* is also a transition metal (particularly V), and thus group 1 elements show a negative correlation with Fe_2O_3^* (Table 8.3). However Ba is an alkaline earth metal, not a transition metal, and so therefore may not be in this group. Compton (1989) suggested V and Y should not be included within this group due to V having a 5+ valency ion and Y^{3+} having an ionic radius of 0.92\AA , which would make

replacement of Fe_2O_3^* unlikely. In my data this appears to hold true for Y, but V displays all the same good correlations as the other group 1 trace elements (Table 8.3). Another correlation that group 1 elements have in common is their moderate to high ($r = -0.66$ to -0.91) negative correlation with K_2O , and hence also their strong positive correlation with % expandables, apart from Y which shows no correlation (Table 8.3). This negative correlation likely relates to the positive relationship between Fe_2O_3^* and K_2O , for as the trace elements increase (occupying octahedral sites) Fe_2O_3^* will decrease, which in turn is accompanied by a decrease in K_2O . Group 1 trace elements demonstrate moderate to strong positive correlations with CaO ($r = 0.49$ to 0.76) and also with Na_2O ($r = 0.46$ to 0.75), apart from Y which shows no correlation (Table 8.3). However, CaO and Na_2O have very low concentrations in the glauconite on central Chatham Rise (Table 8.4), and the relationships may not be significant.

Zn may be included in group 1 as it has a similar concentration of 59 ppm, is a transition metal and demonstrates similar correlations to the others described above apart from a smaller negative correlation with Fe_2O_3^* at $r = -0.17$ (Table 8.3). Nb and Ni are also transition metals and also display similar but not as strong correlations to other elements within group 1 (Table 8.3) and so they may also be included within this group.

2. P and S (sometimes Y)

McConchie (1978) included P and S (and sometimes Y) within group 2, and I have kept the same grouping. S and P (which are mostly locked up in SO_4^{2-} and PO_4^{3-} radicals, respectively) are thought to occupy lattice positions where they are bound to broken edges of tetrahedral layers. Group 2 trace elements are often present within coatings on grains, particularly P (McConchie, 1978). P is measured in P_2O_5 with an average wt% of 0.9 (Table 8.4). P is thought to mostly be present as coatings on grains, but analysis done on grains with fibroradiated rims does not show a significant change in P between the inner grain and its outer rim (see Appendix V). P, measured as P_2O_5 , has a high concentration in the microprobed glauconitised phosphatic grains (see section 8.4.5), which can be attributed to grain coatings. Y, which is related to apatite, a mineral present in some glauconite grains and especially glauconitised phosphatic ones, could also be related to the coatings on grains. S within glauconite may be related to the

presence of pyrite, or be locked up in SO_4^{2-} . SO_3 has been measured in the glauconitised phosphatic grains by microprobe, and has a slightly higher wt% compared to the average glauconite pellet which has no coatings (see Appendix V). S has very high concentrations in the Chatham glauconites, averaging c.1018 ppm (Table 8.6).

3. Rb and Sr (maybe Ca)

Rb and Sr were placed in group 3 by McConchie (1978) and I agree with this grouping, but consider whether Ca may be also included within this group. Hower (1961) suggested that Rb and Sr have interlayer positions, due to their correlations with the % expandables. In the Chatham glauconites Sr shows a moderate positive correlation with % expandables (as calculated from K_2O content) of $r = 0.48$, while Rb shows a moderate negative correlation of $r = -0.63$ (Table 8.3), supporting the interlayer position theory. Due to Sr having a very strong correlation with Ca ($r = 0.98$), a similar ionic potential (Sr^{2+} 1.8 and Ca^{2+} 2.0), and the fact that Ca correlates with K_2O at $r = -0.56$ and the % expandables at $r = 0.56$ (Table 8.3), it is possible that Ca too occupies an interlayer position and may be included within group 3 (Compton, 1989).

4. Pb and Cu (maybe Ga, Zn, Ni, La and Ce)

McConchie (1978) included Cu, Ga, Ni, Pb and Zn, within group 4, but I am certain of only Pb and Cu. He stated that these elements do not show any obvious relationship with any of the major elements or with the % expandables, and therefore their position is not known. However, in the Chatham Rise glauconites, this is not always the case. Clays like glauconite seem to be able to concentrate Cu, Zn and Pb very easily, and apart from Zn at c. 66 ppm they have very low concentrations (Table 8.6), so that these elements are relatively unimportant. Zn may therefore be included within group 1, as it does show correlation with some major elements (Table 8.3). Ga and Ni both have correlations with some major elements, notably Fe_2O_3^* and K_2O (Table 8.3), and so are excluded from group 4. Some trace elements were not recorded by McConchie (1978) in his glauconite study but have been in the central Chatham Rise glauconites. For example, La and Ce are here included within group 4 since they do not show any significant correlation with any major elements (Table 8.3). La and Ce do, however, have

strong positive correlations with P_2O_5 , at $r = 0.97$ and 0.89 , respectively (Table 8.3), which could be due to phosphorite impurities within the glauconite samples.

U, although not included within any of McConchie's (1978) four groups, should be mentioned as it has an average concentration of 15 ppm (Table 8.6). Cullen (1978) suggested that the origin of the U within glauconite may be associated with small quantities of a phosphate phase, due to the presence of up to 1% P_2O_5 and 2% CaO in his bulk samples. Alternatively, the U atoms may have become trapped in interlaminar spaces within the glauconite, or attached to free margins of the laminae.

8.4 GRAIN SPECIFIC MAJOR ELEMENTS

Glauconite grains in thin section were microprobed in order to investigate any geochemical differences between different varieties of glauconite on central Chatham Rise, as well as any grain to grain variation. The glauconite types included different colour varieties, discrete brown fibroradiated rims, foraminiferal infills and glauconitised phosphatic grains (Figure 8.3). The average major elemental geochemistry of individual bottle green glauconite grains has also been compared to the average geochemistry from XRF analysis. Full microprobe results and the photomicrographs of all the microprobed grains are shown in Appendix V.

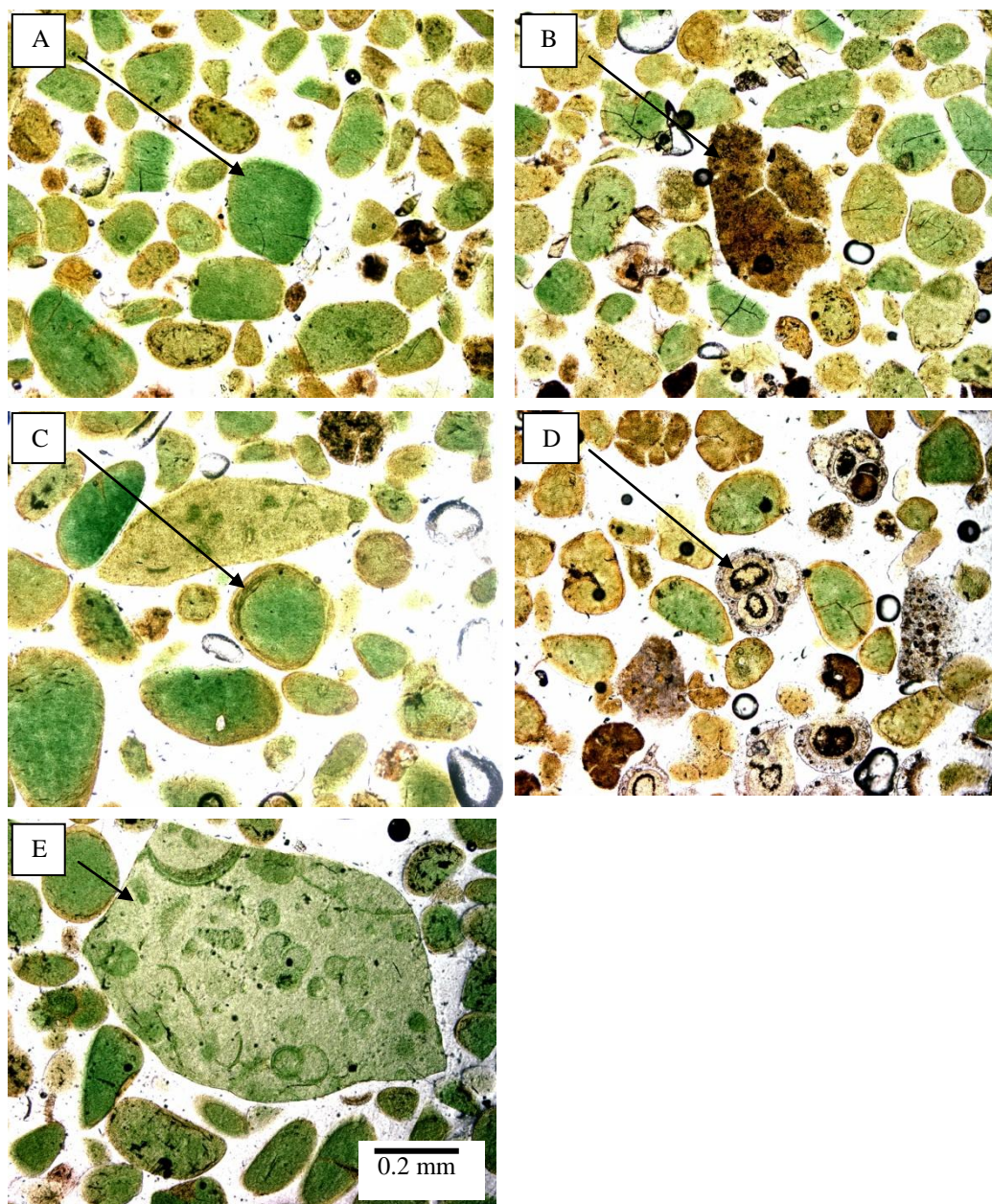


Figure 8.3: Photomicrographs representative of the different glauconite varieties and features investigated by microprobe to determine their major element geochemistry. A(A891): bottle green ovoidal glauconite pellet; B(A891): brown coloured glauconite grain; C(Q325): glauconite pellet with discrete brown rim around the inner core; D(C606): glauconitised foraminiferal infill; E(U6866): glauconitised phosphatic grain.

8.4.1 Bottle green ovoidal grains

A selection of 11 typical bottle green ovoidal (0.15-2 mm size) glauconite pellets (Figure 8.3A), the dominant (>75%) morphological type on Chatham Rise (Section 6.6) were microprobed from several different samples and the average major elemental composition was calculated (Table 8.8).

Table 8.8: Microprobe results (wt%) for individual bottle green ovoidal glauconite pellets from central Chatham Rise.

Sample	SiO₂	Al₂O₃	Fe₂O₃*	MgO	CaO	K₂O	Total
A891	51.1	6.0	19.2	4.9	0.1	9.3	90.5
A891	51.4	5.0	20.3	5.0	0.6	8.9	91.2
Q328	52.3	6.1	18.8	4.9	0.1	9.0	91.0
C606	49.9	2.5	22.5	4.6	0.3	8.8	88.5
C606	50.4	3.5	22.3	4.3	0.2	8.5	89.3
G135	51.6	5.5	21.0	4.3	0.2	9.0	91.5
Q356	51.2	5.6	19.2	4.6	0.3	9.0	89.8
Q356	50.7	4.9	20.7	4.6	0.1	8.9	90.0
C605	52.2	8.3	16.7	4.8	0.2	8.5	90.7
C605	52.2	7.6	17.3	5.0	0.3	8.6	90.9
Q325	52.1	5.6	18.6	5.0	0.2	9.2	90.7
Average	51.4	5.5	19.7	4.7	0.2	8.9	90.4

The average major element geochemistry for the typical bottle green glauconite pellets on the central Chatham Rise shows high iron (19.7%) and potassium (8.9%) contents, supportive of their high maturity and therefore evolved to highly evolved nature (Table 8.1).

The major elemental geochemistry of individual glauconite grains (Table 8.8) has been compared to the major element geochemistry from the bulk XRF glauconite results (Figure 8.4). Results are similar, supporting the effectiveness of the Frantz magnetic separator for concentrating the bulk glauconite samples. The higher content of CaO from XRF analysis likely reflects the occurrence of some glauconite foraminiferal infills and glauconitised (calcium) phosphatic grains in the bulk glauconite samples (Figure 8.4). The microprobed glauconite grains have slightly more K₂O compared to the bulk glauconite values, suggesting that the main ovoidal green glauconite types on central Chatham Rise are indeed highly evolved and mature glauconites (cf. Table 8.1 and Figure 8.4).

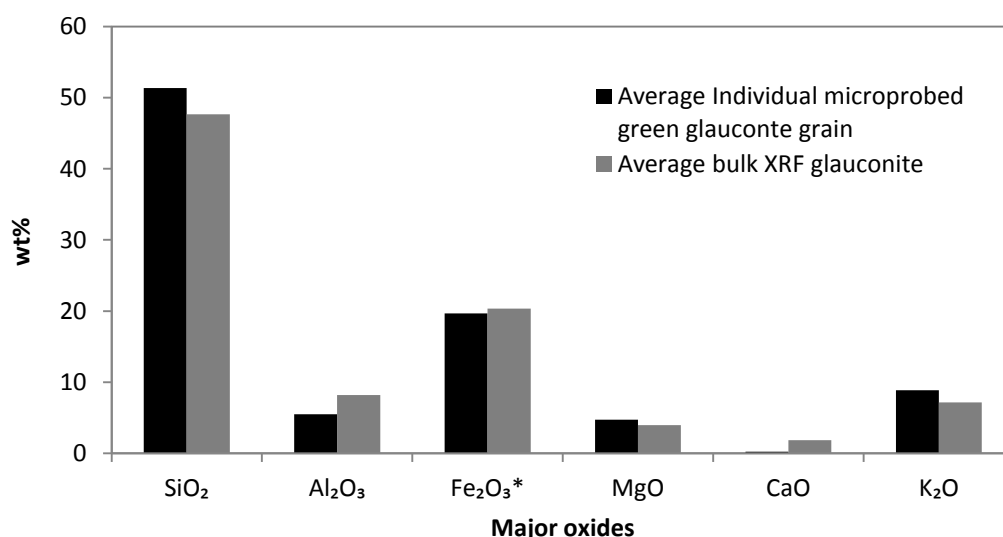


Figure 8.4: Average geochemistry of microprobed individual green glauconite grains, compared to average bulk XRF glauconite analysis from central Chatham Rise.

8.4.2 Brown grains

Glauconite grains can sometimes show colour variations ranging from light to dark brown, which can support irregular cracks (Figure 8.3B). A selection of these brownish glauconite grains were microprobed to prove that they were actually glauconite (Table 8.9) and to investigate any differences in their major element geochemistry compared to the average bottle green ovoidal glauconite variety (Figure 8.5).

Table 8.9: Microprobe analysis (wt%) of brownish glauconite grains from central Chatham Rise (b = brown).

Sample	Colour	SiO ₂	Al ₂ O ₃	Fe ₂ O ₃ *	MgO	CaO	K ₂ O	Total
Q356	Med b	49.1	8.8	19.4	3.5	0.4	6.9	88.2
C606	Light b	48.5	7.3	22.1	3.4	1.0	5.2	87.4
C606	Med b	50.4	6.6	21.8	3.8	0.7	5.6	88.8
C606	Med-dark b	48.4	4.8	23.6	3.2	0.7	6.5	87.1
A891	Dark b	44.9	8.9	21.8	3.6	0.4	7.0	86.6
Q325	Med b	50.1	10.2	18.2	3.8	0.4	7.0	89.6
Average		48.6	7.8	21.14	3.5	0.6	6.4	87.9

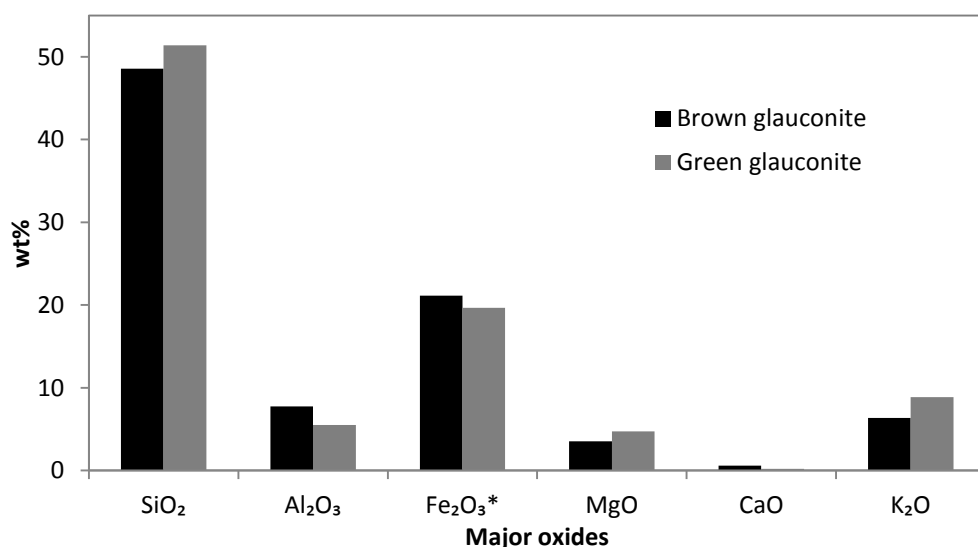


Figure 8.5: The average microprobe results for major oxides in typical green glauconite grains compared to brown glauconite grains from central Chatham Rise.

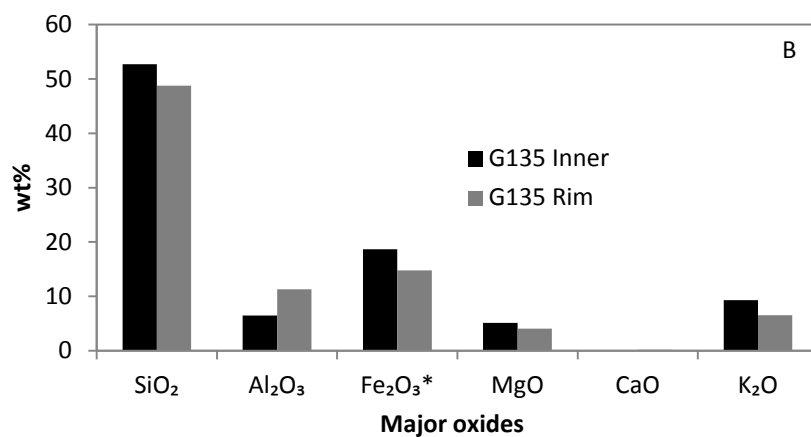
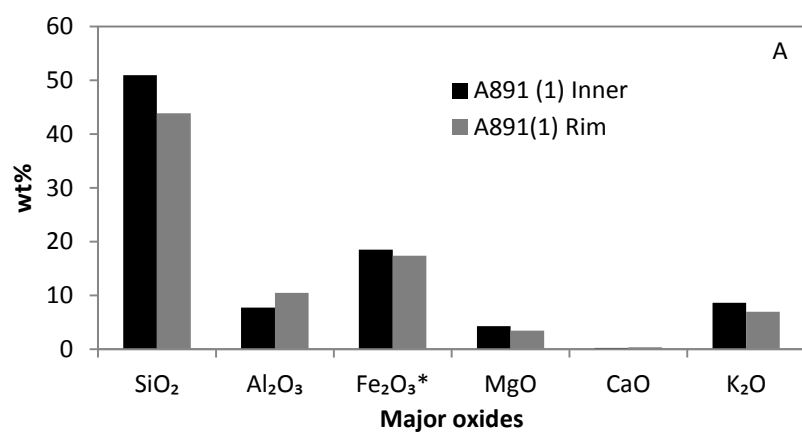
Results show that the brown grains are definitely glauconite, with high Fe₂O₃* and K₂O contents (Table 8.9). However, they have lower K₂O values but slightly higher Fe₂O₃* and Al₂O₃ contents compared to the typical bottle green ovoidal grains (Figure 8.5).

8.4.3 Fibroradiated oriented rims

Some of the glauconite grains on central Chatham Rise support discrete yellow-brown rims (Figure 8.3C). The rims were described in Section 6.7.2 and have an internal fabric, referred to as oriented fibroradiated rims. A selection of these rims and their host inner glauconite cores were microprobed to compare their elemental compositions (Table 8.10). Figure 8.6 summarises results for four different glauconite pellet rims and inner cores in four different samples, while Figure 8.7 shows a comparison between the average major element geochemistry of the brown fibroradiated rims compared to their inner glauconite cores. The brown fibroradiated rims have a lower K₂O and Fe₂O₃* content compared to the inner cores, as well as a lower SiO₂ and MgO content but a higher Al₂O₃ content (Figures 8.6 and 8.7).

Table 8.10: Microprobe analysis (wt%) of the inner and rim portions of several glauconite grains from central Chatham Rise.

Sample	Part of grain	SiO ₂	Al ₂ O ₃	Fe ₂ O ₃ *	MgO	CaO	K ₂ O	Total
A891	Inner	50.9	7.8	18.5	4.3	0.2	8.6	90.3
	Rim	43.8	10.4	17.4	3.4	0.4	7.0	82.4
A891	Inner	51.2	8.3	18.4	4.5	0.1	8.7	91.3
	Rim	47.9	10.4	18.9	3.8	0.3	7.6	88.9
Q325	Inner	51.9	5.6	19.8	4.8	0.2	8.9	91.1
	Rim	49.1	9.7	15.9	3.8	0.2	6.9	85.7
U6866	Inner	48.4	10.6	17.9	3.6	0.4	7.5	88.3
	Rim	49.8	13.5	16.3	3.6	0.4	6.6	90.1
G135	Inner	52.7	6.5	18.7	5.1	0.0	9.3	92.2
	Rim	48.7	11.3	14.8	4.1	0.2	6.6	85.7
Average	Inner	51.0	7.7	18.7	4.5	0.2	8.6	90.6
	Rim	47.9	11.1	16.7	3.7	0.3	6.9	86.5



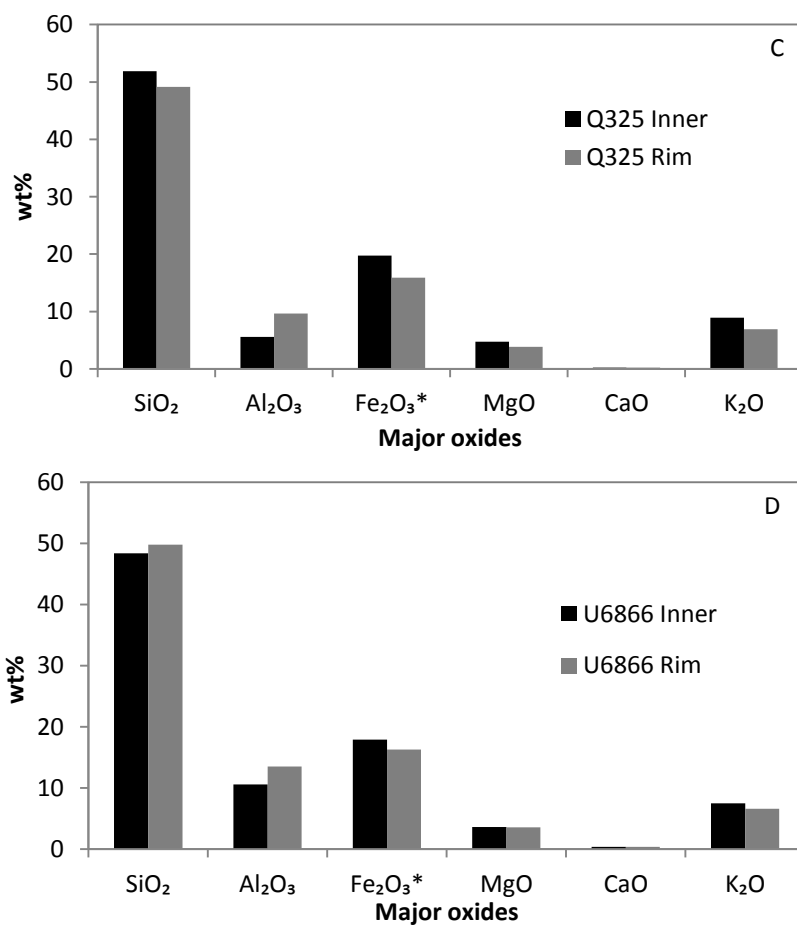


Figure 8.6: Comparison between the major oxide geochemistry of glauconite in the rim and inner pellet of four samples (A to D) from central Chatham Rise.

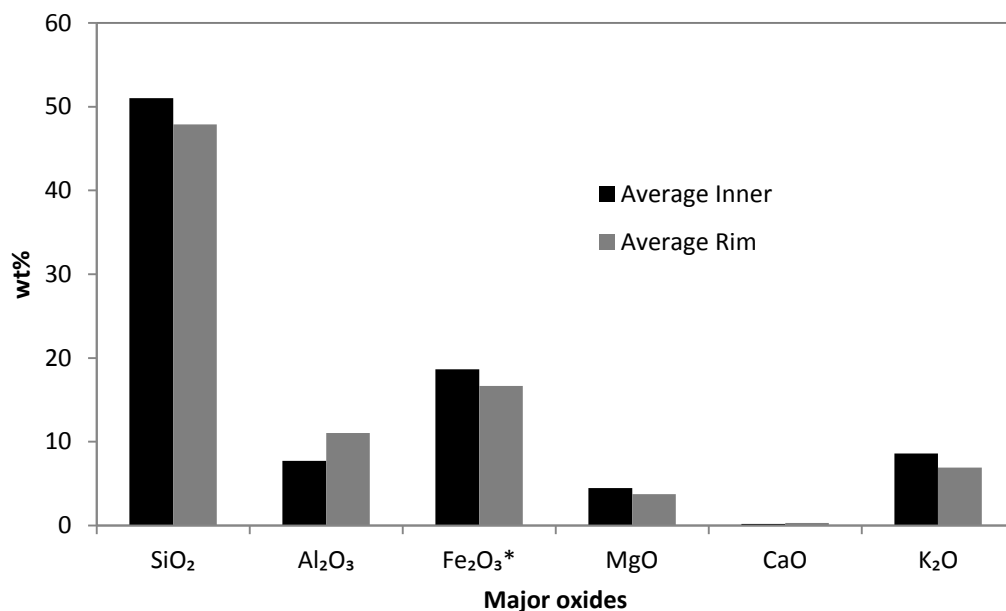


Figure 8.7: Average wt% of the major oxides in the inner core of glauconite grains compared to their surrounding brown rims on central Chatham Rise.

Odom (1976) investigated the variation in geochemistry between the fibroradiated rims and cores of glauconite pellets from the Cambrian of the central USA, and found results very similar to those obtained here for central Chatham Rise glauconites (Table 8.11). However, Odom (1976) reports that the rims in his study show zoning from a dark green to a light green towards the margins of the rim, while the rims of the Chatham glauconites show a distinct brown colour. In both studies the Al_2O_3 content is higher in the rim at about 11% compared to near 8% in the core, while the K_2O content is lower at about 7% compared to approximately 8% in the core (Table 8.11). Also the Fe_2O_3^* content is lower in the rim in both instances, at almost 17%, although Odom's (1976) glauconites have an overall higher Fe_2O_3^* content than the Chatham Rise glauconites (Table 8.11). Importantly, the results prove that the brown rims on the central Chatham Rise glauconites are indeed oriented fibroradiated rims of glauconite.

Table 8.11: Geochemistry of average aggregate inner glauconite cores and their oriented fibroradiated rims in Odom (1976) compared to the central Chatham Rise glauconites (Figure 8.3C and Table 8.10).

Study	SiO_2	Al_2O_3	MgO	Fe_2O_3^*	CaO	K_2O
Oriented rim (Odom, 1976)	47.5	10.9	3.8	16.9	1.9	7.3
Oriented rim of this study	47.9	11.1	3.7	16.6	0.3	6.9
Glauconite aggregate core (Odom, 1976)	46.8	7.9	2.5	25.5	0.5	7.9
Glauconite inner core of this study	51.0	7.7	4.5	18.7	0.2	8.6

8.4.4 Foraminiferal infills

The glauconite infilling foraminiferal chambers (Figure 8.3D) was microprobed for its major elemental composition (Table 8.12) and compared to the average major element geochemistry of the average green ovoidal glauconite grains (Figure 8.8).

Table 8.12: Microprobed analysis (wt%) of glauconite infilling planktic foraminiferal chambers within a large glauconitised phosphatic grain (i.e. composite glauconite) from central Chatham Rise.

Sample	SiO ₂	Al ₂ O ₃	Fe ₂ O ₃ *	MgO	P ₂ O ₅	CaO	K ₂ O	Total
Q325	44.0	5.3	15.9	4.4	6.1	7.6	7.2	90.5
C605	38.8	2.6	18.7	3.7	8.9	10.9	6.5	90.01
U6866	25.5	1.8	9.9	2.6	21.5	26.4	3.9	91.4
Average	36.1	3.2	14.8	3.6	12.2	14.9	5.9	90.6

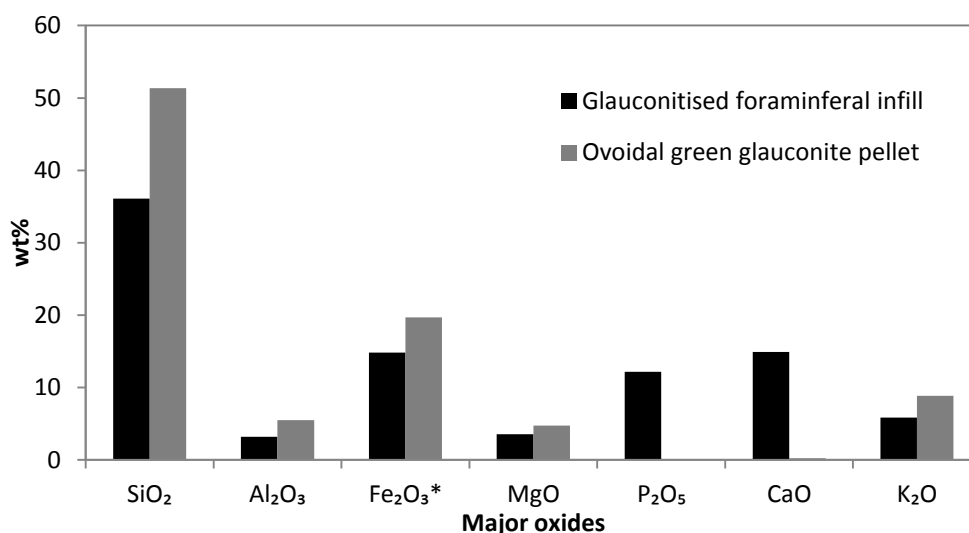


Figure 8.8: Comparison of the average major element geochemistry of glauconite between ovoidal green pellets and foraminiferal infills from central Chatham Rise.

There are major differences between the average major element concentrations in ovoidal green glauconite pellets and glauconite foraminiferal infills (Figure 8.8). The infills (within large glauconitised phosphatic grains) have a geochemistry that is intermediate between glauconite grains and calcium carbonate grains (Table 8.12). All the major oxides that make up a glauconite pellet are lower in content in the foraminiferal infills (i.e. MgO, Al₂O₃, SiO₂, K₂O, Fe₂O₃*). K₂O and Fe₂O₃* values of 5.9 and 14.8 wt%, respectively (Table 8.12 and Figure 8.8), indicate only a moderately mature or slightly evolved form of glauconite for the infills (Table 8.1). The reduced contents of the typical glauconite major oxides are compensated by high values of P₂O₅ (12.17 wt%) and CaO (14.93 wt%) (Table 8.12 and Figure 8.8), typical major elements in skeletal grains. Triplehorn (1966) and McRae (1972) would refer to these glauconite foraminiferal infills as fossil casts or internal molds having an internal fabric indicative of organic replacement (Sections 6.6.4 and 6.7.3, respectively).

8.4.5 Glauconitised phosphatic grains

A final glauconite variety examined under the microprobe for its major elemental geochemistry was the large (0.5-2.5 mm), light green glauconitised phosphatic fragments, which include darker small pellets, foraminiferal infills and glauconite fractures (Figure 8.3E) (Table 8.13). Such fragments were referred to in Chapter 6 as composite grains - defined as large grains (about 2 mm) composed of a mixture of glauconite and other minerals that are set in a pale green glauconitic matrix (cf. Triplehorn, 1966; Konta, 1967; McRae, 1972). These composite grains appear to be composed of phosphate, carbonate and glauconite (Table 8.13). Their glauconite component is illustrated by the average K_2O and $Fe_2O_3^*$ contents of 3.4 wt% and 8.6 wt%, respectively (Table 8.13), which corresponds to a nascent, low maturity form of glauconite (Table 8.1; Odin & Matter, 1981). These composite grains have very high P_2O_5 and CaO contents, averaging 24.6 wt% and 30.5 wt%, respectively (Table 8.13).

Table 8.13: Microprobe analysis (wt%) of glauconitised phosphatic grains from central Chatham Rise.

Sample	Grain	SiO ₂	Al ₂ O ₃	Fe ₂ O ₃ *	MgO	CaO	P ₂ O ₅	K ₂ O	Total
Q328	grain 1	28.5	1.9	12.0	2.8	22.0	17.3	5.1	89.5
	grain 2	22.6	2.9	11.4	1.9	25.7	21.4	3.9	89.7
	grain 3	18.9	2.1	7.8	2.0	31.3	26.3	2.9	91.3
A891	grain 2	9.5	1.1	4.2	1.2	40.8	32.7	1.6	91.1
	grain 6	31.2	3.6	11.2	3.3	20.0	16.8	5.3	91.4
U6866	grain 1	19.7	1.3	8.3	2.1	31.3	25.9	3.3	91.8
	grain 2	26.9	1.6	13.6	2.5	22.8	18.5	4.9	90.9
C606	grain 4	5.8	0.7	2.3	0.9	44.4	35.0	0.9	90.0
C605	grain 6	11.8	1.2	5.5	1.6	38.3	30.2	2.1	90.5
Q325	grain 2	18.9	1.9	7.0	2.0	32.2	25.7	3.1	90.9
	grain 3	34.5	3.3	15.1	3.4	15.1	12.7	6.3	90.3
G135	grain 2	19.0	1.3	8.3	2.1	32.3	25.8	3.4	92.2
	grain 3	12.5	1.3	5.3	1.4	38.5	30.9	2.1	92.0
Average		20.0	1.9	8.6	2.1	30.4	24.6	3.4	90.9

Two parts of the darker green fracture fills within a glauconitised phosphatic fragment were also microprobed (Figure 8.9 and Table 8.14). These show that such fills, occurring in some of the glauconitised phosphatic grains only, are in

fact highly evolved glauconite having K_2O and $Fe_2O_3^*$ contents of c. 8 wt% and 21 wt%, respectively (cf. Table 8.1).

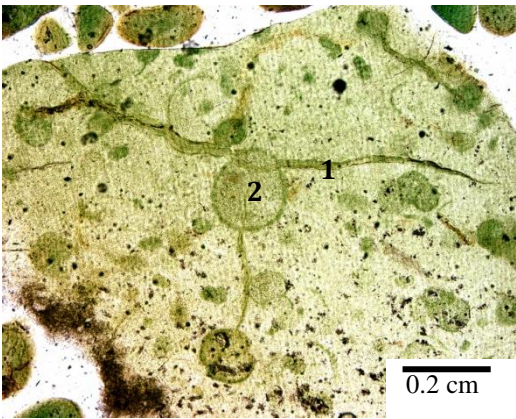


Figure 8.9: Locations 1 and 2 in a glauconite filled fracture were microprobed within a glauconitised phosphatic fragment in sample Q325 (see Table 8.14).

Table 8.14: Major oxide composition of two glauconite filled fractures probed within a glauconitised phosphatic grain in sample Q325 from central Chatham Rise.

Sample	SiO ₂	Al ₂ O ₃	Fe ₂ O ₃ *	MgO	CaO	P ₂ O ₅	K ₂ O	Total
Q325 1	50.4	7.3	18.4	4.3	0.3	0.02	8.1	88.7
Q325 2	48.4	4.9	23.0	3.8	0.4	0.2	8.1	88.5

Figure 8.10 displays backscatter images that were also produced for the microprobed fracture fill in the glauconitised phosphatic fragment of sample Q325-1 in Figure 8.9.

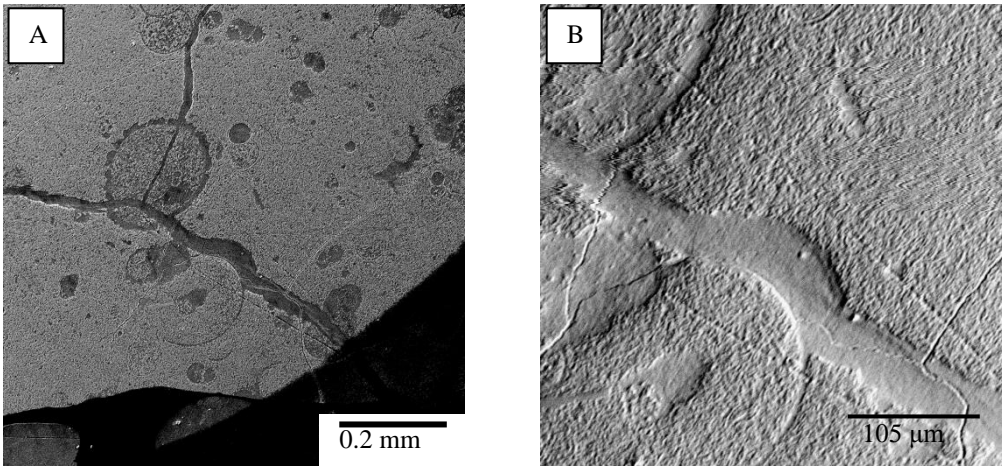


Figure 8.10: A: backscattered image and B: topographic image of the glauconitised phosphatic grain Q325-1 (Figure 8.9) from central Chatham Rise.

The backscatter image in Figure 8.10A shows a mixture of darker and lighter material which corresponds to a mixture of glauconite (darker) and phosphatic (lighter) components, and also the dark glauconite fracture fill extending through the grain. Figure 8.10B is an enlarged topographic image that demonstrates the smooth texture of the glauconite fill compared to the rest of the grain.

The dark small circular structures seen within most glauconitised phosphatic grains (Figure 8.3E) were thought to be small glauconite pellets and glauconitised planktic foraminifera, and so were also microprobed to investigate their major elemental geochemistry (Table 8.15). The results show that the small dark green pellets are indeed mature evolved glauconite (Table 8.1), with high K₂O and Fe₂O₃* contents averaging 7.9 wt% and 19 wt%, respectively.

Table 8.15: Glauconite pellets and glauconite foraminiferal infills within glauconitised phosphatic grains from central Chatham Rise (f=foraminiferal infill; g=glauconite pellet).

Sample	SiO ₂	Al ₂ O ₃	Fe ₂ O ₃ *	MgO	CaO	P ₂ O ₅	K ₂ O	Total
Q356 (g)	50.7	8.0	18.2	4.4	0.3	0.2	8.0	89.7
C606 (f)	49.8	1.9	23.1	4.5	1.2	0.6	8.1	89.2
U6866 1 (f)	51.2	5.1	19.4	4.9	0.2	0	8.4	89.3
U6866 3 (g)	49.0	12.4	16.8	3.7	0.5	0.1	6.5	89.0
Q328 (g)	51.0	10.0	17.0	4.3	0.4	0	7.2	89.8
A891 (f)	51.1	6.0	19.2	4.9	0.1	0	9.3	90.5
Average	50.4	7.2	19.0	4.4	0.4	0.1	7.9	89.6

Chapter 9

AGE OF GLAUCONITE

9.1 INTRODUCTION

Whether the glauconite on central Chatham Rise is a truly authigenic *in situ* deposit that is actively forming today, or whether it is an allogenic or perigenic deposit resulting from the reworking of some older deposit(s) is a pertinent question. This chapter ascertains the age of the glauconite on central Chatham Rise, which sheds light on the origin of the glauconite and whether it is actively forming at the present day. The main way of determining the absolute age of glauconite is via K-Ar and Ar-Ar dating methods (Smith *et al.*, 1988; Smith *et al.*, 1993; Clauer *et al.*, 2005). In the present study the K-Ar method has been employed.

There has been some past work carried out into the age of the glauconite on central Chatham Rise. Norris (1964) first noted that the glauconite on the Rise most likely has a Tertiary age. Not long after this Cullen (1967), who agreed with this Tertiary age, undertook K-Ar age dating on one sample (A799) at the Age Determination Unit at the Institute of Geological Sciences in the United Kingdom, where an age of 5.6 ± 1 Ma was determined on a glauconite sample with a potassium content of 6.65%. However, he stated that the age could actually range from 5-10 Ma due to argon leaking. Another study which looked into the age of the glauconite on Chatham Rise was by Kreuzer (1984) who dated the phosphorite nodules, the glauconite rims about the phosphorite nodules and some pelletal glauconite (as in the present study). For the pelletal glauconite an age of about 7 Ma (Late Miocene) was determined using K-Ar dating.

9.2 METHODS

Glauconite is commonly dated using K-Ar or Ar-Ar dating techniques (Smith *et al.*, 1988; Smith *et al.*, 1993; Clauer *et al.*, 2005). For the glauconite on central Chatham Rise I chose five widely distributed samples to undertake age dating on,

two of which came from different depths down core U6866. These samples were A891, Q325, Q356, U6866 0-2 cm and U6866 10-13 cm. The K-Ar age dating was obtained in a collaborative study with Dr Horst Zwingmann, at CSIRO Perth, Australia.

To carry out the K-Ar dating, 40-50 mg of individual dark green to black ovoidal glauconite pellets of approximately 0.2 mm size were picked from samples (Figure 9.1). These dark green mature glauconites were selected because they are rich in potassium (>7 wt% K₂O) and provide more accurate dates compared to K-poor immature glauconites (Smith *et al.*, 1988; Smith *et al.*, 1993). Also the ovoidal grains do not contain calcareous contaminations such as occurs in the deep surface cracks of the lobate varieties (Section 6.6.2).

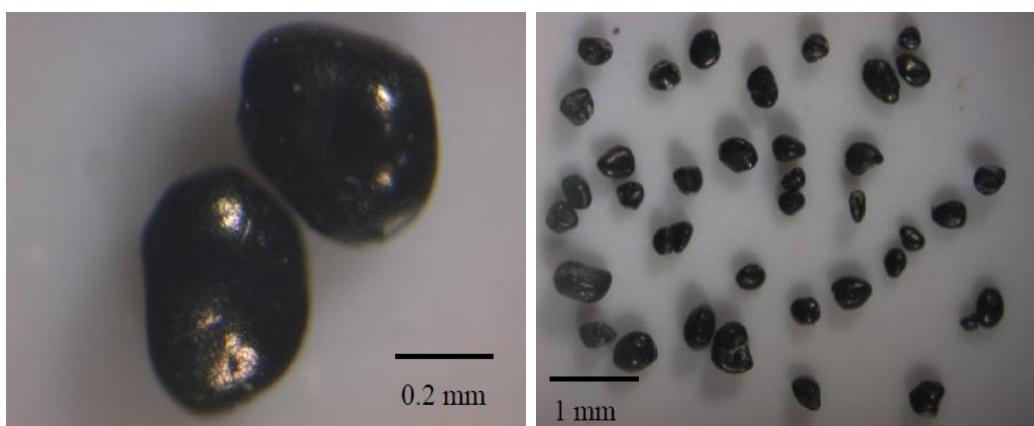


Figure 9.1: Dark green to black ovoidal (0.2 mm) pellets that were selected for age dating.

The K-Ar technique can determine an age of a rock or mineral (in this case glauconite grains) by measuring the amount of ⁴⁰Ar (the argon isotope) relative to the potassium content. This is possible as ⁴⁰Ar is produced by the decay of ⁴⁰K (potassium isotope). Argon is typically negligible within rocks and minerals at the time of formation, however small amounts of atmospheric argon may adhere to the rock and/or minerals, which can be corrected for using the ratio of the atmospheric ⁴⁰Ar/³⁶Ar (i.e. 295.5). This means if the ⁴⁰K is known, and one measures the ⁴⁰Ar to ⁴⁰K ratio, then the age of the rock and/or mineral can be calculated (Dalrymple & Lanphere, 1969; Faure, 1986; Dickin, 1995).

In the present study the potassium content was measured in duplicate by atomic absorption (Varian Spectra AA 50) using Cs at 1000 ppm concentration for

ionisation suppression. For each sample, two aliquots of approximately 100 mg of sample were dissolved with HF and HNO₃ (see for example Heinrichs & Herrmann, 1990). Once in solution, in order to carry out atomic absorption analysis the samples need to be diluted to 0.3 to 1.5 ppm K. The pooled error of duplicate K determination of all samples and standards is better than 2%. The K blank was measured at 0.33 ppm = 0.000040% K (H. Zwingmann, personal communication, November, 2011). The method of calculating the Ar isotope measurements followed that of Bonhomme *et al.* (1975). Each sample (20 mg) was heated at 80°C for several hours in order to reduce the amount of atmospheric Ar adsorbed onto the mineral surfaces during sample handling. Argon was extracted from the separated mineral fractions by fusing samples within a vacuum line serviced by an on-line ³⁸Ar spike pipette. Using a high sensitivity on-line VG3600 mass spectrometer, the isotopic composition of the spiked Ar was calculated. The ³⁸Ar spike was calibrated against international standard biotite GA1550 (McDougall & Roksandic, 1974). After fusion of the sample in a low blank Heine resistance furnace, the released gases were subjected to a two-stage purification procedure with a CuO getter for the first step, and two Ti getters and a SORB-AC getter for the second step. Blanks for the extraction line and mass spectrometer were systematically determined and the mass discrimination factor was determined periodically by airshots. In the present study one international standard HD-B1 and one airshot were analysed (see Appendix VI for raw results). The error for argon analyses is below 1% and the ⁴⁰Ar/³⁶Ar value of the airshot yielded 295.20 ± 0.30. Using recommendations of ⁴⁰K abundance and decay constants suggested by Steiger and Jäger (1977), the K-Ar ages were calculated. The age uncertainties take into account the errors during sample weighing, ³⁸Ar/³⁶Ar and ⁴⁰Ar/³⁸Ar measurements and K analysis. K-Ar age errors are within 2 sigma uncertainty (H. Zwingmann, personal communication, November, 2011).

9.3 K-AR GLAUCONITE AGE RESULTS

The age results obtained for the five analysed samples are displayed in Table 9.1 (full results in Appendix VI), including the potassium and argon contents, and the Phanerozoic timescale epochs of Gradstein *et al.* (2004). Radiogenic ⁴⁰Ar ranges from 27 to 34% indicating reliable analytical conditions for all analyses. The K

concentrations of all samples are homogenous and vary from 6.5 to 6.7 % (Table 9.1) in accordance with glauconite K concentrations (internal CSIRO database) (H. Zwingmann, personal communication, November, 2011).

Table 9.1: Age results for the five glauconite samples, calculated using K-Ar dating (refer to Figure 3.1 for sample locations).

Sample ID	K (%)	Rad. ^{40}Ar (mol/g)	Rad. ^{40}Ar (%)	Age (Ma)	Error (Ma)	Epoch
A891	6.60	6.86E-11	34.57	6.00	0.23	Late Miocene
Q325	6.60	6.52E-11	27.51	5.68	0.22	Late Miocene
Q356	6.70	6.62E-11	27.17	5.72	0.26	Late Miocene
U6866 0-2 cm	6.50	6.17E-11	27.25	5.47	0.20	Late Miocene
U6866 10-13 cm	6.60	6.70E-11	29.64	5.89	0.25	Late Miocene
Average	6.60	6.57E-11	29.23	5.75	0.23	Late Miocene

The results yield an average age of 5.75 Ma, with a range of 5.47-6.0 Ma. The ages are very consistent with small errors. The U6866 core samples have similar ages to the other samples (Table 9.1). Given the wide spread in sample locations it appears that the glauconites on central Chatham Rise have a Late Miocene age of about 5.75 ± 0.25 Ma, and are thus not actively forming today. The Late Miocene age of about 5.75 Ma falls within the New Zealand Kapitean Stage or the global Messinian Stage (Gradstein *et al.*, 2004). The Messinian Stage is known to be a time of lowered eustatic sea level, due to the growth of Antarctic ice sheets (Berggren & Haq, 1976; Vincent *et al.*, 1980; Grant, 2005). Lowered sea level combined with the onset of associated uplift of the Chatham Islands and upwelling within the Subtropical Front (STF) at this time could account for the widespread formation of glauconite, as discussed later in Chapter 11.

It has been suggested that glauconite ages can be unreliable and underestimated (i.e. younger than they actually are) due to daughter argon isotope leaking by recoil during irradiation, which consequently underestimates the potassium content, due to ^{40}Ar being produced by the decay of ^{40}K (Smith *et al.*, 1988; Weaver, 1989; Smith *et al.*, 1993; Clauer *et al.*, 2005). Accordingly, Cullen (1967) suggested that the Chatham glauconite may be older than the K-Ar date he derived and could possibly have an age between 5 and 10 Ma spanning Late Miocene to Pliocene times. The unreliability of glauconite ages can be related to

the timing of geochemical closure, being a point when the glauconite grain no longer exchanges potassium or argon with the containing sediment. Immature K-poor glauconites are thought to undergo closure when they are subjected to burial, whereas mature K-rich (>8.5%) grains, like the ones in the present study, can actually undergo closure before burial (Smith *et al.*, 1988; Weaver, 1989). Due to the fact that the glauconite on central Chatham Rise is predominantly mature/evolved K-rich (av. 8.9%; Section 8.4.1) glauconite that has not yet been subject to burial, it has most likely already undergone closure and should provide reliable dates with minimal Ar loss. However, as shown in Table 9.1, the potassium content measure in the K-Ar dating process is only near 7%, compared to the av. 8.9% calculated from microprobe analysis (Section 8.4.1). This might have led to the ^{39}Ar recoil loss mentioned above, which would underestimate the K content. Consequently, it remains possible that the glauconite on the Rise could in fact be slightly older than the av. 5.75 Ma calculated age.

A further suggestion which would ultimately provide more accurate and/or more confident dates than the K-Ar method is to undertake single grain age analysis using the ^{40}Ar - ^{39}Ar dating technique, which can measure the Ar recoil loss. The ^{40}Ar - ^{39}Ar method is similar to the K-Ar method, but differs in the fact that the neutron irradiation transforms the isotope ^{39}K into ^{39}Ar , and the technique can therefore be used on single grains or even parts of grains (Smith *et al.*, 1993). Smith *et al.* (1993) suggested that the ^{40}Ar - ^{39}Ar technique can provide ages that are up to five times as precise as the K-Ar method. This single-grain dating method would also allow the different morphological types of glauconite occurring on central Chatham Rise (Chapter 6) to be dated. This would help determine whether the different morphologies, which have varying potassium contents, in any way relate to different ages of formation compared to the predominant (>75%) dark green potassium-rich ovoidal grains with an average age of 5.75 Ma.

Chapter 10

ECONOMIC POTENTIAL OF GLAUCONITE

10.1 INTRODUCTION

Glaucinite has economic potential due mainly to its high potassium content and high cation exchange capacity. Assessing the economic potential of the glauconite on central Chatham Rise is relevant to possible future seafloor mining of the mineral. At any rate it is crucial for New Zealand to know what submarine resources it has, the nature of these, the resource estimate, and the potential economics of such a resource.

This chapter summarises the uses of glauconite in general, and establishes a resource estimate for the glauconite over portions of central Chatham Rise.

There has been much previous work done in regard to the economic uses of glauconite in general, but little has been undertaken specific to the glauconite deposits on central Chatham Rise. Norris (1964) constructed a generalised wt% glauconite map, similar to the more detailed one constructed in the present study (Figure 6.2), but a resource estimate was not made. Norris (1964) and Summerhayes (1967) recognised that the glauconite on central Chatham Rise could be a good source of potash fertiliser. Cullen (1967) analysed the uranium content within the glauconite, and concluded that it was very low and would be unlikely to provide a source of uranium.

10.2 USES OF GLAUCONITE

There are two properties of glauconite that correspond to two main potential economic uses – its high potassium content and its cation exchange capacity – which correspond to the use of glauconite as a fertiliser and for water treatment, respectively (McRae, 1972; McConchie, 1978; Coles *et al.*, 2002). These two main uses will be described below, as well as some other possibilities.

10.2.1 Fertiliser

Potassium is one of the three main nutrients needed for plant growth. Over 90% of mined potassium is used as fertiliser, and glauconite is one of the main minerals mined for potassium (Coles *et al.*, 2002; Potash West NL, 2011). Given this, the main use of glauconite is as a soil fertiliser or conditioner due to its ability to slowly release the high contained amounts of potassium and other nutrients. Glauconite is of sand size but can actually absorb 10 times more moisture than most sands, and it makes a good soil conditioner due to its ability to break up clayey soils, and is therefore often used for organic type farming and in the garden. Glauconite also prevents burning of plants and is very beneficial for microbes (McRae, 1972; McConchie, 1978; Odin & Fullagar, 1988).

Glauconite as a fertiliser can either be directly applied in the field or as a source of refined potash by processing to KCl (potassium chloride) or even purer forms of K (McRae, 1972; McConchie, 1978; Odin & Fullagar, 1988). The host rock or sediment containing the glauconite could all be directly applied as a fertiliser, but this is usually impractical and uneconomical due to low potassium contents, as well as the large cost of mining and transporting (Payne, 2008; Glauconite NZ Ltd, 2011). Glauconite as a fertiliser can easily be separated from the host rock or host sediment by de-sliming and magnetic separation to produce a 99% pure glauconite product (Bell & Goodell, 1967; McConchie, 1978, Compton, 1989; Potash West NL, 2011). Apart from the recognised source of potassium, glauconite also provides a beneficial source of magnesium and iron, and small amounts of phosphate, as a soil fertiliser (McRae, 1972; Coles *et al.*, 2002; Payne 2008). The magnetic separation process may lead to some carbonate and quartz impurities being present within the glauconitic fertiliser, but small amounts of these may actually be beneficial to the plants within the soil (Coles *et al.*, 2002).

KCl and K can be purified from glauconite using a process known as calcination, where sulphuric acid is added to the glauconite at temperatures of 500-700°C which can yield potassium recoveries of >50%. One calcination method is referred to as the Tschiner Process, in which greensand is mixed with lime-sand and salt and calcinated in a rotary kiln at 800°C. This enables the potash KCl to be leached out reaching a 90% recovery of potassium. Apart from calcination, acid leaching (or digestion) is another process which can purify potassium from

glaucanite, in the form of K_2SO_4 . The many methods used for the purification of potassium from glauconite have mostly been discovered by the Indian Geological Survey (Glaucanite NZ Ltd, 2011). Figure 10.1 summarises the various methods and also indicates the steps and % potassium recovered in each of these steps and methods (Glaucanite NZ Ltd, 2011).

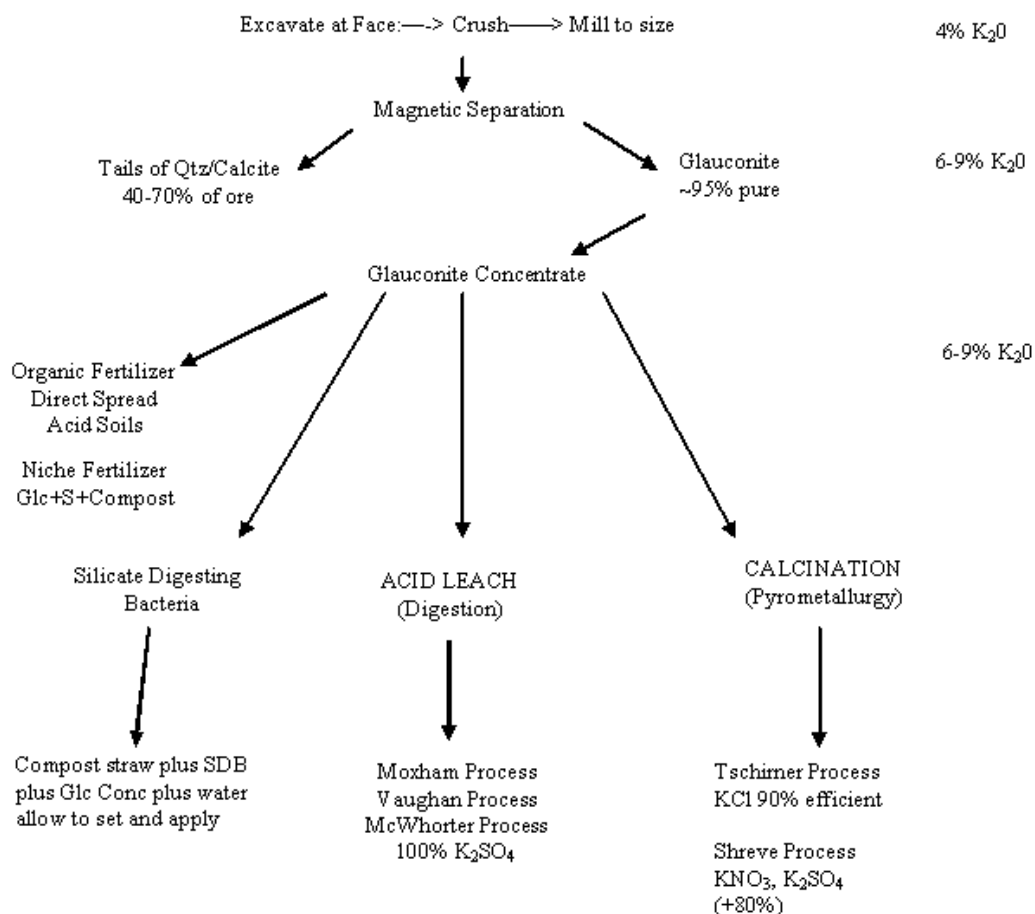


Figure 10.1: Glaucanite fertiliser purifying techniques (after Glaucanite NZ Ltd, 2011).

The KCl price has varied over time from historic prices of US\$150/t to over US\$870/t in 2008. Currently the price has settled to between US\$350 and 450/t (Potash West NL, 2011).

10.2.2 Water treatment

The second main economic use of glauconite is for water treatment, due to its high cation exchange capacity (CEC). The CEC within glauconite has a negative correlation with the potassium content, and therefore a deposit of glauconite is

typically used either as a fertiliser (if potassium is high) or for water treatment (if potassium is low, therefore CEC high), and not both.

Iron and manganese, although not a major health issue within water, do cause staining (on dishes), taste variations and accumulation problems (reducing pressure and availability). Therefore their removal from water is often preferred, which is where glauconite can help (Seelig *et al.*, 1992). Glauconite has a high cation exchange capacity which, depending on the resistance of the grains to disintegration, allows it to act as a water softener to aid water treatment. Glauconite for water treatment is mainly used in groundwater to filter soluble iron or manganese salts and hydrogen sulphide from the water. The glauconite acts in a similar manner to synthetic ion exchange resins, therefore absorbing the soluble iron and manganese (McRae, 1972; McConchie, 1978; Seelig *et al.*, 1992). The soluble iron and manganese contained within the water, once passed through the glauconite filter, will then react into insoluble forms that build up in the glauconite filter, and they can then be removed by backwashing (Seelig *et al.*, 1992).

10.2.3 Other uses

Glauconite is an extremely useful mineral used as a paleoenvironmental indicator of marine conditions, mostly due to its formation and concentration at marine unconformities and during sea level standstills. For this reason, it is often used for stratigraphic correlation, where even the absence or presence of glauconite can infer a lot about past environments (Triplehorn, 1966; McRae, 1972).

McRae (1972) and others recognise that the major use of glauconite in geological studies is for the absolute age dating of sedimentary rocks, which can be achieved using the K-Ar or Rb-Sr isotope dating method. In fact some 40% of the geological record for the last 250 myr has been dated using glauconite. Smith *et al.* (1998) report that glauconite is the only mineral facies that is adequately well spread enough to allow direct K-Ar and Rb-Sr age dating for sediments. However, glauconite may be slightly unreliable due to argon leaking which results in ages being too young, and because it can have variable compositions due to its complicated authigenic evolution on the seafloor. For these reasons, for glauconite

to be used for dating it must be syngenetic with the deposit, have minimal contaminations, and have a high potassium content, and the potential leakage of argon should be acknowledged (McRae, 1972; Smith *et al.*, 1998).

Other uses of greensand include paint pigment agent for artistic oil painting (Russia), mineral pigment (Rome), moulding sand, iron ore (e.g. in Egypt), glass polishing agent and as an industrial effluent filter and landfill lining for radioactive waste and heavy metals (McRae, 1972).

Glaucinite is also one of the most successful mineral absorbents, and so could possibly be used for the decolouration of crude petroleum and other organic liquids such as paraffin (McRae, 1972; McConchie, 1978).

10.3 RESOURCE ESTIMATE

To fully describe the glauconite as a resource on central Chatham Rise, some sort of resource estimate needs to be made, which is attempted here. Across central Chatham Rise, using the glauconite concentration within the analysed bulk surficial sediment samples, a weight percent map of glauconite was able to be constructed (Figure 6.2). Because this map was constructed using GIS software, the area covered by each of the ‘polygons’ (areas) that contain different amounts of glauconite wt% was able to be calculated. This gives a wt% of glauconite within different portions of central Chatham Rise. Using a conservative average thickness of the surficial sediment deposit on central Chatham Rise of 0.5 m (Figure 3.32 shows 26 analysed core depths which gives an average thickness of 0.6 m), the volume of each of the ‘polygons’ can be calculated. Due to the sediment being wet, a bulk average sand porosity of 40% is used, which leaves 60% of the volume being attributed to sediment. By using the volumes of each area and calculating the bulk density of glauconite (i.e. 2.64 t/m³) within each polygon based on 60% (sediment fraction) of the weight percentage (Figure 6.2) of glauconite within each 1 m³, a tonnage resource estimate for each polygon is able to be calculated (Table 10.1 and Figure 10.2). This calculation was carried out for the 50 wt% and greater polygons (i.e. for the most concentrated areas of glauconite over central Chatham Rise). Full calculations are shown in Appendix

VII (with the Excel spreadsheet also in Appendix VII). Table 10.1 and Figure 10.2 show that the glauconite resource estimate in the ≥ 50 wt% area of 4500 km² is approximately 2 Bt of glauconite. Even in the 80% glauconite area (i.e. 290 km²) there is 180 Mt of glauconite. Figure 10.2 demonstrates that the glauconite resource is mostly on or close to the topographic high known as Reserve Bank, on the shallower portion of central Chatham Rise in water depths of 200-300 m.

Table 10.1: Glauconite resource estimates in different sectors of central Chatham Rise, based on wt% glauconite, density, area and volume (see Figure 10.2 for polygon areas).

Polygon glauconite average %	Area m²	Volume m³	Density (t)	Glauconite weight (Mt)
80	285900000	142950000	1.2672	181
75	503280000	251640000	1.1880	299
65	759000000	379500000	1.0296	391
55	2976360000	1488180000	0.8712	1297
50% and above	4524540000	2262270000		2168

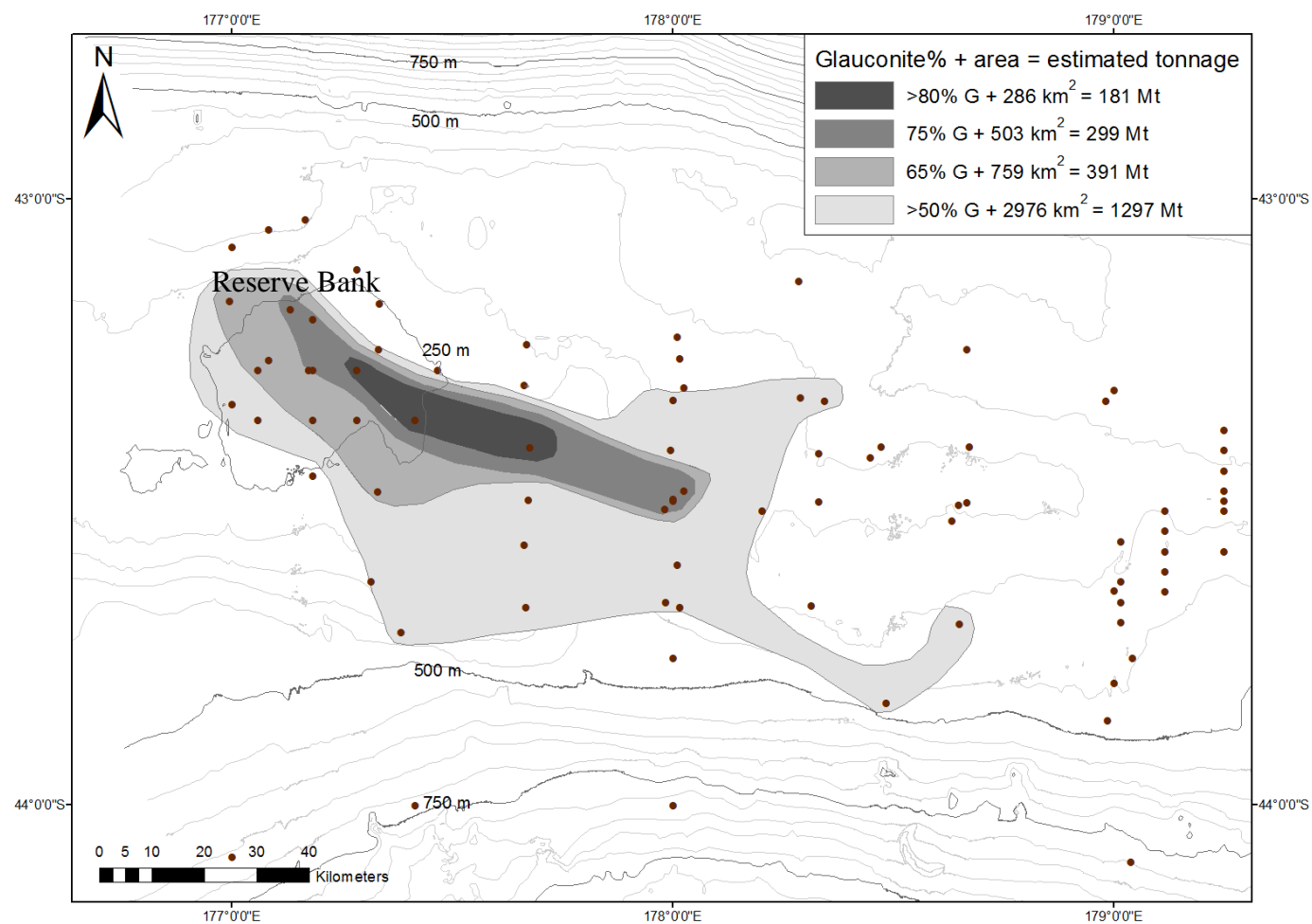


Figure 10.2: Glauconite resource estimates in the four most concentrated areas (based on glauconite wt% in Figure 6.2) across central Chatham Rise (Table 10.1).

Chapter 11

DISCUSSION OF GLAUCONITE

11.1 INTRODUCTION

This chapter discusses the data provided in previous chapters on the physical properties, mineralogy, geochemistry and age of glauconite on central Chatham Rise. It also includes a discussion of the origin(s) and economic potential of the glauconite in relation to this evidence. The final section briefly compares the central Chatham Rise glauconite deposit to some onland Late Cretaceous – Cenozoic greensand deposits in New Zealand, with the aim of seeing whether or not the Chatham glauconites provide any kind of modern analogue for glauconite formation and interpretation in the rock record.

11.2 NATURE OF GLAUCONITE

This section provides a discussion of the nature of glauconite on central Chatham Rise in relation to the data and descriptions presented earlier concerning its physical properties (Chapter 6), mineralogy (Chapter 7), geochemistry (Chapter 8), and age (Chapter 9).

11.2.1 Occurrence and distribution of glauconite

Glauconite makes up a major sediment component within the surficial sediments covering central Chatham Rise which mainly overlie partially indurated Oligocene chalk. The present study involved a re-evaluation of the nature and distribution of the surficial sediment facies across central Chatham Rise (Chapter 3), which led to the production of a new surficial sediment map for the area, reproduced again here in Figure 11.1. The map shows the contribution of the main sediment types (i.e. glauconite, phosphorite nodules and carbonate) and textures, and highlights the importance of the glauconite contribution, particularly in water depths <500 m, where it is often >30 wt%, and over the shallowest parts of the Rise centred on or near Reserve Bank in <250 m water depths where it is >80

wt%. The average thickness of the surficial sediment deposit is about 0.6 m, ranging from 0.06 to over 1.35 m (Figure 3.32).

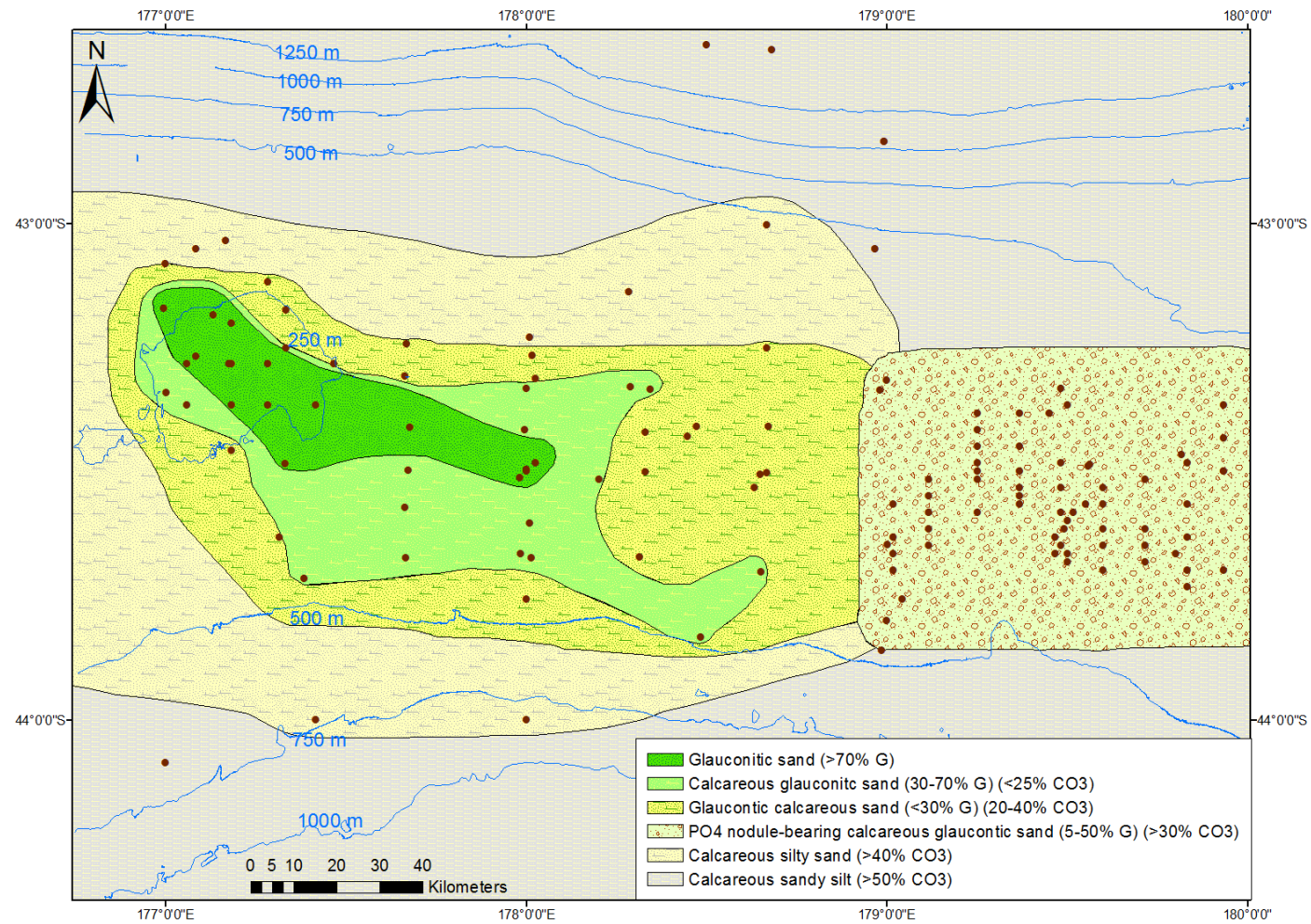


Figure 11.1: Surficial sediment facies map for central Chatham Rise developed in this study. G=glauconite, CO₃ = carbonate, PO₄=phosphate.

11.2.2 Physical properties

The physical properties of the glauconite on central Chatham Rise were described in Chapter 6 following Frantz magnetic separation, detrital observation under a binocular microscope, thin section examination with a petrographic microscope, and some high-magnification SEM. The documented physical properties of glauconite included their distribution (Section 11.2.1), colour, size, morphology and internal fabrics.

The majority (>50%, often >75%) of glauconite on central Chatham Rise has a dark green to black colour, which translates into a bottle green colour in thin section, but other colour varieties present include light green, yellow-brown and red, sometimes with black inclusions. The colour of glauconite grains can reflect their origin, mineralogy and geochemistry. The dominant dark green to almost black glauconite pellets most likely corresponds to a highly mature glauconite rich in potassium and iron, while the lighter green varieties reflect glauconite with a lesser maturity and lower potassium and iron content (Figure 6.3). The yellow-brown glauconite pellets in thin section are a common (15-25%) colour variety on central Chatham Rise and probably relate to a lowish level of glauconite maturity or to grain oxidation (McRae, 1972; Odin & Matter, 1981). Red limonitised glauconite grains seen in thin section are uncommon (1-15%) and have formed from oxidation of the iron within glauconite to yield rusty red-brown limonite (McRae, 1972; Udgata, 2007). Black (opaque) inclusions in some of the glauconite grains (5-20%) often show a sparkly gold colour in reflected light, indicating that they are pyrite. The geochemistry and origin of these colour varieties will be further discussed in Section 11.2.4.

Glauconite pellets on central Chatham Rise have a typical average size between 0.15 and 0.2 mm, or fine sand-sized. Their full size range is from 0.025-2.7 mm, which relates mainly to morphological type.

The present study has recognised seven morphological types of glauconite on central Chatham Rise, namely ovoidal, lobate, composite, fossil casts, pigmentary, tabular, and pellets within rock fragments (Figure 6.10). The morphology of glauconite grains may help reveal their mode of origin, but this can be complicated by any transport or reworking of grains. By far the most common

morphology (>75%) is ovoidal pellets which are typically 0.2 mm in size and have a smooth surface polish with no evidence of breakage. The roundness and very smooth polished surface of these grains indicate they are definitely allogenic (i.e. transported/reworked) (e.g. Triplehorn, 1966). Consequently, they previously may have had a different morphology that was subsequently modified by erosion into smooth ovoidal pellets. This is typical for many lobate pellets in which reworking can reduce their size to an extent that they lose their deep radial cracks and appear as ovoidal grains (Figure 11.2) (e.g. Triplehorn, 1966; Amorosi, 1997; Udgata, 2007).

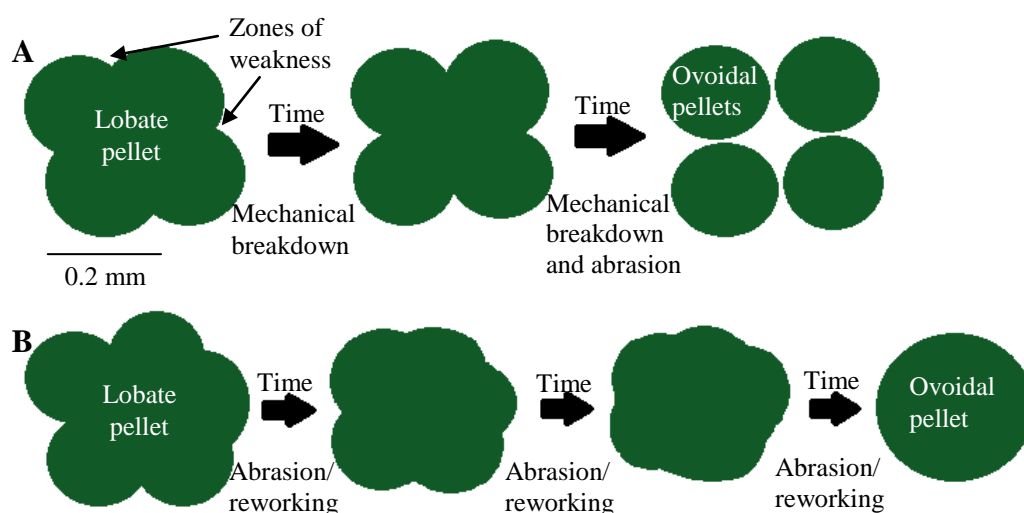


Figure 11.2: Schematic diagram showing how lobate grains can transform into ovoidal grains, due to mechanical breakdown (A) or by abrasion and reworking (B).

Lobate pellets are the second main morphological type of glauconite on central Chatham Rise, averaging about 15% of populations, but as just noted lobate grains may originally have had a higher abundance. Lobate grains are popcorn shaped irregular large (av. 0.3-0.4 mm; Figure 6.12) grains made up of rounded lobes separated by deep radial cracks that are typically infilled with white crystalline material. SEM reveals this white infill comprises over 90% coccolith plates and debris, as well as some foraminiferal and other fine skeletal material, cemented together by microcrystalline calcite. The cracks within lobate grains have most likely formed due to expansion of the pellets during mineral growth, which accounts for the fact that the cracks develop radially and taper inwards. However, partial desiccation is an alternative but less likely reason for crack formation, resulting from dehydration during mineralogical evolution (McRae, 1972; Udgata, 2007). The dark green to black colour of lobate grains and other morphological

types that contain cracks suggests they are a highly mature glauconite variety. However, the cracks within the lobate grains are typically zones of weakness so that they are susceptible to mechanical breakdown into less irregular fragments which upon further abrasion ultimately transform into smaller (<0.2 mm) ovoidal grains (Figure 11.2A). Another mechanism which could cause lobate grains to transform into ovoidal pellets is simply by abrasion and reworking, due to their allogenic nature (Figure 11.2B) (e.g. McRae, 1972; Odin & Matter, 1981; Amorosi, 1997; Udgata, 2007).

The third morphological type of glauconite on central Chatham Rise is composite pellets, which accounts for approximately 5% of the glauconite population. In the present study composite grains are also referred to as glauconitised phosphatic grains, which reflects their origin. These grains are the largest of the morphologies at about 0.6-2 mm size, and are composed of small glauconite pellets and other minerals set in a pale green low maturity glauconitised and phosphatised matrix. Composite grains may also support glauconite filled (precipitated) fractures whose dark green colour is supportive of more mature and highly evolved glauconite compared to the matrix material (Odin & Matter, 1981).

Glauconite can also replace or infill skeletal carbonate grains, resulting in fossil cast and internal molds respectively. These grains are relatively uncommon (1-5%) but widely distributed across the entire central Chatham Rise. Foraminiferal chambers are the main focus of internal molds whose shapes reflect the internal chamber morphology of the host skeletal grains (McRae, 1972). On central Chatham Rise glauconite as internal molds typically has a light yellow brown colour. The chambers of internal mold glauconite may later be destroyed, leaving the pellets with the internal shape of the host skeleton (McRae, 1972). Fossil casts in contrast form due to replacement by glauconite of skeletal test calcite and so their morphology reflects the external shape of the original organism (Figure 11.3) (McRae, 1972); this variety is rare amongst central Chatham Rise glauconites. Planktic foraminifera are the dominant host for both of these glauconite morphologies, followed occasionally by benthic foraminiferal.

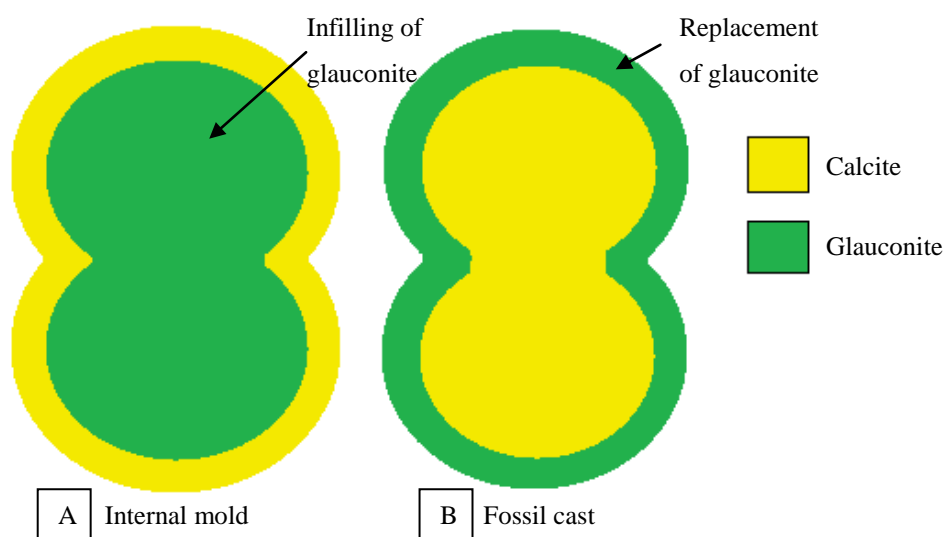


Figure 11.3: Examples of internal mold (A) versus fossil cast (B) morphologies. A also illustrates an example of the internal fabric of skeletal infills.

The final three morphological types of glauconite on central Chatham Rise are tabular/discoidal grains, pigmentary grains, and pellets within rock fragments. Tabular grains appear as flattened elongated discs, are very uncommon and have most likely formed from clay shale flakes or chips (cf. Triplehorn, 1966; McRae, 1972). Pigmentary glauconite occurs as a coating on other grains, typically phosphorite nodules in the case of central Chatham Rise (Figure 6.19), and may have formed due to marginal replacement or precipitation about the nodules. Marginal replacement is the favoured origin since the foraminiferal tests within these rims have been glauconitised (i.e. are fossil casts), but in some cases even their chambers have been completely glauconitised leaving only the shape of the original foraminiferal grain and no calcite (Figure 6.19E and F). Another feature which shows the rim has formed due to replacement is the dark green mature glauconite fractures protruding in places through some of these grains replacing the calcite by glauconitisation. Figure 11.4 shows a diagram of the formation of film glauconite, which is defined as glauconite which forms coatings on large grains. In the case of the central Chatham Rise glauconites this diagram shows how the pigmentary (and possibly composite) glauconite forms, illustrating how glauconite replaces the outside of the grain (i.e. phosphorite nodule) and how fractures of glauconite can protrude through the grain.

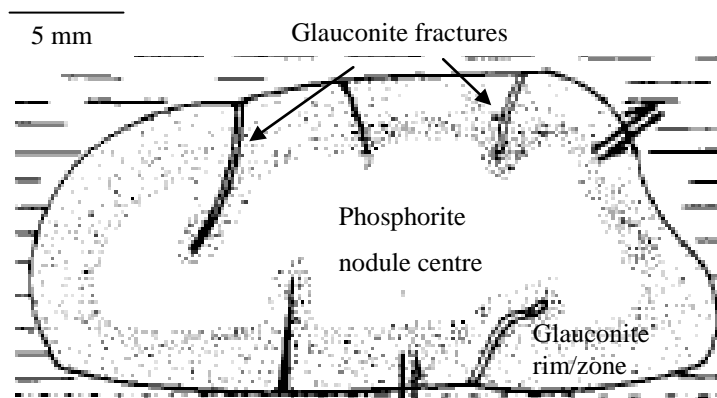


Figure 11.4: Glaucanitisation of a phosphorite nodule by a rim of pigmentary glauconite, with more mature glauconite fractures protruding through the nodule due to replacement (modified after Odin & Matter, 1981).

A much less common (1%) morphological variety of glauconite is where the very abundant ovoidal pellets (av. 0.15-0.2 mm) are found cemented within rock fragments. This could mean that such glauconite may have been submarine eroded out of underlying sediments (Section 11.3.5).

The geochemistry and origin of the morphological varieties of glauconite are discussed further in Section 11.2.4.

Three types of internal fabric have been recognised for central Chatham Rise glauconites, namely random microcrystalline, oriented fibroradiated rims and skeletal infilled grains (Figure 6.21). Random microcrystalline is the most common internal fabric for glauconite globally (Triplehorn, 1966; McRae, 1972), and occurs in >80% of the central Chatham Rise glauconites. The fabric results from the overlapping of tiny micaceous crystals having no preferred orientation. Some 15% of central Chatham Rise glauconites show oriented fibroradiating rims, typically upon an inner core with a random microcrystalline fabric. The rims on such grains are brown and exhibit a much higher birefringence than the green inner core, and they are oriented with a parallel wavy extinction (Triplehorn, 1966; McRae, 1972). Geochemical evidence for the formation of these grains is discussed in Section 11.2.4. The third type of internal fabric is skeletal infilled grains, essentially equating to the internal mold morphological grains mentioned earlier (Figure 11.3A). The variety is uncommon (5%) as an internal fabric which reflects the internal chamber shape of the skeleton infilled.

11.2.3 Mineralogy

Analysis of the mineralogy of the glauconite on central Chatham Rise using XRD has indicated it is a disordered 1Md montmorillonitic glauconitic mica polymorph that has % expandable smectite layers in the range of 10-20%. Results also show that the potassium content within the glauconite increases with decreasing % expandable smectite layers (Figure 7.5), and that the glauconite has an allevardite-like interstratified stacking (Figure 7.10).

The fact that the glauconite has a (001) XRD peak position within the 10-12.5Å range, corresponding to the presence of 10-20% expandables, along with the fact that the glauconite is dark green with a potassium content over 7 wt% K₂O, show that Chatham Rise glauconite has a high to very high maturity and can be classified as evolved to highly evolved glauconitic mica (cf. Table 8.1, redrawn here as Figure 11.5).

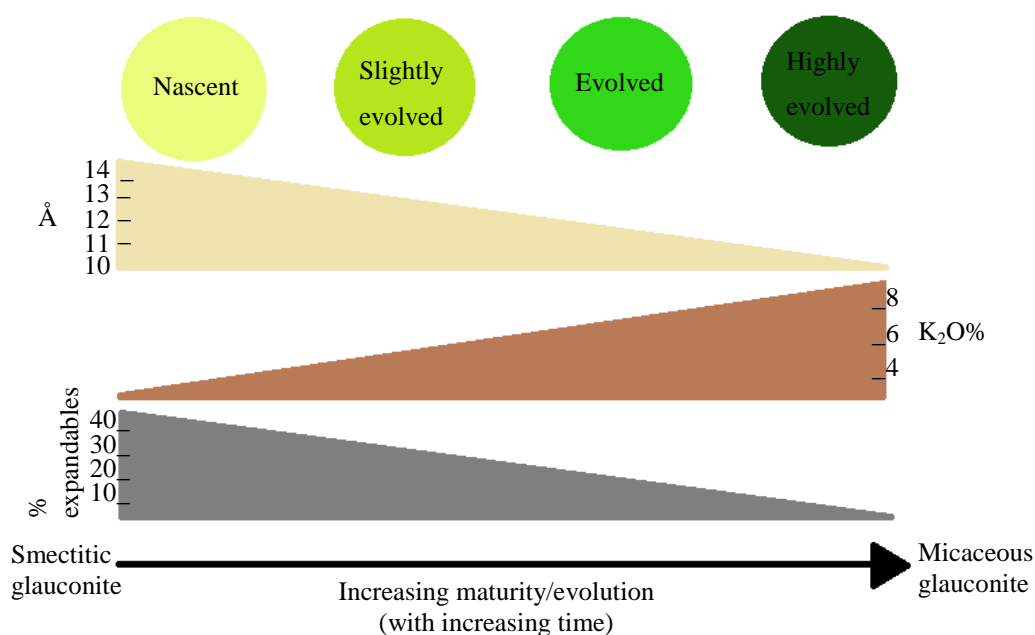


Figure 11.5: Redrawn illustrative version of Table 8.1, showing the four glauconite evolution categories defined by Odin and Matter (1981), their colour, XRD (001) Å peak position, potassium content, % expandables, structure and maturity (after Odin & Matter, 1981; Udgata, 2007).

In Chapter 4, the mineralogy of the clay fraction from the bulk samples on central Chatham Rise was investigated. This showed that the clay minerals present were predominant illite and chlorite. The apparent absence of smectite in the sediment clay fraction at the present day suggests that any active glauconite formation in

the modern is minimal. This is supported by the evolved to highly evolved nature of the glauconite grains on the Rise. Odin and Matter (1981) suggested that the maturity of glauconite reflects the amount of time that grains have been resting on the seafloor pre-burial. Consequently the highly evolved and mature nature of the central Chatham Rise glauconites precludes an actively authigenic origin for the grains.

11.2.4 Geochemistry

The geochemistry of the bulk glauconite and glauconite varieties (i.e. colour, morphology and internal fabric) on central Chatham Rise were described in Chapter 8. This section discusses these results with the aim of fully classifying the glauconite on the Rise and evaluating possible modes of formation and origin (Section 11.3), as well as economic potential (Section 11.4).

The major elemental geochemistry of the glauconite on central Chatham Rise was determined using XRF on pure bulk glauconite concentrates. Average results were given in Table 8.4, and indicated that the glauconite has high potassium and iron contents, av. 7.2 (K₂O) and 20.3 (Fe₂O₃*) wt%, respectively. This geochemical evidence alone indicates that the glauconite on the Rise must have a high maturity level and can be classified as evolved glauconitic mica, on the basis of the common varieties recognised by Odin and Matter (1981) (Figure 11.5).

The relationships and correlations between all the major elements in glauconite were reported in Table 8.3 and some interesting interpretations can be made. As expected for most glauconites, the central Chatham Rise glauconite shows a positive relationship between K₂O and Fe₂O₃* ($r^2 = 0.69$; Figure 8.1). This relationship progresses as the glauconitisation process proceeds (i.e. as the glauconite become more mature/evolved) and both the Fe₂O₃* and K₂O contents increase towards the glauconitic mica/illite end member (McConchie, 1978; Odin & Matter, 1981; Compton, 1989). K₂O content increases with the evolution of glauconite due to absorption into the interlayer crystallographic position, while Fe₂O₃* also increases with glauconite evolution, but does so through absorption and incorporation into the silicate lattice (Hower, 1961). However, according to

Compton (1989), this relationship may not be linear so that the uptake of Fe_2O_3^* may not be controlling the uptake of K_2O .

A correlation was not found between Fe_2O_3^* and Al_2O_3 , which is interesting as typically Fe_2O_3^* increases at the expense of Al_2O_3 as glauconitisation proceeds. This lack of correlation could be due to the evolved nature of the glauconite on central Chatham Rise, since Compton (1989) suggested that the Fe/Al ratio can decrease with the evolution of the glauconite grains, and so the evolved Chatham Rise glauconite would not be expected to show any good Fe-Al correlation.

The central Chatham Rise glauconites show some interesting correlations of MgO with other major elements that are not usually expected in glauconite, despite the MgO content of 4 wt% being typically expected in glauconites (McRae, 1972). MgO shows a good positive correlation with tetrahedral SiO_2 ($r = 0.71$) which may mean that the majority of MgO cannot be in the tetrahedral sheet or else a negative correlation would have been observed due to it replacing SiO_2 , which therefore suggests that most of the MgO must be in interlayer positions. This is further evidenced by the moderately good positive correlation ($r = 0.61$) between MgO and Al_2O_3 , the latter occupying both tetrahedral and octahedral sites. K_2O and MgO are thought to be taken up by glauconite from sea water, where both elements are first attracted to the interlayer sites. However some MgO may enter octahedral sites after being in interlayer sites (Odin, 1975; McConchie, 1978). This could be the case in central Chatham Rise glauconites as shown by the small negative correlation between MgO and octahedral Fe_2O_3^* ($r = -0.28$), which would mean at least some of the MgO must be contained within octahedral sites at the expense of Fe_2O_3^* . Also the positive relationship between MgO and Al_2O_3 described above that concluded MgO must be interlayer, could be more related to tetrahedral Al_2O_3 as opposed to octahedral Al_2O_3 , therefore meaning that some of the MgO is octahedral. McConchie (1978) suggested that high Fe_2O_3^* and Al_2O_3 contents (as occurs in the central Chatham Rise glauconites) may restrict MgO entry into octahedral sites, which is what is most likely causing the majority of the MgO to be contained within interlayer sites in central Chatham Rise glauconites.

Within glauconite the K_2O content typically increases with decreasing water content, and hence the % expandable layers, and so a negative correlation would

be expected. For the glauconite on central Chatham Rise the LOI (loss on ignition, indicative of the water content) does show a slight negative correlation with K_2O ($r = -0.35$). This is because K_2O occupies interlayer sites in order to balance the net negative charge (CEC) that glauconite has, and once an interlayer cation is in place it becomes ‘locked’ and therefore non-exchangeable, thus explaining why the % expandables decrease with increasing K_2O . Hower (1961) and McRae (1972) therefore suggest that the cation exchange capacity varies in an inverse way with potassium content, and hence the % expandables content. Due to the positive correlation between K_2O and $Fe_2O_3^*$, and the negative one between K_2O and both H_2O and % expandables, one would expect a negative correlation between $Fe_2O_3^*$ and both H_2O and % expandables. This is so for the central Chatham Rise glauconites, where the % expandables correlates negatively with $Fe_2O_3^*$ at $r = -0.72$. This situation occurs because as glauconite evolves both the Fe_2O_3 and K_2O increase, which in turn is associated with a decrease in water content and therefore of the % expandable layers.

Geochemical results for trace elements in the central Chatham Rise glauconites determined using XRF, as well as literature analysis, reveals four groups of trace elements based on the correlations with both major and trace elements, and the sites they occupy (Table 11.1).

Table 11.1: Outline of the four groups of trace elements within central Chatham Rise glauconites, based on their associated crystallographic position.

Group	Elements	Crystallographic position
1	Mn, V, Zr, Ti, Ba, Cr, maybe Zn, Nb and Ni, and sometimes Y	Octahedral lattice sites
2	P, S and sometimes Y	Lattice positions, bound to broken edges of tetrahedral sites
3	Rb, Sr and maybe Ca	Interlayer positions
4	Pb and Cu, and possibly La and Ce	Unknown, but possibly exist due to uptake from seawater

Group 1 trace elements are transition metals which occupy octahedral lattice sites within glauconite (McConchie, 1978) and include Mn, V, Zr, Ti, Ba, Cr, maybe Zn, Nb, and Ni, and sometimes Y. These elements are related in terms of their abundance and high positive correlations with each other, and they also correlate

well with Fe_2O_3^* , K_2O , CaO and Na_2O . Group 1 elements correlate negatively with Fe_2O_3^* because they are transition metals, therefore indicating they may occupy octahedral sites over Fe_2O_3^* . These elements thus also correlate negatively with K_2O , but this does not necessarily mean these elements would occupy interlayer sites over K_2O , as the relationship could simply be due to the positive correlation between Fe_2O_3^* and K_2O . Because K_2O and Fe_2O_3^* increase with increasing glauconitisation, and because the central Chatham Rise glauconites are mature/evolved, this means that group 1 trace elements do not have high concentrations, averaging only 26-125 ppm.

Group 2 trace elements include P and S, and sometimes Y. These elements occupy lattice positions where they are bound to broken edges of tetrahedral sites within the crystallographic structure of glauconite on central Chatham Rise. They are mostly present within coatings on grains, therefore within pigmentary glauconite (i.e. glauconite rims on phosphorite nodules), and are also concentrated within composite grains (i.e. glauconitised phosphatic grains). P has a very high concentration within composite grains, which may be attributed to the coatings on grains, but is most likely related to the phosphatic-apatite nature of these grains. In contrast, P does not show a major increase in fibroradiated rims compared to their inner cores, which would be expected as the rims represent coatings on the glauconite grains. However, as the P concentration is so low in fibroradiating rims, any significant differences are hard to detect. Y within this group can be explained by the fact that it is related to apatite, the main phosphatic mineral in the composite grains. S is relatively concentrated within both the composite grains and fibroradiated rims.

Group 3 trace elements on central Chatham Rise typically occupy interlayer positions due to their correlations with the % expandables, and include Rb, Sr and maybe Ca. Both Sr and Ca correlate positively with the % expandables and thus negatively with K_2O , whereas Rb shows the opposite relationship. Sr and Ca are therefore exchangeable within interlayer sites, while most of the Rb present within glauconite must therefore actually be held in non-exchangeable layers (Hower, 1961; McConchie, 1978).

Trace elements within group 4 have very low concentrations and their crystallographic position within central Chatham Rise glauconites is unknown. These elements do not show any correlations with major and other trace elements, and include Pb and Cu, and possibly La and Ce. Phyllosilicate minerals in general, such as glauconite, are capable of concentrating Pb and Cu readily from seawater, so explaining the presence of these elements (Krauskopf, 1956 in Compton, 1989).

Different colour/morphological varieties of glauconite on central Chatham Rise were microprobed in order to evaluate their major elemental geochemistry. Microprobe results on the individual dark green to black ovoidal glauconite varieties yielded a slightly different major elemental geochemistry compared to the bulk glauconite concentrates. The main difference was that the potassium (K_2O) content is 1.7 wt% higher than in the bulk glauconite concentrates from XRF, being 8.9 wt% compared to 7.2 wt%. This difference indicates that the main morphological type of glauconite on central Chatham Rise, namely ovoidal dark green to black pellets, are even more mature than was first concluded from XRF analysis, classifying as highly evolved glauconite (Figure 11.5). XRF results of bulk glauconite samples reveal higher calcium values, undoubtedly due to the presences of CaO impurities associated with composite grains and skeletal infills in particular.

It is an accepted fact that glauconite can have a wide range of colours, and on the central Chatham Rise the main colour is dark green to black. However, some 15-25% of the glauconite grains display a range of greenish-brown to brown shades, in which these grains have irregular cracks and irregular shapes. The major elemental geochemistry of these brownish glauconite grains revealed that they have lower K_2O contents but slightly higher $Fe_2O_3^*$ and Al_2O_3 contents compared to the more typical dark green ovoidal pellets. This could reflect a lower maturity, as indicated by the K_2O content of 6.4 wt%, which would classify the glauconite as evolved or slightly evolved (cf. Figure 11.5; Odin & Matter, 1981). A more likely explanation for the geochemical differences is that these brown grains are slightly limonitised, in which the glauconite has been oxidised by weathering or by heating in oxidising waters, which would increase the iron contents and change the colour to a rusty brown indicative of limonite (Figure 11.6) (McRae, 1972). This explanation is further supported by the occurrence of much more rusty red

grains that are further limonitised and form 1-15% of central Chatham Rise glauconites (Section 6.4). The marine environment may have changed periodically to a relatively more oxidising one if subsurface AAIW (Antarctic Intermediate Water; Figure 2.6) somehow influenced the shallower depths of the Rise, as AIWW is characterised by slightly oxidising waters. This happened at Site 593 in the south Tasman Sea in the Middle Miocene which periodically turned the accumulating nannofossil oozes an orange oxidised colour compared to their regular white-grey colour (Nelson, 1986). If these brown grains are brown due to oxidation, then they may actually be older than the dominant Late Miocene dark green ovoidal grains.

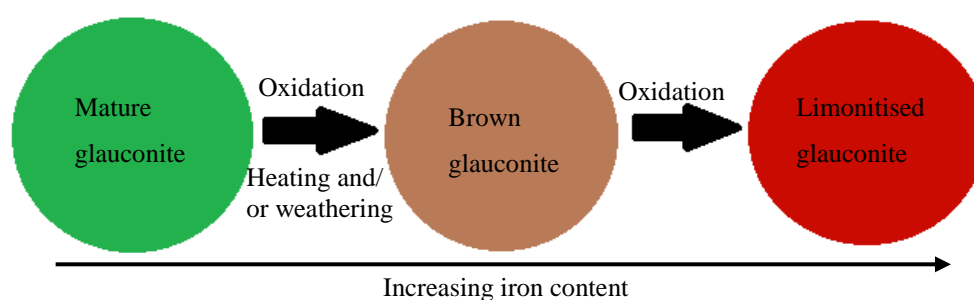


Figure 11.6: Schematic illustration of the progressional development of glauconite being oxidised into brown and then reddish brown (limonite) colours.

An internal fabric of glauconite that is moderately common (~15%) on central Chatham Rise involves grains which support discrete brown fibroradiating oriented rims. These rims have both lower K_2O and $Fe_2O_3^*$ contents compared to their inner core, as well as lower MgO and SiO_2 contents, in which these decreased values are made up for by a much higher Al_2O_3 content. The lower K_2O and $Fe_2O_3^*$ contents suggest that the rims are less mature and thus less evolved than the inner glauconite core (Odin & Matter, 1981), and that they may have formed after core formation. Another possibility is that the rims have been, or are being oxidised/limonitised, in which green Fe^{2+} could be oxidising to brown Fe^{3+} . However, this could not explain the geochemical differences between the inner core and rim.

If the rims were precipitated after the inner core formation they would be less mature, which could explain some of the geochemical differences. If the rims were precipitated, this would explain their higher Al_2O_3 content due to them being less mature and having a higher clay component (i.e. Al_2O_3). This idea of lower

maturity would also explain the lower K_2O content. Others (Triplehorn, 1966; McRae, 1972) have also suggested that rims form due to accumulation or precipitation and are not due to alteration/oxidation, therefore indicating that the rims are less evolved. Odom (1976), who analysed oriented rims on glauconite grains of Cambrian age from central USA, found similar geochemical results as in the central Chatham Rise glauconites (i.e. lower $Fe_2O_3^*$ and higher Al_2O_3). Odom (1976) concluded that the rims formed due to concretionary growth, in which the pellets grew from the repetitive development of smectite clay at the margins of the grains. The smectite was then altered into low maturity brown oriented glauconite (rims), and subsequently into unoriented mature dark green pellets (inner cores) (e.g. Figure 11.7). Such a mechanism could account for the brown rim glauconite on the central Chatham Rise.

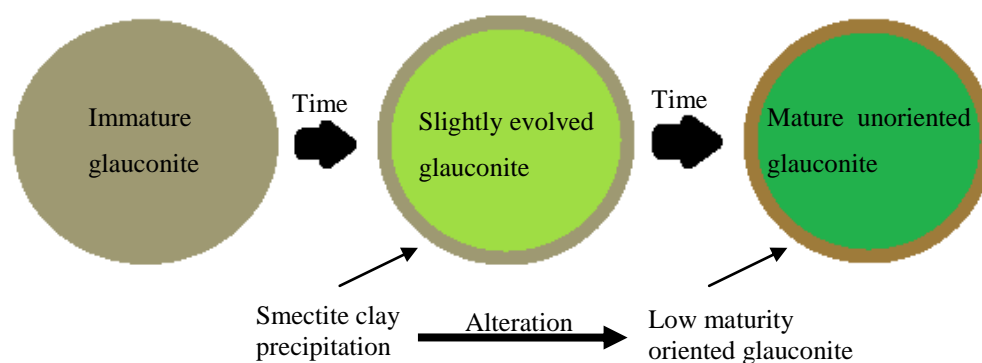


Figure 11.7: Schematic diagram of an oriented rim development about a glauconite pellet.

Another uncommon (1-5%) morphology and internal fabric of glauconite on central Chatham Rise are the glauconite skeletal infills, mostly foraminiferal. The major elemental geochemistry of these grains has marked differences to the more typical ovoidal pellets, having a geochemistry intermediate between more typical glauconite grains and calcium carbonate grains. The original carbonate make-up of the skeletal grains is shown by the average CaO and P_2O_5 values of 14.9 and 12.2 wt%, respectively. However, although the grains still have carbonate major oxides (i.e. CaO and P_2O_5) it is obvious that the grains are being infilled with glauconite as they consist of glauconite major oxides, as shown by the K_2O and $Fe_2O_3^*$ wt% of 5.9 and 14.8, respectively, which indicate a moderately mature or slightly evolved glauconite (Figure 11.5).

From the geochemical analysis of the large (0.5-2.5 mm) glauconitised phosphatic grains (i.e. composite grains) a three step replacement process is suggested. The

first begins as foraminiferal limestone that is calcite dominated. The second step involves limestone clast formation and phosphatisation into a mixture of calcite and apatite, while the last involves the calcite within the grain being replaced by glauconite. This would explain the geochemistry of these grains in which there is high CaO and P₂O₅ wt% values of 30.4 and 24.6, respectively, and much lower glauconite major oxides of K₂O and Fe₂O₃* of 3.4 and 8.6 wt%, respectively, accounting for the lowish glauconite maturity and its slightly evolved form (Figure 11.5). This three step process can also explain the presence of mature darker green glauconite pellets that resemble foraminiferal casts, which must have formed due to glauconitisation of the calcitic planktic foraminifera within the grain, as well as the highly mature glauconite veins or fractures fills which form as glauconite replaces the calcite in small cracks of the grain (Figure 11.4).

11.2.5 Age

The glauconite from five widely separated samples on central Chatham Rise was dated using the K-Ar isotope dating method (Chapter 9). Results indicate an age range of 5.46 – 6.0 Ma for the glauconite, with an average of 5.75 Ma, all with small errors. The narrow age range supports this being a reliable age, including for the downcore (0-13 cm) samples from U6866. 5.75 Ma corresponds to a Late Miocene age, equivalent to the Kapitean Stage in New Zealand or the Messinian Stage internationally (Gradstein *et al.*, 2005). A Late Miocene age for the glauconite on central Chatham Rise is consistent with the conclusion that it is not currently or actively forming today, and so it must be allogenic rather than authigenic. It also raises the question of what happened in the Late Miocene to allow such vast amounts of glauconite to form, addressed in the following sections.

11.3 ORIGIN(S) OF GLAUCONITE

Theories of glauconite formation were discussed in Section 5.8. It was noted that glauconite can have different origins for which the specifics are not well known. Most generally, glauconite typically forms in a marine environment experiencing slow depositional and other conditions (Section 5.9) where a source of smectite is available along with appropriate supplies of potassium and iron. There are seven

main sedimentary conditions to consider for glauconite formation during Late Miocene time on central Chatham Rise, namely organic matter content, Eh and pH values, water temperature, sediment accumulation rate, water turbulence and water depth.

11.3.1 Conditions and place of formation

Glauconite formation is potentially likely in areas where cold and warm water meet resulting in high amounts of organic productivity. This is the case on the Chatham Rise which delineates the position of the STF in the Southwest Pacific adjacent to New Zealand (Figure 2.6) and is a known zone of prominent upwelling and primary organic productivity. Bacterial decay of the organic detritus falling to the seafloor provides the suitable slightly reducing Eh and pH 7-8 conditions needed for glauconite formation. The optimum water temperature for glauconite formation is typically between 15 and 20°C (McRae, 1972). The STF zone over Chatham Rise currently experiences a 15°C surface isotherm temperature in summer and a 10°C isotherm in winter (Wilson *et al.*, 2004). Given that the STF upon Chatham Rise has been in existence since at least the Middle Miocene (Nelson & Cooke, 2001; Carter *et al.*, 2004), the above kinds of conditions would likely have existed during the Late Miocene.

The focus of glauconite formation on Chatham Rise resides upon and near the Reserve Bank (Figure 6.2). Reserve Bank is the shallowest area on central Chatham Rise at <250 m water depth and is sufficiently elevated and isolated to currently ensure low inputs of terrigenous sediment. Sedimentation rate is considered to be the most important controlling factor on glauconite formation, which must be very low or even negative, thus explaining the common association of glauconite with unconformities (Burst, 1958; Hower, 1961; McRae, 1972; McConchie, 1978). Also, because of the shoaling water depths onto Reserve Bank bottom currents may be more influential than in the surrounding deeper waters, providing the slightly agitated water conditions regarded as appropriate for glauconite development (McRae, 1972; McConchie, 1978). Nevertheless, glauconite is known to form over a wide range of water depths from 15-2000 m, although it most typically forms on the continental shelf in water depths <150 m. In this regard, at least during glacial periods in the Late Miocene it is probable the

water depths over much of Reserve Bank were in the order of 100-200 m. The clear pattern of gradual glauconite wt% decrease in a southeastwards direction away from Reserve Bank (Figure 6.2) can be explained by reworking and transport of allogenic grains in the main water flows (e.g. Southland Current) (Figure 2.6) in a south to southeasterly direction on the Rise (von Rad, 1984; Sutton, 2003).

What might have been “special” about the Late Miocene period of time on Chatham Rise? Grant (2005) provides some relevant information in her study of Late Neogene biogenic sedimentation and carbon isotope shifts in the Southwest Pacific Ocean. She demonstrated that between 9 and 3.5 Ma (i.e. Late Miocene to Early Pliocene) the STF zone over Chatham Rise experienced higher than average organic productivity, with maximum productivity in surface waters occurring from about 6-5 Ma, the time of major glauconite formation on the Rise. Such enhanced biogenic blooms relate to intensified upwelling of nutrients enriched subsurface water masses, perhaps of AAIW. The blooms are reliant on and caused by significant increases in nutrient availability, especially of nitrate, phosphate and silicate, some of which also directly promote glauconite formation (Section 11.3.4).

Also occurring in the Late Miocene was the “Chron C3Ar carbon shift” which was associated with a significant decrease of -0.6 to -1.5‰ in the $\delta^{13}\text{C}$ composition of bulk sand foraminiferal carbonate, recognised in deep sea cores globally, and from the Chatham Rise sector of the Southwest Pacific. This event was caused by an overall increase in terrigenous flux rate and presumably an associated increase in the supply of organic material to the Chatham Rise in the latest Miocene, as well as oceanic hydrography variations and changes in the calcite compensation depth (Grant, 2005). Climate change affecting ocean circulation is most likely the ultimate cause of the Late Neogene biogenic blooms and carbon shift which occurred in the Southwest Pacific Ocean, probably driven by the growth of Antarctic ice sheets. More specifically, the hydrographic change within the STF zone affected nutrient cycling and the carbon isotopic variation in the water column (Grant, 2005).

11.3.2 Glauconitisation process

The glauconitisation process has been much disputed over time by different workers; here I suggest two possible processes for the central Chatham Rise glauconites. First, the “layer lattice theory” developed by Burst (1958) and Hower (1961), which requires a smectite source. Second, “verdissement” or “neoformation” suggested by Millot (1970), Odin and Matter (1981) and Odin and Fullagar (1988), which requires a porous substrate/hardground, such as calcareous grains.

The “layer lattice theory” is the most commonly cited process (Burst, 1958; Hower, 1961; McRae, 1972; McConchie, 1978; Udgata, 2007), and states that a mineral having a generally similar crystallographic structure to glauconite, such as smectite, must be present. Given a smectite content in surficial sediments, along with the appropriate environmental conditions discussed in Section 11.3.1, glauconitisation of smectite can occur. This process is often aided by the aggregation of smectite from the passage of fine sediment through the digestive tract of organisms, which can also provide the necessary microenvironment favoured for glauconite formation. For the “layer lattice theory” of glauconite formation to occur, three conditions must be met. First, the presence of a degraded silicate lattice, which is here provided by the smectite source. Second, suitable Eh and pH conditions, which can be met due to an appropriate combination of upwelling, primary productivity and bacterial activity (Section 11.3.1). And third, sufficient potassium and iron availability in pore waters (McConchie, 1978). The degraded silicate lattice or smectite absorbs potassium and iron which subsequently results in a decrease in the content of expandable layers.

Millot (1970), Odin and Matter (1981), and Odin and Fullagar (1981) provide an alternative glauconitisation process as they believe that the “layer lattice theory” is an inadequate glauconitisation process in some instances. The process they suggest is based on “verdissement” (the act of “turning green”) or “neoformation”. This process requires a highly porous substrate or hardground, where minerals like smectite neoform in or on the pores of the substrate, and then new minerals form in any remaining pore spaces at the same time as the earlier minerals are modified by the uptake of potassium, which gradually decreases the % expandables leading ultimately to non-expandable glauconitic mica as the end

member of formation. This explains why there is a large variation in the physical properties, mineralogy and geochemistry of glauconite varieties, and why Odin and Matter (1981) suggested the four categories of evolution/formation illustrated Figure 11.5 and Figure 11.8.

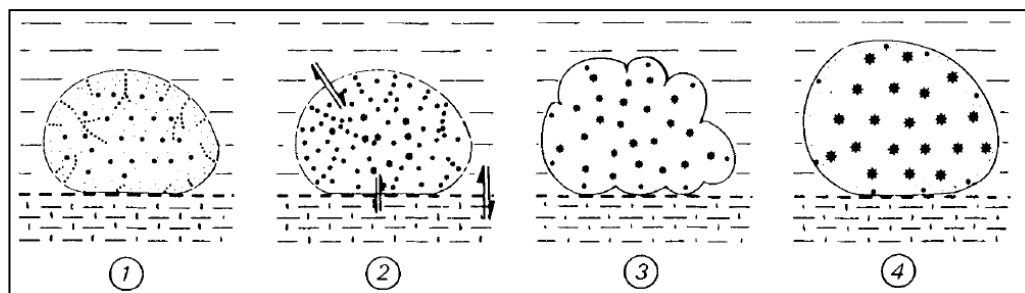


Figure 11.8: Evolution of a glauconite grain, showing the four stages of evolution defined by Odin and Matter (1981). 1: Nascent, 2: Slightly evolved, 3: Evolved, 4: Highly evolved.

Other ways in which glauconitisation may have occurred on central Chatham Rise include via precipitation of glauconite as rims about grains or within cavities of microfossils (i.e. internal molds, particularly foraminifera), and through replacement of other grains, including skeletal calcite (i.e. the replaced foraminifera inside composite grains; Figure 6.1D), phosphorite (i.e. pigmentary glauconite on the phosphorite nodules), rock fragments, quartz, and chert (McRae, 1972; Odin & Matter, 1981; Udgata, 2007).

11.3.3 Smectite source(s) for glauconitisation

In the previous section (Section 11.3.2) it was suggested how the glauconitisation process could proceed in two main ways, both typically requiring a smectite progenitor. In this section I will investigate possible sources of smectite clay in the case of the central Chatham Rise glauconites.

Typically for glauconitisation to occur there needs to be some available source of smectite clays (Thompson & Hower, 1975; Odom, 1976; Odin & Matter, 1981). At DSDP Site 594, southwest of Chatham Rise, Robert *et al.* (1986) noted in core profiles that smectites were very abundant up until about the Early Pliocene at which time they progressively decreased in importance and were replaced by chlorite, illite and irregular mixed-layer clays (Figure 11.9). The change in clay type abundance was related to the acceleration of tectonic uplift of the South Island Southern Alpine chain in the Late Neogene. This is consistent with the

present study in which the bulk surficial sediments did not contain any smectite in their clay fraction, but abundant chlorite and illite clays (Section 3.2.3B).

Robert *et al.* (1986) record smectite as the dominant clay type (45-90%) in Middle to Late Miocene sections of deep sea cores more widely in the Southwest Pacific – Tasman Sea. However, the ultimate origin of this smectite is uncertain, although in the case of the DSDP Site 594 near Chatham Rise they stated that the smectite may have been sourced from the southward-flowing currents out of the central Pacific. Two main origins of the smectite could have been from the alteration of volcanic glass (Weaver, 1989; Spears, 2003) or from authigenic development in carbonate-rich sediment (Millot, 1970; Odin & Matter, 1981; Odin and Fullagar, 1988).

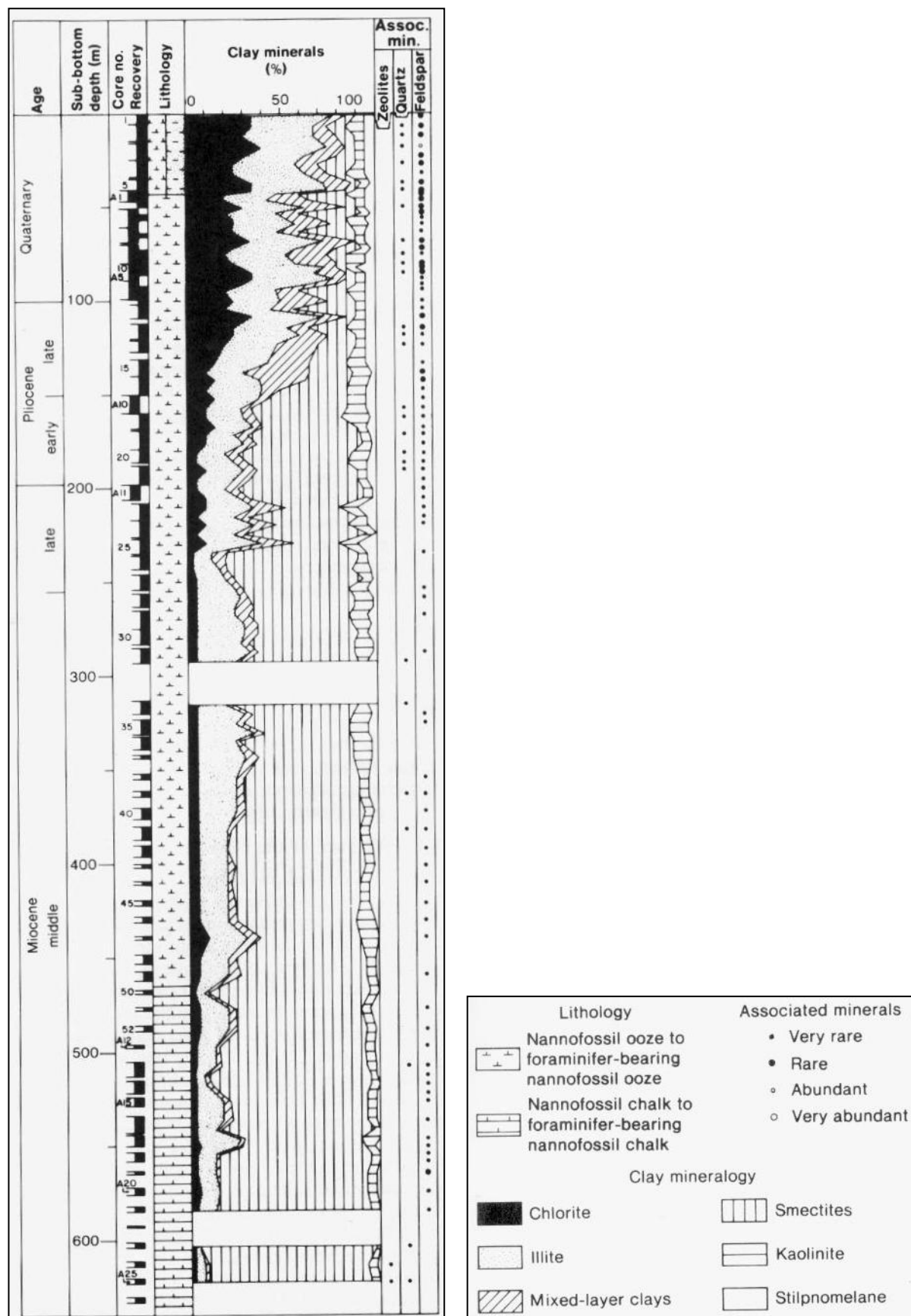


Figure 11.9: Clay mineral assemblage profile from the Middle Miocene to Quaternary at DSDP Site 594 off southwestern Chatham Rise (Robert *et al.*, 1986).

11.3.3A Alteration of volcanic glass into smectite

Smectite can form from the alteration and devitrification of volcanic glass, which leads to the question of whether such an origin is viable for the Chatham Rise location. The smectite can then be glauconitised by either the “layer lattice theory” or by “verdissement” through the four stages of evolution (Section 11.3.2). Potassium-bentonite deposits that are rich in smectite form from the complete devitrification of ash-fall beds under the presence of water (Weaver, 1989; Spears, 2003). The rate of alteration to smectite depends on ash composition and pore solution chemistry, as well as the permeability of the enclosing deposits (Spears, 2003). Such an origin for smectite was suggested by Robert *et al.* (1986) for DSDP Sites 592 and 593 in the southern Tasman Sea. They described how smectite can form during subaerial alteration processes in volcanic deposits to produce the thick smectite laths found at these two sites prior to the Middle Miocene.

Gardiner *et al.* (1986) record the widespread occurrence of “pale green laminae”, or PGLs, that are dominated by smectite clay, in the otherwise carbonate-rich deep sea cores from the Southwest Pacific – Tasman Sea. PGLs were interpreted to be thin basaltic ash layers in which the mafic volcanic glass had been altered in the marine environment to smectite. The ultimate source of the glass was periodic subaerial and submarine eruptions from the many basaltic volcanoes in the wider Southwest Pacific region.

Possible more local sources of volcanic glass for Miocene smectite formation in Chatham Rise sediments include volcanic activity in the Coromandel Volcanic Zone on North Island, New Zealand, or even more locally from the vicinity of Chatham Rise itself. Figure 11.10 shows the location of the four possible local sources of volcanic ash, their composition (rhyolitic or basaltic), and the age ranges of volcanism.

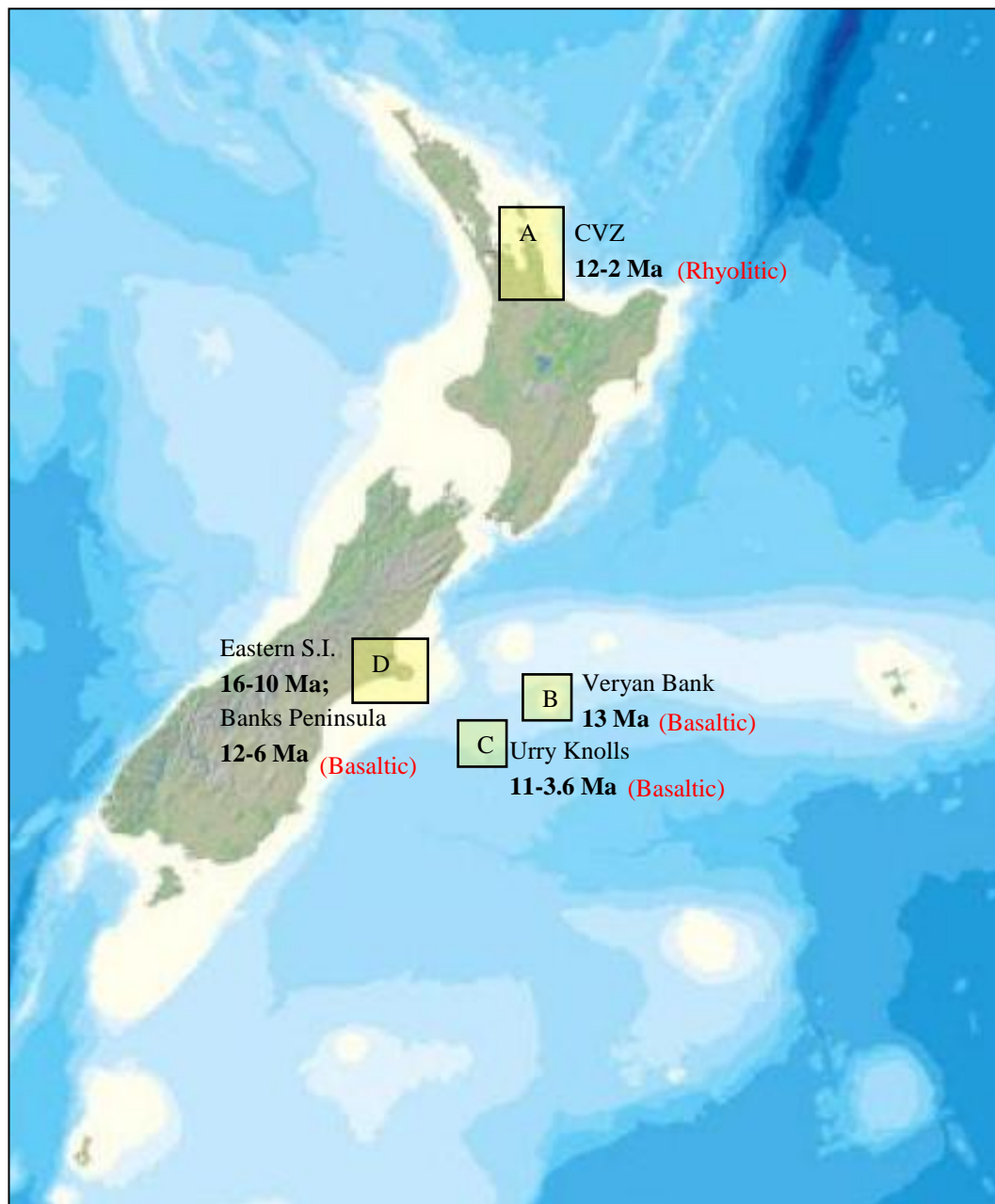


Figure 11.10: Location of possible “local” sources of Miocene-including volcanic ash, their composition (rhyolitic or basaltic) and age ranges of volcanism having that composition. A: CVZ (Coromandel Volcanic Zone), B: Veryan Bank, C: Urry Knolls, D: Eastern South Island and Banks Peninsula.

According to Fiore *et al.* (2001), rhyolitic volcanic material can alter into small flakes of Fe-rich smectite through rearrangements of the hydrated external glass layer and/or through the formation of domains within the rhyolitic glass. These small flakes are very small laminae which are dioctahedral and contain high amounts of Fe. It is known that North Island explosive rhyolitic volcanic ash (Figure 11.10A) has been widely spread across the Chatham Rise (Norris, 1964; Pasho, 1976; Kudrass & von Rad, 1984a) that with time could have been altered into smectite. Volcanism in CVZ has occurred from the Early Miocene to the Late

Pliocene between 18 and 2 Ma, and more specifically rhyolitic volcanism from 12 to 1.9 Ma (Briggs & Krippner, 2006). Only rhyolitic volcanism from the CVZ is considered here, as andesitic and dacitic volcanics cannot be readily altered into smectite (Weaver, 1989).

Kapowai Caldera in CVZ is Late Miocene (8.5-4.9 Ma) in age and is an andesite-dacite-rhyolite volcano. It is one of the largest onland calderas in the CVZ and is the source of the largest and most widespread ignimbrite from the CVZ (Briggs & Krippner, 2006). It is highly likely that the explosive volcanic debris from this centre made it as far as the Chatham Rise. Its age corresponds well with the time of glauconitisation on the Rise, at 6.2-5.4 Ma (Briggs & Krippner, 2006).

Nelson and Froggatt (1986) describe megascopic silicic tephra in deep-sea cores in the Southwest Pacific, two of which (T17 and T18 at DSDP Site 594) come from near Chatham Rise with ages of about 8.6 and 9.4 Ma, or Late Miocene. These tephra were likely sourced from explosive rhyolitic eruptions in the CVZ (Figure 11.10A) and dispersed out into the Pacific Ocean by the prevailing westerly winds. Thus the silicic glass sourced from CVZ is a potential source of some Miocene smectite out on Chatham Rise.

A more local source of smectite clay could be from basaltic volcanism that occurred on or near the Chatham Rise. This would be a more favourable option than the rhyolitic source, as basalt alters much more readily into smectite than does rhyolite (Weaver, 1989). If the smectite was sourced from basaltic eruptives, several possible origins occur in the wider vicinity of Chatham Rise (Figure 11.10).

Veryan Bank (Figure 11.10B), is a truncated basaltic cone (Brodie, 1964; Pasho, 1976) and represents the closest source of basaltic glass to the glauconite deposits on central Chatham Rise. The small mounds on Veryan Bank are thought to be of Late Neogene age, an assumption made from seismic profiles (Herzer *et al.*, 1989), although Timm *et al.* (2010) do provide a supportive age of 12.9 ± 1.1 Ma (i.e. Middle Miocene). Apart from this, little is known about the Veryan volcanic field.

Another possible local source of basaltic glass could be from the submarine intraplate basalts forming the Urry Knolls on Chatham Rise (Figure 11.10C) (Timm *et al.*, 2010; Collins *et al.*, 2011). This volcanic field consists of clusters of cones protruding through flat topography by a few tens to hundreds of metres (Collins *et al.*, 2011). Herzer *et al.* (1989) describe some samples of olivine basalt from the Urry Knolls as a very black, porphyritic, slightly altered and vesicular rock, in which the vesicles are filled with smectite, chlorite and zeolite. In more detail, the smectite has a greenish-yellow to yellow-brown colour and lines the majority of the cavities inside the basalt, reinforcing that basaltic volcanics can be altered to smectite in the marine environment. Alteration of these basalts prevented their absolute dating, although micropaleontological analysis of associated deposits yields a bracketed Late Miocene-Late Pliocene age possibility (Herzer *et al.*, 1989).

Other possible smectite sources could come from eastern South Island (Figure 11.10D). Collins *et al.* (2001) record ages of 16-10 Ma for basalts along the east coast of South Island, and 12-6 Ma for those forming Banks Peninsula. Timm *et al.* (2009, 2010) determined that intraplate volcanism persisted for 7 myr on Banks Peninsula, and was sourced from asthenospheric upwelling which involved carbonated eclogite within a peridotite matrix. The Akaroa mafic shield volcano in this area is the youngest (9.4-6.8 Ma) feature, and interestingly has high Sr and Pb concentrations but low Nd and Hf ratios, much like occurs in the Chatham Rise glauconites.

11.3.3B “Neoformation” of carbonate substrates as smectite source

If the smectite did not come from the alteration of volcanic glass, another possible origin is by “verdissement” or “neoformation” through authigenic precipitation within pore water solutions of carbonate-rich waters, such as carbonate chalk hardgrounds (Section 11.3.2) (Millot, 1970; Odin & Matter, 1981; Nelson & Hume, 1987; Odin & Fullagar, 1988). Odin and Fullagar (1988) state for this process to occur there needs to be a highly porous substrate, which is typical of limestone or chalk. In the case of the central Chatham Rise, this substrate could have been provided by the Oligocene and/or Miocene chalk deposits, with most of the latter having subsequently been eroded away. A “neoformation” origin of

smectite has been suggested for the common smectite in the highly calcareous Oligocene Te Kuiti Group in western North Island of New Zealand (Nelson & Hume, 1987). The glauconites on central Chatham Rise are mostly at the evolved and sometimes highly evolved stage (Figure 11.8), and Odin and Fullagar (1988) state that the evolution process is halted typically by sea level change and burial, which may have been the case here (Section 11.3.5). They also suggest that if conditions remain similar (i.e. absence of alteration or burial), that the glauconite grains may become relict, as is the case for the dominant central Chatham Rise glauconites.

11.3.4 Potassium and iron source(s)

Where did the high amounts of potassium and iron necessary for glauconitisation come from in the Late Miocene? In the Late Miocene, particularly between about 6 and 5 Ma, there was an increase in upwelling and primary productivity within the STF zone, linked to enhanced biogenic blooms, which would have resulted in significant amounts of nutrients falling to the seafloor (Grant, 2005). The age of the glauconite on central Chatham Rise falls within this timeframe (Section 11.2.5). The biogenic bloom arose because of climate-driven changes in ocean circulation patterns due to Antarctic glaciation (Section 11.3.1) (Grant, 2005).

Heightened bacterial activity associated with the increased nutrients arriving at the seafloor of the Rise in the Late Miocene may have prompted an accelerated supply of the iron for glauconite formation (Norris, 1964). Since phytoplankton growth and thus primary productivity is limited by iron availability (Grant, 2005), the Late Miocene biogenic blooms were probably associated with a related increase in iron. Another possible source of iron is from the original smectite clays derived from the devitrification of iron-rich volcanic glass (Section 11.3.2A). Again, Grant (2005) surmised that iron arriving on Chatham Rise could come from iron-bearing dust or perhaps from the upwelling Equatorial Undercurrent (EUC) becoming enriched in iron by erosional and diffusive processes, ultimately due to increased tectonic activity in Papua New Guinea between 8 and 3 Ma. However, such sources would not explain why the biogenic blooms are so widely recorded around the globe in the Late Miocene.

Potassium is common in seawater (Weaver, 1967) and so the biogenic blooms and elevated upwelling (which both result in an increase in nutrients) occurring in the Late Miocene within the STF zone (Grant, 2005) would have been accompanied by enhanced amounts of potassium on Chatham Rise for the subsequent glauconitisation of smectite.

11.3.5 Allogenic versus authigenic glauconite

The age of the glauconite pellets in the modern surficial sediment cover over central Chatham Rise is Late Miocene, not modern or Recent. The international Messinian Stage (i.e. 7.12-5.32 Ma), which encompasses the absolute age range of 5.47-6.0 Ma for the Chatham Rise glauconites, includes a known time of major global sea level fall (Berggren & Haq, 1976; Vincent *et al.*, 1980; Grant, 2005). This fall was controlled by rapid climate change, and more specifically to the growth of Antarctic ice sheets which occurred in the Late Neogene (Berggren & Haq, 1976; Grant, 2005). Berggren and Haq (1976) suggest that the sea level fall was about 40 m and occurred abruptly over 1000-10,000 years at about 5.5 Ma. Within New Zealand the sea level fall, which occurred in the Kapitean Stage, is thought to be controlled mostly by glacio-eustatic causes, as opposed to tectonic events, and was accompanied by much cooler water temperatures than today, due to ice-sheet growth.

The Messinian sea level fall, perhaps supported by the beginnings of tectonic uplift and emergence of the Chatham Islands, may well be responsible for initiating submarine erosion of glauconite and/or phosphorite nodules out of the underlying fine chalky sediments. This could also explain why most of the Miocene sediments on Chatham Rise are now only sporadically distributed or non-existent, and are represented mainly by a major unconformity (Section 11.3.6). Figure 11.11 is a schematic illustration showing the Neogene evolution of glauconite and phosphorite formation on central Chatham Rise, and the reasons why glauconite and phosphorite nodule formation ceased after the Late Miocene, and how they have been reworked and redistributed across the Rise.

Why did the glauconite on central Chatham Rise stop actively forming after the Late Miocene, and why does it appear to not be actively forming at the present day? (refer to Figure 11.11).

Grant (2005) stated that there was an overall increase in terrigenous fluxes to the Chatham Rise sector of the Southwest Pacific at about 5.4 Ma, which coincides with the minimum age obtained for the glauconite on the Rise in this study. Moreover, it also coincides with the sudden decrease in smectite from 60 to 10% of the clay fraction in Pliocene deep-sea sediments at DSDP Site 594 (Figure 11.9) (Robert *et al.*, 1986). Many authors (e.g. Burst, 1958; Hower, 1961; McRae, 1972; McConchie, 1978) have stated that a low to non-existent sedimentation rate is the single most important factor controlling glauconite formation. Consequently, an overall sudden increase in terrigenous input at about 5.4 Ma could provide one explanation as to why glauconite stopped forming at this time on central Chatham Rise (Figure 11.11). Another possible reason for the lack of any active glauconite formation since the Late Miocene is the rarity or absence of smectite clay progenitors available since that time (Robert *et al.*, 1986).

An interesting point to add is that relict iceberg furrows are present across Chatham Rise, with a general S-N orientation due to north-directed currents, and sometimes NE-SW, most likely due to westerly winds (Kudrass & von Rad, 1984b). This scouring occurred after the Late Miocene into the Pliocene and Quaternary (Figure 11.11), and therefore post-dates glauconite formation. The scouring is partly responsible for the redistribution, jostling and exposure of the phosphorite nodules in the eastern sector of the central Chatham Rise (Kudrass & von Rad, 1984b), and could explain the paucity or lack of nodules in the most glauconite-rich area of the Rise upon Reserve Bank. Ice scouring may have also helped erode glauconite out of underlying sediment, assisting in the allogenic nature of the grains.

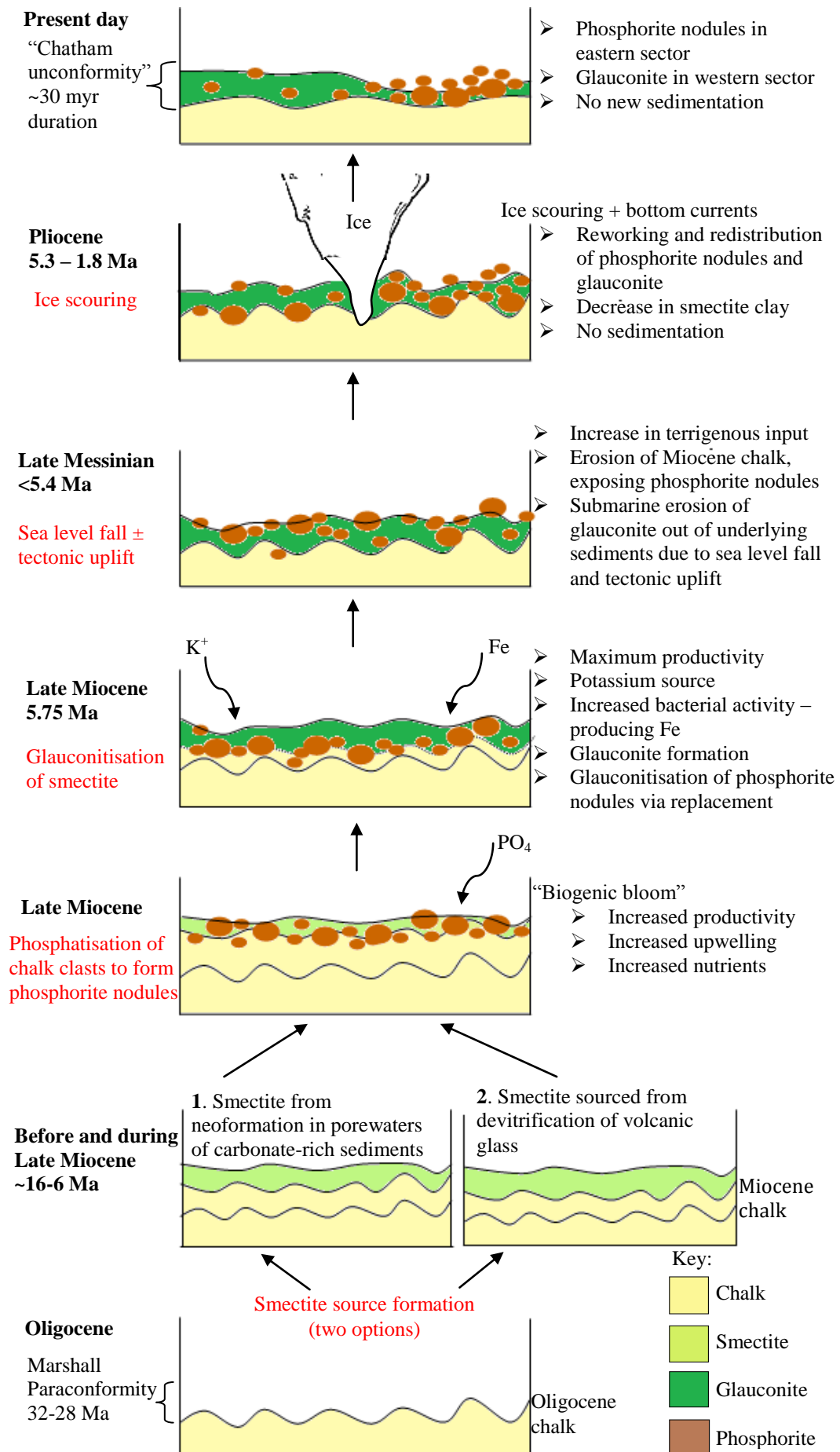


Figure 11.11: Schematic illustration showing the Neogene evolution of glauconite and phosphorite formation on central Chatham Rise (modified after Kudrass & von Rad, 1984a).

11.3.6 Chatham unconformity

The thin (av. 0.6 m) unconsolidated surficial glauconite-rich deposit on central Chatham Rise sits directly upon partially indurated Oligocene chalk of probable Whaingaroan age (~34-27 Ma). Effectively there exists a widespread “Chatham unconformity” (mid-Oligocene to Recent) which cuts out most of the last 30 myr of the sedimentary record on central Chatham Rise, except for the highly condensed surficial deposits whose glauconite grains formed 5-6 Ma, in the late Miocene. This long-lasting “Chatham unconformity” is a greatly extended version of the well documented Oligocene Marshall Paraconformity first defined by Carter and Landis (1972) in Oligocene marine sediments in South Island, and subsequently more widely in the Southwest Pacific. In the vicinity of its type locality in southeastern South Island it represents a duration of about 4 myr between about 32 and 28 Ma, or mid – to upper Whaingaroan (Carter, 1985; Fulthorpe *et al.*, 1996; Dagg, 2010). Elsewhere the Marshall Paraconformity has been shown to represent a larger hiatus of up to 15 myr (Carter 1985). Consequently the “Chatham unconformity” began developing at much the same time as the Marshall Paraconformity, but has more or less continued to form on central Chatham Rise through to the present day. It is represented only by a “thin skin” of mixed glauconite, phosphorite and planktic carbonate sediments – a highly condensed deposit (Figure 11.11). Even the foraminifera in these “modern” surficial deposits are of Miocene age (Section 3.2.6), further emphasizing the “relict” nature of the majority of the sediment components.

Figure 11.11 schematically summarises the sequence of events which led to the formation of glauconite and phosphorite nodules on central Chatham Rise, and also the “Chatham unconformity” described here. It shows how this unconformity can be explained by a combination of a lack of terrigenous input and thus glauconite formation, major periods of erosion linked to bottom currents, and phosphatisation. It also shows that much of the once widespread Early Oligocene chalk was phosphatised during the Late Miocene, and the Miocene foraminiferal ooze was subsequently removed by erosion leaving the present phosphorite nodules exposed on the seafloor. This was followed or overlapped by the formation of glauconite during the Late Miocene. Thus the present stratigraphy represents a major “Chatham unconformity” in which there is little sediment resting on the Oligocene chalk deposit, apart from the phosphate nodules now

embedded in unconsolidated muddy glauconitic sand and silt (Norris, 1964; Kudrass & Cullen, 1982).

11.4 ECONOMIC POTENTIAL OF GLAUCONITE

Given the very high potassium content of 7-9 wt% (amongst other properties) of the glauconite on central Chatham Rise and the strong agricultural based economy of New Zealand, there exists the economic potential to use the glauconite as a potassium fertiliser. Norris (1964) first suggested that the glauconite on central Chatham Rise has a much greater initial release of potassium and also a value of K_c (constant rate of release) that is about twice that of onland New Zealand glauconite deposits. Apart from being a recognised source of potassium, glauconite also provides sources of magnesium and iron, as well as small amounts of phosphate, all of which can be beneficial to the soil system (McRae, 1972; Coles *et al.*, 2002; Payne 2008).

Glauconite as a fertiliser can either be directly applied to the soil or can provide a source of refined potash by processing to KCl (potassium chloride) or even purer forms of K. It is also often mixed with other fertilisers, such as superphosphate. If glauconite from Chatham Rise was applied directly as a fertiliser there would naturally be minor contaminants of quartz and carbonate brought through from the host surficial sediment, but small amounts of these have been recognised to be beneficial to many plants within the soil (Coles *et al.*, 2002). This type of fertiliser is most desirable for organic type farming, and therefore may not be the most suitable way to utilise the glauconite on central Chatham Rise in New Zealand due to an insufficient demand and economics. Alternatively the glauconite can be processed as a potash (KCl) fertiliser through various techniques such as calcination and acid leaching (Figure 10.1). Globally this is the most used of the glauconite fertiliser options, due to the increased concentration of potassium and the removal or reduction of other elements within glauconite that are not so necessary, such as silica, aluminium and magnesium (Coles *et al.*, 2002; Glauconite NZ Ltd, 2011; Potash West NL, 2011). It is most likely the best option for the use of glauconite from central Chatham Rise. Potassium chloride is the cheapest form of potassium fertiliser and is also readily available to plants (Dairy

NZ, 2008). Norris (1964) and Summerhayes (1967) noted that for fertiliser use, fine grinding of the glauconite would aid a better source of potash fertiliser, enabling the slow release of potassium which is within exchangeable sites and interlayer positions. Processing the glauconite even further to concentrated potassium could be an option, but this is a much more expensive process and recovery rates are not as great as for the processing to KCl (Glauconite NZ Ltd, 2011).

The International Fertiliser Association recorded in 2008 that in excess of 30 Mt of potash was mined globally each year and most (>90%) of this was used in the fertiliser industry. In the modern world, only potash fertilisers can provide potassium on a large enough scale to support the global food industry, with global prices and demand rising in recent years (Glauconite NZ Ltd, 2011; Potash West NL, 2011). Potash West NL (2011) has suggested that for the upcoming year (2012) potash demand will increase by 8%. For these reasons the exploration for large potassium resources is becoming more and more essential. Also, because only 12 countries have significant production, yet 160 countries consume potash, new large resources of potash need to be discovered and exploited.

New Zealand has an agricultural-based economy, largely contributing to our status as a first world economy. Therefore any options to improve or sustain this industry are vital to study. In New Zealand, there has been a focus on ryegrass-clover pastures within the agricultural industry, and so a high reliance on phosphate fertilisers has occurred to meet the high phosphate demand. In turn this has led to a degree of neglect for the need for potassium fertilisers within these pasture systems. This neglect may be a consequence of New Zealand soils typically containing relatively high amounts of available potassium, and because the farming methods employed result in potassium being cycled through the dung and urine of cows, which is now recognised as a huge loss mechanism (Kirkman *et al.*, 1994). These factors have meant that historically potassium deficiency has gone largely unrecognised within New Zealand soils, but in more recent decades an appreciation of the need for potassium within soils has increased, with an increase in demand predicted for the future.

When potassium fertilisers were first used in New Zealand their use increased dramatically, from only 830 t during 1910-14 to 149,577 t in 1973-74 (Kirkman *et al.*, 1994). Over the past decade, approximately 120,000 t of potassium fertiliser has been imported on an annual average basis, costing over \$50 million each year (Morgan, 2011). In more recent times this declined to only 81,000 tonnes in 2009/10 – down 40% from the 2002/03 high (Fert Research, 2011). A note to add is that potassium fertiliser application on New Zealand soils is best applied in spring, in which up to 60 kg K/ha can be applied in a single application, and the potassium is directly available to plants (Dairy NZ, 2008).

It would ultimately be desirable and economically sensible for New Zealand to become self-sufficient in potash mining, or to have a fallback position if imports were no longer available (Glaucinite NZ Ltd, 2011). This is where the glauconite deposits on central Chatham Rise come in. There would also be the option for exporting the central Chatham Rise glauconite to other countries requiring potash fertiliser, so benefitting the New Zealand economy.

The second main use of glauconite overseas is for water treatment due to its high cation exchange capacity which, depending on the resistance of the grains to disintegration, allows it to act as a water softener to aid water treatment. However, the effectiveness as a water softener relies on the glauconite having a high cation exchange capacity (CEC), which typically means a lowish potassium content. The central Chatham Rise glauconites have very high potassium contents (7-9 wt%) and generally potassium is negatively correlated with CEC, so it is unlikely that the glauconite on the Rise would be especially suitable for water treatment.

Apart from its use as a potash fertiliser, the glauconite on central Chatham Rise also contains many desirable trace elements, including some rare earth elements, some of which could be of economic use. According to the US DoE (2010), the following elements are either critical or near critical in terms of supply: yttrium (Y), indium (In), tellurium (Te), lanthanum (La), cerium (Ce), neodymium (Nd), europium (Eu), terbium (Tb), and dysprosium (Dy). The central Chatham Rise glauconites contain various amounts of the first six elements, while the last three were not analysed in the present study. In New Zealand, the main trace elements which are typically lacking in soils, and are therefore needed within fertiliser

application, include boron (B), cobalt (Co), copper (Cu), iodine (I), iron (Fe), manganese (Mn), zinc (Zn) and selenium (Se) (Morton *et al.*, 1999). Within the central Chatham Rise glauconites some of these are present, for example I (av. 12 ppm), Fe (av. 20.3 wt%), Mn (av. 0.01 wt%), and Zn (av. 66 ppm). Within New Zealand pastures I is typically needed at 0.15-0.25 ppm, Fe at 45-49 ppm, Zn, at 13-14 ppm and Mn at 20-24 ppm (Morton *et al.*, 1999). The central Chatham Rise glauconites could provide these levels except for Mn.

Resources estimates for the glauconite on central Chatham Rise, in the 4500 km² area containing >50 wt% glauconite, have been calculated to be about 2 Bt (Section 10.3). On this basis New Zealand could become self-sufficient in glauconite production for hundreds of years. A similar offshore glauconite exploration study was carried out by Coles *et al.* (2002) on a glauconite deposit off southern Africa. They estimated that at the lowest extraction level of 1500 t per day the annual yield from glauconite sand would be US\$117 M (based on US\$300/t price), and for potash US\$45 M (based on US\$117/t). The KCl price has varied over time from US\$150/t to over US\$870/t in 2008, and has currently settled to a price of between US\$350-450/t. Prices are likely to increase as demand increases, with an 8% demand growth predicted for the 2012 year (Potash West NL, 2011).

Mining techniques suitable for the extraction of glauconite at typical water depths of 200-350 m on central Chatham Rise would need to be developed, with the most suitable technique likely to be suction grabbing/dredging. Currently the company “Chatham Rock Phosphate Ltd” is actively pursuing the design of these kinds of mining options with some of the world’s largest dredging companies, in anticipation of mining the phosphorite nodules (and possibly the glauconite) on central Chatham Rise. Coles *et al.* (2002) recognised three potential mining methods for glauconite (and phosphate) deposits, namely drillship, seabed crawler and dragline, each with its positives and negatives as shown in Figure 11.12. The drillship and seabed crawler methods are currently being employed to mine diamond deposits off the west coast of southern Africa by a company called DeBeers Marine (Pty) Ltd and Namco (Pty) Ltd.

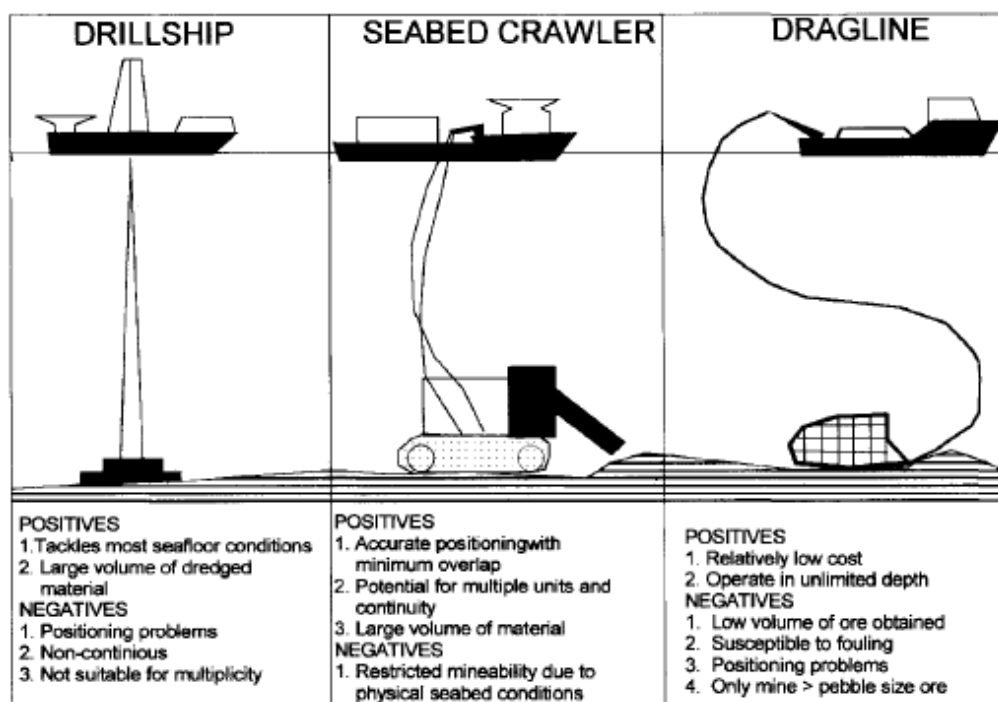


Figure 11.12: Three potential mining methods for seafloor glauconite and phosphate deposits (Coles *et al.*, 2002).

In summary, the glauconite deposits on central Chatham Rise have a substantial economic potential as a potash fertiliser, which merits further investigation. There are very large resource estimates of at least 2 Bt, combined with a high demand market. The glauconite is of desirable type with a high potassium content and high constant release rates. It should be noted that the glauconite on central Chatham Rise is mainly of Late Miocene age and is already highly evolved, and so is not going to become “any better” in terms of its “mining credentials” i.e. potassium contents are not going to increase, and glauconite is not actively forming. In fact it is possible that with time the resource could actually become less suitable and less economic, due to oxidation, limonitisation, weathering, and breakage and continued dispersal due to bottom currents.

11.5 ONLAND NEW ZEALAND TERTIARY GLAUCONITE

Glauconite is widespread in uplifted Tertiary deposits found in various parts of onland New Zealand, but its nature, origin and significance are typically poorly understood. The geological and oceanographic setting of the Chatham Rise at the time of glauconite formation could be relevant for the paleoenvironmental

interpretation of many of these ancient greensands deposits. Similar kinds of conditions of temperature, depth, chemical environment, organic activity, sedimentation rate and degree of isolation from terrigenous input that existed on the Chatham Rise at and following the time of glauconite formation in the Late Miocene, must have prevailed to some extent during the deposition of the Tertiary greensand deposits in New Zealand (Norris, 1964).

11.5.1 Physical and morphological comparison

The easiest way to compare Chatham glauconites to onland New Zealand deposits is through the physical (i.e. colour) and morphological nature of the glauconite grains. Figure 11.13 is a map of New Zealand on which the five main areas containing glauconite deposits are shown.

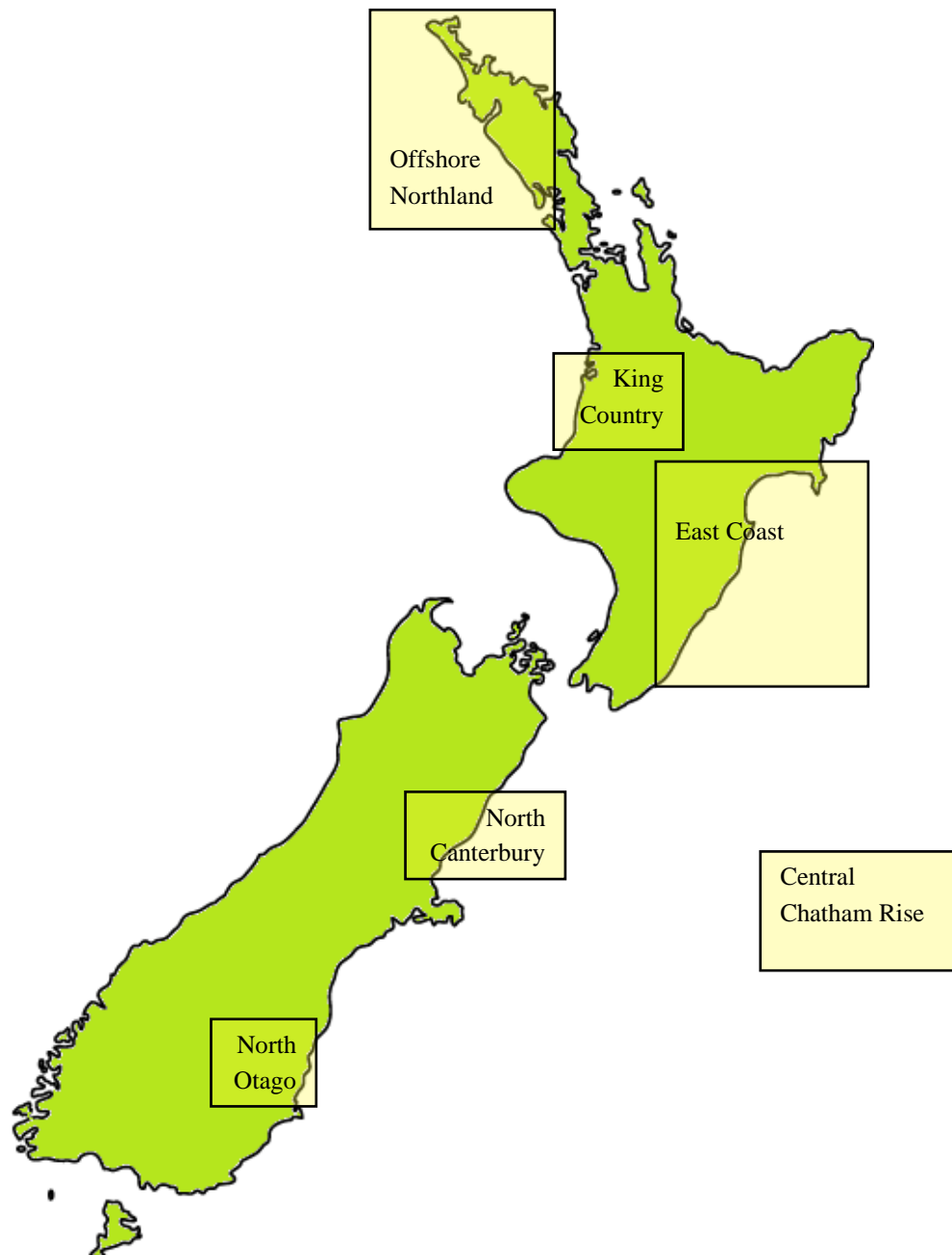


Figure 11.13: Map of New Zealand with the five main onland areas which contain Cenozoic glauconite deposits outlined, as well as the central Chatham Rise glauconites of the present study.

Firstly, glauconite occurs in varying abundances across the North Kaipara continental margin (NKCM) off the west coast of Northland (Figure 11.13), which has been described in detail by Payne (2008). The glauconites found here are similar to the Chatham glauconites, with dark green smooth ovoidal grains clearly dominating (84-96%). Other morphologies found in the North Kaipara glauconites include tabular/discoidal, lobate, vermicular, casts/internal molds and composite grains, all of which occur in the central Chatham Rise glauconites except for the vermicular grains. Another difference is the abundance of lobate

grains amongst the Chatham glauconites (av. 15%) compared to the North Kaipara glauconites (av. 1%). The lobate grains in the North Kaipara sediments are also a much lighter green colour (Payne, 2008). Other than this, the glauconite grains in both of these deposits are similar physically and morphologically.

The next main occurrence of glauconitic deposits in New Zealand is in the King Country in the Oligocene Te Kuiti Group (Figure 11.13), well documented by Nelson (1973) and Compton (1989). Again the glauconites within the Te Kuiti Group are dominated by dark green to black polished ovoidal pellets. Other morphological varieties include (in order of decreasing abundance) fragmentary, lobate, casts/internal molds, tabular, capsule and vermicular (Nelson, 1973; Compton, 1989). The vermicular occurrence is as at North Kaipara, but not amongst the central Chatham Rise glauconites. Lobate grains are of similar abundance (5-15%) to those in the Chatham glauconites, but in the Te Kuiti Group the lobate grains are much more fragile and Compton (1989) suggested a fully authigenic origin for these grains. Otherwise, the ovoidal and fragmentary grains are interpreted to be perigenic or allogenic grains, having been transported from nearby sites before being incorporated into their present deposits (Nelson & Hume, 1987; Compton, 1989), similar to the allogenic nature of the Chatham glauconites.

The East Coast, North Island represents another onland area that has many glauconite-rich deposits (Figure 11.13). Here the glauconite is typically found within Paleocene to Miocene strata with large deposits especially in the Gisborne and Wairarapa areas (Glauconite NZ Ltd, 2011). The morphological nature of the glauconites in the East Coast region have not been fully analysed, but appear to be generally similar to other onland New Zealand deposits.

McConchie (1978) investigated the Cretaceous and Lower Tertiary glauconite in the South Island, covering the two main areas of glauconite deposits in North Canterbury and North Otago (Figure 11.13). Due to the large number of locations investigated by McConchie (1978) it is unclear as to the exact abundance of the morphological varieties across these two areas. However, it is clear that in the South Island glauconites the fragmentary morphology is dominant, in contrast to the North Island and Chatham glauconites where ovoidal morphologies dominate.

In most locations the glauconite deposits contain several morphological types, including ovoidal, tabular/discoidal, lobate, vermicular, fossil casts/internal molds, composite pellets, corroded, and pigmentary glauconite. The South Island glauconites in some locations also show a much higher abundance of lobate glauconite than in the North Island, more similar to the situation occurring for the central Chatham Rise glauconites.

In summary, New Zealand onland Tertiary glauconites are mostly similar in morphology to the Chatham glauconites, both having a clear dominance of dark green to black smooth polished ovoidal pellets, with minor quantities of other morphologic types. Two differences are the occurrence of vermicular pellets in the onland glauconites, which is not seen in the Chatham glauconites, and the typically higher abundance (av. 15%) of lobate pellets in the Chatham glauconites compared to onland North Island deposits. Also the Chatham lobate pellets are typically a much darker green to black colour, compared to a lighter green colour in many of the onland lobate pellets.

11.5.2 Geochemical comparison

A more quantitative way of comparing glauconites from different areas is through their major oxide elemental geochemistry. When comparing the geochemistry of central Chatham Rise glauconites to onland New Zealand deposits, and also to glauconites universally, the microprobe data for the dark green ovoidal grains is the most appropriate and reliable to use because the bulk XRF results may include some small contributions from contaminant mineral particles.

Globally, the geochemical range of the major oxides within glauconite is as follows: SiO₂ 43-53%, Fe₂O₃ 8-25%, FeO 1-6% (total Fe 13-30%), Al₂O₃ 3-14%, K₂O 4-7%, and MgO 2-5% (McRae, 1972; Nelson, 1973; Payne, 2008). Despite this, the glauconite classification set by Odin and Matter (1981) based on the maturity ranges of glauconites and their K₂O content (Figure 11.5) shows that highly mature and evolved glauconite should have a K₂O content >8%, which is outside the universal range noted above.

The geochemistry of the central Chatham Rise glauconites fits well within the global major oxide ranges suggested by McRae (1972) and Nelson (1973), as noted above, apart from the K₂O content. Here the global range is 4-7%, while the central Chatham Rise glauconites have an average K₂O content of 8.88%, with a range of 8.5-9.3% as indicated by microprobe data. This is well above the suggested maximum of 7%, but is in agreement with the highly evolved class of glauconite in the classification of Odin and Matter (1981), making it glauconitic mica. In contrast, the Al₂O₃ content is at the lower end of the global range of 3-14%, with central Chatham Rise glauconites ranging from 2.5-8.3% (av. 5.5%), and one sample falling below the global range.

Table 11.2 shows the major oxide geochemistry for glauconite from the five main areas within New Zealand noted on Figure 11.13, the data coming from Hutton and Seeyle (1941), Nelson (1973), McConchie (1978), Payne (2008), and the present Chatham study.

Table 11.2: Major oxide geochemistry for glauconite from the five main areas within New Zealand shown in Figure 11.13. A: Offshore Northland – north Kaipara (Payne, 2008); B: King Country – Te Kuiti Group (Nelson, 1973; Nelson & Hume, 1987); C: East Coast – Gisborne (Hutton & Seeyle, 1941); D: South Island – including both North Canterbury and North Otago (McConchie, 1978); E: North Otago (Hutton & Seeyle, 1941); F: Average onland geochemistry; G: central Chatham Rise (present study); H: Difference between onland and central Chatham Rise. + = more in onland than Chatham; – = less in onland than Chatham.

	SiO ₂	Al ₂ O ₃	Total Fe	TiO ₂	CaO	MgO	Na ₂ O	K ₂ O	P ₂ O ₅
A	47.90	3.70	23.70	-	0.90	4.80	-	6.90	-
B	47.87	10.55	17.31	0.28	0.83	4.05	1.10	6.02	0.27
C	52.64	5.87	21.73	0.16	0.12	3.43	0.18	7.42	0.18
D	54.50	6.10	22.30	-	0.70	1.50	0.70	6.80	-
E	47.47	7.10	23.63	0.17	0.39	3.27	0.11	6.64	0.19
F	50.08	6.66	21.73	0.20	0.59	3.41	0.52	6.76	0.21
G	51.37	5.50	19.68	0.20	0.22	4.73	0.70	8.88	0.90
H	-1.29	+1.16	+2.05	0.00	+0.37	-1.32	-0.18	-2.12	-0.69

According to Nelson (1973), the relative abundance of the major elements in New Zealand glauconites is SiO₂>Fe₂O₃>Al₂O₃>K₂O>MgO>FeO. However, there seems to be some exceptions to this. For the North Kaipara, North Canterbury and East Coast – Gisborne glauconites, the K₂O content is actually higher than the Al₂O₃ content (Table 11.2). The microprobe results (Section 8.4.1) for the central Chatham Rise glauconites also show higher K₂O contents than Al₂O₃ contents.

The other elements within the central Chatham Rise glauconites show the abundance trend suggested by Nelson (1973).

The potassium content within central Chatham Rise glauconites is the most significant difference, being much higher by c.2.1 wt% compared to the other New Zealand glauconite occurrences. This extremely high potassium content of central Chatham Rise glauconites has been previously reported by Norris (1964) and Bell and Goodell (1967), but the actual reasons for this are unknown. Possible reasons were discussed in Section 11.3.4, in which it was concluded that there may have been more potassium for uptake contained in the water column at the time of formation, due to a combination of major biogenic blooms and intense upwelling within the STF zone (e.g. Grant, 2005). However, the iron within the Chatham glauconites is lower by 2 wt% compared to the average other New Zealand glauconites (Table 11.2). This may simply reflect variations in the starting iron content of the various smectite source clays. The higher (1.3 wt%) silica content in the Chatham glauconites may reflect the lower iron content. The overall slightly lower (1.2 wt%) aluminium content probably reflects the evolved to highly evolved nature of the central Chatham Rise glauconites, with very high potassium contents and consequently lower aluminium values (Table 11.2). The slightly higher (0.7 wt%) phosphate values for the central Chatham Rise glauconites (Table 11.2) likely relates to the close glauconite-phosphate mineral association occurring on the Rise (Section 11.2.4).

Chapter 12

SUMMARY AND CONCLUSIONS

The general aims of this study, outlined in Chapter 1, were mostly fulfilled, as well as a few new discoveries which were not part of those original aims. This chapter summarises the main outcomes of the present study in relation to the aims, as well as the new discoveries. I conclude by making some suggestions for future research.

12.1 ECHO CHARACTER

Analysis of the 3.5 kHz sub-bottom profiles revealed little new information about the echo-character of central Chatham Rise, other than a relative monotony of echo-type A character. However, it did indicate that the eastern sector of central Chatham Rise has prominent irregular sea floor morphologies associated with phosphorite nodule occurrences, while the western sector has flat-lying morphologies more indicative of glauconite-rich sandy and silty areas. The thickness of the surficial sediment and the underlying Oligocene chalk deposit shows a relationship to water depth and bottom gradient. Sediment thickness increases with decreasing water depth and decreasing gradient (i.e. sediment is thickest (>60 m) in flat areas with a water depth of <500 m), and vice versa.

12.2 BULK SEDIMENT FACIES

The nature and distribution of the surficial sediment facies across central Chatham Rise have been studied in detail, leading to the production of a new surficial sediment map that shows a much clearer indication of the glauconite- and phosphorite-rich areas, sediment textures, and percentages. This map illustrates the dominance of phosphorite nodules in the eastern sector, embedded in glauconite-carbonate-rich sand. In contrast, the western sector is clearly dominated by glauconite-rich sandy deposits, especially in water depths <300 m on or near Reserve Bank. Water depths >500 m are dominated by calcareous sandy silt and silty sand deposits. Analysis also revealed an average thickness of 0.6 m for the surficial sediment deposits, with a range from 0.06-1.35 m.

12.3 NATURE OF GLAUCONITE

The nature of the different glauconite varieties on central Chatham Rise has been fully documented in the present study. Seven morphologies were discovered, each having different specific origins and geochemistries. These morphologies include ovoidal (75%), lobate (15%), composite (5%), fossil casts (3%), pigmentary and tabular (1%) and pellets within rock fragments (1%). Three internal fabrics were recognised, namely, random microcrystalline (80%), oriented fibroradiating rims (15%), and skeletal infilled grains (5%). XRD analysis revealed that the glauconite is a mature disordered 1Md montmorillonite glauconite polymorph, which has 10-20% expandable smectite layers. Geochemical analysis indicated a highly mature, and thus evolved to highly evolved glauconite, with Fe_2O_3 of 18-22 wt%, and K_2O of 7-9 wt%.

12.4 AGE AND ORIGIN

K-Ar isotope age analysis of five pure glauconite concentrates from central Chatham Rise revealed an average age of 5.75 Ma, with a range of 5.47-6.0 Ma; only the very abundant (>75%) ovoidal grains could be dated. This Late Miocene age lies within the Messinian Stage internationally, and the Kapitean Stage in New Zealand. This is a time of known global sea level fall, which helped reveal information into the origin of the glauconite on central Chatham Rise. The overall origin of glauconite on central Chatham Rise is complicated, and the outcomes of the present study can only reveal assumptions or possibilities, as opposed to definite facts. A schematic illustration of the sequence of events leading to the formation of the glauconite and phosphorite nodules, and also the “Chatham unconformity” (described below), is provided.

The time of glauconite formation was in the Late Miocene, and so something special must have happened at this time to foster vast amounts of glauconite production. The Late Miocene was a time of major increased upwelling and primary productivity due to enhanced “biogenic blooms” and the “Chron C3Ar carbon shift”, events that were probably triggered by Antarctic ice sheet growth related to climate and ocean circulation changes. This can account directly for the formation of phosphorite nodules, but the glauconite story is a little more complicated. A source of smectite is needed for glauconitisation to proceed, and

the present study recognises two possibilities. Firstly, smectite may have been sourced from the devitrification of volcanic glass, with at least four possible volcanic eruptive centres of appropriate age being recognised, namely CVZ, Veryan Bank, Urry Knolls, and the eastern South Island and Banks Peninsula area. Secondly, smectite can form due to “neoformation” in the pore waters of carbonate-rich deposits like the substrate chalks. The sources of potassium and iron were likely linked to the enhanced biogenic blooms in the Late Miocene. So, given a smectite, iron and potassium source at this time, as well as the bottom sediment Eh and pH requirements provided by bacterial activity, a low sedimentation rate, and water temperatures from 10-15°C, the glauconitisation process was active.

12.5 *IN SITU* VERSUS ALLOGENIC

This study concludes that the glauconite on central Chatham Rise is not currently forming, and so is not strictly authigenic, nor *in situ*, but is predominantly allogenic (transported). This conclusion is based on the ovoidal, smooth surface polished nature of most (>75%) of the grains, the rarity or absence of smectite clay progenitors available after the Late Miocene, and the relict age (i.e. 5.75 Ma; Late Miocene) and high chemical maturity of the grains. Due to sea level fall in the Messinian and possibly subsequent tectonic uplift and ice scouring, the glauconite is inferred to have been reworked out of underlying fine chalky Late Miocene sediments by submarine erosion, and then redistributed by bottom currents in a southeasterly direction from the main glauconite “factory” on and about Reserve Bank. Such a scenario led to the postulation of a “Chatham unconformity”, as described below.

12.6 “CHATHAM UNCONFORMITY”

The thin (av. 0.6 m) unconsolidated surficial glauconite-rich deposits and of phosphate nodules embedded in unconsolidated muddy glauconitic sands and silts on central Chatham Rise, sit directly upon partially indurated Early Oligocene chalk of probable Whaingaroan age (~34-27 Ma). This means that effectively there exists a widespread “Chatham unconformity” (mid-Oligocene to Recent) which cuts out most of the last 30 myr of the sedimentary record on central Chatham Rise, except for the highly condensed surficial deposits whose

glauconite grains formed 5-6 Ma, in the late Miocene. This long-lasting “Chatham unconformity” is a greatly extended version of the well documented Oligocene Marshall Paraconformity.

12.7 ECONOMIC POTENTIAL

Data from the present study are used to calculate a resource estimate of over 2 Bt in the most glauconite-rich area of the central Chatham Rise covering an area of 4500 km² on or near the Reserve Bank. If mined, the most suitable future economic use of this glauconite would be as a potash fertiliser due to its highly evolved nature with very high potassium contents (7-9 wt%), high K_c value (constant rate of release), and the continuing demand for potash fertilisers in New Zealand agriculture. The KCl price has currently settled at between US\$350-450/t, and prices are likely to increase as demand increases, with an 8% demand growth predicted for the 2012 year.

12.8 ONLAND NEW ZEALAND TERTIARY GLAUCONITE

The glauconite grains on central Chatham Rise are mostly similar to the five main onland areas of Tertiary glauconite deposits, with dark green to black ovoidal grains dominating, but other morphological varieties are always also present. One of the main differences is the greater abundance of lobate grains on Chatham Rise, which appear to be a darker green to black colour compared to the lighter lobate varieties found in the Tertiary strata. Chatham glauconites also do not contain any vermicular varieties. A notable difference is that the Chatham glauconites have much higher potassium contents (7-9 wt%) than onland occurrences (5-7 wt%), presumably reflecting their evolved to highly evolved nature.

12.9 FUTURE RESEARCH

The glauconite on central Chatham Rise merits further investigation, particularly in relation to grain specific morphological and mineralogical variations. Absolute age determinations in the present study were limited to the dominant (>75%) dark green mature ovoidal grains, and so further investigation into the ages of the other less common glauconite morphologies is warranted, perhaps using individual grain Ar-Ar isotope dating. If these proved to be younger than the Late Miocene

may not represent the end of glauconite formation, and possibly some glauconite could still be forming at the present day. However, microprobe geochemical analysis of these different morphologies revealed that they all have relatively high potassium and iron contents, and this chemical maturity strongly suggests that the ages would most likely also be “old”. Again, these different glauconite morphologies warrant investigation of their individual mineralogical composition, possibly using the General Area Detector Diffraction System (GADDs). If mining became a real possibility, then investigation and research into the mining feasibility, economics, environmental impacts, and the fertiliser application results for New Zealand soils, would all need to be explored. A more in-depth comparison of the central Chatham Rise glauconites to onland Tertiary glauconite deposits should be researched, so that fuller paleoenvironmental interpretation of many of these ancient greensand deposits can be made.

REFERENCE LIST

- Bailey, S.W. (1980). Structures of Layer Silicates. In G.W. Brindley & G. Brown (Eds.), *Crystal structures of clay minerals and their x-ray identification* (pp. 1-123). Great Britain: The Mineralogical Society.
- Bell, D.L., & Goodell, H.G. (1967). A comparative study of glauconite and the associated clay fraction in modern marine sediments. *Sedimentology*, 9, 169-202.
- Berggren, W.A., & Haq, B.U. (1975). The Andalusian Stage (Late Miocene): Biostratigraphy, Biochronology and Paleoecology. *Palaeogeography, Palaeoclimatology, Palaeoecology*, 20, 67-129.
- Bonhomme, M.G., Thuizat, R., Pinault, Y., Clauer, N., Wendling, R., & Winkler, R. (1975). Méthode de datation potassium-argon. *Appareillage et technique. Strasbourg*, 3, 53.
- Briggs, R.M., & Krippner, S.J.P. (2006). The Control by Caldera Structures on Epithermal Au-Ag Mineralisation and Hydrothermal Alteration at Kapowai, Central Coromandel Volcanic Zone. In A. B. Christie & R. L. Brathwaite (Eds.), *Geology and Exploration of New Zealand Mineral Deposits* (pp. 101-107). Carlton: Australasian Institute of Mining and Metallurgy.
- Brindley, G.W. (1980). Order-Disorder in Clay Mineral Structures. In G.W. Brindley & G. Brown (Eds.), *Crystal structures of clay minerals and their x-ray identification* (pp. 125-195). Great Britain: The Mineralogical Society.
- Brodie, J.W. (1964). *Bathymetry of the New Zealand region*. Wellington, New Zealand: Government Printer.
- Burst, J.F. (1958). Mineral heterogeneity in “glauconite” pellets. *The American Mineralogist*, 43, 481-497.
- Carter, L., Carter, R.M., & McCave, I.N. (2004). Evolution of the sedimentary system beneath the deep Pacific inflow off eastern New Zealand. *Marine Geology*, 205, 9-27.
- Carter, R.M. (1985). The mid-Oligocene Marshall Paraconformity, New Zealand: coincidence with global eustatic fall or rise? *Journal of Geology*, 93, 359-371.
- Chiswell, S.M. (2000). Tidal Energetics over the Chatham Rise, New Zealand. *Journal of Physical Oceanography*, 30, 2452-2460.
- Chiswell, S.M. (2001). Eddy energetics in the Subtropical Front over the Chatham Rise, New Zealand. *New Zealand Journal of Marine and Freshwater Research*, 35, 1-15.

- Clauer, N., Huggett, J.M., & Hillier, S. (2005). How reliable is the K-Ar glauconite chronometer? A case study of Eocene sediments from the Isle of Wight. *Clay Minerals*, 40, 167-176.
- Coles, S.K.P., Wright, C.I., Sinclair, D.A., & Van den Bossche, P. (2002). The Potential for Environmentally Sound Development of Marine Deposits of Potassic and Phosphatic Minerals Offshore, Southern Africa. *Marine Georesources and Geotechnology*, 20(2), 87-110.
- Collins, J.A., Molnar, P., & Sheehan, A.F. (2011). Multibeam bathymetric surveys of submarine volcanoes and mega-pockmarks on the Chatham Rise, New Zealand. *New Zealand Journal of Geology and Geophysics*, 54(3), 329-339.
- Compton, M.S. (1989). *Morphology and geochemistry of glauconite from the Te Kuiti Group, South Auckland Region, New Zealand* (Unpublished master's thesis). University of Waikato, Hamilton, New Zealand.
- Cook, C. (2002). *Petrogenesis and Evolution of Alkalic Basaltic Magmas in a Continental Intraplate Setting: The South Auckland Volcanic Field, New Zealand* (Unpublished PhD thesis). University of Waikato, Hamilton, New Zealand.
- Crundwell, M., Scott, G., Naish, T., & Carter, L. (2008). Glacial – interglacial ocean climate variability from planktonic foraminifera during the Mid-Pleistocene transition in the temperate Southwest Pacific, ODP Site 1123. *Palaeogeography, Palaeoclimatology, Palaeoecology*, 260, 202-229.
- Cuadros, J., Caballero, E., Huertas, F.J., Jimenez De Cisneros, C., Huertas, F., & Linares, J. (1999). Experimental alteration of volcanic tuff: smectite formation and effect on ^{18}O isotope composition. *Clays and Clay Minerals*, 47(6), 769-776.
- Cullen, D.J. (1967). The Age of glauconite from the Chatham Rise, east of New Zealand. *New Zealand Journal of Marine and Freshwater Research*, 1(4), 399-406.
- Cullen, D.J. (1978). The uranium content of submarine phosphorite and glauconite deposits on Chatham Rise, east of New Zealand. *Marine Geology*, 28, 67-76.
- Cullen, D.J. (1987). *The submarine phosphate resource on central Chatham Rise*. Wellington, New Zealand: Division of Marine & Freshwater Science, DSIR.
- Dagg, R. (2010). *The Greensand at the Marshall Paraconformity* (Master's thesis, University of Otago, Dunedin, New Zealand). Retrieved from <http://otago.ourarchive.ac.nz/handle/10523/1634>.
- Dairy NZ. (2008). *Dairy NZ Farmfact 7-9: Using Potassium fertiliser*. Retrieved from www.dairynz.co.nz/file/fileid/37262.

- Dalrymple, G.B., & Lanphere, M.A. (1969). *Potassium-argon dating*. San Francisco: W.H. Freeman.
- Damuth, J.E. (1978). Echo Character of the Norwegian-Greenland Sea: Relationship to Quaternary Sedimentation. *Marine Geology*, 28, 1-36.
- Damuth, J.E. (1980). Use of High-Frequency (3.5-12 kHz) Echograms in the study of Near-Bottom Sedimentation Processes in the Deep-Sea: A review. *Marine Geology*, 38, 51-75.
- Dickin, A.P. (1995). *Radiogenic isotope geology*. Cambridge: Cambridge University Press.
- Fairbridge, R.W. (1967). Phases of diagenesis and authigenesis in sediments. In G. Larsen & G.V. Chilingar (Eds.), *Diagenesis in Sediments* (pp. 19-89). Amsterdam: Elsevier.
- Falconer, R.K.H., von Rad, U., & Wood, R. (1984). Regional Structure and High-Resolution Seismic Stratigraphy of the Central Chatham Rise (New Zealand. *Geologisches Jahrbuch*, 65, 29-56.
- Faure, G. (1986). *Principles of isotope geology*. New York: John Wiley & Sons.
- Fert Research. (2011). *Annual Update 2009-2010*. Retrieved from www.fertresearch.org.nz.
- Fiore, S., Huertas, F.J., Huertas, F., & Linares, J. (2001). Smectite formation in rhyolitic obsidian as inferred by microscope (SEM-TEM-AEM) investigation. *Clay Minerals*, 36(4), 489-500.
- Folk, R.L. (1968). *Petrology of sedimentary rocks*. Austin, Texas: The University of Texas.
- Fulthorpe, C.S., Carter, R.M., Miller, K.G., & Wilson, J. (1996). Marshall Paraconformity: a mid-Oligocene record of inception of the Antarctic Circumpolar Current and coeval Glacio-eustatic lowstand? *Marine and Petroleum Geology*, 13(1), 66-77.
- Glaucinite NZ Ltd. (2011). *Glaucinite resources in NZ*. Retrieved from <http://www.glaucinitenz.co.nz>.
- Gradstein, F.M., Ogg, J.G., & Smith, A. (2004). *A Geologic Time Scale 2004*. Cambridge: Cambridge University Press.
- Grant, K.M. (2005). *Late Neogene biogenic sedimentation and carbon isotope shifts in the southwest Pacific Ocean* (Unpublished honour's thesis). James Cook University, North Queensland, Australia.
- Grim, R.E. (1968). *Clay mineralogy*. New York: McGraw – Hill.

- Hayward, B., & Gross, O. (2011). *Orbulina universa* d'Orbigny. In B.W. Hayward, T. Cedhagen, M. Kaminski & Q. Gross (Eds.), *World Modern Foraminifera Database*. Retrieved from <http://www.marinespecies.org/aphia.php?p=taxdetails&id=113460> on 18-10-2011.
- Heath, R.A. (1981). *Physical oceanography of the waters over the Chatham Rise*. Wellington, New Zealand: New Zealand Oceanographic Institute.
- Heath, R.A. (1983). Observations on Chatham Rise currents. *New Zealand Journal of Marine and Freshwater Research*, 17(3), 321-330.
- Heinrichs, H., & Herrmann, A.G. (1990). *Praktikum der Analytischen Geochemie*. Berlin-Heidelberg: Springer-Verlag.
- Herzer, R.H., Challis, G.A., Christie, R.H.K., Scott, G.H., & Watters, W.A. (1989). The Urry Knolls, late Neogene alkaline basalt extrusives, southwestern Chatham Rise. *Journal of Royal Society of New Zealand*, 19(2), 181-193.
- Hoskins, A.P. (1895). On glauconite from Woodburn, Carrickfergus, County Antrim. *Geology Magazine*, 32, 317-321.
- Hower, J. (1961). Some factors concerning the nature and origin of glauconite. *The American Mineralogist*, 46, 313-334.
- Hume, T.M., & Nelson, C.S. (1982). *X-ray diffraction analytical procedures and some mineralogical characteristics for South Auckland region sediments and sedimentary rocks, with special reference to their clay fraction*. Hamilton, New Zealand: University of Waikato, Department of Earth Sciences.
- Hutton, C.O., & Seelye, F.T. (1941). Composition and properties of some New Zealand glauconites. *American Mineralogist*, 26, 595-604.
- James, N.P., Jones, B., Nelson, C.S., & Campbell, H.J. (2011). Cenozoic temperate and sub-tropical carbonate sedimentation on an oceanic volcano – Chatham Islands, New Zealand. *Sedimentology*, 58, 1007-1029.
- Kirkman, J.H., Basker, A., Surapaneni, A., & MacGregor, A.N. (1994). Potassium in the soils of New Zealand – A review. *New Zealand Journal of Agricultural Research*, 37(2), 207-227.
- Konta, J. (1967). Remarks to some terms in the paper “Morphology, internal structure, and origin of glauconite pellets”. *Sedimentology*, 8, 169-171.
- Kreuzer, H. (1984). K-Ar Dating of Glauconite Rims of Phosphorite Nodules (Chatham Rise, New Zealand). *Geologisches Jahrbuch*, 65, 121-127.
- Kriaa, A., Handi, N., Goncalves, M.A., & Srasra, E. (2009). Acid-base Properties of Tunisian Glauconite in Aqueous Suspensions. *Intentional Journal of Electrochemical Science*, 4, 535-550.

- Kudrass, H-R., & Cullen, D.J. (1982). *Submarine Phosphorite Nodules from the Central Chatham Rise off New Zealand – Composition, Distribution, and Reserves – (VALDIVIA-Cruise 1978)*. Hannover, Germany: Bundesanstalt für Geowissenschaften und Rohstoffe und den Geologischen Landesämtern in der Bundesrepublik Deutschland.
- Kudrass, H-R., & von Rad, U. (1984a). Geology and some Mining Aspects of the Chatham Rise Phosphorite: a Synthesis of SONNE-17 Results. *Geologisches Jahrbuch*, 65, 235-252.
- Kudrass, H-R., & von Rad, U. (1984b). Underwater Television and Photography Observations, Side-Scan Sonar and Acoustic Reflectivity Measurements of Phosphorite-rich Areas on the Chatham Rise (New Zealand). *Geologisches Jahrbuch*, 65, 69-89.
- Lewis, D.W., & McConchie, D. (1994). *Practical Sedimentology* (2nd ed.). New York, United States of America: Chapman and Hall.
- Mass, E.W., Nodder, S.D., Voyles, K.M., Cowie, R.O.M., Morono, Y., Northcote, L., & Bowden, D.A. (2009, August). *Physical and microbial characterisation of marine sediment from two contrasting areas in New Zealand*. Paper presented at the SAME – 11th Symposium on Aquatic Microbial Ecology. Retrieved from <http://www.mbss.org/same11/abstracts/tuesday/>
- McClatchie, S., Macaulay, G.J., & Coombs, R.F. (2004). Acoustic backscatter and copepod secondary production across the Subtropical Front to the east of New Zealand. *Journal of Geophysical Research*, 109, C03013, 1-16.
- McConchie, D.M. (1978). *Cretaceous and Lower Tertiary Glauconite in the South Island of New Zealand* (Unpublished master's thesis). University of Waikato, Hamilton, New Zealand.
- McConchie, D.M., & Lewis, D.W. (1980). Varieties of glauconite in late Cretaceous and early Tertiary rocks of the South Island of New Zealand, and new proposals for classification. *New Zealand Journal of Geology and Geophysics*, 23, 413-437.
- McDougall, I., & Roksandic, Z. (1974). Total fusion $^{40}\text{Ar}/^{39}\text{Ar}$ ages using HIFAR reactor. *Journal of the Geological Society of Australia*, 21, 81-89.
- McDougall, J.C. (1982). *Bounty sediments*. N.Z. Oceanographic Institute. Chart, Oceanic Series, 1:1,000,000.
- McRae, S.G. (1972). Glauconite. *Earth-Science Reviews*, 8, 397-440.
- Millot, G. (1970). *Geology of clays: weathering, sedimentology, geochemistry*. Translated by W.R. Farrand and Helene Paquet. New York: Springer-Verlag.

- Morgan, J. (2011). East coast flush with green mineral. *Fairfax NZ News*. Retrieved from <http://www.stuff.co.nz/business/farming/5399050/East-coast-flush-with-green-mineral>.
- Morton, J.D., Grace, N.D., O'Connor, M.B., & AgResearch (Eds.). (1999). *Use of trace elements in New Zealand pastoral farming*. Created by Fert Research & AgResearch. Auckland, New Zealand: New Zealand Fertiliser Manufacturers' Research Association.
- Nelson, C.S. (1973). *Stratigraphy and sedimentology of the Te Kuiti Group, Waitomo County, South Auckland* (Unpublished PhD thesis). University of Auckland, Auckland, New Zealand.
- Nelson, C.S. (1986). Lithostratigraphy of deep sea drilling project leg 90 drill sites in the Southwest Pacific: an overview. In J.H. Blakesless (Eds.), *Initial Reports of the Deep Sea Drilling Project. Volume XC, Part 2, U.S* (pp. 1471-1491). Washington, D.C: Government Printing Office.
- Nelson, C.S. (2011). *Chatham Rise sediment sample analysis report*. Hamilton, New Zealand: The University of Waikato (unpublished).
- Nelson, C.S., & Cooke, P.J. (2001). History of oceanic front development in the New Zealand sector of the Southern Ocean during the Cenozoic – a synthesis. *New Zealand Journal of Geology and Geophysics*, 44(4), 535-553.
- Nelson, .C.S., & Froggatt, P.C. (1986). Nature, chemistry, and origin of Late Cenozoic megascopic tephra in leg 90 cores from the Southwest Pacific. In J.H. Blakesless (Eds.), *Initial Reports of the Deep Sea Drilling Project. Volume XC, Part 2* (pp. 1161-1172). Washington, D.C: U.S. Government Printing Office.
- Nelson, C.S., & Hume, T.M. (1987). Paleoenvironmental controls on mineral assemblages in a shelf sequence: Te Kuiti Group, South Auckland, New Zealand. *New Zealand Journal of Geology and Geophysics*, 30, 343-362.
- Ngatimozart. (2001). *A map of the Chatham Rise, a submarine feature, which extends 1300 km eastward of Christchurch, New Zealand*. Retrieved from http://en.wikipedia.org/wiki/File:Fig_1_Chatham_Rise_Map.jpg.
- Nodder, S.D., Duineveld, G.C.A., Pilditch, C.A., Sutton, P.J., Probert, P.K., Lavaleye, M.S.S., Witbaard, R., Chang, F.H., Hall, J.A., & Richardson, K.M. (2007). Focusing of phytodetritus Deposition beneath a Deep-Ocean Front, Chatham Rise. New Zealand. *Limnology and Oceanography*, 52(1), 299-314.
- Norris, R.M. (1964). *Sediments of Chatham Rise*. Wellington, New Zealand: Department of Scientific and Industrial Research.

- Odin, G.S. (1988). *Green Marine Clays: oolitic ironstone facies, verdine facies, glaucony facies and celadonite-bearing facies - a comparative study*. Amsterdam; New York: Elsevier; New York, N.Y., U.S.A: Distributors for the U.S. and Canada, Elsevier Science Pub. Co.
- Odin, G.S., & Fullagar, P.D. (1988). Geological significance of glaucony facies. In G.S. Odin (Eds.), *Green Marine Clays: oolitic ironstone facies, verdine facies, glaucony facies and celadonite-bearing facies - a comparative study* (pp. 295-332). Amsterdam; New York: Elsevier; New York, N.Y., U.S.A: Distributors for the U.S. and Canada, Elsevier Science Pub. Co.
- Odin, G.S., & Letolle, R. (1980). Glauconitization and phosphatization environments: A tentative comparison. *Society of Economic Paleontologists and Mineralogists Special Publication*, 29, 227-237.
- Odin, G.S., & Matter, A. (1981). De glauconiarum origine. *Sedimentology*, 28, 611-641.
- Odom, E.I. (1976). Microstructure, mineralogy and chemistry of Cambrian glauconite pellets and glauconite, central U.S.A. *Clays and Clay Minerals*, 24, 232-238.
- Oyama, M., & Takehara, H. (1970). *Revised standard soil color charts*. Japan.
- Pasho, D.W. (1976). *Distribution and Morphology of Chatham Rise Phosphorites*. Wellington, New Zealand: New Zealand Oceanographic Institute.
- Payne, D.S. (2009). *Shelf-to-slope sedimentation on the North Kaipara continental margin, Northwestern North Island, New Zealand* (Unpublished master's thesis). University of Waikato, Hamilton, New Zealand.
- Porrenga, D.H. (1967). Glauconite and chamosite as depth indicators in the marine environment. *Marine Geology*, 5, 495-501.
- Potash West NL. (2011). *Breakaway Research Report: Potential for significant potassium deposits*. Retrieved from <http://www.potashwest.com.au/UserFiles/Breakaway%20Research%20Report%2018-05-2011.pdf>.
- Robert, C., Stein, R., & Acquavia, M. (1986). Cenozoic evolution of clay associations in the New Zealand region of the Southwest Pacific, deep sea drilling project, leg 90. In J.H. Blakesless (Eds.), *Initial Reports of the Deep Sea Drilling Project. Volume XC, Part 2, U.S* (pp. 1225-1238). Washington, D.C: Government Printing Office.
- Seelig, B., Derickson, R., & Bergsrud, F. (1992). Treatment Systems for Household Water Supplies: Iron and Manganese Removal. *University of Minnesota, Agriculture*. Retrieved from <http://www.extension.umn.edu/distribution/naturalresources/DD5940.html>.

- Smith, P.E., Evensen, N.M., & York, D. (1993). First successful ^{40}Ar - ^{39}Ar dating of glauconies: Argon recoil in single grains of cryptocrystalline material. *Geology*, 21, 41-44.
- Smith, P.E., Evensen, N.M., York, D., & Odin, G.S. (1998). Single-Grain ^{40}Ar - ^{39}Ar Ages of Glauconies: Implications for the Geologic Time Scale and Global Sea Level Variations. *Science*, 279, 1517-1519.
- Spears, A.D. (2003). Bentonites and tonsteins. In G. V. Middleton (Ed.), *Encyclopedia of sediments and sedimentary rocks* (pp. 61-63). Boston: Kluwer Academic Publishers.
- Steiger, R.H., & Jäger, E. (1977). Subcommittee on Geochronology: convention on the use of decay constants in geo- and cosmochemistry. *Earth and Planetary Science Letters*, 36, 359-362.
- Stilwell, J.D., Consoil, C.P., Sutherland, R., Salisbury, S., Rich, T.H., Vickers-Rich, P.A., Currie, P.J., & Wilson, G.J. (2006). Dinosaur sanctuary on the Chatham Islands, Southwest Pacific: First record of theropods from the K-T boundary Takatika Grit. *Palaeogeography, Palaeoclimatology, Palaeoecology*, 230(3-4), 243-250.
- Summerhayes, C.P. (1967). Marine environments of economic mineral deposition around New Zealand: a review. *New Zealand Journal of Marine and Freshwater Research*, 1(3), 267-282.
- Sutton, P. (2001). Detailed structure of the Subtropical Front over Chatham Rise, east of New Zealand. *Journal of Geophysical Research*, 106(C12), 31045-31056.
- Sutton, P.J.H. (2003). The Southland Current: a subantarctic current. *New Zealand Journal of Marine and Freshwater Research*, 37, 645-652.
- Thompson, G.R., & Hower, J. (1975). The mineralogy of glauconite. *Clays and Clay Minerals*, 23, 289-300.
- Timm, C., Hoernle, K., Van den Bogaard, P., Bindeman, I., & Weaver, S. (2009). Geochemical Evolution of Intraplate Volcanism at Banks Peninsula, New Zealand: Interaction between Asthenospheric and Lithospheric Melts. *Journal of Petrology*, 50(6), 989-1023.
- Timm, C., Hoernle, K., Werner, R., Hauff, F., Van den Bogaard, P., White, J., Mortimer, N., & Garbe-Schönberg, D. (2010). Temporal and geochemical evolution of the Cenozoic intraplate volcanism of Zealandia. *Earth-Science Reviews*, 89, 38-64.
- Triplehorn, D.M. (1966). Morphology, internal structure, and origin of glauconite pellets. *Sedimentology*, 6, 247-266.

- Udgata, D.B.P. (2007). *Glaucinite as an indicator of sequence stratigraphic packages in lower Palaeocene passive-margin shelf succession, central Alabama* (Master's tech thesis, Indian School of Mines, Dhanbad, India). Retrieved from http://etd.auburn.edu/etd/bitstream/handle/10415/134/UDGA_TA_DEVI_55.pdf?sequence=1.
- US DoE. (2010). U.S. *Department of Energy Critical Materials Strategy*. Retrieved from http://energy.gov/sites/prod/files/piprod/documents/cms_dec_17_full_web.pdf.
- Velde, B. (1985). *Clay Minerals: A Physico-Chemical Explanation of their occurrence*. Amsterdam; New York: Elsevier.
- Vincent, E., Killingley, J.S., & Berger, W.H. (1980). The magnetic epoch-6 carbon shift: a change in the ocean's $^{13}\text{C}/^{12}\text{C}$ ratio 6.2 million years ago. *Marine Micropaleontology* 5, 185-203.
- Von Rad, U. (1984). Outline of SONNE Cruise SO-17 on the Chatham Rise Phosphorite Deposits East of New Zealand. *Geologisches Jahrbuch*, 65, 5-23.
- Von Rad, U., & Rösch, H. (1984). Geochemistry, Texture, and Petrography of Phosphorite Nodules and Associated Foraminiferal Glaucinite Sands (Chatham Rise, New Zealand). *Geologisches Jahrbuch*, 65, 129-178.
- Weaver, C.E. (1956). The distribution and identification of mixed-layer clays in sedimentary rocks. *American Mineralogist*, 41, 202-221.
- Weaver, C.E. (1967). Potassium, illite and the ocean. *Geochimica et Cosmochimica Acta*, 31, 2181-2196.
- Weaver, C.E. (1989). *Clays, Muds, and Shales: Developments in Sedimentology 44*. Amsterdam, The Netherlands: Elsevier Science Publishers B.V.
- Wilson, K., Hayward, B.W., Sabaa, A.T., Scott, G.H., & Kennett, J.P. (2004). A one-million-year history of a north-south segment of the Subtropical Front, east of New Zealand. *Paleoceanography*, 20, 1-10.
- Wood, R.A., Andrews, P.B., & Herzer, R.H. (1989). *Cretaceous and Cenozoic Geology of the Chatham Rise Region, South Island, New Zealand*. Lower Hutt, New Zealand: New Zealand Geological Survey.
- Worrall, W.E. (1968). *Clays: Their Nature, Origin and General Properties*. London: Maclaren.

Appendix I: Sample list

Station Number	Latitude	Longitude	Depth (m)	Glauconite %	Sample method
A799	-43.283298	177.175003	209	60	DC
A891	-43.366699	177.183304	263	61	DCMB
A892	-43.283298	177.183304	253	78	DCMB
A893	-43.200001	177.183304	263	50	DCMB
A895	-43.033298	177.166702	381	2	DCMB
A896	-43.116699	177.283295	321	15	DCMB
A897	-43.283298	177.283295	221	10	DCMB
A898	-43.366699	177.283295	231	42	DCMB
A899	-43.458302	177.183304	241	56	DCMB
A900	-43.366699	177.058304	251	58	DCMB
A901	-43.283298	177.058304	251	45	DCMB
C593	-43.50	178	351	76	G
C605	-43.666698	179.5	441	51	DP
C606	-44.2533	179.589996	985	41	DP
C607	-43.799999	179	431	5	DP
C608	-43.3167	179	450	0	DP
C609	-43.049999	178.966705	578	0	DP
C660	-42.643299	178.679993	187	0	G
C667	-42.633301	178.5	31	1	G
C961	-43.266701	177.083298	210	54	DCMB
D116	-43.00	178.666702	377	10	DCMB
D117	-43.25	178.666702	432	0	DCMB
E75	-44.00	177.416702	715	0	DCMB or TAM
E76	-44.00	178	821	0	DCMB
E82	-43.366699	179.5	402	0	DCMB or TAM
G34	-43.716702	177.383301	377	74	DP
G35	-43.758301	178	433	20	DP
G36	-43.833302	178.483307	415	40	DP
G37	-43.758301	179.041702	433	10	DP
G38	-43.616699	179.491699	415	0	DP
G112	-43.483299	178.024994	338	81	DP
G113	-43.333302	178	287	3	DP
G134	-43.049999	177.083298	357	10	DP
G135	-43.1833	177.133301	234	71	DP
G136	-43.283298	177.466705	282	50	DP
G137	-43.366699	177.416702	274	89	DP
G138	-43.25	177.333298	223	50	DP
G207	-43.700001	179.933304	399	2	DP
G208	-43.50	179.933304	413	8	DP
G210	-43.50	179.933304	424	2	DP
G211	-43.4333	179.933304	426	5	DP
G212	-43.366699	179.933304	455	2	DP
G213	-43.466702	179.816696	443	3	DP
G214	-43.483299	179.833298	413	5	DP
G217	-43.5667	179.833298	395	52	DP
G220	-43.633301	179.833298	402	8	DP

G221	-43.666698	179.800003	406	2	DP
G222	-43.700001	179.833298	395	2	DP
G223	-43.733299	179.833298	421	2	DP
G225	-43.6833	179.716705	417	2	DP
G226	-43.650002	179.716705	402	1	DP
G228	-43.616699	179.716705	406	2	DP
G231	-43.516701	179.716705	424	2	DP
G233	-43.533298	179.600006	412	5	DP
G234	-43.5667	179.600006	430	3	DP
G237	-43.616699	179.600006	402	3	DP
G239	-43.650002	179.600006	410	3	DP
G241	-43.700001	179.600006	432	15	DP
G242	-43.650002	179.483307	421	15	DP
G243	-43.633301	179.466705	424	15	DP
G244	-43.599998	179.5	406	2	DP
G245	-43.583302	179.516693	421	5	DP
G246	-43.5667	179.550003	413	2	DP
G249	-43.333302	179.483307	424	5	DP
G251	-43.383301	179.449997	395	10	DP
G252	-43.483299	179.483307	410	2	DP
G253	-43.533298	179.483307	380	3	DP
G254	-43.583302	179.483307	417	5	DP
G256	-43.6833	179.5	455	25	DP
G258	-43.5667	179.366699	402	35	DP
G259	-43.549999	179.366699	419	25	DP or TAM
G260	-43.533298	179.366699	395	5	DP
G262	-43.50	179.366699	412	10	DP
G265	-43.450001	179.366699	410	2	DP
G267	-43.383301	179.366699	410	5	DP
G269	-43.383301	179.25	439	3	DP
G270	-43.416698	179.25	443	5	DP
G271	-43.450001	179.25	435	5	DP
G272	-43.483299	179.25	426	10	TAM
G273	-43.50	179.25	410	5	DP
G274	-43.516701	179.25	424	5	DP
G276	-43.583302	179.25	413	10	TAM or DP
G279	-43.650002	179.116699	426	50	DP
G280	-43.616699	179.116699	395	45	DP
G281	-43.583302	179.116699	369	5	DP
G282	-43.549999	179.116699	399	8	TAM or DP
G283	-43.516701	179.116699	413	8	DP
G287	-43.5667	179.016693	351	15	DP
G289	-43.633301	179.016693	369	40	DP
G290	-43.666698	179.016693	327	25	DP
G291	-43.700001	179.016693	402	35	TAM
H637	-43.486698	179.561707	430	5	DP
H921	-43.490002	179.558304	394	2	DP small
H958	-43.513302	177.981705	348	81	DP large
H959	-43.4967	178	336	76	DP large
N883	-43.516701	178.201706	350	65	DP
Q317	-43.228298	178.009995	347	2	PC

Q318	-43.264999	178.016693	337	5	PC
Q319	-43.313301	178.024994	304	45	PC
Q320	-43.416698	177.994995	327	50	PC
Q323	-43.241699	177.668304	297	7	PC
Q324	-43.3083	177.6633	252	9	PC
Q325	-43.411701	177.676697	341	79	PC
Q326	-43.498299	177.673294	344	50	PC
Q327	-43.573299	177.6633	310	35	PC
Q328	-43.674999	177.666702	360	55	PC
Q330	-43.605	178.009995	360	50	PC
Q331	-43.674999	178.014999	407	50	PC
Q333	-43.485001	177.331696	265	69	PC
Q337	-43.173302	177.335007	245	64	PC
Q351	-43.169998	176.994995	276	45	PC
Q353	-43.41	178.671707	355	30	PC
Q354	-43.5033	178.666702	345	25	PC
Q356	-43.7033	178.649994	411	69	PC
Q357	-43.673302	178.313293	391	10	PC
Q359	-43.501701	178.330002	352	15	PC
Q360	-43.4217	178.330002	350	15	PC
Q361	-43.334999	178.343307	367	45	PC
U1602A	-43.428817	178.447733	350	17	MC
U2582F	-43.41	178.472283	347	24	MC
U6866	-43.1985	178.1691	343	55	MC
U6872	-43.81	178.17	349	4	MC
V361	-43.5065	178.647507	340	25	DBA or TAM
V368	-42.830799	178.992493	1048	0	DBA or TAM
V369	-42.830799	178.992493	1048	10	DBA or TAM
V372	-43.3353	178.981293	418	5	DBA or TAM
V373	-43.647499	179.000504	392	5	DBA or TAM
V374	-43.860802	178.985306	470	5	DBA or TAM
V375	-44.092701	179.039307	470	5	DBA or TAM
V376	-44.3382	179.000702	1238	2	DBA or TAM
V378	-44.084499	177.000198	663	0	DBA or TAM
V381	-43.341	177.000793	242	59	DBA
V382	-43.0798	177.000198	324	30	DBA
Z993	-43.666698	177.983307	585	45	DP
Z994	-43.633301	177.316696	530	35	DP
Z995	-43.533298	178.633301	549	5	DP
Z996	-43.666698	179.466705	402	2	DP

Key notation	Sample method
DBA	Dredge
DCMB	Cone dredge with cylindrical steel wire mesh bag
DP	Dredge pipe
G	Grab
MC	Multi core
PC	Piston core
TAM	Agassiz trawl

Note: Full sample information, i.e. sample location (latitude and longitude), cruise identification, cruise date, depth, percentage of glauconite and overall remarks, as well as The Waikato University Pet Lab numbers for all 137 samples, are listed in an Excel spread sheet in Appendix I found on the digital appendices CD located at the back of this thesis.

Appendix II-A: Munsell colours, glauconite abundance and % blackness

Sample	Munsell colour	% Black- ness	Glauconite abundance
A799	Black 2.5Y 2/1, with 40% light grey 5Y 8/2 specs	60	G
A891	Black with 70-80% light yellow 5Y 7/3 specs	30	G
A892	Black with 30% light grey 2.5Y 8/1 specs	70	G
A983	Black with 50% light grey 5Y 7/2 specs	50	G
A985	Light grey 5Y 7/2	0	-
A896	Light grey 5Y 7/2 with 15% black specs	15	g
A897	Black with 20% light grey 2.5Y 8/2 specs	80	G
A898	Black with 70% light grey 5Y 7/2 specs	30	G
A899	Black with 55% light grey 5Y 8/2 specs	45	G
A900	Black with 60% light grey 5Y 8/2 specs	40	G
A901	Black with 55% light grey 5Y 8/2 specs	50	G
C593	Light grey 5Y 7/2 with 50% black specs	50	G
C605	Black with 50% light grey 5Y 8/2 specs	50	G
C606	Black with 70% light grey 5Y 7/1 specs	30	G
C607	Light grey 5Y 7/2 with 5% black specs	5	g
C608	Light grey 5Y 7/1	0	-
C609	Light grey 5Y 8/1	0	-
C660	Light grey 7.5Y 7/1	0	-
C667	Few black specs with mostly greyish olive 5Y 5/2	3	-
C961	Black with greyish yellow 2.5Y 7/2 specs	90	VG
D116	Light grey 7.5Y 7/2 with 10% black specs	10	g
D117	Light grey 10Y 7/1	0	-
E75	Light grey 7.5Y 7/1	0	-
E76	Light grey 10Y 7/1	0	-
E82	Light grey 5Y 8/1	0	-
G34	Olive black 5Y 2/2 with 30% light grey 5Y 7/2 specs	70	G
G35	Light grey 5Y 7/2 with 20% black specs	20	g
G36	Grey 5Y 6/1 with 40% black specs	40	G
G37	Light grey 5Y 7/2 with 10% black specs	10	g
G38	Light grey 5Y 8/1	0	-
G112	Olive black 5Y 2/2 with 10% greyish olive 5Y 6/2 specs	90	VG
G113	Olive black 5Y 2/2 with 20-30% light grey 5Y 8/2 specs	75	G
G134	Light grey 7.5Y 7/2 with 5% black specs	5	g
G135	Black with 40% pale yellow 2.5Y 8/2 specs	60	G
G136	Black with 50% light grey 5Y 7/1 specs	50	G
G137	Black with 5% light grey 5Y 8/1 specs	95	VG
G138	Black with 50% light grey 5Y 8/2 specs	50	G
G207	Light grey 5Y 7/2 with 2% black specs	2	-
G208	Light grey 5Y 7/1 with 5-10% black specs	7.5	g
G210	Light grey 5Y 8/2 with 2% black specs	2	-
G211	Light grey 5Y 7/2 with 5% black specs	5	g
G212	Light grey 5Y 7/2 with 2% black specs	2	-
G213	Light grey 5Y 7/2 with 3% black specs	3	-
G214	Light grey 5Y 7/2 with 5% black specs	5	g

G217	Black with 25% light grey 2.5Y 8/1 specs	75	G
G220	Light grey 5Y 7/2 with 5-10% black specs	7.5	g
G221	Light grey 5Y 7/1 with 2% black specs	2	-
G222	Light grey 5Y 7/2 with 2% black specs	2	-
G223	Light grey 5Y 7/1 with 2% black specs	2	-
G225	Light grey 5Y 7/2 with 2% black specs	2	-
G226	Light grey 7.5Y 8/1 with 1% black specs	1	-
G228	Light grey 7.5Y 7/1 with 2% black specs	1	-
G231	Light grey 5Y 7/2 with 2% black specs	1	-
G233	Light grey 5Y 7/2 with 5% black specs	5	g
G234	Light grey 5Y 7/1 with 3% black specs	3	-
G237	Light grey 5Y 7/1 with 3% black specs	3	-
G239	Light grey 5Y 7/1 with 3% black specs	3	-
G241	Light grey 5Y 8/1 with 15% black specs	15	g
G242	Light grey 5Y 7/1 with 15% black specs	15	g
G243	Greyish olive 5Y 6/2 with 5% black specs	5	g
G244	Light grey 5Y 7/2 with 2% black specs	2	-
G245	Light grey 5Y 7/1 with 5% black specs	5	g
G246	Light grey 7.5Y 8/1 with 2% black specs	2	-
G249	Light grey 5Y 7/2 with 5% black specs	5	g
G251	Light grey 5Y 7/2 with 10% black specs	10	g
G252	Light grey 5Y 7/2 with 2% black specs	2	-
G253	Light grey 5Y 7/2 with 3% black specs	3	-
G254	Light grey 5Y 7/1 with 5% black specs	5	g
G256	Light grey 5Y 6/1 with 25% black specs	25	g
G258	Light grey 5Y 7/2 with 40% black specs	40	G
G259	Light grey 5Y 7/2 with 25% black specs	25	g
G260	Light grey 5Y 7/1 with 5% black specs	5	g
G262	Light grey 5Y 7/2 with 10% black specs	10	g
G265	Light grey 5Y 7/2 with 2% black specs	2	-
G267	Light grey 5Y 7/2 with 5% black specs	5	g
G269	Light grey 5Y 7/2 with 3% black specs	3	-
G270	Light grey 5Y 7/2 with 5% black specs	5	g
G271	Light grey 5Y 7/1 with 5% black specs	5	g
G272	Light grey 5Y 7/2 with 10% black specs	10	g
G273	Light grey 5Y 7/2 with 5% black specs	5	g
G274	Light grey 5Y 8/2 with 5% black specs	5	g
G276	Light grey 5Y 7/2 with 10% black specs	10	g
G279	Greyish olive 5Y 6/2 with 40% black specs	60	G
G280	Light grey 5Y 7/1 with 60% black specs	60	G
G281	Light grey 5Y 7/2 with 5% black specs	5	g
G282	Light grey 7.5Y 7/2 with 5-10% black specs	7.5	g
G283	Light grey 5Y 7/2 with 5-10% black specs	7.5	g
G287	Light grey 5Y 7/2 with 15% black specs	15	g
G289	Light grey 5Y 7/2 with 40% black specs	40	G
G290	Greyish olive 5Y 6/2 with 5% black specs	5	g
G291	Light grey 5Y 7/2 with 35% black specs	35	G
H637	Light grey 7.5Y 7/2 with 5% black specs	5	g
H921	Greyish olive 5Y 6/2	0	-
H958	Olive black 5Y 3/1 with 30% greyish olive 5Y 6/2 specs	85	VG
H959	Olive black 5Y 3/1 with 30% light grey 5Y 7/2 specs	70	G

N883	Greenish grey 7.5GY 5/1	90	VG
V361	Light grey 5Y 7/1 with 30% black specs	70	G
V368	Light grey 7.5Y 7/2	0	-
V369	Light grey 5Y 7/1 with 10% black specs	10	g
V372	Light grey 5Y 7/1 with 5% black specs	5	g
V373	Light grey 5Y 7/2 with 5% black specs	5	g
V374	Light grey 5Y 7/1 with 5% black specs	5	g
V375	Light grey 7.5Y 7/1 with 5% black specs	5	g
V376	Light grey 10Y 8/1 with 2% black specs	2	-
V378	Light grey 7.5Y 7/1	0	-
V381	Black with 65% greyish yellow 2.5Y 7/2 specs	35	G
V382	Greyish olive 5Y 6/2 with 20% black specs	50	G
Z993	Greyish olive 5Y 6/2	0	-
Z994	Light grey 5Y 7/2 with 5% black specs	5	g
Z995	Light grey 5Y 7/2 with 5% black specs	5	g
Z996	Light grey 5Y 7/1	0	-
Q317	Light grey 7.5Y 8/1 with 2% black specs	2	-
Q318	Light grey 7.5Y 8/1 with 5% black specs	5	g
Q319	Grey 7.5Y 6/1 with 45% black specs	45	G
Q320	Light grey 7.5Y 7/2 with 50% black specs	50	G
Q323	Light grey 5Y 7/1 with 5-10% black specs	7.5	g
Q324	Light grey 5Y 7/1 with 3-5% black specs	3	-
Q325	Grey 7.5Y 5/1 with 80% black specs	80	G
Q326	Grey 7.5Y 5/1 with 50% black specs	50	G
Q327	Light grey 7.5Y 7/2 with 35% black specs	35	G
Q328	Greyish olive 7.5Y 6/2 with 70% black specs	70	G
Q330	Grey 7.5Y 6/2 with 50% black specs	50	G
Q331	Grey 7.5Y 6/1 with 50% black specs	50	G
Q333	Grey 7.5Y 6/1 with 75% black specs	75	G
Q337	Light grey 5Y 7/2 with 25% black specs	25	g
Q351	Grey 7.5Y 6/1 with 60% black specs	60	G
Q353	Light grey 7.5Y 7/2 with 30% black specs	30	G
Q354	Greyish olive 5Y 6/2 with 25% black specs	25	g
Q356	Grey 7.5Y 5/1 with 75% black specs	75	G
Q357	Light grey 5Y 7/2 with 10% black specs	10	g
Q359	Light grey 5Y 8/1 with 15% black specs	15	g
Q360	Light grey 5Y 8/2 with 15% black specs	15	g
Q361	Light grey 7.5Y 7/1 with 45% black specs	45	G
U1602A	Olive grey 10Y 5/2 with 35% black specs	35	G
U2582F	Olive grey 10Y 5/2 with 50% black specs	50	G
U6866	Olive grey 10Y 5/2 with 65% black specs	65	G
U6872	Olive grey 10Y 5/2 with 10% black specs	10	g

Glaucanite abundance key

VG Very glauconite rich

G Glaucanite rich

g Some glauconite present

- Little or no glauconite present

Appendix II-B: Samples used in various laboratory techniques

Laser-sizer; texture: All 137 bulk surficial samples used.

XRD: Bulk surficial samples used (50)

A891, A892, A893, A896, A897, A899, C593, C605, C606, C608, C667, C961, D116, E76, G34, G35, G36, G112, G113, G136, G137, G239, G249, G256, G271, G282, G289, H921, H958, Q325, Q326, Q328, Q333, Q356, Q357, U1602A, U2582F, U6866 2-3 cm, U6866 7-8 cm, U6866 11-12 cm, U6872 2-3 cm, U6872 11-15 cm, V361, V369, V372, V374, V375, V376, V381, V382.

XRD: Clay fraction samples used

Air-dried (35): A891, A892, A897, A898, A899, A900, A901, C593, C605, C606, C667, C961, G34, G36, G112, G113, G135, G136, G137, G138, G217, H958, H959, N883, Q319, Q325, Q326, Q328, Q333, Q356, U1602A, U2582F, U6866 0-2 cm, U6872 0-5 cm, V381.

3-step analysis (13): A900, C605, C606, G34, G36, G135, G137, H959, Q325, Q328, Q356, U1602A, U6866 0-2 cm.

XRD: Chalk fraction samples used (5)

G228, Q317, Q318, Q359, Q360.

XRF trace elements: Bulk surficial samples used (49)

A891, A893, A896, A897, A899, C593, C605, C606, C608, C667, C961, D116, E76, G34, G35, G36, G112, G113, G136, G137, G239, G249, G256, G271, G282, G289, H921, H958, Q325, Q326, Q328, Q333, Q356, Q357, U1602A, U2582F, U6866 2-3 cm, U6866 7-8 cm, U6866 11-12 cm, U6872 2-3 cm, U6872 11-15 cm, V361, V369, V372, V374, V375, V376, V381, V382.

CaCO₃ % acid digestion: Bulk surficial samples used (10)

A899, C605, C606, D116, G34, G113, G136, G271, Q325, Q356.

CaCO₃ % acid digestion: Chalk samples used (5)

G228, Q317, Q318, Q359, Q360.

Appendix II-C: Bulk sample texture

The results for the bulk surficial sediment samples texture analysed using the Malvern laser-sizer and the Folk (1968) classification, are found on the digital appendices (II-C) CD located at the back of this thesis.

Appendix II-D: % gravel, sand and mud fractions

Sample	Bulk weight	Gravel weight	Sand weight	Mud weight	% Gravel	% Sand	% Mud
A891	37.00	0.47	34.72	1.81	1.27	93.84	4.89
A892	54.54	0.45	51.06	3.03	0.83	93.62	5.56
A897	40.08	0.18	38.17	1.73	0.45	95.23	4.32
A898	83.22	30.50	45.49	7.23	36.65	54.66	8.69
A899	47.35	0.20	44.30	2.85	0.42	93.56	6.02
A900	55.60	0.00	51.52	4.08	0.00	92.66	7.34
A901	66.05	19.75	42.61	3.69	29.90	64.51	5.59
C605	39.31	0.82	29.34	9.15	2.09	74.64	23.28
C606	85.92	0.02	72.62	13.28	0.02	84.52	15.46
C593	43.85	0.00	37.07	6.78	0.00	84.54	15.46
C667	57.21	2.41	52.91	1.89	4.21	92.48	3.30
C961	72.81	0.39	60.06	12.36	0.54	82.49	16.98
G34	130.09	2.67	111.37	16.05	2.05	85.61	12.34
G36	86.09	0.02	65.03	21.04	0.02	75.54	24.44
G112	56.99	0.31	50.11	6.57	0.54	87.93	11.53
G113	76.18	0.32	69.37	6.49	0.42	91.06	8.52
G135	123.68	2.48	116.43	4.77	2.01	94.14	3.86
G136	79.98	2.46	68.86	8.66	3.08	86.10	10.83
G137	40.99	0.08	38.51	2.40	0.20	93.95	5.86
G138	46.23	0.46	43.06	2.71	1.00	93.14	5.86
G217	34.72	0.68	32.34	1.70	1.96	93.15	4.90
H958	63.13	0.31	53.66	9.16	0.49	85.00	14.51
H959	124.85	0.47	110.81	13.57	0.38	88.75	10.87
N883	18.38	0.24	12.95	5.19	1.31	70.46	28.24
Q319	53.66	0.05	36.38	17.23	0.09	67.80	32.11
Q325	42.91	0.29	37.49	5.13	0.68	87.37	11.96
Q326	39.77	1.55	27.84	10.38	3.90	70.00	26.10
Q328	54.52	0.10	44.69	9.73	0.18	81.97	17.85
Q333	33.59	0.83	30.89	1.87	2.47	91.96	5.57
Q356	33.30	0.37	27.03	5.90	1.11	81.17	17.72
V381	78.87	0.17	74.31	4.39	0.22	94.22	5.57
U2582F	67.91	1.63	28.12	38.16	2.40	41.41	56.19
U1602A	72.85	0.34	29.05	43.46	0.47	39.88	59.66
U6866 0-2 cm	60.00	0.25	39.08	20.67	0.42	65.13	34.45
U6866 2-4 cm	70.00	0.10	53.34	16.56	0.14	76.20	23.66
U6866 4-6 cm	135.00	0.29	74.67	60.04	0.21	55.31	44.47
U6866 6-8 cm	95.00	0.26	54.12	40.62	0.27	56.97	42.76
U6866 8-10 cm	115.00	0.09	61.52	53.39	0.08	53.50	46.43
U6866 10-13 cm	145.00	0.87	84.52	59.61	0.60	58.29	41.11
U6872 0-5 cm	120.7	0.00	31.32	89.38	0.00	25.95	74.05
U6872 10-15 cm	183.48	0.06	64.01	119.41	0.03	34.89	65.08
U6872 20-25 cm	268.4	0.17	112.63	155.60	0.06	41.96	57.97

Note: Weights all in grams.

Appendix II-E: XRD mineralogy

The results of all XRD scans for the bulk surficial sediment samples, clay samples and chalk samples, are found on the digital appendices (II-E) CD located at the back of this thesis.

Appendix II-F: Geochemistry

The results for the bulk XRF geochemical major and trace elemental results, as well as the geochemistry versus texture results, are found on the digital appendices (II-F) CD located at the back of this thesis.

Appendix II-G: CaCO₃% acid digestion results

Bulk surficial samples

Sample	Beaker wt	Sample+beaker wt after 105°C	Sample wt	Sample+beaker wt after digestion	Sample wt after digestion	CaCO ₃ %
A899	33.554	38.431	4.877	36.798	1.633	33.4837
C605	40.91	44.596	3.686	43.59	1.006	27.29246
C606	38.742	41.152	2.41	40.235	0.917	38.04979
D116	32.072	34.134	2.062	33.464	0.67	32.49273
G34	28.563	33.22	4.657	32.328	0.892	19.15396
G113	37.282	42.246	4.964	41.594	0.652	13.13457
G136	33.499	36.205	2.706	34.941	1.264	46.71101
G271	30.289	35.003	4.714	33.049	1.954	41.451
Q325	35.615	40.512	4.897	39.657	0.855	17.45967
Q356	42.596	47.463	4.867	46.615	0.848	17.42346

Chalk samples

Sample	Beaker wt	Sample+beaker wt after 105°C	Sample wt	Sample+beaker wt after digestion	Sample wt after digestion	CaCO ₃ %
G228	31.928	33.985	2.057	32.245	1.740	84.58921
Q317	34.146	38.884	4.738	34.34	4.544	95.90545
Q318	33.583	35.35	1.767	33.901	1.449	82.0034
Q359	34.992	40.029	5.037	37.569	2.460	48.83859
Q360	40.885	43.224	2.339	41.435	1.789	76.48568

Note: wt = weight, and weights are all in grams.

CaCO₃% results for the four techniques

The results for CaCO₃% comparison calculated using the four following techniques; XRD, XRF, petrographic analysis and CaCO₃ acid digestion; are found in the digital appendices (II-G) CD found at the back of this thesis.

Appendix II-H: Bulk surficial sample photos

All bulk surficial sample petrography photomicrographs and all SEM images are found on the digital appendices (II-H) CD located at the back of this thesis.

Appendix III: Glauconite physical properties

Weight percentages of various fractions from the original bulk surficial samples.

Sample	Magnetic/ glauconite %	Non-magnetic %	Mud %	Gravel %	Lost %
A891	60.26	32.11	4.89	1.27	1.47
A892	77.75	15.38	5.56	0.83	0.49
A897	82.37	12.08	4.32	0.45	0.79
A898	30.42	23.62	8.69	36.65	0.63
A899	62.62	30.11	6.02	0.42	0.83
A900	63.45	28.23	7.34	0.00	0.98
A901	43.72	20.21	5.59	29.90	0.58
C605	49.41	23.15	23.28	2.09	2.07
C606	44.11	39.78	15.46	0.02	0.62
C593	76.31	7.10	15.46	0.00	1.13
C667	5.28	86.18	3.30	4.21	1.03
C961	59.01	23.07	16.98	0.54	0.41
G34	76.23	9.38	12.34	2.05	0.00
G36	57.31	17.66	24.44	0.02	0.56
G112	81.09	6.61	11.53	0.54	0.23
G113	77.57	4.81	8.52	0.42	8.68
G135	74.33	18.82	3.86	2.01	0.99
G136	38.69	46.74	10.83	3.08	0.66
G137	89.22	4.30	5.86	0.20	0.44
G138	63.96	28.22	5.86	1.00	0.96
G217	51.03	40.49	4.90	1.96	1.62
H958	79.70	4.68	14.51	0.49	0.62
H959	80.51	7.38	10.87	0.38	0.87
N883	64.40	4.32	28.24	1.31	1.74
Q319	59.94	7.34	32.11	0.09	0.52
Q325	78.59	8.04	11.96	0.68	0.74
Q326	59.76	9.18	26.10	3.90	1.06
Q328	63.91	18.00	17.85	0.18	0.06
Q333	68.03	22.50	5.57	2.47	1.44
Q356	68.68	10.79	17.72	1.11	1.71
V381	59.32	34.74	5.57	0.22	0.16
U2582F	23.53	17.11	56.19	2.40	0.77
U1602A	17.62	16.93	59.66	0.47	5.33
U6866 0-2 cm	52.99	9.85	34.45	0.42	2.29
U6866 2-4 cm	61.03	14.64	23.66	0.14	0.53
U6866 4-6 cm	42.84	11.98	44.47	0.21	0.49
U6866 6-8 cm	43.91	12.57	42.76	0.27	0.48
U6866 8-10 cm	40.37	12.73	46.43	0.08	0.40
U6866 10-13 cm	47.44	10.54	41.11	0.60	0.31
U6872 10-15 cm	5.27	29.06	65.08	0.03	0.56

Photos: All glauconite detrital, petrography photomicrographs and SEM images can be found the digital appendices (III) CD located at the back of this thesis.

Appendix IV: XRD raw results

Sample	(001) Å air-dried spread	(001) Å glycolated spread	(001) Å heated spread	Peak pattern class	% expandables using K ₂ O content	% expandables from glycolation
A891	12.45	10.00	10.78	2	13	10
A892	12.28	10.00	10.65	2	9	10
A897	13.00	10.53	11.19	1	10	16
A898	12.41	10.00	10.92	2	-	10
A899	12.63	10.16	11.05	1	-	11
A900	11.63	10.78	10.78	3	13	18
A901	12.28	10.78	11.05	1	-	18
C605	12.60	10.16	11.79	2	16	11
C606	14.00	10.40	12.81	3	26	15
C593	12.28	10.00	10.92	2	-	10
C961	11.95	10.78	10.78	2	10	18
G34	13.20	10.00	11.05	2	12	10
G36	13.00	10.16	11.33	3	17	11
G112	12.28	10.90	11.19	2	11	19
G113	12.28	10.30	10.92	2	12	13
G135	12.45	10.50	11.05	2	-	16
G136	12.45	10.50	10.65	3	-	16
G137	12.45	10.50	10.78	1	11	16
G138	12.81	10.50	10.78	3	11	16
G217	11.05	10.90	11.05	1	15	19
H958	10.78	10.00	10.53	3	-	10
H959	11.79	10.65	10.78	3	10	17
N883	11.79	10.78	10.92	1	12	18
Q319	12.11	10.65	10.92	2	14	17
Q325	12.63	10.50	10.92	1	11	16
Q326	11.05	10.00	10.53	3	13	10
Q328	11.05	10.00	10.78	3	-	10
Q333	12.11	10.90	10.78	1	10	19
Q356	13.40	10.00	11.05	3	11	10
U1602A	11.95	10.00	10.78	3	-	10
U2582F	12.23	10.4	11.05	2	13	15
U6866	11.20	10.30	11.05	2	13	13
average						
U6872	11.22	10.00	10.78	3	22	10
V381	12.45	10.00	11.19	2	14	10

Note: Not all samples have a % expandables calculated from the potassium content, as these samples were not analysed for their major elemental geochemistry using XRF.

XRD Scans: All glauconite XRD scans can be found the digital appendices (IV) CD located at the back of this thesis.

Appendix V: Glauconite geochemistry

Microprobe results: All glauconite microprobe results, including photomicrographs of the grains probed as well as the results, are found the digital appendices (V) CD located at the back of this thesis.

XRF raw results: All glauconite XRF results are in Excel spreadsheets, which can be found the digital appendices (V) CD located at the back of this thesis.

XRF major element results: (see Table below).

	SiO ₂	TiO ₂	Al ₂ O ₃	Fe ₂ O ₃ *	MnO	MgO	CaO	P ₂ O ₅	Na ₂ O	K ₂ O	LOI	Total %
A891	46.78	0.11	8.46	20.48	0.01	3.88	2.16	0.86	0.56	7.19	8.42	98.91
A892	49.50	0.11	8.37	21.19	0.01	4.07	1.49	0.91	0.56	7.61	7.53	101.33
A897	49.31	0.12	8.47	21.27	0.01	4.08	1.21	0.73	0.60	7.48	6.24	99.51
A900	42.41	0.13	8.48	20.56	0.01	3.85	1.58	0.53	0.54	7.21	7.80	93.10
C605	49.67	0.19	8.94	18.92	0.01	4.22	1.99	0.96	0.60	6.77	7.02	99.29
C606	46.06	0.25	6.45	21.72	0.02	3.72	3.30	0.36	0.86	5.45	7.86	96.07
C961	48.13	0.11	8.18	20.99	0.01	3.95	1.56	0.88	0.58	7.51	6.86	98.76
G34	48.11	0.13	8.28	21.10	0.01	3.74	1.19	0.64	0.73	7.24	8.16	99.31
G36	49.30	0.19	8.99	19.06	0.01	3.98	1.60	0.63	0.89	6.64	7.31	98.60
G112	49.12	0.13	8.48	20.12	0.01	4.01	1.14	0.66	0.64	7.37	7.22	98.89
G113	48.66	0.13	8.25	20.46	0.01	4.00	1.50	0.86	0.66	7.28	7.92	99.73
G135	48.37	0.10	7.95	20.88	0.01	3.96	2.21	1.11	0.60	7.46	7.17	99.81
G137	49.12	0.12	8.49	20.79	0.01	4.05	1.11	0.60	0.66	7.47	7.30	99.72
G217	45.12	0.26	6.89	18.71	0.02	3.92	6.12	3.71	0.68	6.86	7.66	99.95
H959	48.23	0.12	8.03	20.64	0.01	4.12	1.21	0.62	0.70	7.54	7.33	98.54
N883	48.73	0.16	8.43	20.37	0.01	3.93	1.25	0.74	0.45	7.33	7.31	98.72
Q319	41.44	0.13	6.88	19.90	0.01	3.74	1.77	0.80	0.51	7.04	7.20	89.42
Q325	49.66	0.13	8.21	20.75	0.01	4.03	1.40	0.75	0.72	7.35	7.16	100.17
Q326	49.64	0.13	8.15	20.40	0.01	3.98	1.02	0.70	0.60	7.14	7.48	99.26
Q333	46.37	0.12	8.17	21.28	0.01	3.80	1.55	0.78	0.61	7.48	7.62	97.78
Q356	50.94	0.16	9.04	19.85	0.01	4.13	1.47	0.71	0.73	7.40	6.98	101.42
U2582F	49.30	0.22	9.06	19.77	0.02	4.15	2.24	0.98	0.70	7.10	7.04	100.58
U6866 0-2 cm	48.47	0.14	8.31	20.25	0.01	3.99	1.78	0.97	0.63	7.20	7.13	98.88
U6866 2-4cm	47.60	0.13	8.17	20.07	0.01	3.94	1.61	0.88	0.72	7.19	8.30	98.62
U6866 4-6cm	47.47	0.13	8.13	20.19	0.01	3.92	1.68	0.93	0.70	7.16	8.32	98.63
U6866 6-8cm	47.89	0.14	8.26	20.21	0.01	3.94	1.60	0.85	0.82	7.18	6.85	97.74
U6866 8-10 cm	48.06	0.14	8.27	20.38	0.01	3.95	1.63	0.90	0.68	7.26	7.58	98.87

U6866 10-13 cm	46.85	0.12	7.78	20.11	0.01	3.90	1.94	1.12	0.63	7.20	8.31	97.97
U6872	45.57	0.37	8.68	18.84	0.04	3.99	3.59	0.64	1.02	6.00	8.59	97.33
V381	44.64	0.13	8.09	20.17	0.01	3.71	1.72	0.72	0.64	7.01	7.91	94.74

XRF main trace element results: (see Table below).

	A891	A892	A897	A898	A899	A900	A901	C593	C605	C606	C961	G34	G36	G112	G113
S	1531	775	743	636	631	601	741	1150	998	682	589	1040	1860	645	570
Cl	947	854	1016	186	506	257	768	1712	387	389	174	1253	2905	1715	1524
V	108	109	102	118	112	110	108	126	148	161	105	125	142	122	123
Cr	199	210	216	192	202	211	202	250	275	323	198	246	251	250	262
Ni	28	30	33	27	30	30	30	33	46	29	28	27	42	32	33
Zn	59	59	61	58	62	59	56	66	94	125	58	60	68	62	64
Ga	14.2	13.6	13.6	13.8	14.8	13.9	13.8	14.5	15.1	14.2	13.6	13.8	15.1	14	13.5
Ge	2.3	2.9	3.7	3.3	3	2.6	2.8	3.5	3.1	3	2.9	2.7	4.1	3.3	3.4
As	32.6	28	25	32	32	32	31	21	21	13.3	31	25	19	20	18.1
Br	12.1	8.9	8.7	4.3	6.2	6.4	7.9	12.1	6.9	8.1	2.8	9.5	15.2	12.6	11.4
Rb	179	188	188	179	181	181	183	188	185	180	186	184	182	190	192
Sr	81	62	54	92	67	60	60	48	86	121	64	54	71	51	61
Y	34	37	33	38	31	24	27	29	50	26	37	30	31	33	37
Zr	30	32	33	33	35	34	32	34	42	56	31	32	47	34	33
Nb	4	4.6	4.8	4.5	4.8	4.2	4.4	4.1	4.8	4.9	4.5	4.1	5.3	4.5	4.5
Sb	4	3.8	3.4	4.7	3.7	3.1	3	3.2	2.3	2.5	4.2	3.4	2.7	3.1	4.9
I	14.8	?	?	9.9	?	11.8	13.1	11.8	14.4	19.3	?	12.4	?	?	?
Cs	5.8	?	?	4.4	?	6.5	7.2	6.3	7.6	11.2	?	6	?	?	?
Ba	18.7	13.3	14.1	49	18.6	19.4	17.8	22	28	77	12.5	21	38	16.7	18.4
La	18.3	17.6	18.3	18.5	17.1	13.8	15	14.3	21	10.4	17.6	16.3	14	14.3	19
Ce	29.9	30	29	29.3	25	21	20.5	22	25	15.3	29	28	23	20	25
W	30	33	39	26	31	30	28	27	34	16.6	23	16.6	22	26	43
Pb	7.9	7.2	8.7	8.2	8.9	6.9	6.8	4.8	7.6	6.8	6.4	5.9	6.6	4	6.3
U	14.7	18.3	17.1	16.7	17.4	12.7	10.5	13.9	14.2	8.7	14.4	13.7	20	15.1	17.4

	G135	G136	G137	G138	G217	H958	H959	N883	Q319	Q325	Q326	Q328	Q333	Q356	U1602A	U2582F
S	831	1082	1192	874	1714	693	696	566	3519	673	568	1134	1120	92	1483	950
Cl	1070	1685	1630	482	995	468	1447	78	1008	1002	441	653	1365	591	62	132
V	100	125	106	106	181	128	123	129	133	118	122	123	116	137	148	144
Cr	204	232	224	207	301	249	248	243	267	231	252	259	220	257	268	268
Ni	27	32	29	28	40	35	31	38	42	25	30	30	30	38	47	40
Zn	55	61	59	59	89	65	65	72	81	54	57	61	65	66	70	70
Ga	13.3	13.7	13.6	13.5	16.9	15.6	14.4	14	14.1	14	15.3	13.7	14.7	14.3	15.4	14.8
Ge	2.9	2.7	3.4	3.2	3.9	2.7	3.4	3.3	3	2.7	2.7	3.3	3.7	3.3	3.3	3.8
As	30	27	25	30	21	19.5	18.7	22	22	25	22	22	27	18.6	26	26
Br	9.9	12	13.5	8.3	6.5	5.8	12.2	0.6	4.6	8.6	5.9	8.2	9.5	8	3.1	5.2
Rb	183	168	188	181	184	191	192	190	193	186	187	185	189	187	181	182
Sr	81	115	50	59	270	48	52	57	72	58	46	59	64	64	79	88
Y	37	39	29	28	133	31	32	41	42	31	27	27	38	39	39	42
Zr	30	36	32	32	48	33	35	35	42	31	33	37	32	37	40	43
Nb	4.5	4.5	4.6	3.8	5.9	4	4.5	4.6	4.4	4.5	4.8	5	4.7	4.1	4.7	4.9
Sb	4.5	4.3	4.6	3.5	5.2	3.2	3.6	3.9	4.2	3.4	3.3	3.9	5	3.1	4.8	4.9
I	?	22	?	13.4	16.8	9.9	?	?	?	?	?	?	?	15.2	7	?
Cs	?	3.6	?	6.4	4.7	6.5	?	?	?	?	?	?	?	5.4	7.7	?
Ba	13.9	42	15.2	17.3	47	15.5	17.3	14.8	17.2	19	18.2	26	14.9	26	39	43
La	17.4	21	14.5	14.1	64	13.7	13.6	16.3	19.2	13.2	12.8	10	16.8	17.1	16.4	17.2
Ce	28	31	27	22	54	22	21	22	25	24	23	21	30	22	20	20
W	18.1	44	31	24	45	25	30	35	31	20	33	18.9	46	27	25	41
Pb	6.8	8.6	5.9	8.1	10.2	4.7	6.5	12.6	8.4	5.8	5.1	5.8	9.6	4.7	8.1	8.6
U	20	14.6	12.2	13	25	14.1	15.2	11.4	19.7	16	16.5	17.9	15.2	14.4	14.5	16.3

	U6866 0-2cm	U6866 2-4cm	U6866 4-6cm	U6866 6-8cm	U6866 8-10cm	U6866 10-13cm	U6872	V381
S	1256	852	997	1132	868	947	1801	1420
Cl	173	149	257	438	68	57	4028	1159
V	132	132	130	132	131	126	151	110
Cr	259	260	257	261	260	251	264	216
Ni	40	38	36	38	37	36	49	29
Zn	64	64	63	65	65	63	74	60
Ga	15.2	13.7	14.4	15.3	14.6	15.1	15.8	15.9
Ge	3.7	4	3.3	3.6	3.3	3.3	2.7	3
As	24	24	24	25	25	24	21	34
Br	3.6	3.5	4	4.5	2.8	2.7	24	9.6
Rb	186	187	186	188	184	184	162	181
Sr	75	69	72	67	67	82	129	70
Y	47	45	46	44	43	49	35	29
Zr	32	33	31	31	32	34	56	33
Nb	3.7	3.8	3.7	3.8	4	3.8	6.2	4.6
Sb	4.6	4	4.1	4.5	4.2	4	3.3	3.9
I	9.1	9.1	10.9	10.8	8.9	9.4	?	?
Cs	5.4	4.4	5.8	6	6.2	5.2	?	?
Ba	26	24	27	23	25	26	85	17.5
La	22	21	22	19.6	22	24	13.3	11.3
Ce	27	26	26	25	27	28	21	21
W	21	22	17.5	17.4	21	21	51	20
Pb	5.5	5.7	6.6	5.2	5.2	5.6	12.5	8.9
U	12.7	12.8	13.5	13.4	13.1	14.7	14.1	10

Appendix VI: Age data

Client ID	Sample ID	K	Rad. ⁴⁰ Ar	Rad. ⁴⁰ Ar	Age	Error	Error	"G-O" (2004) Period-Epoch-Stage
		[%]	[mol/g]	[%]	[Ma]	[Ma]	[%]	
Standard	HD-B1-102	7.96	3.3385E-10	92.43	24.03	0.37	1.50	Palaeogene-Oligocene-Chattian
A891	1583	6.58	6.8624E-11	34.57	6.00	0.23	3.80	Neogene-Miocene-Messinian
Q325	1584	6.61	6.5184E-11	27.51	5.68	0.22	3.80	Neogene-Miocene-Messinian
Q356	1585	6.66	6.6189E-11	27.17	5.72	0.26	4.60	Neogene-Miocene-Messinian
U6866 0-2cm	1586	6.50	6.1712E-11	27.25	5.47	0.20	3.60	Neogene-Miocene-Messinian
U6866 10-13cm	1587	6.55	6.6972E-11	29.64	5.89	0.25	4.30	Neogene-Miocene-Messinian
Average	1585	6.58	6.5728E-11	29.23	5.75	0.23	4.00	Neogene-Miocene-Messinian

* "G-O" (2004) = Gradstein *et al.*, 2004.

Appendix VII: Economics

Resource estimate calculation procedure

- Porosity of typical sand in seawater = 40%, therefore sediment represents 60% of each area/volume.
- Typical glauconite density = 2.64 t/m³.
- Surficial sediment depth of 0.5 m.
- Volume of each polygon = area x depth
- Refer back to Figure 10.2 for the polygon locations.

1. >80 (av. 80) wt% glauconite polygon:

- Area calculated by GIS: $2.859 \times 10^8 \text{ m}^2$, therefore
- Volume: $2.859 \times 10^8 \text{ m}^2 \times 0.5 \text{ m} = 1.4295 \times 10^8 \text{ m}^3$
- Glauconite % in 1 m³: 80 wt% glauconite x 60% (sediment fraction)/100 = 48% glauconite in each 1 m³
- Glauconite density in each 1 m³: 48% glauconite x 2.64 t/m³ (glauconite density)/100 = 1.2672 t/m³
- Glauconite estimated tonnage within polygon: glauconite density 1.2672 t/m³ x $1.4295 \times 10^8 \text{ m}^3$ (volume) = 181146240 t = 181 Mt

2. 70-80 (av. 75) wt% glauconite polygon:

- Area calculated by GIS: $5.0328 \times 10^8 \text{ m}^2$, therefore
- Volume: $5.0328 \times 10^8 \text{ m}^2 \times 0.5 \text{ m} = 2.5164 \times 10^8 \text{ m}^3$
- Glauconite % in 1 m³: 75 wt% glauconite x 60% (sediment fraction)/100 = 45% glauconite in each 1 m³
- Glauconite density in each 1 m³: 45% glauconite x 2.64 t/m³ (glauconite density)/100 = 1.188 t/m³
- Glauconite estimated tonnage within polygon: glauconite density 1.188 t/m³ x $2.5164 \times 10^8 \text{ m}^3$ (volume) = 298948320 t = 299 Mt

3. 60-70 (av. 65) wt% glauconite polygon:

- Area calculated by GIS: $7.59 \times 10^8 \text{ m}^2$, therefore
- Volume: $7.59 \times 10^8 \text{ m}^2 \times 0.5 \text{ m} = 3.795 \times 10^8 \text{ m}^3$
- Glauconite % in 1 m³: 65 wt% glauconite x 60% (sediment fraction)/100 = 39% glauconite in each 1 m³
- Glauconite density in each 1 m³: 39% glauconite x 2.64 t/m³ (glauconite density)/100 = 1.0296 t/m³
- Glauconite estimated tonnage within polygon: glauconite density 1.0296 t/m³ x $3.795 \times 10^8 \text{ m}^3$ (volume) = 390733200 t = 391 Mt

4. 50-60 (av. 55) wt% glauconite polygon:

- Area calculated by GIS: $2.97636 \times 10^9 \text{ m}^2$, therefore
- Volume: $2.9763 \times 10^8 \text{ m}^2 \times 0.5 \text{ m} = 1.48818 \times 10^9 \text{ m}^3$
- Glauconite % in 1 m^3 : $55 \text{ wt\% glauconite} \times 60\% \text{ (sediment fraction)}/100 = 33\% \text{ glauconite in each } 1 \text{ m}^3$
- Glauconite density in each 1 m^3 : $33\% \text{ glauconite} \times 2.64 \text{ t/m}^3 \text{ (glauconite density)}/100 = 0.8712 \text{ t/m}^3$
- Glauconite estimated tonnage within polygon: $\text{glauconite density } 0.8712 \text{ t/m}^3 \times 1.48818 \times 10^9 \text{ m}^3 \text{ (volume)} = 1296502416 \text{ t} = 1297 \text{ Mt}$

- Total resource estimate in $\geq 50 \text{ wt\% glauconite polygons}$: $181 \text{ Mt} + 299 \text{ Mt} + 391 \text{ Mt} + 1297 \text{ Mt} = 2168 \text{ Mt} = \sim 2 \text{ Bt glauconite}$.

Full resource estimate calculate procedures:

The full resource estimate calculations were made in Excel, therefore this Excel spreadsheet can be found in the digital appendices (VII) CD located at the back of this thesis.